

---

# VISIBLE LIGHT-TRIGGERED PRECURSOR MOLECULES: RELATING REACTIVITY AND ULTRAFAST DYNAMICS

Zur Erlangung des akademischen Grades eines

DOKTORS DER NATURWISSENSCHAFTEN

(Dr. rer. nat.)

von der KIT-Fakultät für Chemie und Biowissenschaften

des Karlsruher Instituts für Technologie (KIT)

genehmigte

DISSERTATION

von

Philipp Jöckle

aus

Bellheim

Dekan: Prof. Dr. Reinhard Fischer

Referent: PD Dr. Andreas-Neil Unterreiner

Korreferent: Prof. Dr. Christopher Barner-Kowollik

Tag der mündlichen Prüfung: 25.07.2019



## Danksagung

Ich möchte mich bei allen bedanken, die zum Gelingen meiner Dissertation beigetragen haben.

Allen voran bedanke ich mich herzlichst bei PD Dr. Andreas-Neil Unterreiner und Prof. Dr. Christopher Barner-Kowollik, die mir dieses spannende Projekt erst ermöglicht haben. Ich habe die persönliche Betreuung einschließlich der lehrreichen Diskussionen und humorvollen Unterhaltungen immer sehr geschätzt. Darüber hinaus war der internationale Austausch eine sehr große Bereicherung für mich.

Besonderen Dank möchte ich an Dr. Caroline Schweigert, Nadine Michenfelder, Julia Leier, Dr. Markus Zieger, Dennis Gratzfeld, Leonie Golka, Dr. Dominik Voll, Dr. Sarah Walden und Desmond Kelly für die nützlichen Korrekturen und Diskussionen während der Anfertigung der vorliegenden Arbeit richten.

Ich bedanke mich bei der Firma Ivoclar für die finanzielle Unterstützung sowie für die anregenden Diskussionen bei unseren gemeinsamen Projekttreffen in Liechtenstein. Besonders möchte ich mich dabei bei Herrn Prof. Dr. Norbert Moszner und Frau Dr. Iris Lamparth für die Synthesen, den freundlichen Umgang und die effektive Zusammenarbeit bedanken. In diesem Zusammenhang bedanke ich mich auch bei den Kollegen der TU Graz Judith Radebner, Michael Haas und Prof. Dr. Harald Stüger für die erfolgreiche Kooperation, sowie Anna Eibel und Prof. Dr. Georg Gescheidt für den anregenden Austausch.

Ich bedanke mich bei Waldemar Konrad, Dr. Eva Blasco und Carolin Heiler für die Synthesen und Diskussionen bezüglich des Tetrazol-Projekts.

Vielen Dank an Herrn Prof. Dr. Hans-Achim Wagenknecht und an das Graduiertenkolleg der Deutschen Forschungsgemeinschaft (GRK2039) für die finanzielle Unterstützung und den interdisziplinären Austausch bei Tagungen. Ich danke dabei allen Mitgliedern für das angenehme Miteinander.

Dank gilt dem Deutschen Akademischen Austauschdienst (DAAD) welcher mich bei meinem Forschungsaufenthalt in Australien finanziell unterstützt hat.

Herzlichen Dank an meine beiden Arbeitskreise für die stetige Hilfsbereitschaft, angenehme Arbeitsatmosphäre und unterhaltsamen Mittagspausen. Insbesondere möchte ich mich bei Dr. Caroline Schweigert, Philipp Kamm, Andrea Lauer, Nadine Michenfelder, Julia Leier, Philipp Menzel, Waldemar Konrad und Dr. Markus Zieger für die Zusammenarbeit und vielen anregenden Diskussionen bedanken.

Vielen Dank an Waldemar Konrad, Andrea Lauer, Janin Offenloch und Charlotte Petite für die ständige Wartung des Massenspektrometers, sodass meine Messkampagnen erfolgreich sein konnten. Dank an Lukas Michalek und Dr. Markus Zieger für die XPS-, beziehungsweise NMR-Messungen im Stannan-Projekt. Außerdem bedanke ich mich bei Dennis Haffner für die Quantenausbeutenbestimmung der Acyl-basierten Photoinitiatoren.

Ich bedanke mich bei Patricia Hibomvshi, Desmond Kelly, Evelyn Stühling, Dr. Anja Goldmann, Daniela Rohmert-Hug, Olivia Spanier und Vera Noga für die technische und organisatorische Unterstützung. Vielen Dank für die Beratung von Dr. Sebastian Höfener bei quantenchemischen Fragestellungen sowie für die Unterstützung von Wolfram Feuerstein bei der Einarbeitung in Turbomole.

Besonders herzlichen Dank an meine Familie und Freunde die immer für mich da sind.

# Table of Contents

<b>Summary .....</b>	<b>I</b>
<b>Zusammenfassung.....</b>	<b>III</b>
<b>List of Abbreviations.....</b>	<b>V</b>
<b>1. Introduction.....</b>	<b>1</b>
<b>2. Fundamentals.....</b>	<b>4</b>
2.1 Photophysical and -Chemical Processes in Molecules.....	4
2.2 (Photo-Initiated) Free Radical Polymerization (FRP).....	12
2.3 Nitrile Imine-Mediated Tetrazole-Ene Cycloaddition (NITEC).....	16
2.4 Laser Optics .....	17
2.4.1 Laser Principle and Laser Pulses.....	18
2.4.2 Nonlinear Optics and Parametric Processes.....	21
2.4.3 Generation of ns-Laser Pulses: Q-Switch .....	25
2.4.4 Generation of fs-Laser Pulses: Mode-Locking .....	26
2.4.5 Transient Broadband Absorption Spectroscopy (fs-TA).....	28
2.5 Mass Spectrometry (MS).....	30
2.5.1 Ion Source: Electrospray Ionization (ESI) .....	31
2.5.2 Mass Analyzer: Orbitrap .....	32
2.5.3 Pulsed Laser Polymerization (PLP) Coupled with SEC-ESI-MS.....	33
2.6 Computational Quantum Chemistry.....	34
2.6.1 Density Functional Theory (DFT) .....	34
2.6.2 Time-Dependent Density Functional Theory (TDDFT).....	36
<b>3. Methods .....</b>	<b>38</b>
3.1 Materials.....	38
3.2 Steady-State Spectroscopy.....	38
3.2.1 UV/Vis Absorption Spectroscopy .....	38
3.2.2 Fluorescence Spectroscopy.....	39

3.3	Pulsed Laser Polymerization coupled with Electrospray Ionization Mass spectrometry (PLP-ESI-MS).....	40
3.3.1	Pulsed Laser Polymerization (PLP) .....	40
3.3.2	Size Exclusion Chromatography (SEC) and Direct Infusion (DI) Electrospray Orbitrap Mass Spectrometry (ESI-MS).....	42
3.4	Time Resolved Spectroscopy.....	43
3.4.1	Time-Correlated Single Photon Counting (TCSPC).....	43
3.4.2	Transient Broadband Absorption Spectroscopy (fs-TA).....	44
3.5	Computational Methods.....	48
3.5.1	Time-Dependent Density Functional Theory (TDDFT) Calculations .....	48
<b>4.</b>	<b>Acylgermane-Based Visible Light Photoinitiators .....</b>	<b>49</b>
4.1	Steady-State Spectroscopic Properties.....	52
4.1.1	Absorption and Luminescence Properties of Exemplary Acylgermanes	53
4.1.2	Extinction Coefficients of <i>Para</i> -Fluoro and Methoxy-substituted Mono-, Bis- and Tetraacylgermanes .....	55
4.2	PLP-ESI-MS End Group Analysis: Initiating Radicals.....	56
4.2.1	Radical Fragments of Efficient Monoacylgermane-Derivatives .....	57
4.2.2	Radical Fragments of Weak Monoacylgermanes-Derivatives.....	59
4.2.3	Bis- and Tetraacylgermanes: Prediction of Germane-Centered n-Fold Star Polymers .....	65
4.3	PLP-ESI-MS Cocktail Experiments: Overall Initiation Efficiency of Benzoyl-Radicals .....	75
4.3.1	Quantification of Overall Initiation Efficiencies in Cocktail-Experiments	77
4.3.2	Excursus: Automated Evaluation of PLP-ESI-MS Cocktail Experiments	85
4.3.3	An Intrinsic Validation: Calculation with Overall Initiation Efficiencies...	86
4.3.4	Non-Stoichiometric Size-Dependence .....	88
4.3.5	Outlook: PLP-ESI-MS Cocktail-Experiments with Ortho-Substituted Tetraacylgermanes .....	91
4.4	fs-TA Investigations on Acylgermanes .....	92

4.4.1	<i>para</i> -Substitution Pattern-Dependent Photophysics of Monoacylgermane Derivatives .....	93
4.4.2	Efficient Tetraacylgermanes.....	102
4.5	Summary and Outlook Acylgermanes .....	110
4.5.1	Outlook I: wavelength-dependent PLP-conversion experiments.....	111
4.5.2	Outlook II: fs- vs. ns-Pulsed Laser Polymerization.....	112
<b>5.</b>	<b>Tin-Based Visible Light Initiators .....</b>	<b>115</b>
5.1	Stability of Triphenylbenzoyl- and Tetramesitoylstannane.....	116
5.2	PLP-ESI-MS Investigations on Tetramesitoylstannane .....	117
5.2.1	PLP-ESI-MS End Group Analysis of Tetramesitoylstannane .....	118
5.2.2	PLP-ESI-MS Cocktail Experiment of Tetramesitoylstannane.....	119
5.3	fs-TA Investigation on Tetramesitoylstannane.....	121
5.4	Summary Tetramesitoylstannane.....	123
<b>6.</b>	<b>Investigation on Visible Light-Triggered Tetrazoles via fs-TA.....</b>	<b>124</b>
6.1	Steady-State Fluorescence Spectra of Tet, PyTet, BiphTet in DCM and Quenching Effects of IEt.....	125
6.2	fs-TA: Investigation on Diaryl-Tetrazoles in DCM.....	127
6.2.1	Tet in DCM.....	127
6.2.2	PyTet in DCM.....	129
6.2.3	BiphTet in DCM.....	142
6.2.4	Summary and Outlook: Visible Light-Triggered Diaryl-Tetrazoles.....	148
<b>7.</b>	<b>Outlook: Visible Light-Triggered Precursor Molecules .....</b>	<b>150</b>
<b>A.</b>	<b>Appendix of Chapter 4.....</b>	<b>154</b>
<b>B.</b>	<b>Appendix of Chapter 5.....</b>	<b>205</b>
<b>C.</b>	<b>Appendix of Chapter 6.....</b>	<b>210</b>
	<b>References .....</b>	<b>222</b>
	<b>List of Publications.....</b>	<b>230</b>



## Summary

The present investigation focuses on the relationship between the reactivity and ultrafast dynamics of two examples for visible light-triggered precursor molecules.

First, a library of fourteen acylgermane derivatives as well as one tetramesitylstannane visible light-triggered Norrish type I photoinitiator used for free radical polymerization (FRP) between 400-490 nm were characterized in their initiation efficiency via pulsed laser polymerization coupled with electrospray orbitrap mass spectrometry (PLP-ESI-MS). The results were correlated to ultrafast dynamics obtained via transient broadband absorption spectroscopy (fs-TA) supported by time-dependent density functional theory (TDDFT). Remarkably, an unexpected non-stoichiometric increase of 40-100 % in the overall initiation efficiency is observed, which scales with the number of benzoyl moieties for mono-, bis-, and tetraacylgermanes, e.g. a factor of  $8.13 \pm 0.76$  for tetrabenzoylgermane versus benzoyltrimethylgermane. The result is in accordance with a much faster primary radical formation within 70-127 ps in comparison to the cleavage expected on a post-ns time scale for bis- and monoacylgermanes. In addition, a multiple cleavage mechanism for bis- and tetraacylgermanes is evidenced via a new developed prediction method for isotopic patterns of n-armed star polymers. The size-dependence is partially correlated to the maximal  $n\pi^*$ -extinction coefficients. However, substitution patterns in *para*-position of the benzoyl moieties lead to higher deviations from this correlation due to a strong influence of the substituents on the potential energy surfaces of the excited states. Based on a model study on five benzoyltrimethylgermanes, electron withdrawing groups (Cyano, Nitro) lead to a fast relaxation via internal conversion (IC), within 2-12 ps, back to ground states after photoexcitation, which can be correlated to a weak initiation efficiency (monomer conversion 0.1-1% at high total irradiation energies of ~110 J). In contrast, donating-*para*-substituents show an ultrafast intersystem crossing (ISC) within a 2-4 ps leading to efficient initiation of FRP (monomer conversion of 4-5 % at total irradiation energies of ~30 J).

The tetramesitylstannane indicates a factor two lower overall initiation efficiency than tetrabenzoylgermane, which can be correlated to a reduced ground state stability and dominant ultrafast relaxation pathway (~90 %) from singlet states competing with ISC within hundreds of fs. Consequently, the radical formation via triplet states and, in turn, the initiation efficiency is reduced.

Second, two visible 2-phenyl-5-pyrene- (PyTet) and 2-phenyl-5-biphenyl- (BiphTet) and one UV light-triggered 2,5-diphenyl-tetrazole (Tet) applied for nitrile imine-mediated tetrazole-ene cycloaddition (NITEC) reactions are investigated via fs-TA in dichloromethane (DCM) as a solvent. Herein, the transient spectra of BiphTet and PyTet are dominated by singlet state dynamics after excitation at 400 nm in accordance to high fluorescence quantum yields  $\Phi_F$  of ~8 and ~11 % as well as lifetimes of 1.3 and 1.8 ns, respectively. By utilizing iodoethane (IEt) as a fluorescence quencher in fs-TA, a long-living triplet state in PyTet is revealed, while stimulated emission is quenched in accordance with a reduced  $\Phi_F$  from 8.3 to 6.7 %. In turn, an ISC within ~500 fs is determined in line with the non-fluorescent reference system Tet. In contrast, the transient spectrum of BiphTet is exclusively dominated by singlet dynamics. In comparison with literature-known reactivity properties of PyTet and Tet, the nitrile imine intermediate formation can be considered to proceed from excited triplet states, while BiphTet is deactivated via singlet dynamics due to insufficient ISC probability.

The present thesis exemplifies, in turn, the deep relationship between the reactivity and ultrafast dynamics of visible light-triggered precursor molecules.

## Zusammenfassung

Die vorliegende Untersuchung konzentriert sich auf Korrelationen zwischen Reaktivität und ultraschneller Dynamik für zwei Arten von reaktionsauslösenden Molekülen, welche mit sichtbarem Licht angeregt werden können.

In einer ersten Untersuchung wurde eine Bibliothek von vierzehn Acylgermanen sowie einem Tetramesitylgermanen mittels gepulster Laser Polymerisation, gekoppelt mit Elektrosprüh-Ionisations Massenspektrometrie (PLP-ESI-MS), transientser Breitbandabsorptionsspektroskopie (fs-TA) und zeitabhängiger Dichtefunktionaltheorie (TDDFT) in Nettoinitierungseffizienz und ultraschneller Dynamik charakterisiert. Es handelt sich bei den untersuchten Verbindungen um Norrish Typ I Photoinitiatoren, welche für photoinduzierte freie radikalische Polymerisation (FRP) im Wellenlängenbereich von 400-490 nm verwendet werden. Bei der Untersuchung der Nettoinitierungseffizienz von Mono-, Bis- und Tetraacylgermanen wurde ein herausragender nicht-stöchiometrischer Anstieg von 40-100 % beobachtet, welcher mit der Anzahl an Benzoyleinheiten skaliert. Zum Beispiel konnte ein Faktor von  $8.13 \pm 0.76$  für ein Tetrabenzoylgerman im Vergleich zu einem Benzoyltrimethylgerman bestimmt werden. Die am höchsten beobachtete Nettoinitierungseffizienz für Tetraacylgermane korreliert dabei mit einer deutlich schnelleren primären Radikalbildung innerhalb von 70-127 ps im Unterschied zu Bis- und Monoacylgermanen, welche vermutlich auf einer ns-Skala spalten. Außerdem zeigen Bis- und Tetraacylgermane ein ausgeprägtes Mehrfachspaltungsverhalten, welches mittels einer neu entwickelten Vorhersagemethode für Isotopenmuster von n-armigen Sternpolymeren nachgewiesen wurde. Die beobachtete Größenabhängigkeit korreliert teilweise mit den  $n\pi^*$ -Extinktionskoeffizienten. Allerdings führen Substitutionsmuster in *para*-Position der Benzoyleinheiten zu größeren Abweichungen von 20-50 %, die durch einen starken Einfluss der Substituenten auf die Potentialhyperflächen in den angeregten Zuständen verursacht werden. Eine Modellstudie an fünf *para*-substituierten Benzoyltrimethylgerman-Derivaten zeigt, dass Initiatoren mit Elektronen-ziehenden Gruppen (Cyano, Nitro) eine schnelle Relaxation mittels innerer Konversion (IC) innerhalb von 2-12 ps zurück in den Grundzustand bevorzugen, was mit einer schwachen Initiierungseffizienz korreliert (Monomerumsatz von 0.1-1 % bei maximalen Einstrahlungsenergien von  $\sim 110$  J). Dagegen offenbarten Initiatoren mit Elektronen-drückenden *para*-Substituenten (Fluoro, Methoxy) eine ultraschnelle Interkombination (ISC) in

angeregte Tripletzustände innerhalb von 2-4 ps. Dieser Befund kann dabei mit einer effizienten Initiierung in FRP korreliert werden (Monomerumsatz von 4-5 % bei maximalen Einstrahlungsenergien von ~30 J).

Das Tetramesitoylstannan weist eine um den Faktor 0.5 reduzierte Nettoinitiierungseffizienz im Vergleich zum Tetrabenzoylgerman auf. Die Ursache liegt dafür in einer geringeren Grundzustandsstabilität sowie einer dominierenden Singulett-Relaxation (90 %) innerhalb von hunderten von fs, die in Konkurrenz zu einem ISC und möglicher Radikalbildung steht.

In einer zweiten Studie wurden die mit sichtbarem Licht anregbaren 2-Phenyl-5-Pyren- (PyTet), 2-Phenyl-5-Biphenyl- (BiphTet) und ein UV-anregbares 2,5-Diphenyl-Tetrazol (Tet) gelöst in Dichloromethane (DCM) mittels fs-TA untersucht. Die Verbindungen werden als Startermoleküle in Nitril-Imin-vermittelte Tetrazol-Ene Zykloadditionen (NITEC) eingesetzt. In Übereinstimmung mit hohen Fluoreszenzquantenausbeuten  $\Phi_F$  von ~8 und 11 %, sowie mit Lebenszeiten von 1.3 beziehungsweise 1.8 ns zeigen die transienten Spektren von PyTet und BiphTet eine dominierende Singulettynamik nach Anregung mit sichtbarem Licht bei 400 nm. Durch die Fluoreszenz-löschenden Eigenschaften von Iodethan wurde ein langlebiger Tripletzustand in PyTet im Einklang mit reduzierten  $\Phi_F$  von 8.3 nach 6.7 % nachgewiesen. In Konsistenz mit dem nicht-fluoreszierenden Referenzsystem Tet zeigt PyTet folglich ein ultraschnelles ISC innerhalb von ~500 fs. Im Unterschied dazu ist das transiente Spektrum von BiphTet ausschließlich von einer Singulettynamik dominiert. Im Vergleich zu Literatur-bekanntem Reaktionseigenschaften von PyTet und Tet kann die Bildung des Nitril-Imin-Intermediates aus einem angeregten Tripletzustand angenommen werden, während BiphTet mittels Singulettrelaxation deaktiviert wird.

In der vorliegenden Arbeit wurde damit der tiefgreifende Zusammenhang zwischen Reaktivität und ultraschneller Dynamik an zwei beispielhaften Studien verdeutlicht.

## List of Abbreviations

AcN	acetonitrile
B <sub>1</sub> G	benzoyltrimethylgermane
B <sub>2</sub> G	bisbenzoyldiethylgermane
BBO	β-barium borate
BiBuQ	4,4-bis-(2-butyloctyloxy)-p-quaterphenyl
BiphTet	2-dimethylaminobiphenyl-5-phenyl-tetrazole
BS	beam splitter
C307	coumarin 307
CaF <sub>2</sub>	calcium fluoride
CB <sub>1</sub> G	<i>para</i> -cyano-benzoyltrimethylgermane
CIDNP	chemical induced dynamic nuclear polymerization
CPA	chirped pulse amplification
DAS	decay associated spectra
DCM	dichloromethane
DFM	difference frequency mixing
DFT	density functional theory
DI	direct infusion
EI	electron ionization
ESA	excited state absorption
ESI	electrospray ionization
ESI-MS	electrospray mass spectrometry
ESR	electron spin resonance spectroscopy
FB <sub>1</sub> G	<i>para</i> -fluoro-benzoyltrimethylgermane
FB <sub>2</sub> G	bis- <i>para</i> -fluoro-benzoyldiethylgermane
FCF	Franck-Condon Factor
FFT	fast Fourier-transformation
FM	focusing mirror
FRP	free radical polymerization
fs-TA	transient broadband absorption spectroscopy
FT-ICR	Fourier transform ion cyclotron resonance
GSB	ground state bleaching
GVM	group-velocity mismatch
HAE	heavy-atom-effect

HGSA	hot ground state absorption
HPLC	high-performance liquid chromatography
IC	internal conversion
IEt	iodoethane
ISC	intersystem crossing
IVR	vibrational energy redistribution
KML	Kerr-lens mode-locking
LASER	light amplification by stimulated emission of radiation
LBO	lithium triborate
m/z	mass-to-charge ratio
MALDI	matrix assisted laser desorption ionization
MB <sub>1</sub> G	<i>para</i> -methoxy-benzoyltrimethylgermane
MB <sub>2</sub> G	bis- <i>para</i> -methoxy-benzoyldiethylgermane
MB <sub>4</sub> G	tetra- <i>para</i> -methoxy-benzoylgermane
MeOH	methanol
Mes <sub>4</sub> T	tetramesitylstannane
MMA	methyl methacrylate
MS	mass spectrometry
NaTFA	Sodium trifluoroacetate
NB <sub>1</sub> G	<i>para</i> -nitro-benzoyltrimethylgermane
ND	neutral density
Nd:YAG	neodym-doped yttrium aluminum garnet
Nd:YLF	neodym-doped yttrium lithium fluoride
NITEC	nitrile imine-mediated tetrazole-ene cycloaddition
NMR	nuclear magnetic spin resonance
NOPA	non-collinear optical parametric amplification
NR	Newton-Raphson-method
OD	optical density
oEtB <sub>4</sub> G	tetra- <i>ortho</i> -ethyl-benzoylgermane
oMeB <sub>4</sub> G	tetra- <i>ortho</i> -methyl-benzoylgermane
OPA	optical parametric amplification
Φ <sub>F</sub>	fluorescence quantum yield
PLP	pulsed laser polymerization
PMMA	poly(methyl methacrylate)

PrOB <sub>4</sub> G	tetra- <i>para</i> -propoxy-benzoylgermane
PyTet	2-pyrenel-5-pyrene-tetrazole
RGA	regenerative amplifier
SCF	self-consistent field
SE	stimulated emission
SEC	size-exclusion chromatography
SFM	sum frequency mixing
SG	Schrödinger equation
SHG	second harmonic generation
SIMS	secondary ion mass spectrometry
SOC	spin-orbit coupling
SPM	self-phase modulation
TA	transient absorption
TCSPC	time-correlated single photon counting
TDDFT	time-dependent density functional theory
TD-R	time-dependent response theory
TEMPO	4-carboxy-2,2,6,6-tetra methyl piperidine 1-oxyl
Tet	2-5-diphenyl-tetrazole
THF	tetrahydrofuran
TPBT	triphenylbenzoylstannane
UV/Vis-spectrum	steady-state UV/Vis absorption spectrum
VR	vibrational relaxation
XPS	solid-state X-ray photoelectron spectroscopy



# 1. Introduction

Visible light induced phenomena in nature are usually determined at much earlier times than the consequences can be experienced by human perception. A prominent example is the light-triggered cis/trans-isomerization of retinal in vision,<sup>1</sup> which is the starting point for a cascade of photophysical and -chemical events leading to an image in brain. The absorption as well as the subsequent cis/trans isomerization of retinal occur on a ultrafast time scale within femtoseconds ( $1 \text{ fs} \cong 10^{-15} \text{ s}$ ), while the reaction time of a human is in the order of milliseconds ( $1 \text{ ms} \cong 10^{-3} \text{ s}$ ). Thus, the first trigger to final experience is temporally separated by a factor of a trillion ( $10^{12}$ ). For comparison, a factor of a trillion approximately separates the time span of one day ( $8.6 \cdot 10^4 \text{ s}$ ) in relation to the age of the earth (4.5 billion years  $\approx 1.4 \cdot 10^{17} \text{ s}$ ). Since Ahmed H. Zewail has introduced femtochemistry in the 1980s,<sup>2</sup> the observation of ultrafast photophysical and -chemical processes is possible by utilizing transient laser spectroscopy with fs-time resolution.<sup>3</sup> Herein, a powerful tool was presented to investigate the ultrafast dynamics, which are crucial for subsequent chemical reactions. Besides the cis/trans isomerization of retinal, many more examples in photochemistry are determined by ultrafast dynamics, e.g. photo-switching used for cell-imaging and drug delivery<sup>4-6</sup> as well as photo-triggered intermediate formation for chemical reactions.<sup>7-8</sup>

Ultrafast dynamics are defined by the channel branching of photophysical and -chemical processes within the electronic excited states after photoexcitation.<sup>9</sup> After light absorption of the ground state, an excited singlet state is populated, from which different relaxation pathways are available, e.g. radiationless relaxation pathways via internal conversion (IC) back to the ground state or intersystem crossing (ISC) into triplet states. All relaxation pathways are accompanied by vibrational relaxation (VR). In addition, photochemical reactions can occur from excited singlet and triplet states. Further, radiative relaxation processes can proceed from the lowest excited electronic and vibrational state after IC and VR (Kasha's rule) into the ground state, which can occur from singlet and triplet states as known as fluorescence and phosphorescence, respectively. ISC is a so-called spin-forbidden process, which is nevertheless enabled by the spin-orbit coupling (SOC) of the system.<sup>10</sup> SOC can be increased by internal or external perturbation of heavy-atoms (Kasha effect, or heavy-atom-effect, HAE),<sup>11-12</sup> which enhances singlet-triplet transitions with the consequence of quench-

ing competing singlet relaxation pathways, e.g. fluorescence. An in-depth understanding of the outlined channel branching is important for modern photochemistry, i.e. faces the tailor-made synthesis of light-triggered applications.<sup>13-14</sup>

In particular, photoinitiators – or more general – precursors with visible light absorption properties are highly desired in scientific and industrial research, e.g. for photo-induced free radical polymerization (FRP) applied in curing technologies,<sup>15-20</sup> or nitrile imine-mediated tetrazole-ene cycloaddition (NITEC)<sup>14, 21</sup> used for ( $\lambda$ -orthogonal) polymer linkage,<sup>22-25</sup> fluorescence markers in biology,<sup>26-27</sup> and surface modifications.<sup>28-29</sup> Red-shifted wavelengths within the visible spectrum of light (400-700 nm) have the advantage of bioorthogonality and higher penetration depths. In a simplified view, (visible) light-triggered precursors consist of a photon-absorbing chromophoric moiety and functionality, which lead to reaction, or intermediate formation, after photoexcitation. Hence, the design of visible light-triggered precursors is critically depending on the complex interplay of absorption and reactivity units featuring a specific channel branching within the excited states. For instance, apparently suitable chromophores can change the potential energy surface topology resulting in insufficient reactivity.<sup>30-31</sup> Thus, the correlation of reactivity properties with ultrafast dynamics of the molecule is required for a systematic mechanistic investigation of light-triggered precursors, which can support the tailor-made synthesis.

In the present thesis a unique methodological combination of pulsed laser polymerization coupled with electrospray mass spectrometry (PLP-ESI-MS) and transient broadband absorption spectroscopy (fs-TA) supported by time-dependent density functional theory (TDDFT) calculations are applied to visible light-triggered photoinitiators used for FRP. The approach was introduced in previous collaborative studies of the Barner-Kowollik and Unterreiner groups,<sup>32-35</sup> which enables the correlation of the efficiency of photoinitiators after final macromolecular growth via PLP-ESI-MS (*post-mortem*) with the ultrafast excited state dynamics after photoexcitation via fs-TA (*in-situ*).

Promising examples for visible light-triggered photoinitiators with large structural variety are mono-, bis- and tetraacylgermanes. Pioneering experiments for the development of germanium-based initiators were done by Mochida *et al.* in the beginning 1980's.<sup>36-37</sup> Recently, mono-, bis- and tetraacylgermanes are developed with sufficient initiation efficiency at wavelengths between 400-450 nm within the visible spec-

trum of light.<sup>38-40</sup> In addition, the synthesis of a tetramesitylstannane compound was published in 2018,<sup>41</sup> which achieves a further red shift of its absorption spectrum up to 490 nm. In contrast to organo-germanium compounds, tin-containing systems show weaker covalent bonds, which can explain a further red shift but also probably lead to a reduced stability.<sup>42</sup> Based on laser flash photolysis coupled with UV/Vis spectroscopy<sup>38</sup>, actinometry,<sup>39</sup> electron spin resonance spectroscopy (ESR) and chemical induced dynamic nuclear polarization (CIDNP),<sup>43</sup> cleavage of acylgermanes is considered to occur via a Norrish type I mechanism. Norrish type I initiators are known for very fast radical formation from singlet or triplet states after photo-excitation, which is determined by the topology of the excited state energy surfaces.<sup>44</sup> For instance, differently substituted benzoin Norrish type I initiators show only an efficient initiation for derivatives featuring an ultrafast ISC (2-4 ps) into an energetically lower triplet state with  $n\pi^*$ -character and subsequent radical formation within ~50 ps.<sup>35</sup> In analogy, a recent theoretical study on different *para*-substituted monoacylgermanes considers an efficient ISC for precursors with electron donating substituents, while electron withdrawing substituents are expected to induce a higher probability for relaxation pathways back to the ground state.<sup>31</sup> In addition, the cleavage of bisbenzoyldiethylgermane is reported to occur on a ns-time scale after a ultrafast ISC within tens of ps.<sup>43</sup>

Within the present thesis, the overall initiation efficiency of diversely *para*-substituted mono-, bis-, and tetraacylgermanes with different system sizes is quantified in so-called PLP-ESI-MS cocktail experiments after final macromolecular growth. In addition, the relevant radicals for FRP are identified via PLP-ESI-MS end group analysis. Subsequently, the initiation properties of the initiators are correlated with excited state dynamics obtained from fs-TA. For extension of the systematic methodological approach, one tetramesitylstannane is additionally investigated. Hence, mechanistic models from first excitation to final macromolecular growth are developed for a comprehensive library of initiators. The results are critically discussed with respect to publications.

Within a second project, the interplay between chromophoric and reactivity properties for visible light-triggered diaryl-tetrazoles is investigated via transient and steady-state spectroscopy. UV-driven 2-5-diphenyl-tetrazoles have been used as precursors for NITEC since 1967,<sup>45</sup> while the visible light-triggered systems have been very re-

cently developed.<sup>14</sup> Red-shifting of the absorption spectrum of diaryl-tetrazoles can be achieved by substitution in 5-N-position of the phenyl ring with larger aromatic chromophores, e.g. pyrene,<sup>21</sup> or biphenyl moieties.<sup>30</sup> Herein, 2-pyrene-5-phenyl-tetrazole (PyTet) features an efficient NITEC reaction, while the 2-dimethylaminobiphenyl-5-phenyl-tetrazole (BiphTet) is not reactive towards alkene species, e.g. maleimides.<sup>21, 30</sup> In addition, both systems show a strong fluorescence pathway.<sup>21, 30</sup> Based on quantum chemical calculations, the formation of the nitrile imine intermediate is expected to occur from triplet states after sufficient ISC.<sup>30, 46</sup> However, N<sub>2</sub>-release via singlet states cannot be safely excluded in line with calculations on high energetic tetrazole compounds.<sup>47</sup> Furthermore, the photophysical mechanism after light excitation has not been investigated by experiments, yet.

Within the present thesis, a photophysical and -chemical mechanism of two visible light-triggered tetrazoles (PyTet, BiphTet) and 2-5-diphenyl-tetrazole (Tet) as an UV-reference system, dissolved in dichloromethane (DCM) is developed on a ps-to-ns time scale via transient and steady-state UV/Vis-absorption, as well as fluorescence spectroscopy. In particular, the fluorescence properties of PyTet and BiphTet hamper the spectroscopic investigation. Thus, fluorescence quencher molecules are utilized to elucidate possible triplet state dynamics of the visible light tetrazoles. The results are related to the corresponding NITEC-reactivity known from literature.<sup>30</sup>

## 2. Fundamentals

In the following, a general overview is given on the photophysical and -chemical properties of molecules with respect to radical polymerization and ligation reactions. Subsequently, the necessary methodological fundamentals are presented, e.g. non-linear optics, mass spectrometry, and quantum chemistry.

### 2.1 Photophysical and -Chemical Processes in Molecules

A fundamental property of molecules is the ability to absorb photons, which leads to the population of electronic excited states. The dynamics of the excited state population are determined by the photophysical and -chemical processes of the molecule. In general, photophysical processes can be defined as transitions between potential energy surfaces of the excited states as well as between the excited states and the ground state of a molecule, e.g. fluorescence, or ISC.<sup>48</sup> In contrast, photochemical

processes lead to change in the chemistry of the molecule after photoexcitation, e.g. cleavage reactions or formation of intermediates.

As a result of perturbation theory of the time-dependent Schrödinger equation, the rate of an electronic transition  $i \rightarrow f$  between an initial state  $\psi^i$  and a final state  $\psi^f$  is given by Fermi's golden rule (**Eq 2.1**).<sup>49</sup>

$$\text{rate}_{i \rightarrow f} = \frac{2\pi}{h} \rho \langle H' \rangle^2. \quad \text{Eq 2.1}$$

$h$  is the Planck constant,  $\rho$  is the density of states, and  $\langle H' \rangle^2$  is the square value of the matrix element for the perturbation coupling the initial and final states. Thus, the rate of a transition depends on the number of accessible final states, which are coupled to the initial states in the order of magnitude of the matrix element.<sup>48</sup> Thus, the selection rules of a transition, in turn, can be derived from the condition  $\langle H' \rangle = 0$ . Herein, if a transition is "allowed" or "forbidden" depends on the character of orbitals involved, Franck-Condon-factors (FCF), and SOC.<sup>48</sup> Examples for "allowed" and "forbidden" transitions in molecules are presented in the following.

Complex molecules with many degrees of freedom feature a manifold of excited states, which leads to channel branching of photophysical and -chemical processes. The characterization of the channel branching is crucial for the development of a mechanism for the excited state dynamics. A simple and powerful tool to sketch excited dynamics of complex molecules is the Jabłoński diagram.<sup>50</sup> Herein, potential energy surfaces of the excited states are simplified to energy levels, while arrows indicate the photophysical and -chemical processes. An example Jabłoński diagram including the most important processes is presented in **Figure 2.1**.

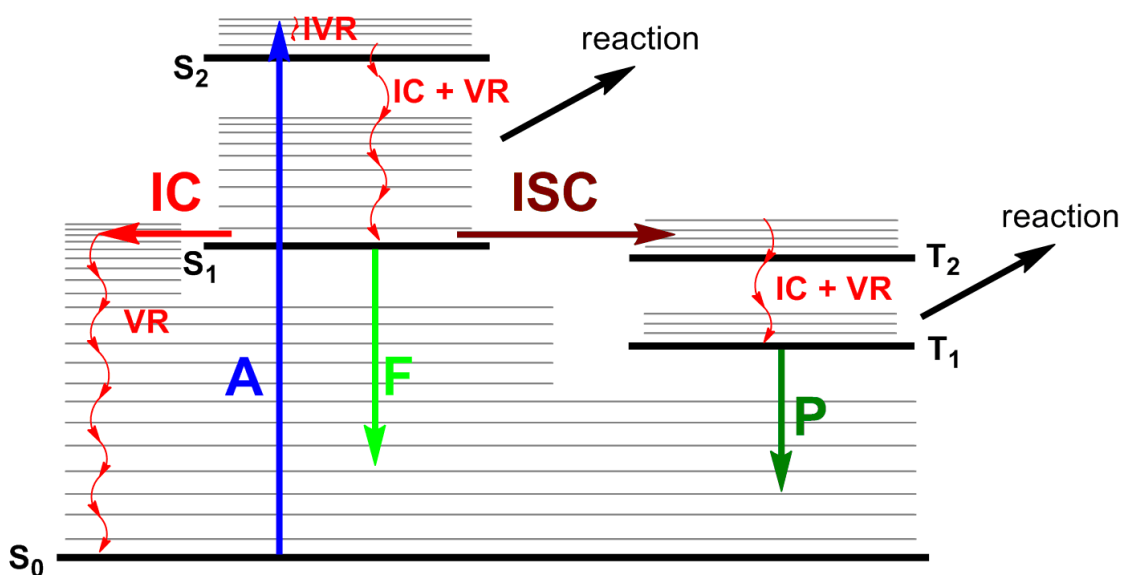


**Figure 2.1.** Jablonski diagram depicting electronic energy levels (black lines) and vibrational energy levels (grey lines) of the ground state  $S_0$  and the first two excited singlet  $S_{1,2}$  and triplet states  $T_{1,2}$ . Arrows indicate the most important photophysical and -chemical processes: Absorption (A) in blue, radiative relaxation pathways of spin-allowed fluorescence (F) in green and spin-forbidden phosphorescence (P) in dark green. Radiationless relaxation pathways of spin-allowed internal conversion (IC) and vibrational relaxation (VR) in red color, and spin-forbidden intersystem crossing (ISC) in dark red color. Photochemical reactions from singlet and triplet states are depicted in black arrows.

The absorption (A, **Figure 2.1**) of a photon leads to transitions from the ground state  $S_0$  into higher vibration levels (grey lines) of an excited singlet state, e.g.  $S_2$ . Experimentally, absorption can be measured by recording the optical density OD in steady-state UV/Vis spectroscopy by comparison of an incident  $I_0$  and passed light intensity  $I$  after the sample for a certain concentration  $c$  and optical pathlength  $l$ , and the molecule-specific extinction coefficient  $\epsilon$ , which is given by Beer-Lambert's law in **Eq 2.2**.<sup>51</sup>

$$OD = \log\left(\frac{I_0}{I}\right) = \epsilon c l. \quad \text{Eq 2.2}$$

Immediately after absorption, the population of excited molecules is cumulated in a higher vibrational level of the excited state under conservation of the initial ground state geometry due to the Franck-Condon principle (more details below). Subsequently, the population is redistributed to adjacent vibrational modes on an ultrafast scale  $\sim 10^{11}$ - $10^{13}$  s<sup>-1</sup>, which is known as intramolecular vibrational energy redistribution (IVR).<sup>48</sup> In addition, interactions with the environment lead to energy dissipation

(heat) via VR. For example, the environment of a solvent provides a manifold of rotational, vibrational and translation modes, which can assimilate the dissipating heat from the VR of the molecule featuring ultrafast rates of  $10^9$ - $10^{11}$  s<sup>-1</sup>.<sup>48</sup>

Accompanied by VR, non-radiative “allowed” transitions between potential surfaces of the same spin-multiplicity can occur from higher to lower energy levels via IC, e.g. between singlet states  $S_2 \rightarrow S_1$ ,  $S_1 \rightarrow S_0$  or triplet states  $T_2 \rightarrow T_1$  (**Figure 2.1**). The rate of IC is in general higher between higher excited states than between an excited state and the ground state due to an increased density of states.<sup>48</sup> However, ultrafast relaxation via IC from excited to ground states is possible for very close lying potential energy surfaces due to non-adiabatic effects leading to conical intersections, e.g. the photoisomerization event in vision or sigmatropic H-shift of cycloheptatriene derivatives.<sup>1, 52-55</sup> Non-adiabatic effects are caused by vibronic coupling of the electrons to the nuclei between different states, which leads to the breakdown of the Born-Oppenheimer approximation by mixing of states.<sup>48, 54</sup> A conical intersection is a (3N-8)-dimensional seam (N: number of atoms), where the relevant coordinates of the potential energy surfaces are curved to one very efficient relaxation pathway.<sup>54, 56-58</sup>

For completeness, additional non-radiative deactivation can occur via predissociation, autoionization or energy transfer for a donor-acceptor pair.<sup>59</sup> However, these processes are only of minor interest within the scope of the present thesis.

Non-radiative “forbidden” transitions between excited states with different spin-multiplicity are called ISC, e.g. singlet-triplet transitions like  $S_1 \rightarrow T_2$ . In general, “forbidden” transitions are expected on a much longer time scale (ns-ms) than “allowed” transitions (fs-ns). In contrast, ISC within a few ps is literature-known for several compounds, e.g. Norrish type I photoinitiators.<sup>35, 60</sup>

Radiative relaxation pathways are fluorescence (F) and phosphorescence (P, **Figure 2.1**), which occur from lowest vibrational level of  $S_1$  and  $T_1$ , respectively (Kasha’s rule).<sup>9</sup> The reason for Kasha’s rule lies in the much faster VR and IC within the higher excited states. F is an “allowed” transition  $S_1 \rightarrow S_0$  between states with the same spin-multiplicity, while P is “forbidden” due to spin-flip during the transition  $T_1 \rightarrow S_0$ . Typical time scales for fluorescence and phosphorescence are  $10^{-12}$ - $10^{-6}$  s and  $10^{-6}$ - $10^{-1}$  s, respectively.<sup>51</sup>

Further, the population can leave the excited potential surfaces due to chemical reactions as indicated by black arrows in **Figure 2.1**, e.g. by formation of intermediates. The branching between the described processes is determined by the topology of the potential energy surfaces. For photochemistry, it is crucial to design molecules, which feature relaxation pathways leading to the desired reaction channels. For example, the cleavage of Norrish Type I photoinitiators into radical fragments used for radical polymerization occurs efficiently from excited triplet states.<sup>35, 60</sup> Thus, a precursory ISC is crucial, while relaxation pathways (IC+VR, F) back to ground states are competing. In general, the channel branching cannot be predicted due to missing information about the wave functions of the electronic states. However, a qualitative understanding can be achieved by a quantum dynamic view on the above described photophysical processes. In turn, quantum mechanical concepts for FCF and SOC are presented in greater detail, which are crucial for photochemistry in the scope of the present thesis.

### **Franck-Condon Factors, Oscillator Strengths and Extinction Coefficients**

Absorption is a radiation-induced transition from ground state to an electronic excited singlet state of a molecule, e.g.  $S_2 \leftarrow S_0$ , which results from perturbation of the dipole moments of electrons by the electric field of a photon. Thus, the rate of the absorption is proportional to the square value of the transition dipole moment  $|\mu_{fi}|^2 = \langle \psi^i | \hat{\mu} | \psi^f \rangle^2$  for the transition between the electronic states  $\psi^i$  and  $\psi^f$  (e.g.  $i = S_0$  and  $f = S_2$ ) and the dipole operator  $\hat{\mu}$ . Electron motions are considered to be much faster in comparison to the nucleus motions due to a factor  $\sim 10^{-3}$  lower mass, which allows the separation of the wave functions for electrons and nuclei (Born-Oppenheimer approximation)  $\psi^{i,f} = \psi_e^{i,f} \psi_v^{i,f}$ . In addition, the dipole operator can be split into electronic and nucleus contributions  $\hat{\mu} = \hat{\mu}_e + \hat{\mu}_N$ . Hence, the transition dipole moment can be written in **Eq 2.3**.<sup>61</sup>

$$\begin{aligned} \mu_{fi} &= \langle \psi^i | \hat{\mu} | \psi^f \rangle = \langle \psi_e^i \psi_v^i | \hat{\mu}_e + \hat{\mu}_N | \psi_e^f \psi_v^f \rangle \\ &\approx \langle \psi_e^i | \hat{\mu}_e | \psi_e^f \rangle \langle \psi_v^i | \psi_v^f \rangle = \langle \psi_e^i | \hat{\mu}_e | \psi_e^f \rangle \cdot S. \end{aligned} \tag{Eq 2.3}$$

Herein,  $S$  is the overlap integral of the wave functions in the initial and final state and the square value  $|S|^2$  is called the FCF.<sup>61</sup> The magnitude of the absorption can be expressed by the oscillator strength  $f$  (**Eq 2.4**).<sup>51, 61</sup>

$$f = \frac{4\pi m_e v_{fi}}{3e^2 \hbar} |\mu_{fi}|^2 \propto |S|^2. \quad \text{Eq 2.4}$$

$m_e$ : mass of electron,  $v_{fi}$ : resonance frequency for transition  $f \leftarrow i$ ,  $e$ : elementary charge.

In general, fully “allowed” transitions are reflected by  $f = 1$ , while “forbidden” transitions lead to much smaller oscillation strengths between  $10^{-5}$ - $10^{-4}$ .<sup>61</sup>

The extinction coefficient  $\varepsilon$  reflects the molecule specific absorption properties (refer to **Eq 2.2**), which is, in turn, proportional to the oscillator strength and consequently to the FCF as summarized in the following relation.<sup>51, 61</sup>

$$\varepsilon \propto f \propto |\mu_{fi}|^2 \propto |S|^2.$$

Thus, the maximal extinction coefficients are detected for vertical transitions from the ground state to excited states with the highest FCF of the corresponding vibrational wave functions under conservation of the initial ground state geometry of the nuclei. Herein, the FCF are the reason why an electronic excitation is always accompanied by vibrational relaxation processes (as described above) as the starting point for further branched relaxation processes, e.g. IC, F and ISC.

In general, FCF are valid for radiative transitions in general, e.g. absorption, excited state absorption (ESA), as well as stimulated emission, fluorescence and phosphorescence.<sup>48</sup> For example, the mirror-inverted shape of the fluorescence compared to the corresponding absorption spectrum is a result of Kasha’s rule and the FCF for similar potential energy surfaces of the excited and the ground state.

### **Spin-orbit Coupling (SOC), Heavy-Atom-Effect (HAE) and Fluorescence Quenching**

Radiationless “forbidden” transitions between excited states with different spin-multiplicity proceed via ISC, which depends on the spin-flip mechanism by perturbation by magnetic field due to SOC or spin-spin-coupling (SSC).<sup>9-11, 48, 62</sup> SSC results from interaction of paramagnetic states, which is important for the mechanism of ISC in diradicals.<sup>48</sup> The more common mechanism of ISC results from SOC, which is caused by the magnetic interaction of the orbital motions coupled to the spin angular momentum of an electron as reflected by the operator for SOC (**Eq 2.5**).<sup>10, 48, 63</sup>

$$\hat{H}_{SOC} = \xi_{nl} \hat{l} \hat{s} \propto \left\langle \frac{Z}{r^3} \right\rangle_{nl}. \quad \text{Eq 2.5}$$

$\hat{l}$  is the orbital angular momentum number,  $\hat{s}$  the spin momentum operator and  $\xi_{nl}$  is the SOC-constant for a specific state, given by the principal quantum number  $n$  and the orbital angular momentum number  $l$ . The SOC-constant is proportional to  $\left\langle \frac{Z}{r^3} \right\rangle_{nl}$  where  $Z$  is the nuclear charge and  $r$  the distance between an electron and a nucleus for quantum state  $nl$ . Thus, a high SOC can be achieved for heavy-atoms with high atomic numbers, which is known as the HAE. For instance, SOC in a hydrogen-like atom scales with  $Z^4$ .<sup>10-11</sup> In addition, the interaction between the spin- and orbital momentums of an electron increases for shorter distances to the nucleus with  $\xi_{nl} \propto r^{-3}$ . For illustration,  $\xi_{nl}$  for a carbon- ( $Z = 6$ ), iodine ( $Z = 53$ ), and lead-atom ( $Z = 82$ ) are in the order of 28, 5060, and 7800  $\text{cm}^{-1}$ , respectively.<sup>10</sup> In conclusion, heavy-atoms in the proximity of a molecule increase SOC leading to a higher spin-flip probability, which enhance the rate of singlet-triplet transitions.<sup>10-11, 48</sup>

Herein, the HAE-effect can be utilized for influencing the channel branching of photo-physical processes within the excited states of molecules, e.g. fluorescence quenching via enhanced ISC into triplet states. Fluorescence quenching via HAE can be achieved in two approaches. On the one hand, by synthesis of heavy-atom containing compounds.<sup>64</sup> On the other hand, by external perturbation of a heavy-atom containing quenching molecule (quencher) also known as Kasha-effect<sup>12</sup>, e.g. via iodoethane (IEt).<sup>11, 65</sup>

Fluorescence quenching via the external perturbation of SOC in  $\pi$ -orbitals proceeds i) stationary or ii) dynamically via collisions of the target molecule with the quencher.<sup>11</sup> i) The increase of SOC depends on the penetration of the  $\pi$ -electron into the electric field of the nucleus of the heavy-atom as well as on the atomic number due to  $\xi_{nl} \propto Z$ .<sup>10-11</sup> ii) For collision-induced HAE, the overlap between the  $\pi$ -orbital of the perturbed molecule and the p-orbital of the heavy-atom depends additionally on the quencher-concentration due to low-range interaction of the SOC perturbation as reflected by  $\xi_{nl} \propto r^{-3}$ .<sup>10-11</sup>

## Quantum Yields, Rate Coefficients, and Time Constants

As schematically depicted in **Figure 2.1**, excitation of a molecule with many degrees of freedom always results in a channel branching of radiative and non-radiative relaxation pathways including possible chemical reactions. For quantification of the channel branching quantum yields can be determined, which are related to the rate coefficients and time constants  $k$  and  $\tau$ , respectively.

The quantum yield  $\phi_i$  of a photophysical or -chemical process  $i$  is defined by the velocity of the photo-induced processes  $v_i$  and by the absorption of photons  $I_{\text{abs}}$  [photons per second], which is proportional to the sum of the velocities of all processes  $I_{\text{abs}} \propto \sum_i v_i$  (**Eq 2.6**).<sup>51</sup>

$$\phi_i = \frac{v_i}{I_{\text{abs}}} = \frac{v_i}{\sum_i v_i}, \text{ with } \sum_i \phi_i = 1. \quad \text{Eq 2.6}$$

For example by excluding a chemical reaction, the relaxation of an excited singlet state  $S^*$  occurs after the absorption of photons with the elementary processes of fluorescence  $v_F = k_F[S^*]$ , internal conversion  $v_{IC} = k_{IC}[S^*]$  and intersystem crossing  $v_{ISC} = k_{ISC}[S^*]$ , leading to a first order decay of the excited singlet state with the starting concentration of the excited state  $[S^*]_0$  as shown in **Eq 2.7**.<sup>51</sup>

$$[S^*] = [S^*]_0 e^{-kt} = [S^*]_0 e^{-t/\tau_0}, \text{ with } \tau_0 = \frac{1}{k_F + k_{IC} + k_{ISC}}. \quad \text{Eq 2.7}$$

Herein,  $\tau_0$  is the lifetime of the excited singlet state. Since  $v \propto k$ , the fluorescence quantum yield is given by  $\phi_F = k_F \cdot (k_F + k_{IC} + k_{ISC})^{-1}$ . For continuous absorption of photons, the concentration of the excited state can be assumed as quasi-constant, which leads to the approximation  $k_F = \frac{\phi_F}{\tau_0}$ . Thus, for a continuous excitation the rate coefficient of each process can be determined by the knowledge of its quantum yield and the total lifetime of the excited state.<sup>51</sup>

For a non-quasi-stationary system, the determination of rate coefficients for photophysical processes of a molecule is challenging due to the need to have the exact duration and the quantum yield of the considered elementary step as given by **Eq 2.8**.<sup>51</sup>

$$k_i = \frac{\phi_i}{\tau_i}. \quad \text{Eq 2.8}$$

For example, time constants of elementary photophysical and -chemical processes can be obtained by multiexponential fitting analysis of responses from fs-TA by assuming a combination of first-order processes. However, transient absorption spectra of molecules with many degrees of freedom are often superimposed by a manifold of processes (refer to **Figure 2.1**), which allows the quantification of  $k$  only in special cases.

## 2.2 (Photo-Initiated) Free Radical Polymerization (FRP)

FRP is an important polymerization technique in industrial and scientific research. An extensive variety of polymers can be obtained by FRP with many accessible monomers since it presents a straightforward polymerization method with a high orthogonality towards various functionalities.<sup>66</sup> As an advantage of FRP, high molecular weights can be obtained in a rapid fashion.<sup>67</sup> In contrast, limitations of FRP are the lack of control over the poly-dispersity and low end group fidelity.<sup>68</sup> Remarkably, the initiation of FRP can be achieved thermally, electrochemically, or photo-induced, which leads to a wide field of applications.<sup>66</sup> For instance, photo-induced FRP (photo-FRP) can be performed at low temperatures, which results in less side reactions (e.g. chain-transfer reactions) compared with thermally initiated FRP. Hence, photo-FRP can be used in biochemical applications e.g. immobilization of enzymes, as well as for polymerization of monomers with low ceiling temperatures, which favor depolymerization above a specific temperature limit. In addition, light can be applied in curing of large coated surfaces or filigree structures leading to a manifold of applications, e.g. curing technologies,<sup>15-16</sup> dental fillings,<sup>17-18</sup> tissue engineering,<sup>19</sup> and 3D-lithography.<sup>20</sup>

The mechanism of photo-FRP is presented in **Figure 2.2**, which depicts initiation, propagation, termination and chain transfer as elementary reaction steps.<sup>67</sup>

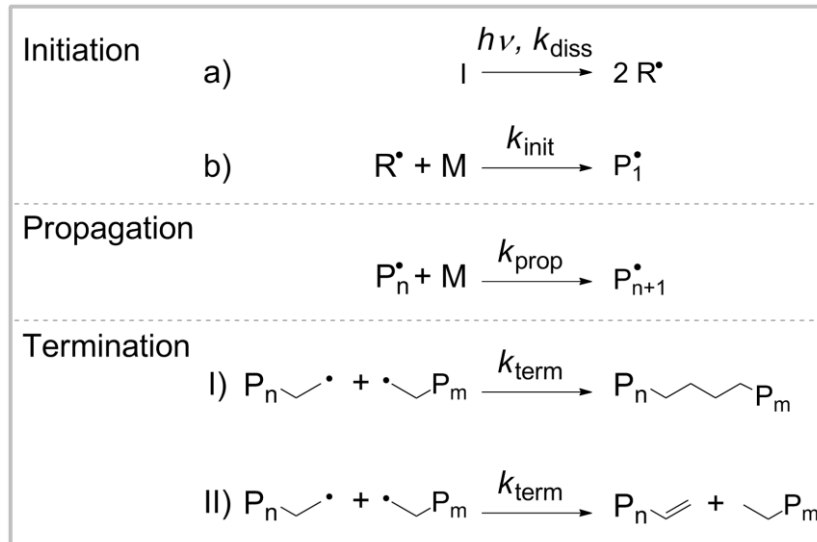


**Figure 2.2.** Mechanistic aspects of FRP. After fragmentation of the initiator I into radicals R, the monomer M is consumed via the addition to the radical center generating a growing polymer chain. Termination occurs via I) recombination or II) disproportionation of macroradicals.

The initiation is divided in two reaction steps: a) (photo-) dissociation of initiator I into radical fragments R, b) the attack of the radical R upon the first monomer unit M (association step). Herein, step a) is determined by the cleavage mechanism of the initiator, which is described by first order kinetics as defined in **Eq 2.9**.<sup>67</sup>

$$\frac{d[R^\bullet]}{dt} = 2 \cdot f_{eff} \cdot k_{diss}[I]. \quad \text{Eq 2.9}$$

The formation of the radical is dependent on the rate of fragmentation  $k_{diss}$  of the initiator I into two radicals (hence, **Eq 2.9** requires a factor of 2).  $f_{eff} \leq 1$  is a scaling factor for the radical formation, which take into account that not every initiator-derived radical starts a polymerization process. In general,  $f_{eff}$  is smaller than one due to e.g. recombination and H-abstraction reactions of the formed radicals. In the case of a photoinitiator,  $k_{diss}$  depends on the photophysical and -chemical mechanism after photoexcitation, e.g. efficient cleavage from triplet states for Norrish Type I initiators. b) The addition of monomer to the initiator-derived radical is a second order process as described in **Eq 2.10**.<sup>67</sup>

$$\frac{d[P_1^\bullet]}{dt} = k_{init}[M][R^\bullet]. \quad \text{Eq 2.10}$$

During propagation, further addition of monomer units to the growing chain results in the formation of macroradicals  $P_n$ . The propagation rate  $k_{prop}$  is dependent on the

steric and electronic properties of the monomer, e.g. values of  $10^2 \text{ L mol}^{-1} \text{ s}^{-1}$  for  $k_{prop}$  are experimentally determined for slow polymerizations such as of styrene, and  $10^4 \text{ L mol}^{-1} \text{ s}^{-1}$  for fast propagation of acrylate derivatives. The consumption of the monomer during propagation is given by **Eq 2.11**.<sup>67</sup>

$$-\frac{d[M]}{dt} = k_{prop}[P_n\cdot][M]. \quad \text{Eq 2.11}$$

Besides the chemical properties of the monomer,  $k_{prop}$  is dependent on temperature as well as on the viscosity which increases during the polymer process.

Termination of the polymer chain growth can occur via two reaction pathways: I) combination, and II) disproportionation. In the first process, recombination of two macroradicals leads to a so-called “dead polymer chain”.<sup>69</sup> Since every chain is conventionally initiated by an initiator-derived radical, combination products bear two end groups at both chain ends. In contrast, disproportionation proceeds by hydrogen abstraction of one macroradical by a second radical chain via  $\beta$ -elimination. Thus, two terminated polymers are obtained, which feature in  $\alpha$ -position (start of the polymer chain) the end group originating from the initiating radical fragment and a hydrogen or double bond functionality in  $\omega$ -position (end of the polymer chain), respectively. The latter polymer chain carrying a double bond in  $\omega$ -position is able to act as macromonomer for additional polymerization processes leading to chain branching.<sup>70</sup> In general, the termination step is a diffusion-controlled process, which results in both mechanisms in one second-order rate coefficient  $k_{term}$  with values in the range of  $10^6$  to  $10^8 \text{ L mol}^{-1} \text{ s}^{-1}$  (**Eq 2.12**).<sup>67</sup>

$$-\frac{d[P_n\cdot]}{dt} = 2 k_{term}[P_n\cdot]^2. \quad \text{Eq 2.12}$$

Herein, termination occurs statistically, which leads to a distribution of polymers species with various chain lengths. However, the steric properties of monomer have an impact on the mode of termination, e.g. methyl methacrylate (MMA) favors termination via disproportionation due to high steric hindrance caused by the high number of substituents of the olefin moiety, while less steric demanding monomers such as styrene prefer combination reactions.<sup>71</sup> For high monomer conversion, the viscosity of the polymerization mixture increases. Therefore, the rate of termination step decreases since it is highly diffusion-controlled.

One major topic within the present thesis is the determination of the overall initiation efficiencies of radicals originated from an initiator towards a monomer after the final polymerization process. All polymerization experiments have to be conducted with the same monomer, here MMA. Thus, propagation and termination reactions can be neglected due to identical rate coefficients. Consequently, differences in the FRP mechanism are limited to the initiation step, which depends on the nature of the employed initiators. Herein, the absorption spectrum and excited state channel branching after photoexcitation of an initiator as well as the reactivity of the formed radicals towards the monomer has to be considered for efficient initiation.<sup>32-33</sup>

### Norrish Type I Radical Photoinitiators

Besides the employed monomer, the conditions for efficient FRP are determined by the absorption spectrum and cleavage mechanism of a photoinitiator, e.g. excitation wavelength, curing depth, and initiation efficiency. Photodecomposition of aldehydes and ketones can be classified in Norrish type I and type II reactions.<sup>72</sup> Norrish type I reactions undergo homolytic  $\alpha$ -cleavage of aldehydes or ketones into radical fragments upon irradiation, while type II initiators produce radical species via hydrogen-abstraction. Examples for Norrish type I initiators are acetophenones,<sup>34-35, 73</sup> hydroxylalkylphenones,<sup>74</sup> oxime esters,<sup>75</sup> acylphosphines,<sup>76-77</sup> and acylgermanes.<sup>39-40</sup> Typical Norrish type II initiators are benzophenones,<sup>78-79</sup> thioxanthenes,<sup>79</sup> anthraquinones,<sup>8</sup> camphorquinones,<sup>80</sup> and ketocoumarins.<sup>81</sup> The general decomposition mechanism of a ketone-based Norrish type I initiator is presented in **Figure 2.3**.

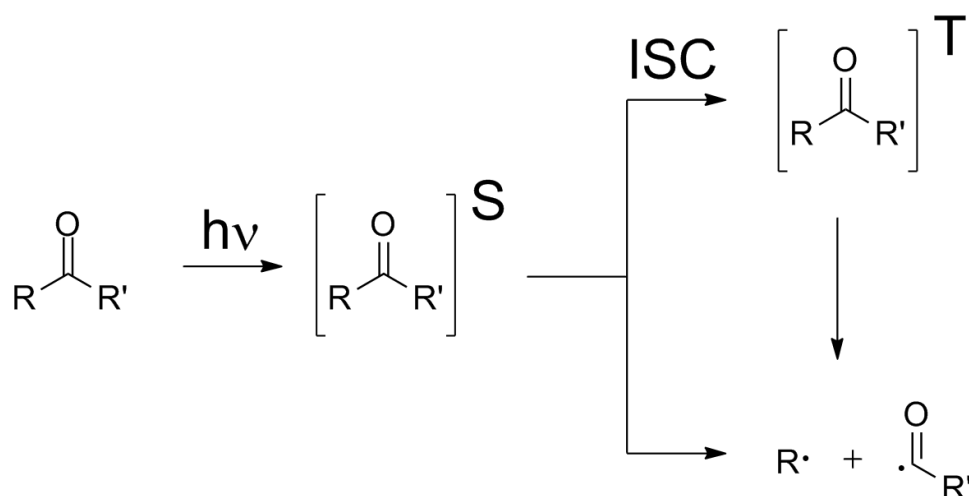


**Figure 2.3.** General Norrish Type I mechanism of keto-based photoinitiator. After photoexcitation into an excited singlet state S, the radical formation can occur from singlet states or after ISC from triplet states T. Which reaction path is preferred, depends on the topology of the potential energy surfaces within the excited states.

In principle, the decomposition of a keto-based Norrish type I initiator can occur from an excited singlet or triplet state.<sup>44</sup> With respect to channel branching after light excitation, the favored reaction pathway is determined by the topology of the excited state potential energy surfaces.

A comprehensive investigation on the initiation efficiency in correlation to the photo-physical and -chemical mechanism of different substituted mono-, bis- and tetraacylgermane-derivatives as an example for Norrish type I initiators is presented in **chapter 4**.

### 2.3 Nitrile Imine-Mediated Tetrazole-Ene Cycloaddition (NITEC)

NITEC was firstly reported by Huisgen and coworkers in 1967,<sup>45</sup> as an efficient, irreversible and catalyst-free ligation method.<sup>21</sup> Nowadays, the conjugation reaction has found many applications in recent research fields, e.g. ( $\lambda$ -orthogonal) polymer linkage,<sup>22-25</sup> fluorescence markers in biology,<sup>26-27</sup> and surface modifications.<sup>28-29</sup> The NITEC reaction proceeds in two steps: First, the formation of a nitrile imine 1,3-dipole intermediate (b) from a diaryl tetrazole (a) after photo-induced  $N_2$ -release. The second step entails subsequent cycloaddition of the 1,3-dipole intermediate with a dipolarophile to form the cycloadduct (c) as presented in **Figure 2.4**.<sup>82</sup>

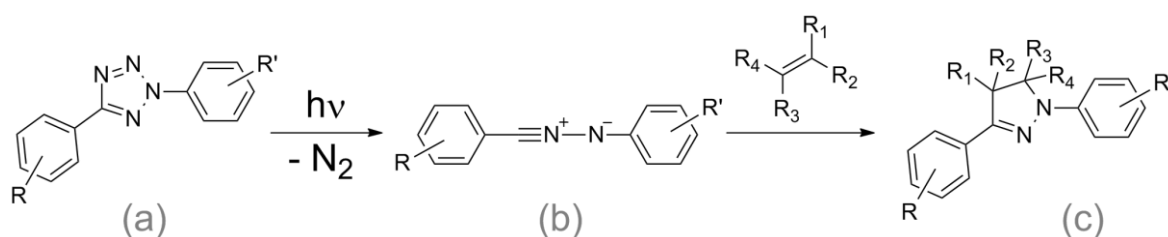


**Figure 2.4.** Mechanism of NITEC.<sup>82</sup> Structure (a) represents the photoreactive tetrazole compound, while the nitrile imine intermediate formed by photo-induced  $N_2$ -release is assigned to structure (b). Structure (c) is the cycloadduct formed via the 1,3-dipole cycloaddition of the 1,3-dipole and an alkene as a dipolarophile.

The fluorescence properties of the resulting cycloadduct are dependent on the substituents of the employed diaryl-tetrazole derivative.<sup>83</sup> In addition, the substituents influence the reactivity of the nitrile imine intermediate towards a dipolarophile as well, e.g. methoxy or dimethyl amine groups in *para*- $R'$ -position enhance the addition towards non-activated and electron rich alkene species.<sup>26, 84</sup> However, nitrile imine intermediates can undergo several side reactions in the absence of a dipolarophile.

Herein, reactions of the intermediate with water,<sup>85</sup> imidazoles and acetonitrile,<sup>86</sup> as well as the dimerization of two 1,3-dipoles<sup>83</sup> are reported.

In the current thesis, the ultrafast dynamics of two visible and one UV light-triggered diaryl-tetrazoles are investigated via fs-TA, which is presented in **chapter 6**.

## 2.4 Laser Optics

Generation of coherent light by light amplification by stimulated emission of radiation (LASER) has become an important tool in optics as well as chemical research.<sup>20, 87-90</sup> Especially, pulsed laser techniques provide high peak intensities for very short durations, which enable the investigation of dynamics of chemical and biological systems in real time without damaging the samples.<sup>3, 91</sup> In polymer chemistry, the use of pulsed laser systems with pulse durations of  $10^{-9}$  seconds (ns) bears possibilities of PLP techniques, which can be coupled to chromatographic and mass spectrometric methods as a powerful tool for investigation of the propagation rate of monomers and cleavage mechanism of initiators in FRP.<sup>32, 92-96</sup> In addition, photophysical processes of atoms and molecules occur on a fs-to-ps time scale. Thus, ultrashort laser pulses with durations in the order of  $10^{-15}$  seconds (fs) enables a wide field of transient spectroscopic methods with a sufficient time resolution to observe molecular motions, e.g. fs-TA.<sup>3</sup> The high peak intensities lead to nonlinear optical effects for light-matter interactions, which can be utilized to generate laser pulses with tunable wavelengths over a spectrally wide range.

In the following, the fundamentals of the laser principle, nonlinear optics and the generation of ns- and fs-laser pulses are described.

### 2.4.1 Laser Principle and Laser Pulses

A laser consists of a resonator, an active medium and an energy source for pumping the medium as sketched in **Figure 2.5**.<sup>97</sup>

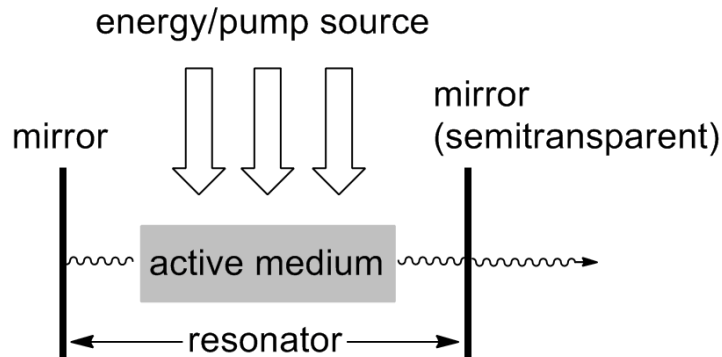


**Figure 2.5.** Basic setup of a laser, which is composed of an active medium in a resonator consisting of two mirrors. The active medium is pumped with energy, which leads to emission of the medium. The emission is amplified by stimulated emission for each oscillation within the resonator. A semitransparent mirror enables the ejection of intense coherent laser light after a defined number of resonator circuits.

The pump source excites the active medium, which leads to population inversion and spontaneous emission of photons. Herein, population inversion can be achieved for at least three-level systems (**Figure 2.6**), which designates a population of a higher excited state compared to the ground state population  $\Delta N = N_1 - N_0 > 0$ .<sup>97</sup>

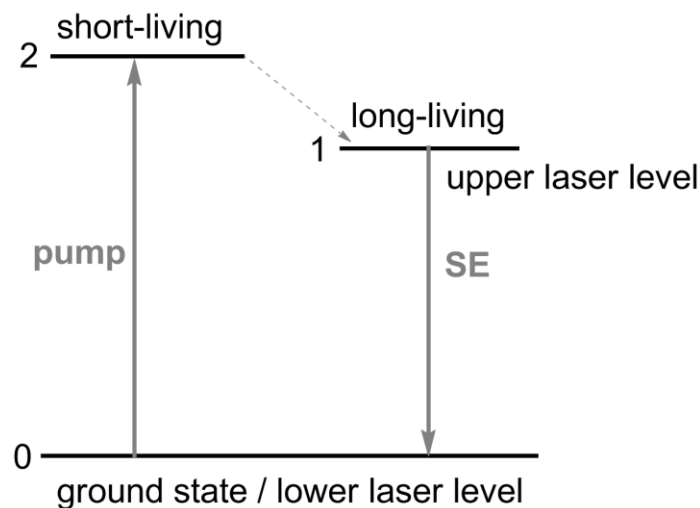


**Figure 2.6.** Schematic three-level system for illustration of the laser-principle. For further detail refer to main text.

Excitation into a short-living higher pump level leads to ultrafast relaxation into a long-living upper laser level ( $\mu\text{s}$ - $\text{ms}$ ),<sup>98-99</sup> which can be depopulated by stimulated emis-

sion (SE) into the lower laser level or ground state, respectively. A more efficient population inversion is achieved for a four level system. Herein, the lower laser level is short-living, which leads to fast depopulation via radiationless transitions into the ground state. The relaxed population is again available for pumping of the upper laser level. Thus, a higher population inversion occurs compared to the three-level system due to highly populated upper and depopulated lower laser levels. A prominent example for a four level system is the neodym:yttrium aluminum garnet (Nd:YAG) laser.<sup>100</sup>

The resonator features a self-amplifying effect of the active medium by feedback of stationary waves of oscillating photons between the end mirrors. For each passing photon through the active medium, a second photon with the same spatial and temporal phase (coherence) as the incident photon is produced via SE leading to amplification of light. The amplified coherent laser light can leave the resonator via a semi-transparent mirror for each oscillation.<sup>97</sup>

The temporal behavior of the laser emission depends on the lifetimes of the involved upper and lower laser level, the amplification per resonator cycle and the pump frequency.<sup>87</sup> For continuous pumping of the laser medium with a long-living upper laser level, a quasi-stationary population inversion is provided, which leads to a continuous laser operation. Is the lifetime of the upper laser level short in comparison to the rising time of the pump process, the population inversion is steadily reached and degraded, which leads to a high repetition rate of laser pulses, e.g. excimer-laser.<sup>87</sup> For very high amplifications of the SE, the population inversion can be degraded faster than repopulation via pumping can occur. Consequently, a periodic or irregular series of laser pulses (spikes) are generated with pulse durations smaller 1  $\mu$ s, e.g. for flash light-pumped ruby lasers. Q-switching enables a controlled generation of short and intensive pulses in the ns-region instead of irregular ejected spikes, e.g. flash diode-pumped Nd:YAG-laser. Ultrashort laser pulses with pulse durations of  $10^{-12}$ - $10^{-15}$  s can be generated by mode-locking in a nonlinear laser medium, which produces a fixed phase-relationship between fluctuating laser modes within the resonator.<sup>87</sup>

## Properties of laser pulses

Laser pulses can be described as a wave package as the result of superposition of coupled laser modes with various phases.<sup>101</sup> Thus, a laser pulse experiences a spectral broadening due to the transform limit in analogy to the Heisenberg's uncertainty principle of time and energy as given by **Eq 2.13**.<sup>101</sup>

$$\tau_p \Delta\nu \geq K. \quad \text{Eq 2.13}$$

Here,  $\tau_p$  is the pulse duration,  $\Delta\nu$  the spectral width and  $K$  a constant, which is dependent on the pulse shape, e.g. 0.441 for a Gaussian-shaped pulse.<sup>101</sup> However, the effect of the transform limit leads to a significant spectral width for ultrashort pulses like ps- and fs-pulses, e.g. a spectral width of  $\Delta\lambda \sim 2 \cdot 10^{-5}$  nm can be calculated for a pulse of  $\tau_p \sim 10$  ns at  $\lambda_0 = 400$  nm. Hence, ns-pulses can be considered to be quasi-monochromatic in relation to the broadening of an electronic transition of a molecule in solution. In contrast, fs-pulses show spectral widths of several up to tens of nm. In addition, dispersion effects in optical media can lead to additional spectral broadening (chirp) of the envelope of the pulse or wave package, respectively. Dispersion is caused by different phase velocities  $v_{ph}$  of the coupled modes within a wave package due to the frequency dependence of the refractive index  $n(\omega)$  of a medium as given by **Eq 2.14**.<sup>89</sup>

$$v_{ph} = \frac{\omega}{k} = \frac{c_0}{n(\omega)}. \quad \text{Eq 2.14}$$

**Eq 2.14** is called dispersion relation with the speed of light constant  $c_0$ , and the absolute value of the wave vector  $k$ . In general, the wave vector  $\vec{k}$  determines direction of a propagating electromagnetic wave.<sup>89</sup> The velocity of the propagating wave package is called group velocity, which is dependent on the derivation of phase velocities with respect to the wavelength  $\lambda$  according to **Eq 2.15**.<sup>89</sup>

$$v_{gr} = v_{ph} - \lambda \frac{dv_{ph}}{d\lambda}. \quad \text{Eq 2.15}$$

In vacuum, the group velocity is equal to the phase velocity, while the derivation of the phase velocity reflects the influence of the dispersion in a medium. Consequently, the temporal overlapping of two pulses with different central wavelengths propagating in an optical medium suffers from so-called group velocity mismatch (GVM) due to

dispersion. GVM is given as the difference between the inverse group velocities  $v_{gr,1/2}$  of both pulses (**Eq 2.16**).<sup>102</sup>

$$\text{GVM} = \left| \frac{1}{v_{gr,1}} - \frac{1}{v_{gr,2}} \right|. \quad \text{Eq 2.16}$$

In the following the basic principles of nonlinear optics are presented, which are necessary for the generation of ultrashort laser pulses and the tuning of their frequencies.

## 2.4.2 Nonlinear Optics and Parametric Processes

The interaction of light and matter results in the polarization  $\vec{P}$  of an optical medium proportional to the vacuum permittivity  $\varepsilon_0$ , the electrical field  $\vec{E}$  of the incident beam and the electrical susceptibility tensor of the medium  $\tilde{\chi}$  as follows in **Eq 2.17**.<sup>103</sup>

$$\vec{P} = \varepsilon_0 \tilde{\chi} \vec{E}. \quad \text{Eq 2.17}$$

For very high intensities in the order of atomic electric fields, the polarization of an optical medium is not only linearly correlated to the electrical field anymore due to additional nonlinearities of the potential of a medium at larger elongations, e.g. the electric field of an electron of a hydrogen atom at the distance of one bohr relative to the nucleus corresponds to an intensity of  $\sim 4 \cdot 10^{16} \text{ W cm}^{-2}$ .<sup>103</sup> Thus, higher orders of the polarization have to be considered, which can be described by expansion of **Eq 2.17** as given below in **Eq 2.18**.<sup>101, 103</sup>

$$\begin{aligned} P_i &= \varepsilon_0 \sum_j \chi_{ij}^{(1)} E_j + \varepsilon_0 \sum_{jk} \chi_{ijk}^{(2)} E_j E_k + \varepsilon_0 \sum_{jkl} \chi_{ijkl}^{(3)} E_j E_k E_l + \dots \\ &= P_i^{(1)} + P_i^{(2)} + P_i^{(3)} + \dots \end{aligned} \quad \text{Eq 2.18}$$

$\chi_{ij}^{(1)}$ ,  $\chi_{ijk}^{(2)}$ ,  $\chi_{ijkl}^{(3)}$  are the linear, second-order and third-order susceptibility represented by second-, third- and fourth-rank tensors, respectively. The indices ijkl label the electrical field components with respect to the corresponding Cartesian coordinates.

Important nonlinear phenomena, resulting from the second- and third-order polarization term, are discussed in the following.

## Second Order Nonlinear Optics: Parametric Processes

The second order nonlinearities are dependent on the second power of the electrical field as described by the second term of **Eq 2.18**. Second-order processes can be generated in special nonlinear media without an inversion center, e.g.  $\beta$ -barium borate (BBO), or lithium triborate (LBO). An inversion center leads to an odd polarization function. Consequently, even terms would vanish in **Eq 2.18**.<sup>89</sup>

The superposition of two planar electromagnetic waves  $E_{1,2}(x, t)$ , which exclusively propagate in x-direction ( $\frac{\partial E_x}{\partial x} \neq \frac{\partial E_y}{\partial y} = \frac{\partial E_z}{\partial z} = 0$ ) and oscillate with  $\omega_1, \omega_2$ , can be expressed by **Eq 2.19**.<sup>103</sup>

$$\begin{aligned} E_x(x, t) &= E_{x,1}(x)e^{-i\omega_1 t} + E_{x,2}(x)e^{-i\omega_2 t} + E_{x,1}^*(x)e^{i\omega_1 t} + E_{x,2}^*(x)e^{i\omega_2 t} \\ &= E_{x,1}e^{-i\omega_1 t} + E_{x,2}e^{-i\omega_2 t} + \text{c.c.} \end{aligned} \quad \text{Eq 2.19}$$

Complex conjugated terms are designated by c.c.. Inserting **Eq 2.19** to the second term of **Eq 2.18** leads to the following expression (**Eq 2.20**) for the second-order nonlinear polarization.<sup>103</sup>

$$\begin{aligned} P_i^{(2)} = \epsilon_0 \chi_{ixx}^{(2)} \left[ \underbrace{2E_{x,1}E_{x,1}^* + 2E_{x,2}E_{x,2}^*}_{\text{optical rectification}} + \underbrace{E_{x,1}^2 e^{-i2\omega_1 t}}_{\text{SHG } \omega_1} + \underbrace{E_{x,2}^2 e^{-i2\omega_2 t}}_{\text{SHG } \omega_2} \right. \\ \left. + \underbrace{2E_{x,1}E_{x,2} e^{-i(\omega_1 + \omega_2)t}}_{\text{SFM}} + \underbrace{2E_{x,1}E_{x,2}^* e^{-i(\omega_1 - \omega_2)t}}_{\text{DFM}} + \text{c.c.} \right]. \end{aligned} \quad \text{Eq 2.20}$$

The first term is called optical rectification, which has a static contribution to the polarization leading to charge separation within the medium. The second and third terms contain the doubled frequencies  $2\omega_{1,2}$  of the incident electromagnetic waves. Thus, the nonlinear process is called second harmonic generation (SHG). The addition ( $\omega_1 + \omega_2$ ) and subtraction ( $\omega_1 - \omega_2$ ) of the frequencies of both electromagnetic waves are called sum frequency mixing (SFM, fourth term) and difference frequency mixing (DFM, fifth term), respectively. SHG, SFM and DFM belong to parametric processes, which obey the conservation of energy and momentum.<sup>103</sup>

For the special case of  $E_{x,1} = E_{x,2}$  and  $\omega_1 = \omega_2$ , only SHG occurs as can easily be seen from **Eq 2.20**. In a particle picture, SHG is achieved by the interaction of two photons of the same energy in a nonlinear medium resulting in a photon with doubled

energy. Due to conservation of the momentum  $\vec{p} = \sum_i \hbar \vec{k}_i = \text{const.}$ , the incident and the SHG-photons need a constructive phase relationship as given by the phase matching condition **Eq 2.21** of the corresponding wave vectors  $\vec{k}_{inc}$  and  $\vec{k}_{SHG}$ , respectively.<sup>89, 97</sup>

$$\Delta \vec{k} = \vec{k}_{SHG} - \vec{k}_{inc} = 0. \quad \text{Eq 2.21}$$

In general, the wave vector in a medium is dependent on the frequency due to the dispersion relation  $k \propto n(\omega)$ , where  $n(\omega)$  is the refractive index. The phase matching condition can be fulfilled by utilizing the angular dependence of the extraordinary refractive index  $n^{eo}(\theta)$  for double refractive anisotropic nonlinear crystals without inversion center, e.g. BBO.<sup>89</sup>  $\theta$  defines the angle between the optical axis of the crystal and the propagation direction of the incident laser pulse. Herein, two types of phase matching are possible. For type I the incident photon corresponds to the ordinary ray, which leads to SHG reflected by the extraordinary ray, if the condition  $n_{2\omega}^{eo}(\theta) = n_{\omega}^o$  is true. Type II phase matching occurs for  $n_{2\omega}^{eo}(\theta) = 1/2(n_{\omega}^{eo} + n_{\omega}^o)$ , where the incident ray consist of an ordinary and extraordinary part. If the phase matching condition is fulfilled, the intensity of the SHG is proportional to  $l^2$  corresponding to the optical pathway ( $l$ ) through the nonlinear crystal.<sup>104</sup> However, the conversion efficiency is limited for ultrashort pulses due to pulse broadening caused by dispersion with a highest conversion efficiency ~60 %.<sup>104</sup>

Parametric processes can be used for noiseless optical parametric amplification (OPA) of a signal laser pulse at the frequency  $\omega_s$ , which is achieved by overlapping with an intense pump pulse with  $\omega_{pump} > \omega_{signal}$  in a nonlinear medium.<sup>97</sup> Due to conservation of energy, an additional so-called idler pulse with  $\omega_{idler} = \omega_{pump} - \omega_{signal}$  is generated. OPA can be constructed in a non-collinear optical parametric amplification (NOPA) setup, which is an efficient technique to tune the frequencies of fs-laser pulses.<sup>105</sup> Herein, phase-matching is achieved for  $\Delta \vec{k} = \vec{k}_{pump} - \vec{k}_{signal} - \vec{k}_{idler} = 0$ . This condition is fulfilled by matching the group velocity of the signal wave with the idler group velocity by adjusting the angle  $\theta$  of the nonlinear crystal axis relatively to the direction of the pump pulse propagation.<sup>105</sup> By using a white light continuum for the signal pulse, the amplified frequency of the signal pulse can be varied by changing the angle of the nonlinear crystal as well as for the delay between the optical pathways of signal and pump pulse. Thus, dependent

on the spectrum of the white light continuum and geometry of the NOPA, fs-laser pulses can be tuned in a wide range. The generation of a white light continuum is based on third-order nonlinear optical effects, which are discussed in the following paragraph.

An alternative method to achieve tunable laser pulses is OPA in a resonator setup, so-called optical parametric oscillator (OPO),<sup>97</sup> which is used for example in frequency-tunable ns-laser systems (**Figure 2.7**).

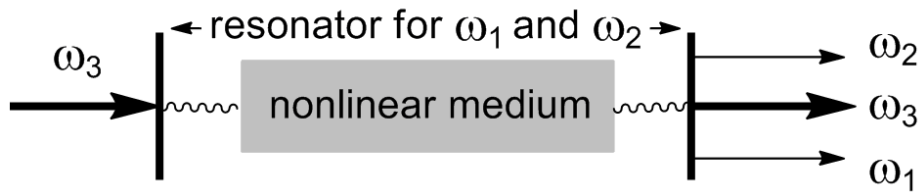


**Figure 2.7.** Schematic setup of an optical parametric oscillator, which leads to conversion of a photon with  $\omega_3$  into two further photons with  $\omega_1 + \omega_2 = \omega_3$ .

Analogous to a laser resonator, an OPO makes use of the electronic transitions of the nonlinear medium, which is pumped by high intensities at  $\omega_3$ . As a result of quantum fluctuations, two additional photons  $\omega_1$  and  $\omega_2$  are obtained. The frequencies are determined by  $\omega_1 + \omega_2 = \omega_3$ , which must not correspond to an electronic transition of the medium.<sup>97</sup> In a photon picture, an OPO features the inverse effect of SFM, where a photon is converted to two photons with lower frequencies  $\omega_3 \rightarrow \omega_1 + \omega_2$  instead of the addition of two photons to one with higher frequency  $\omega_1 + \omega_2 \rightarrow \omega_3$ . Efficient OPO-operation is achieved for the phase-matching condition  $\vec{k}_1 + \vec{k}_2 = \vec{k}_3$ . In turn, a high frequency range is accessible, which can be tuned by changing the feedback conditions within the resonator, e.g. crystal-angle.<sup>97</sup>

### Third Order Nonlinear Optics: White Light-Generation and Kerr-Lens Effect

As given by the third term of **Eq 2.18**, the third-order nonlinear polarization is proportional to the third order of the electromagnetic field. Thus, third-order effects are not limited to birefringent media without an inversion center. Due to the weak third order susceptibility,<sup>103</sup> third order processes only occur for very high pulse energies or strongly focused laser beams. Consequently, frequency tripled electromagnetic waves are usually not generated via third-order nonlinear effects due to the more ef-

ficient combination of second-order SHG and subsequent SFM with the fundamental wave.

The most important third-order nonlinear effect is the optical Kerr effect. The optical Kerr effect is a result of the nonlinear refractive index  $n(I)$ , which depends on the intensity  $I \propto \vec{E}^2$  as reflected by **Eq 2.22**.<sup>87, 103</sup>

$$n(I) = n_0 + \frac{1}{2} n_2 I. \quad \text{Eq 2.22}$$

Herein, radial-symmetrical laser pulses with high intensities experience spatial self-focusing known as Kerr effect. In addition, the phase of the laser pulse is modulated by so-called self-phase modulation (SPM), as a consequence of the orientation of dipole moments alongside the direction of the strongest incident field, which can be understood as the temporal Kerr effect.<sup>87</sup>

SPM leads to pulses with high peak intensities and highly broadened frequency spectra due to chirp as a result of the intensity dependence of the self-modulated phase. Thus, SPM can be utilized for white light-generation in thin substrates, e.g. sapphire, or calcium fluoride (CaF<sub>2</sub>).<sup>105-107</sup> In addition, mode-locking induced by the Kerr effect of a nonlinear crystal can be used for the generation of ultrashort laser pulses, e.g. titanium-sapphire laser.<sup>87</sup>

### 2.4.3 Generation of ns-Laser Pulses: Q-Switch

Laser pulses with ns-duration can be generated by Q-switching of a flash light-pumped resonator. To this end, an optical switch causes energy losses within the resonator (low quality resonator), which prevents the oscillation and amplification of SE until the switch is triggered. Consequently, the population of the upper laser level is increased to very high excess by persistent pumping. When the Q-switch is triggered, the oscillation-threshold can be reached (high quality resonator), which leads to the sudden generation of a very intensive pulse.<sup>87</sup> The cycles of the Q-switched pulse generation define the repetition frequency.

The optical switch consists of two crossed polarizers and a Pockels cell. A Pockels cell is an anisotropic crystal, which rotates the polarization plane with the angle  $\vartheta$  of the transmitted linear-polarized light proportional to an applied electrical potential  $U$ . Herein, the transmittance  $T$  for a Q-switch is given by **Eq 2.23**.<sup>87</sup>

$$T = T_0(1 - \cos \vartheta), \text{ with } \vartheta \propto U. \quad \text{Eq 2.23}$$

For  $U$  leading to  $\vartheta = 90^\circ$ , the transmittance is high and light can oscillate without losses within the resonator. In contrast,  $\vartheta = 0^\circ$  for  $U = 0$  prevents the transmittance due to crossed polarizers.

The optimal trigger for switching the Pockels cell depends on the temporal properties of the pump pulse as well as the lifetime of the upper laser level. Long excited state lifetimes and short pump pulse durations lead to only small losses of the population in the upper laser level caused by spontaneous emission or radiationless relaxation processes. Thus, the trigger for the Pockels cell should be chosen at the end of the pump pulse duration, where the highest population inversion is expected. Consequently, ns-laser pulses with peak intensities up to several megawatts (MW) are generated.<sup>87</sup> A broad tunability of ns-laser pulses can be achieved by using parametric processes, e.g. OPO and SHG. A detailed description of the tunable laser setup used within the present thesis is presented in **section 3.3.1**.

#### 2.4.4 Generation of fs-Laser Pulses: Mode-Locking

One efficient technique for generation of ultrashort laser pulses is passive mode-locking. The generated fs-pulses can be amplified via chirped pulse amplification (CPA), which was discovered by Strickland and Mourou in 1985 and recently rewarded with the Nobel Prize in 2018.<sup>108</sup> Both principles are described in the following.

In general, light oscillates with an arbitrary phase relationship in a laser resonator. Herein, the single modes circulate with frequencies close to the resonance ( $q = 1$ ) or overtone ( $q = 2, 3, 4, \dots$ ) frequencies  $\nu_q$  of the resonator which are defined by the constant speed of light  $c_0$  and the length between the two end mirrors  $L$  as given by **Eq 2.24**.<sup>101</sup>

$$\nu_q = \frac{qc_0}{2L}. \quad \text{Eq 2.24}$$

Fluctuations in the intensity of the laser modes occur due to interference between longitudinal modes as well as arbitrary phase relaxations. Introducing a special non-linear active medium, the laser mode with the highest intensity experiences the strongest self-focusing due to the Kerr effect (refer to **Eq 2.22**). After a few cycles, an intense laser pulse is generated, which consists only of the most intensive modes with a stable phase relationship (Kerr-lens mode-locking, KML). Consequently, the

laser emission consists predominantly of laser pulses with a repetition rate  $\nu_{\text{rep}} = \frac{c}{2L}$ , which is dependent on the geometry of the resonator.<sup>87</sup>

Dispersion caused mainly by the resonator mirrors has to be compensated, e.g. introducing negative dispersion via a prism compressor.<sup>104, 109</sup> Otherwise, the dispersion would lead to dephasing of the modes accompanied by a temporal broadening of the laser pulses. For example, a passive mode-locked, dispersion-compensated titanium:sapphire-laser achieves laser pulses down to 5 fs.<sup>87</sup>

The peak intensity of the laser pulses is limited by the self-focusing effect. An increase of the laser pulse energy can be carried out via CPA.<sup>108</sup> Herein, the generated laser seed pulses are temporally stretched in a combination of gratings, subsequently amplified in a second resonator (regenerative amplifier, RGA), and finally recompressed to the approximately original pulse duration as depicted in **Figure 2.8**.<sup>102</sup>

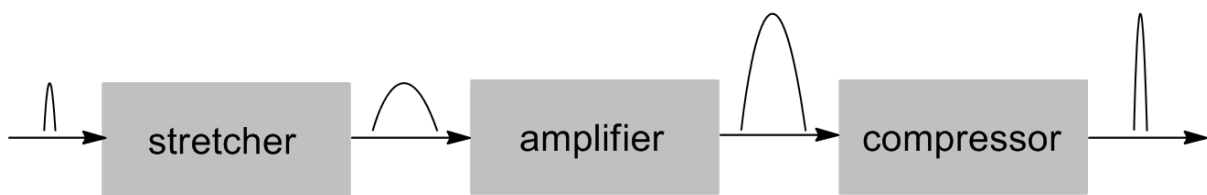


**Figure 2.8.** Chirped pulse amplification (CPA) of short laser pulses is achieved by amplifying a stretched initial pulse, which is subsequently recompressed approximately to the original pulse duration.

Stretching the laser pulses before amplification has the advantage of a better temporal overlap between the seed and pump pulse as well as to prevent damaging of the optics. The RGA-medium is pumped with a second laser. In contrast to OPA, RGA is based on amplification by the stimulated emission of the pumped crystal. To this end, a crystal is applied which provides a similar emission spectrum as the seed pulse. For instance, titanium:sapphire can be used for the generation of the initial seed pulse as well as amplifier medium within the RGA unit, which leads to the amplification of pulses at 800 nm by several orders of magnitude.<sup>102</sup>

### 2.4.5 Transient Broadband Absorption Spectroscopy (fs-TA)

In the current thesis, fs-laser pulses are used for fs-TA, which is a pump-probe technique. The fundamental principle for all pump-probe techniques is visualized in **Figure 2.9**.

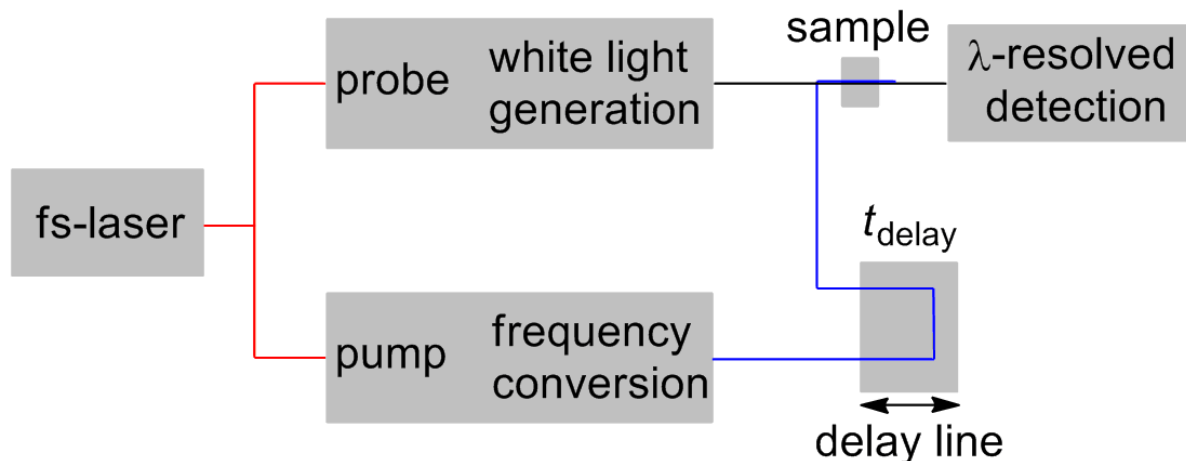


**Figure 2.9.** Basic setup for (fs-)pump-probe techniques. For a detailed description refer to main text.

Generated laser pulses at a given repetition rate and wavelength are split into a pump and probe pathway. The probe pulses are used for white light generation in a thin substrate (e.g.  $\text{CaF}_2$ ), while the frequency of pump pulses can be converted via optical parametric processes, e.g. NOPA, SHG, or SFM. Both pulses are temporally and spatially overlapped in a sample. The temporal overlapping-point  $t_0$  is dependent on the wavelength as a consequence of the GVM between the spectral contributions of the white light probe pulse and the pump pulse. Depending on specific properties of this pulse (e.g. chirp and pulse duration), a transient intensity artifact in the region of the temporal zero-point occurs due to cross-correlation of the pump and probe pulse. The rise of the cross-correlation artifact can be used to estimate the time-resolution of the experiment.

The transient response of the system is probed at  $t = t_{\text{delay}} - t_0$  after excitation by the pump pulse at zero time  $t_0$ . The temporal delay  $t_{\text{delay}}$  is adjusted by varying the pathway of the pump with respect to probe pulse due to constant velocity of light. Thus, transient difference absorption spectra  $\Delta A(t, \lambda)$  of the excited states can be measured by the time- and wavelength-dependent absorbance as follows in **Eq 2.25**.

$$\Delta A(t, \lambda) = A_w(t, \lambda) - A_{w/o}(\lambda). \quad \text{Eq 2.25}$$

$A_w(t, \lambda)$  is the transient absorbance spectrum after pumping at time  $t$ , while  $A_{w/o}(\lambda)$  is the ground state absorbance spectrum of the sample without excitation. In general, different processes can contribute to  $\Delta A(t, \lambda)$ : Excited state absorption (ESA), stimulated emission (SE), ground state bleaching (GSB), and “hot” ground state absorption (HGSA) as illustrated in **Figure 2.10**.

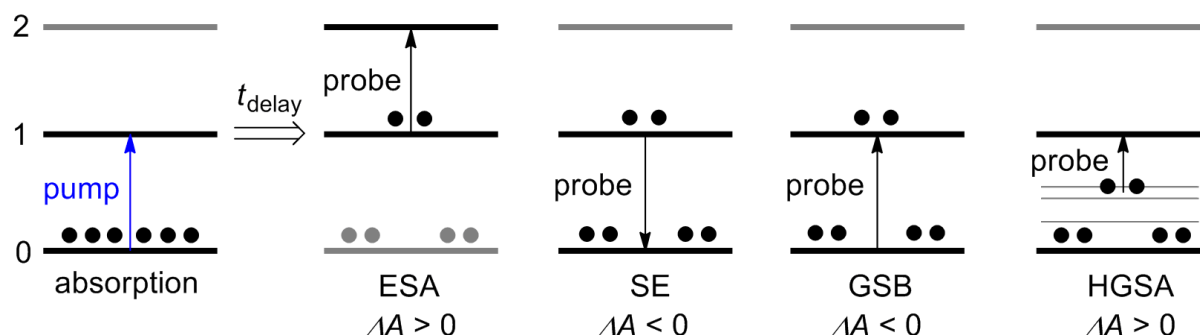


**Figure 2.10.** Overview of possible transitions causing a transient response within pump-probe experiments. After pumping, population from ground state 0 to an electronic excited state 1 several processes can be observed after the delay time, e.g. from left to right: excited state absorption (ESA), stimulated emission (SE), ground state bleaching (GSB), and hot ground state absorption (HGSA).

ESA contributes with a positive response to  $\Delta A(t, \lambda)$  and results from the transient absorption of the excited state into energetically higher excited states. Negative contributions to  $\Delta A(t, \lambda)$  are SE and GSB. SE occurs for the radiative deactivation of the excited state induced by probe-photons. GSB is the negative response of the depopulated ground state after excitation due to  $A_{w/o} > A_w$ . “Hot” ground state absorption (HGSA) occurs for probing higher vibrational levels of the ground state, which were populated after fast relaxation (IC+VR) of previously pumped excited states.

In general, transient spectra of complex molecules are superimposed by more than one of the described processes due to several correlated relaxation pathways as expected from photophysical and -chemical channel branching.

## 2.5 Mass Spectrometry (MS)

Mass spectrometry (MS) is a widely used technique for analysis of the chemical composition of molecules and their fragments.<sup>110</sup> Fields of application include investigation on biomolecules,<sup>111-113</sup> cells<sup>114</sup> and interstellar space chemistry,<sup>115-116</sup> structure determination and quality control of drugs,<sup>117</sup> food,<sup>118</sup> and polymers.<sup>96, 119</sup>

A mass spectrometer is constructed of an ion source, a mass analyzer for separation and sorting of the generated ions and a detection unit. In general, the right choice of the ion source in combination with the mass analyzer depends on the investigated systems.

Electron ionization (EI) can be used for structure determination of small molecules, while secondary ion mass spectrometry (SIMS) can be applied for surface analysis. However, both methods lead to fragmentation. In contrast, soft ionization techniques, which avoid fragmentation, are matrix assisted laser desorption ionization (MALDI) and electrospray ionization (ESI). MALDI and ESI are especially used for analysis of polymers and biopolymers.<sup>119</sup> The advantage of ESI-ion sources is the production of multiple charged ions, which significantly extends the accessible mass range compared to other ionization techniques. In addition, ESI can be coupled to precursory high-performance liquid chromatography (HPLC) or size-exclusion chromatography (SEC).<sup>119</sup>

In principle, the first mass analyzer was applied in the Thomson-experiment 1897 for the determination of the mass to charge-ratio ( $m/z$ ) of an electron.<sup>120</sup> A moving charged particle in a magnetic field experiences a Lorentz-force, which leads to deflection. The deflection depends on the mass of the charged particle. Thus, dependent on the deflection coordinate, the particles can be separated in their specific  $m/z$ . Today, Coulomb forces of electric fields can as well be utilized for analysis of ions, e.g. quadrupole. As an alternative, ions can be trapped in an electric or magnetic field for recording their specific oscillations with respect to  $m/z$ , e.g. cyclotron, orbitrap.<sup>119</sup>

In modern mass spectrometry several mass analyzers are available, which are different in their separation process with i.e. specific resolution (mass resolving power,  $R$ ), mass accuracy, and mass range, e.g. quadrupole mass filters ( $R = 100-1000$ ), time-of-flight (ToF,  $R = 1000-40000$ ) mass analyzers.<sup>119</sup> A very high resolution of

$R = 10000-100000$  is achieved for orbitraps, which was published by Makarov in the year 2000.<sup>119, 121</sup>

The combination of an ESI-ion source and Orbitrap-mass analyzer is ideal for the analysis of the distinct end group distribution of the repeating units for the characterization of macromolecules obtained from PLP used in the present thesis. In addition, precursory size-exclusion-chromatography enables the separation of macromolecules due to their hydrodynamic volume before ionization, which facilitate the evaluation of complex mass spectra.

In the following the principles of the ESI-ion source and Orbitrap-mass analyzer are presented in detail.

### 2.5.1 Ion Source: Electrospray Ionization (ESI)

ESI is a soft ionization method, which can be applied for MS-analysis of polymers without fragmentation. A scheme of the setup is provided in **Figure 2.11**.

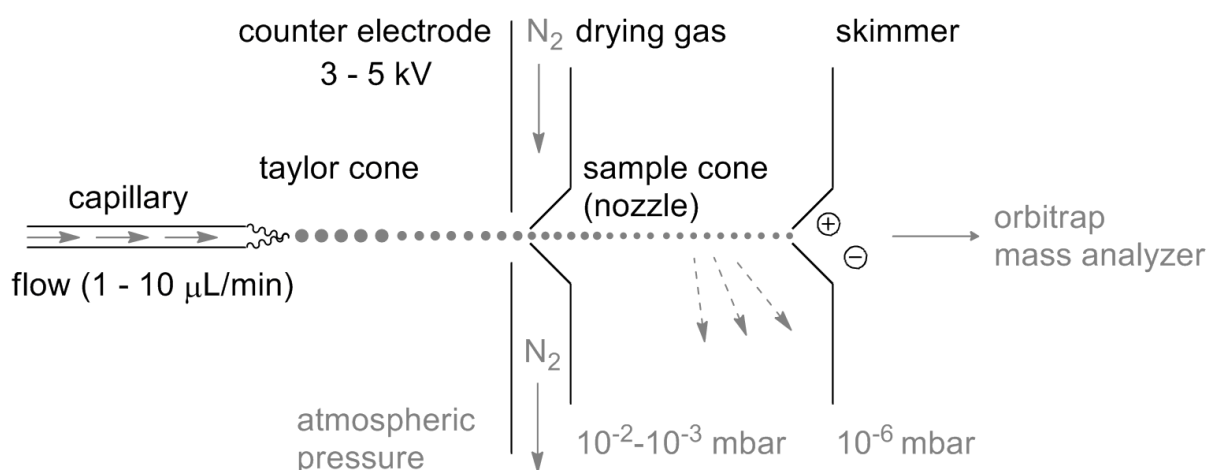


**Figure 2.11.** Schematic setup of an ESI-ion source. For a detailed description refer to main text.

A highly diluted polymer sample is inserted via a capillary at atmospheric pressure and a high potential of ~4 kV, which leads to highly charged fluid droplets. A counter electrode at 4-5 kV accelerates the droplets at the nozzle tip under formation of an elliptically shaped Taylor-cone of the fluid, which tapers to a relatively sharp point.<sup>119, 122</sup> Subsequently, the diminished charged droplets enter a low vacuum chamber of 10<sup>-3</sup>-10<sup>-4</sup> mbar, where the solvent is evaporated while ions are retained. The nebulization and evaporation is supported by a heated drying gas, e.g. nitrogen.<sup>110</sup> The shrinkage of droplets proceeds until the repulsive forces between the ions outweigh

the cohesive forces of the solvent (Rayleigh-limit) leading to cascades of droplet bursts into even smaller droplets (Coulomb explosions). Finally, the completely solvent-freed ions are pulled via an electric gradient through a skimmer into the mass analyzer.<sup>119</sup>

The ESI process leads to generation of highly charged species without fragmentation. Intrinsically uncharged polymer chains can be ionized by doping the solvent of the sample with millimolars of Na<sup>+</sup>. However, the polydispersity of many different charged species can lead to a manifold of isobaric patterns in MS.<sup>119</sup> This disadvantage is avoided by using SEC, which sorts the polymers depending on their hydrodynamic volumes before injecting into the ESI-source. For instance, an isobaric overlap of double-charged species in the region of single-charged species, featuring the half of the mass of the former, can be circumvented by utilizing SEC for ESI-MS.

### 2.5.2 Mass Analyzer: Orbitrap

In principle, orbitraps are ion-traps similar to Fourier transform ion cyclotron resonance mass analyzers (FT-ICR), which achieve high  $R > 10000$  and mass accuracies  $< 5$  ppm.<sup>119</sup> In contrast, a unique feature of orbitraps is ion trapping in absence of a magnetic field, which leads to a significant reduce of costs and laboratory space requirements compared to FT-ICR instruments with superconducting magnets.<sup>119</sup>

An orbitrap is constructed of a specific arrangement of axial-symmetric outer barrel-shaped and inner coaxial spindle electrodes, which generate a logarithmic electrostatic potential  $U(r, z)$  as shown in **Eq 2.26**.<sup>121, 123</sup>

$$U(r, z) = \frac{k}{2} \left( z^2 - \frac{r^2}{2} \right) + \frac{k}{2} (R_m)^2 \ln \left( \frac{r}{R_m} \right) + C. \quad \text{Eq 2.26}$$

Here,  $r$  and  $z$  are cylindrical coordinates,  $k$  is the field curvature,  $R_m$  the characteristic radius and  $C$  is an arbitrary constant. Perpendicular infusion of ions at the equatorial position relatively to the  $r$  and  $z$ -coordinates leads to stable trajectories in orbiting motions around the central electrode. Since no cross terms between  $r$  and  $z$  are present in  $U(r, z)$ , the potential in  $z$ -direction is exclusively quadratic, which leads to harmonic oscillations. Thus, the oscillation frequency in  $z$ -direction  $\omega_z$  is anti-proportional to square root of  $m/z$  as given by **Eq 2.27**.<sup>121, 123</sup>

$$\omega_z = \sqrt{k \frac{z}{m}} \quad \text{Eq 2.27}$$

The oscillation frequency  $\omega_z$  is achieved by fast Fourier-transformation (FFT) of the time-dependent detected current, which is induced by the trapped oscillating ions between two electrodes.<sup>121, 123</sup> As a consequence of FFT, the signal-to-noise ratio can be improved for longer recording times.<sup>110</sup> In addition, rotational and radial frequencies can also be determined for ion trajectories in the orbitrap potential.<sup>110</sup>

Infusion of ions obtained from an ESI-source is achieved via serially employed quadrupoles between the ion source and the orbitrap. A collision gas ( $N_2$ ) slows the ions (cooling) in turn, and causes them to accumulate in an axial potential at the end of the last quadrupole (C-trap). Subsequently, the ions are periodically inserted with a kinetic energy of  $\sim 1.3$  keV at ultrahigh vacuum to the orbitrap-mass analyzer.<sup>110, 123</sup>

### 2.5.3 Pulsed Laser Polymerization (PLP) Coupled with SEC-ESI-MS

The accessible mass range of ESI-orbitrap-MS is between 150 and 6000 m/z. Thus, the analysis of excellently resolved single charged macromolecules is limited to relatively short chain lengths, e.g. maximum of 60 MMA repeating units. Consequently, a controlled chain termination is highly desired for analysis of polymers in ESI-MS. PLP has the advantage of successive radical formation, which can be controlled via the repetition rate. PLP is widely used in combination with SEC for the determination of the propagation rate coefficients.<sup>92-95</sup>

PLP occurs as follows. The first laser pulse generates radicals by photoexcitation of a suitable initiator. The radicals initiate the monomer to start FRP, where the propagation proceeds during the dark-time until the second laser pulse arrives. The second pulse generates again radicals via initiator cleavage. Parts of the radical concentration will initiate further polymerizations, while other parts will increase the probability for termination reactions of already grown macroradicals. Termination is a diffusion-controlled statistical process (refer to FRP). Thus, some macroradicals from the first initiation step persist growing due to missing collision with another radical. As a result, a multimodal distribution of short polymers with different chain lengths is produced. Depending on the laser repetition rate, the chain-propagation during the dark time can be influenced.<sup>95</sup> Thus, higher repetition rates produce shorter polymers due to higher amount of radical formation events leading to termination. For example PLP of MMA with an ns-laser system, which generates pulses with a duration of  $\sim 7$  ns,

and a repetition rate of 100 Hz, results in a polymer distribution consisting of 2-30 repeating units. Thus, the generated oligomers are ideally suited for the analysis by ESI-orbitrap-MS, which leads to mass spectra with isotopic patterns within 200 and 3000 m/z. The obtained mass spectra from PLP-samples feature information about the cleavage mechanism of the initiator, which can be evaluated via end group analysis (**section 4.2**) as well as in so-called cocktail experiments (refer to **section 4.3**).

## 2.6 Computational Quantum Chemistry

Computational quantum chemistry is a powerful supplement to the experimental determination of molecular properties. Nowadays, *ab-initio* calculations with high accuracy are provided, which can support or even falsify experimental models.<sup>124-125</sup> A very efficient method for the calculation of molecules in ground state is density functional theory (DFT). With the expansion of DFT with time-dependent response theory (TD-R), the responses of excited states can be calculated by external perturbation of the molecular ground state.<sup>126</sup> TDDFT enables the rapid simulation of optical properties of organic and inorganic molecules. Hence, TDDFT became the most widely-used quantum chemical method in this field within the last decades.<sup>127</sup> DFT and TDDFT for calculation of the ground state properties and the vertical excitation energies of a molecule, respectively, are presented in the following.

### 2.6.1 Density Functional Theory (DFT)

The Hohenberg-Kohn-theorem is fundamental for DFT, which reduces the many-body Schrödinger equation (SG) to an electron-density problem.<sup>124, 128</sup> The electron density covers the energy and, in turn, the orbitals of the ground state of an N electron system. Thus, the energy of the system  $E$  for an electron density  $\rho$  is represented by the following equation **Eq 2.28**.<sup>124</sup>

$$E[\rho] = E_{\text{Ne}}[\rho] + F_{\text{HK}}[\rho]. \quad \text{Eq 2.28}$$

$E_{\text{Ne}}$  is the energy according to the electron-nucleus interactions and  $F_{\text{HK}}$  is a functional, which depends on the kinetic energy  $T_{\text{S}}$ , the Coulomb interactions  $J$  and the non-classical exchange-correlation potential  $V_{\text{xc}}$  of the electrons as shown in **Eq 2.29**.<sup>124</sup>

$$F_{\text{HK}}[\rho] = T_{\text{S}}[\rho] + J[\rho] + V_{\text{xc}}[\rho]. \quad \text{Eq 2.29}$$

The advantage of DFT is the reduction from 3N-electron coordinates to a one density problem with only three spatial coordinates.<sup>124</sup> However, the accuracy of the correla-

tion between the energy of the system and the electron density depends on the approximation of the functional, which is generally unknown. The success of DFT in computational chemistry is based on reintroducing an auxiliary set of orbitals for the calculation of the kinetic energy by Kohn and Sham in 1965.<sup>124, 129</sup> To this end,  $T_S[\rho]$  can be exactly calculated from Slater determinants consisting of orbitals  $\varphi_i$  of non-interacting electrons as indicated by the index S. As a consequence, the exchange-correlation functional has to be approximated, which roughly has a factor 10 smaller contribution to the total energy. Analogously to the HF-equations, the orbitals and energy of the ground state can be determined by an iterative procedure by solving the Kohn-Sham-equations for the orbitals  $\varphi_i$ . Herein, the orbitals have to fulfill the following criteria in **Eq 2.30**.<sup>124</sup>

$$\rho = \sum_i^N |\varphi_i|^2. \quad \text{Eq 2.30}$$

The choice of the functional  $F_{\text{HK}}$  is crucial for the quality of the results. In the present thesis the hybrid functional B3LYP is applied,<sup>130-131</sup> which is a linear combination of various exchange and correlation functionals including the exact HF-exchange functional  $V_{\text{XC}}^{\text{HF}}$  as represented by **Eq 2.31**.<sup>132</sup>

$$V_{\text{XC}}^{\text{HF}} = -\frac{1}{2} \sum_{i,j} \int \int \varphi_i^*(\mathbf{r}_1) \varphi_j^*(\mathbf{r}_2) \frac{1}{r_{12}} \varphi_j(\mathbf{r}_1) \varphi_i(\mathbf{r}_2) d\mathbf{r}_1 d\mathbf{r}_2. \quad \text{Eq 2.31}$$

Herein, **Eq 2.31** is a two electron integral with the exchange operator  $r_{12}^{-1}$  depending on electron coordinates  $r_1, r_2$ .

### Optimization of the Ground State Structure

An optimized structure is defined by a stationary point on the potential surface of the system, which is reached for a zero energy gradient.<sup>124</sup> In particular, stationary points can be classified by evaluation of the Hessian, which contains the second derivatives of energy with respect to the nuclei coordinates. For a positive definite matrix with eigenvalues strictly higher than zero, the stationary point is a minimum.<sup>124</sup> Herein, the global minimum with the lowest energy of the whole potential energy surface can be interpreted as the optimized ground state structure. In contrast, a saddle point is found for exactly one negative eigenvalue, which indicates a transition state with one imaginary vibrational frequency.

Stationary points can be found by iterative procedures.<sup>124</sup> Herein, the energy of an initial structure is calculated via self-consistent-field (SCF) techniques.<sup>124</sup> Subsequently, the energy gradient and Hessian are calculated to determine an optimized structure via a Newton-Raphson-method (NR). NR is based on the second order expansion of the energy using the Hessian to scale the direction and length of the iteration steps towards a stationary point.<sup>124</sup> For the optimized structure a new energy value can be calculated. The procedure is repeated in cycles until the energy and gradient reach defined convergence criteria.

NR always leads to the closest local stationary point, which is not necessarily the global minimum of the system.<sup>124</sup> Thus, the vibrational spectrum derived from the Hessian can be used to exclude a transition state by proving the absence of an imaginary frequency.

## 2.6.2 Time-Dependent Density Functional Theory (TDDFT)

Using TD-R theory enables the calculation of electronic transition energies from DFT-optimized ground state structures via TDDFT.<sup>124, 126</sup> In analogy to time-dependent perturbation theory, the amplitudes of a response function are diverging at the resonance frequencies of the system resulting from a time-dependent perturbation, e.g. perturbation of the molecular dipole moment by an electric field of a photon.

Fundamental for TDDFT is the Runge-Gross theorem,<sup>133</sup> which states that the correspondence between the electron density and an external field holds for time-dependent cases as well as for time-independent cases.<sup>124</sup> Thus, the time-dependent Kohn-Sham equations including the time-dependent electron density  $\rho(t, \mathbf{r}) = \sum_{i=1}^N |\varphi_i(\mathbf{r}, t)|^2$  consisting of single-electron orbitals  $\varphi_i$  are presented in **Eq 2.32**.<sup>124</sup>

$$i \frac{\partial}{\partial t} \varphi_i(t, \mathbf{r}) = \hat{H}[\rho](t, \mathbf{r}) \varphi_i(t, \mathbf{r}). \quad \text{Eq 2.32}$$

The Hamiltonian  $\hat{H}[\rho](t, \mathbf{r})$  can be written as follows in

**Eq 2.33**.<sup>124</sup>

$$\hat{H}[\rho](t, \mathbf{r}) = T_S[\rho](\mathbf{r}, t) + V_{ne}[\rho](\mathbf{r}, t) + J[\rho](\mathbf{r}, t) + V_{xc}[\rho](\mathbf{r}, t, \rho_0) + v_{ext}(t, \mathbf{r}). \quad \text{Eq 2.33}$$

Herein,  $v_{ext}(t, \mathbf{r})$  is corresponding to the external perturbation, e.g. via the electric field of a photon. Remarkably, the exchange-correlation energy is dependent on the

initial electron density  $\rho_0$  at  $t_0$  as well as on the time-dependent density  $\rho(t, \mathbf{r})$  for the entire time-interval  $t - t_0$  of the perturbation. Therefore, the time-dependent Kohn-Sham equation (**Eq 2.32**) has to be solved via SCF-methods in the time- and spatial-domain.<sup>124</sup> The effect can be neglected by employing an adiabatic approximation, which assumes that the electron density is a slowly varying function of time. As consequence of the adiabatic approximation, the exchange-correlation energy is reduced to a time-independent functional. In addition, the approximation of weak perturbation can be assumed for the calculation of electronic transitions, which presumably lead only to small changes in the ground state density after excitation. A perturbation by photons is weak as long as the external electric field is smaller than the field generated by nuclear charge, e.g.  $\sim 5 \cdot 10^9 \text{ V m}^{-1}$  for an electron in a hydrogen atom at the distance of 1 bohr.<sup>124</sup> Thus, instead of solving the full time-dependent Kohn-Sham equation via SCF, only the linear response of the system has to be calculated by solving the reduced eigenvalue problem as written below (**Eq 2.34**).<sup>124</sup>

$$\begin{bmatrix} \mathbf{A} & \mathbf{B} \\ \mathbf{B}^* & \mathbf{A}^* \end{bmatrix} \begin{bmatrix} \mathbf{Y} \\ \mathbf{Z} \end{bmatrix} = \omega \begin{bmatrix} 1 & 0 \\ 0 & -1 \end{bmatrix} \begin{bmatrix} \mathbf{Y} \\ \mathbf{Z} \end{bmatrix}. \quad \text{Eq 2.34}$$

The vector  $(\mathbf{Y}, \mathbf{Z})$  represents the real and imaginary parts of the first order response. The matrix  $\mathbf{A}$  contains the matrix elements of singly excited Slater determinants, while  $\mathbf{B}$  includes the matrix elements between doubly excited and a HF-reference Slater determinant.<sup>124</sup> Hence, the eigenvalues  $\omega$  reflect the excitation energies of the system. TDDFT-linear response theory in the scope of adiabatic approximation is efficient for calculation of transitions from ground state to electronic excited singlet and triplet states. The theory fails for calculation of strong perturbations or non-adiabatic phenomena, e.g. laser-induced ionization, or conical intersections, respectively.<sup>124</sup>

## 3. Methods

### 3.1 Materials

Mono-, bis- and tetraacylgermanes were provided by Ivoclar Vivadent. All used tetrazoles were synthesized by Waldemar Konrad of the Barner-Kowollik group. Iodoethane (IEt, Sigma-Aldrich, 99 %) and 4-carboxy-2,2,6,6-tetra methyl piperidine 1-oxyl (TEMPO, Sigma-Aldrich) were used for quencher studies as received. Methyl methacrylate for PLP-experiments (MMA, Sigma-Aldrich, 99 %, stabilized with < 30 ppm MEHQ) was freed from inhibitor by passing through a column of activated basic alumina (Sigma-Aldrich). Sodium trifluoroacetate (NaTFA, Sigma-Aldrich), tetrahydrofuran (THF, Scharlau, multisolvent GPC grade, 250 ppm BHT), and methanol (MeOH, Roth, HPLC ultra gradient grade) for SEC-ESI-MS sample preparation were used as received. Dichloromethane (DCM, Carl Roth GC grade 99.9 %), acetonitrile (AcN, Fisher Chemical, HPLC grade and Carl Roth UV/IR-grade 99.9 %), MeOH (Carl Roth, 99.9 %), ethanol (EtOH, Carl Roth, 99.8 %), and toluene (Merck) for fs-TA steady-state UV/Vis and fluorescence spectroscopy were applied without further purifications. Extra dry DCM (Acros organics, 99.8 %, molecular sieve, stabilized, AcroSeal) was used for quencher studies in steady-state fluorescence spectroscopy.

### 3.2 Steady-State Spectroscopy

#### 3.2.1 UV/Vis Absorption Spectroscopy

Steady-state UV/Vis absorption spectra (UV/Vis-spectra) were recorded with a Cary 500-UV/Vis/NIR-spectrometer (Varian) in the wavelength range of 200-800 nm at room temperature. All experiments were carried out in quartz cuvettes (Suprasil, Hellma Analytics). The size of the cuvette defining the optical path length was chosen with respect to the specific experiments. The optical density (OD) of samples used for fs-TA was characterized in 1 mm cuvettes. UV/Vis spectra of samples intended for fluorescence spectroscopy are recorded in the respective 10 mm fluorescence cuvettes (Suprasil, Hellma Analytics). Extinction coefficients  $\epsilon$  were carried out in 10 mm cuvettes at concentrations with respect to investigated systems.

## Sample Preparation for Determination of Extinction Coefficients

For determination of  $n\pi^*$ -extinction coefficients of acylgermane photoinitiators dissolved in MMA concentrations of  $< 2 \text{ mmol L}^{-1}$  were used. Bis- and tetrabenzoylgermanes were dissolved in acetonitrile at concentrations  $< 0.04 \text{ mmol L}^{-1}$  for comparison with TDDFT calculations.

### 3.2.2 Fluorescence Spectroscopy

Steady-state fluorescence spectra were carried out with a FluoroMax 4 (Horiba Scientific) fluorescence spectrometer at  $20 \text{ }^\circ\text{C}$  (tempered sample holder), which was provided by the working group of Prof. H.-A. Wagenknecht. All experiments are conducted in  $10 \times 10 \text{ mm}^2$  cuvettes. As an exception, the steady-state fluorescence spectrum of Tet dissolved in DCM was conducted with a Cary Eclipse fluorescence spectrometer (Varian). Fluorescence quantum yields were determined via **Eq 3.1**.<sup>134</sup>

$$\phi_F^i = \phi_F^{\text{ref}} \frac{f_{\text{OD}}^{\text{ref}}(\lambda_{\text{exc.}}) \int_{\lambda_{\text{em.}}} I_{\text{em.}}^i(\lambda_{\text{em.}}) d\lambda_{\text{em.}} n_1^2}{f_{\text{OD}}^i(\lambda_{\text{exc.}}) \int_{\lambda_{\text{em.}}} I_{\text{em.}}^{\text{ref}}(\lambda_{\text{em.}}) d\lambda_{\text{em.}} n_{\text{ref}}^2}, \quad \text{Eq 3.1}$$

$$\text{with } f_{\text{OD}}^{\text{ref}/i}(\lambda_{\text{exc.}}) = 1 - 10^{-\text{OD}_{\text{ref}/i}(\lambda_{\text{exc.}})}.$$

The fluorescence quantum yield of the investigated sample  $\phi_F^i$  can be obtained by using a quantum yield of a known reference system  $\phi_F^{\text{ref}}$ . Herein,  $f_{\text{OD}}^{\text{ref}/i}$  is the absorption factor given by the  $\text{OD}_{\text{ref}/i}$  at the excitation wavelength  $\lambda_{\text{exc.}}$ .  $I_{\text{em.}}^{i/\text{ref}}(\lambda_{\text{em.}})$  the emission spectrum integrated for all emission wavelengths  $d\lambda_{\text{em.}}$ , and  $n_{1/\text{ref}}^2$  the refractive index of the applied solvent.

### Sample Preparation

Tetrazole samples for quantum yield determination with excitation at  $\lambda_{\text{exc.}} = 395 \text{ nm}$  and slit sizes of  $1 \text{ nm}$  were concentrated at  $10^{-4} \text{ mol L}^{-1}$  in extra dry dichloromethane (molecular sieve, stabilized, 99.8 %). For quencher concentration-dependent studies, tetrazoles were dissolved in DCM:IEt-mixtures with IEt-concentrations between  $0.05$  and  $0.5 \text{ mol L}^{-1}$ . C307 dissolved in EtOH was exploited as a reference system<sup>135</sup> ( $\phi_F^{\text{ref}} = 56 \%$  at  $\lambda_{\text{exc.}} = 395 \text{ nm}$ ) at a concentration of  $4.5 \cdot 10^{-6} \text{ mol L}^{-1}$ .

Very low quantum yields of acylgermane- and acylstannane-photoinitiators are determined at  $\lambda_{\text{exc.}} = 400 \text{ nm}$  with high slit sizes of  $5 \text{ nm}$  by using a C307 EtOH reference at a recorded OD of  $0.325$ , which was subsequently diluted by a factor of  $5000$

resulting in a calculated OD of  $\sim 6.5 \cdot 10^{-5}$  (for reference spectra refer to **Figure A2c**). Emission spectra of the photoinitiators are recorded at sample ODs between 0.4 and 0.6.

### 3.3 Pulsed Laser Polymerization coupled with Electrospray Ionization Mass spectrometry (PLP-ESI-MS)

#### 3.3.1 Pulsed Laser Polymerization (PLP)

For PLP experiments, the flash diode-pumped Q-switched Nd:YAG tunable laser system SpitLight EVO 200 OPO (InnoLas Laser GmbH) was applied. A broad wavelength tunability of the system is achieved by using an OPO (410-670 nm) in combination with switchable SFM (295-410 nm) and SHG (270-310 nm) as schematically depicted in **Figure 3.1**.

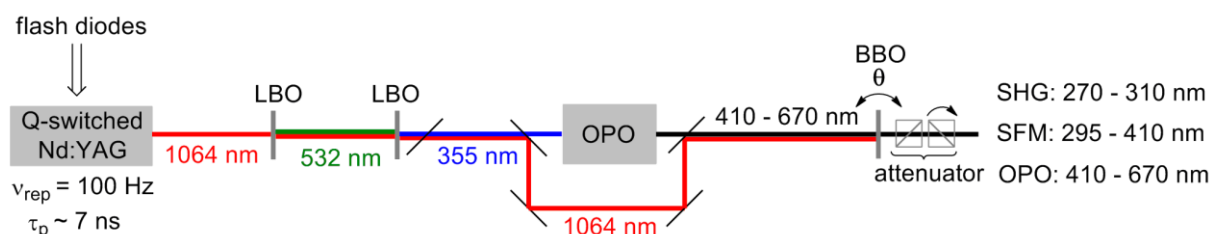


**Figure 3.1.** Simplified schematic setup of tunable ns-laser (InnoLas). Broad wavelength tunability between 270 and 670 nm is achieved by applying an OPO in combination with SFM and SHG.

The flash diode-pumped Q-switched Nd:YAG-laser generates laser pulses with a duration of  $\sim 7$  ns and a repetition rate of 100 Hz at 1064 nm. A combination of SHG and SFM by two LBO-crystals is used for generation of laser pulses at 355 nm as the third harmonic of the fundamental wavelength. 355 nm-pulses are used for pumping an OPO in a special configuration consisting of two mirror-symmetrical BBO crystals. The BBOs are mounted on high-speed and accuracy galvanometer-stages to adjust the crystal angle achieving wavelength tunability. The angle can be automatically controlled by the SpitLight control software. The OPO generates laser pulses with wavelengths between 410 and 670 nm. Subsequently, the OPO-generated pulses can be further frequency converted by another BBO crystal mounted on a galvanometer stage. Depending on the crystal angle  $\theta$ , the BBO is either used for SFM of the OPO output with the fundamental 1064 nm-pulse, or SHG of the OPO-output leading to accessible wavelength ranges of 295-410 nm and 270-310 nm, respectively. At  $\theta = 0^\circ$ , the OPO light is transmitted without further frequency conversion. In sum-

mary, a broad tunability from 270 to 670 nm is achieved. The maximum pulse energy varies for the three different frequency conversion processes due to the different frequency conversion efficiencies of the parametric processes. Herein, the maximal pulse energy from OPO generated pulses is ~12 mJ, while maximal energies for SFM and SHG are between 1-2 mJ. For fine-tuning of the pulse energy output, an attenuator is used, which consists of two crossed polarizers from which the latter one can be adjusted until both polarizers are in parallel configuration leading to the maximum output energy. In addition, the first polarizer of the attenuator can be adjusted to remove the OPO-pump light after SHG or SFM, which has a 90°-rotated polarization with respect to the frequency converted pulses.

For PLP-experiments, an in-house built setup<sup>75</sup> was used as depicted in **Figure 3.2**.

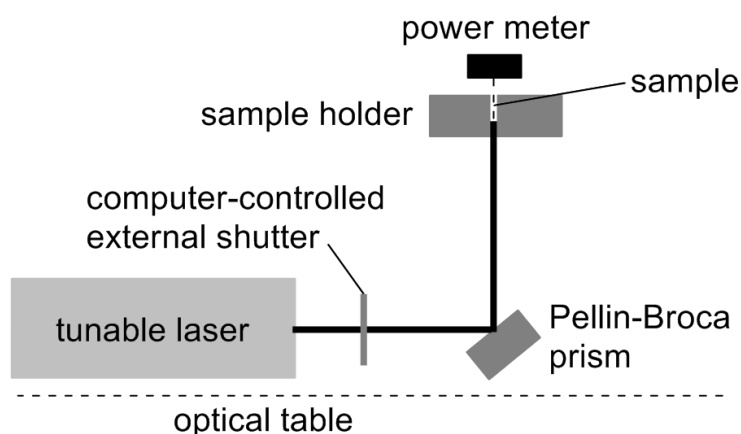


**Figure 3.2.** In-house built experimental setup for PLP-experiments consisting of tunable laser system, a computer-controlled external shutter, a Pellin-Broca prism for wavelength-selective vertical reflection into the sample holder. The sample holder has a cylindrical hole with a diameter of ~5 mm for inserting the corresponding sample vials. The pulse energy after the sample holder can be measured via a power meter (Coherent) and removed sample vial.

Tuned laser pulses are deflected via a Pellin-Broca prism into the sample holder, which is a metal block with a cylindrical slot for carrying a sample vial with a diameter of 5 mm. The deflection angle of a Pellin-Broca prism is wavelength dependent. Thus, possible residual secondary OPO-light used for frequency conversion processes (SFM, SHG) is safely separated. The pulse energy at the sample position is estimated by a power meter (Coherent), which is placed on top of the sample holder with removed sample vial. A computer controlled external shutter (InnoLas) is used to define start and ending points for irradiation experiments.

## Sample Preparation and PLP-Conditions

The majority of PLP-experiments are conducted in MMA in bulk with a total initiator concentration of  $5 \text{ mmol L}^{-1}$  and a sample volume of  $0.5 \text{ mL}$ . PLP-experiments with tetraacylgermane derivatives are carried out at a concentration of  $2.5 \text{ mmol L}^{-1}$  due to much higher monomer conversion. All samples are freed from oxygen via nitrogen purging for at least 5 min. Unless noted otherwise, the typically applied conditions for PLP-experiments were  $320 \mu\text{J/pulse}$ , 90000 pulses at a repetition rate of 100 Hz (15 min per experiment) resulting in a total irradiation energy of  $\sim 29 \text{ J}$ . The irradiation wavelength was chosen with respect to the absorption spectra of the investigated systems.

### 3.3.2 Size Exclusion Chromatography (SEC) and Direct Infusion (DI) Electropray Orbitrap Mass Spectrometry (ESI-MS)

Mass spectrometry is conducted via direct infusion (DI) and SEC coupled with ESI-MS as depicted in **Figure 3.3**.

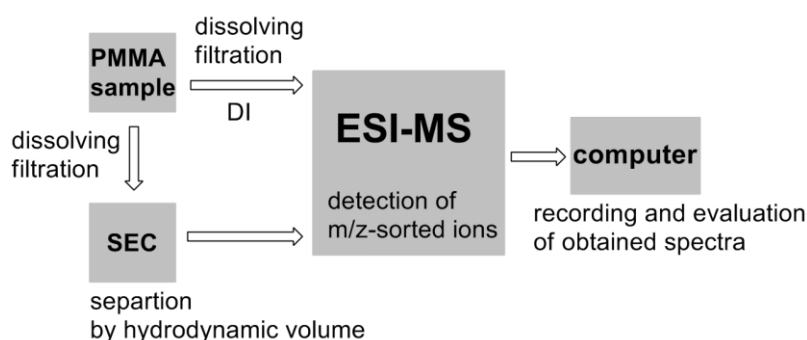


**Figure 3.3.** Schematic overview of applied instrumentation for PMMA-sample analysis via direct infusion (DI)-ESI-MS as well as SEC-ESI-MS.

For DI, poly(methyl methacrylate) (PMMA) samples were dissolved in a  $100 \mu\text{molar}$  NaTFA 3:2 THF:MeOH-mixture at sample concentration of  $\sim 0.05 \text{ mg mL}^{-1}$ . Subsequently, the solutions are filtered and infused into the ESI-source by a computer-controlled syringe at a flow of  $5 \mu\text{L min}^{-1}$ . Alternatively, the PMMA-samples could be infused into the ESI-source after pre-separation via SEC. Herein, samples were dissolved at a concentration of  $2 \text{ mg mL}^{-1}$  in THF and filtered before placing into the autosampler of the SEC system.

SEC of PMMA species was carried out with a Polymer Laboratories (Varian) PL-GPC 50 Plus Integrated System, which consists of an autosampler, a PLgel 5 mm bead

size guard column (50 x 7.5 mm), one PLgel 5 mm Mixed E column (300 x 7.5 mm), three PLgel 5 mm Mixed C columns (300 x 7.5 mm), and a differential refractive index detector. THF was applied as the eluent at 35 °C with a flow rate of 1 mL min<sup>-1</sup>. Calibration of the SEC system was conducted by using linear poly(styrene) standards and PMMA standards, which are ranging from 370 g mol<sup>-1</sup> to 2.52·10<sup>6</sup> g mol<sup>-1</sup> and 800 g mol<sup>-1</sup> to 1.6·10<sup>6</sup> g mol<sup>-1</sup>, respectively.

Mass spectra were measured on a Q exactive orbitrap mass spectrometer (Thermo Fisher Scientific) equipped with an HESI II probe. For calibration within the m/z range of 74-1822, premixed calibration solutions (Thermo Scientific) were exploited. For the ESI-process, a constant spray voltage of 4.7 kV and a dimensionless sheath gas of 5 and a capillary temperature of 320 °C were applied. S-lens RF level was set to 62.0. For recording the mass spectra the software package Tune (Thermo Scientific) was applied.

### **3.4 Time Resolved Spectroscopy**

#### **3.4.1 Time-Correlated Single Photon Counting (TCSPC)**

Determination of fluorescence lifetimes were conducted via time-correlated single photon counting (TCSPC) by using the DeltaTime accessory on FluoroMax fluorescence spectrometer (Horiba), which was provided by the working group of Prof. H.A. Wagenknecht. Herein, the controller (DeltaHub including NanoLED Controller, Horiba) triggers the pulsed LED (NanoLED, Horiba, 366 nm, 4 pJ/pulse,  $\nu_{rep} = 1.2$  ns) for excitation of the sample as well as the time-correlated detection of the emitted photons via photomultiplier (R928P, Hamamatsu) in photon counting mode (200-980 nm, 950 V, linearity to 2·10<sup>6</sup> counts s<sup>-1</sup>). The TCSPC-data analysis including deconvolution and exponential fitting was conducted with program package DAS6 (Horiba). A LUDOX standard solution (30 wt % colloidal silica in H<sub>2</sub>O, Sigma Aldrich) was used for recording the prompt signal for deconvolution of the system responses and recorded emission decay of the sample.

#### **Sample Preparation and Conditions**

After excitation at 366 nm, the emission decays for visible light-triggered tetrazole systems BiphTet and PyTet dissolved in in DCM were recorded at 434 and 507 nm, respectively. The samples were highly diluted with concentrations of

$\sim 10^{-6}$  mol L<sup>-1</sup>. Thus, the detector saturation was always below 2 % at photomultiplier voltage of 1500 V.

### 3.4.2 Transient Broadband Absorption Spectroscopy (fs-TA)

The applied setup for pump-probe experiment is schematically depicted in **Figure 3.4**, which was in-house built within previous works.<sup>34, 136</sup>

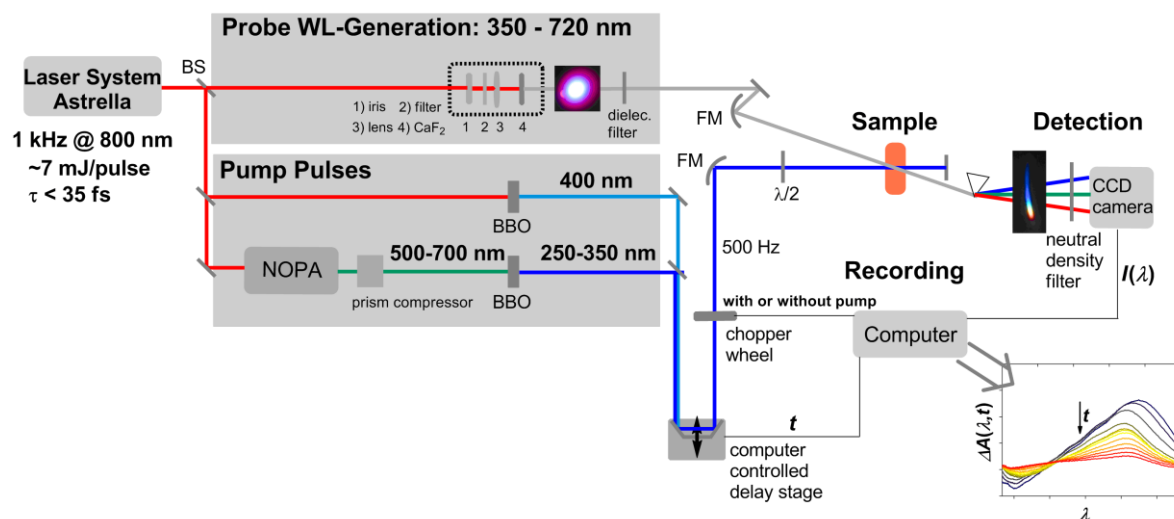


**Figure 3.4.** Experimental setup for fs-TA. For a detailed description refer to main text.

Fs-laser pulses for transient pump-probe experiments were generated by a CPA-femtosecond laser system (Astrella, Coherent). Herein, fs-seed-pulses (800 nm,  $\sim 450$  mW, 80 MHz) were generated by a mode-locked Ti:sapphire oscillator (Vitara-S, Coherent), which is pumped by a frequency-doubled optical semi-conductor-laser (532 nm, 3.2 W Verdi-G, Coherent). The fs-seed pulses were amplified via CPA by using a frequency-doubled neodym-doped yttrium lithium fluoride (Nd:YLF) laser (Revolution, Coherent) emitting ns-pulses at 527 nm with 39 mJ/pulse at 1 kHz. The number of oscillations of the seed-pulse within the amplifier was controlled by two Pockels cells. Finally, the recompressed laser pulses featured a duration of  $\sim 35$  fs with a repetition rate of 1 kHz at  $\sim 7.3$  mJ (Revolution power  $\sim 36.5$  W at a diode current of 22.5 A, Vitara power  $\sim 440$  mW) per pulse energy and central wavelength of 800 nm.

For recording of transient spectra only a fraction of the laser energy was used for the pump-probe experiment by exploiting an arrangement of beam splitters (indicated by BS, **Figure 3.4**).

2-3  $\mu\text{J}/\text{pulse}$  of the fundamental wavelength was used for continuum generation in a 2 mm thick  $\text{CaF}_2$  crystal leading to white light-pulses featuring probing wavelengths from 350 to 720 nm. To this end, the fundamental pulse was focused via an achromatic double lens ( $f = 100$  mm, 610-1150 nm anti-reflection coating, Thorlabs) into the  $\text{CaF}_2$  crystal, which is mounted on a vertical translation stage. The stability of the white light continuum was fine-adjusted via a combination of a neutral density (ND)-filter and iris. Remaining 800 nm-light is removed via dielectric filtering.

Pump pulses were generated in two possible setups, which led to excitation wavelengths of 400 and 300 nm, respectively. For generation of 400 nm pulses a fraction with  $\sim 200$   $\mu\text{J}/\text{pulse}$  of the fundamental beam of 800 nm was frequency-doubled via SHG of a BBO crystal (0.1 mm, Nortus Optronic GmbH). Pump pulses at 300 nm were generated by a frequency-doubled non-collinearly optical parametric amplifier (NOPA). Herein,  $\sim 300$   $\mu\text{J}/\text{pulse}$  at 800 nm were used for pumping the NOPA, which led to laser pulses between 500 and 700 nm with 3.5-4.5  $\mu\text{J}/\text{pulse}$ . The pulses were compressed by a prism compressor to achieve a high frequency conversion ( $\sim 10$  %) in a subsequent 0.2 mm thick BBO crystal for SHG. The residual NOPA light was removed by using three dielectric mirrors with high reflectance between 300 and 360 nm and high transmittance between 470 and 750 nm. Hence, UV-pulses were generated with energies of 0.35-0.45  $\mu\text{J}/\text{pulse}$ .

Pump and probe pulses were deflected via focusing mirrors (FM) to the sample position providing a larger focus diameter of the pump ( $\sim 60$   $\mu\text{m}$ ) than for the probe beam ( $\sim 20$   $\mu\text{m}$ ). Delay times between pump and probe pulses were achieved by delaying the pump pulse with retro-reflector (PLX Inc., UV-enhanced aluminum reflectance  $> 89$  % for 225 to 700 nm), which was mounted on a computer-controlled translation stage (Thorlabs). The spatial overlap was accomplished via aligning pump and probe beams to a 50  $\mu\text{m}$  pinhole at the sample position. Spatial fine-alignment as well as optimization of the temporal overlap was achieved by using a suitable reference dye in a 1 mm quartz cuvette, e.g. coumarin 307 (C307) at 400 nm, and 4,4-bis-(2-butylloctyloxy)-p-quaterphenyl (BiBuQ) for UV-excitation.

To exclude polarization-dependent anisotropy effects, both pulses were overlapped under magic angle conditions at  $54.7^\circ$  with respect to the relative polarization between pump and probe pulse by using a tunable  $\lambda/2$ -plate (ALPHALAS, 150-6000 nm, 2.5 mm). Sample solutions were continuously stirred with a cylindrical

micro stir bar (length  $\times$  radius:  $3 \times 0.1 \text{ mm}^2$ ) in a 1 mm thick fused silica cuvette to ensure the replenishment of the sample at the focus.

For detection of the probe pulse, the white light continuum was split in its spectral components via a quartz prism polychromator, which were deflected to a CCD line scan camera (series 2000, Entwicklungsbüro Stresing). Wavelength calibration of the CCD camera was carried out via interference filters (Thorlabs).

For recording transient absorption spectra, a chopper wheel was implemented to the pump beam line, which chops the repetition rate down to 500 Hz. The CCD camera and chopper wheel was synchronized via a 1 kHz external trigger signal according to the laser repetition rate, which was shared by a delay generator (DG535). Thus, the CCD camera records the intensity of the probe pulse with  $I_w$  and without  $I_{w/o}$  excitation of the sample due to blocking of every second pump pulse by the chopper wheel. The setup was operated with an in-house developed LabView-program (National Instruments), which records the data detected by the CCD camera with respect to the current delay position defining the time  $t$  between pump and probe pulse (for principle of pump-probe technique refer to **section 2.4.5**). By using **Eq 2.25** and assuming a constant  $I_0$  of the white light pulse without sample, the transient absorption is measured as given by **Eq 3.2**.<sup>136</sup>

$$\Delta A(t, \lambda) = \log \frac{I_{w/o}(\lambda)}{I_w(t, \lambda)}. \quad \text{Eq 3.2}$$

### Sample Preparation and Conditions

All TA-spectra are recorded in 1 mm quartz cuvettes (Suprasil, Hellma Analytics). Samples were stirred with a micro stir bar for continuously replenishment of the sample within the pump region of the laser focus. All samples were probed by a CaF<sub>2</sub>-generated white light continuum between 350 and 720 nm.

## Acylgermane and -Tin Photoinitiator Systems

TA-spectra of photoinitiators were probed after excitation at 400 nm, which have shown in general weak transient responses in line with previous transient initiator studies.<sup>35</sup> Thus, high sample ODs were applied to achieve well-resolved TA-spectra.

Monoacylgermanes in MeOH were excited at pump energies of  $\sim 0.40$   $\mu\text{J}/\text{pulse}$  and sample ODs of  $\sim 1.4$  for  $\text{B}_1\text{G}$ ,  $\text{MB}_1\text{G}$ ,  $\text{FB}_1\text{G}$ , and  $\sim 0.4$  for  $\text{C}_1\text{BG}$  and  $\text{N}_1\text{BG}$  (refer to Figure 4.26). Bis-  $\text{B}_2\text{G}$  and tetraacylgermanes  $\text{B}_4\text{G}$ ,  $\text{oMeB}_4\text{G}$ ,  $\text{oEtB}_4\text{G}$  and  $\text{PrOB}_4\text{G}$  dissolved in AcN were excited with pump energies at  $\sim 0.30$   $\mu\text{J}/\text{pulse}$  and ODs between 0.6 and  $\sim 1.6$  (refer to **Figure A41**, **Figure 4.33**).

$\text{Mes}_4\text{T}$  was dissolved in toluene and excited with pump energy of  $\sim 0.44$   $\mu\text{J}/\text{pulse}$  and OD of  $\sim 3.2$ .

## Tetrazole systems

Visible light-triggered tetrazole systems were excited at 400 nm with pump energies of 0.32-0.64  $\mu\text{J}/\text{pulse}$ . PyTet and BiphTet were dissolved in DCM and DCM:IEt-mixtures at concentrations between  $10^{-4}$  and  $5 \cdot 10^{-3}$   $\text{mol L}^{-1}$  resulting in an OD of 0.1-0.7. IEt was applied in concentrations from 0.2-8.4  $\text{mol L}^{-1}$ . Reference experiments of PyTet in DCM with TEMPO used as a quencher were conducted with a PyTet concentration of  $\sim 5 \cdot 10^{-3}$  and TEMPO concentration of  $\sim 4 \cdot 10^{-2}$   $\text{mol L}^{-1}$ . The exact concentrations of tetrazoles and quenchers are indicated at the respective figures in **chapter 6**.

A reference experiment with UV-tetrazole Tet dissolved in DCM was carried out at a high OD of  $\sim 2$  due to low pump energy of 0.22  $\mu\text{J}/\text{pulse}$  at 300 nm.

## Data Evaluation

Due to GVM (refer to **section 2.4.1**), all transient spectra are zero-time-corrected by using an in-house built LabView program. Multi-exponential fitting and global analysis were conducted with Origin 2018b and an in-house written matlab script by utilizing **Eq 3.3**.<sup>137</sup>

$$\Delta A = g(t, \tau_0) \cdot \sum_{i=1}^n C_i(\lambda) \cdot e^{-\frac{t}{\tau_i}}, \quad \text{Eq 3.3}$$

$$\text{with } g(t, \tau_0) = \frac{1}{2} \left[ 1 + \operatorname{erf} \left( \sqrt{4 \ln 2} \frac{t}{\tau_0} \right) \right].$$

$C_i(\lambda)$  is the wavelength-dependent amplitude of the process  $i$ , which corresponds to an exponential decay with a time-constant  $\tau_i$ . The error-function  $g(t, \tau_0)$  consists of the convolution of a Gaussian with a step function, which approximately reflects the cross-correlation artifact resulting from overlapping pump and probe pulses including the time-resolution of the experiment  $\tau_0 \sim 80$  fs.<sup>136</sup> In comparison to Origin 2018b, the matlab-script enables much faster global analysis for the entire wavelength range of a TA-spectrum. Herein, a multi-exponential fitting routine is executed for all wavelengths with an initial guess of shared time constants and time-resolution. Manual evaluation via Origin 2018b was necessary for transient spectra with wavelength-dependent chirp-artifacts, which were not covered within the GVM-correction. Global analysis leads to decay associated spectra (DAS) via plotting the amplitudes  $C_i(\lambda, \tau_i)$  versus the wavelength  $\lambda$  according to each exponential process with respective  $\tau_i$ .<sup>138</sup> Negative amplitudes are associated to increasing transient responses, while positive indicate decay. For the comparison of amplitudes of different spectra, relative amplitudes  $C_i^{\text{rel}}(\lambda)$  can be obtained from **Eq 3.4**.

$$C_i^{\text{rel}}(\lambda) = \frac{C_i(\lambda)}{\sum_{i=1}^n C_i(\lambda)}. \quad \text{Eq 3.4}$$

## 3.5 Computational Methods

### 3.5.1 Time-Dependent Density Functional Theory (TDDFT) Calculations

Time-dependent and -independent DFT calculations were carried out via the TURBOMOLE V7.0 program package.<sup>139</sup> The optimization of the DFT-ground state was conducted by applying a B3LYP functional<sup>130-131</sup> with a def2-TZVPP basis set.<sup>140</sup> Convergence was reached at an energy change smaller than  $10^{-8} E_h$  and density matrix change of  $10^{-7}$ . A structure was considered to be optimized for a Cartesian gradient lower than  $10^{-4} E_h/a_0$ . For validation of an optimized ground state structure, the vibrational spectra were conducted by calculating the Hessian via TURBOMOLE's aoforce module.<sup>141</sup> Finally, the vertical excitation energies into excited singlet and triplet states are obtained via TDDFT-calculations at the optimized ground state coordinates.

## 4. Acylgermane-Based Visible Light Photoinitiators<sup>1</sup>

Light-induced FRP has a broad application field in industrial and scientific research, e.g. tissue engineering,<sup>19, 142</sup> advanced curing techniques,<sup>15-16</sup> and dental fillings.<sup>17-18</sup> However, a systematic understanding for a tailor-made design of new photoinitiator system is not available, which demands an in-depth mechanistic characterization of initiators. Main issues are the design of initiators with high initiation efficiencies, visible light absorption and sufficient bleaching properties. Visible light absorption is crucial to achieve a higher penetration depth during curing processes as well as a general applicability in bioorthogonal chemistry.<sup>14, 23, 39</sup> Sufficient bleaching ensures colorless polymer formation via photo FRP, which is important for special requirements, e.g. cosmetic aspects for dental fillings.<sup>17</sup>

Acylgermanes are promising photoinitiator systems for visible light-triggered FRP. Since the first approach of Mochida *et al.* in the 1980s,<sup>36</sup> a manifold of synthesis routes for mono-, bis-<sup>39</sup> and tetraacylgermane<sup>40</sup> derivatives were developed, which reveal a high initiation efficiency for visible light-irradiation between 400-490 nm.<sup>38</sup> Hence, the broad variety of accessible derivatives enables a fundamental investigation on the structure-property correlations for the systematic mechanism development of visible light-driven Norrish type I photoinitiators. All events from light excitation and initiator cleavage to the final macromolecular growth are of striking importance for a comprehensive characterization of photoinitiators. Herein, extinction coefficients, channel branching within the excited states, cleavage of the initiator into radical fragments, as well as reactivity of the radical towards monomers including competing reaction channels need to be investigated.<sup>32, 143</sup> In fact, a wide range of methods were applied in the past to study the photophysical and -chemical properties of mono-, bis- and- tetraacylgermanes, e.g. via ESR and CIDNP,<sup>43</sup> laser flash photolysis- coupled with UV/Vis spectroscopy<sup>38</sup> and actinometry<sup>39</sup>.

In the present thesis, a methodical combination of fs-TA and PLP-ESI-MS is applied as presented in a schematic overview in **Figure 4.1**.<sup>34-35</sup>

---

<sup>1</sup> Parts of this chapter were reproduced with permission from P. Jöckle, C. Schweigert, I. Lamparth, N. Moszner, A.-N. Unterreiner, C. Barner-Kowollik, *Macromolecules* **2017**, *50*, 8894-8906; P. Jöckle, J. Radebner, M. Haas, I. Lamparth, H. Stueger, N. Moszner, A.-N. Unterreiner, C. Barner-Kowollik, *ACS Macro Letters* **2018**, *7*, 132-136; P. Jöckle, P. W. Kamm, I. Lamparth, N. Moszner, A.-N. Unterreiner, C. Barner-Kowollik, *Macromolecules* **2019**, *52*, 281-291. Copyright 2017-2019 American Chemical Society.

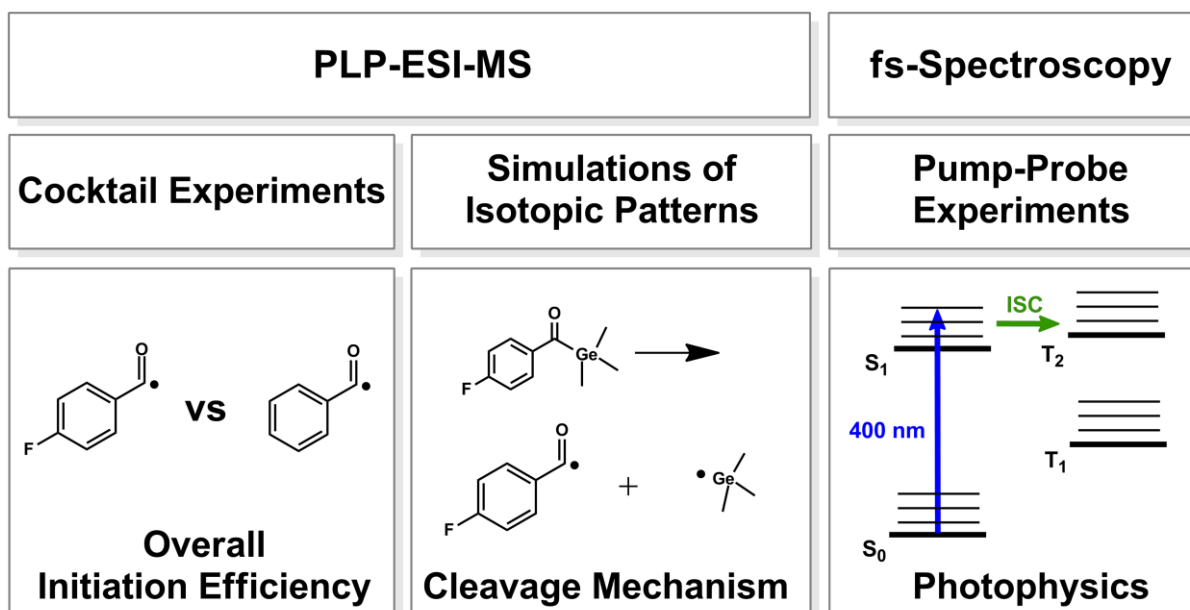


**Figure 4.1.** Overview of the applied methodological approach as a combination of PLP-ESI-MS and fs-TA to investigate the correlation between the overall initiation efficiency and photophysics of acylgermane initiators. Adapted with permission from ref. 144. Copyright 2017 American Chemical Society. Modified presentation.

Critical steps for the photophysics of Norrish type I initiators are determined – *in-situ* – on a ps-time scale after excitation,<sup>44</sup> which can be traced by fs-TA. In addition, TDDFT-calculations and steady-state spectroscopy can support the development of the photochemical and -physical mechanism.<sup>33-35</sup> In contrast, valuable information about the overall performance of an initiator in photo FRP can only be derived – *post-mortem* – after final macromolecular growth, e.g. overall initiation efficiency as well as characterization of the quality of the obtained polymer species. Well-established PLP-ESI-MS methods are a powerful tool to quantify the overall initiation efficiency from the final polymer distribution in so-called cocktail experiments.<sup>32, 34-35, 143</sup> In the current chapter, the combination of PLP-ESI-MS and fs-TA is applied on a library of mono-, bis- and tetraacylgermane photoinitiators, which are depicted in **Figure 4.2**.

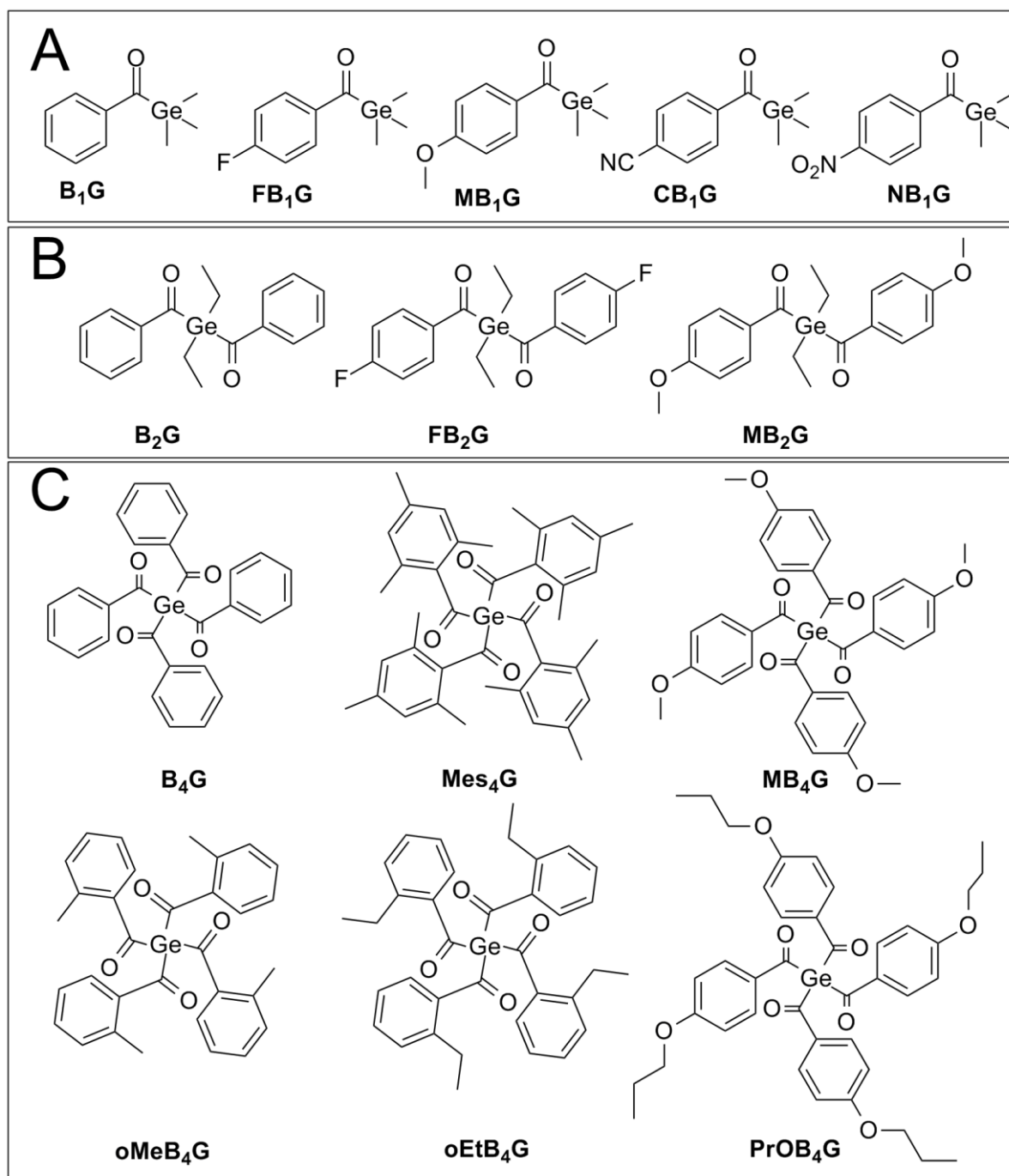


**Figure 4.2.** Overview of investigated mono- (A), bis- (B), and tetra (C)-acylgermanes, e.g. benzoyltrimethylgermane ( $B_1G$ ), *para*-fluorobenzoyltrimethylgermane ( $FB_1G$ ), *para*-methoxybenzoyltrimethylgermane ( $MB_1G$ ), *para*-cyanobenzoyltrimethylgermane ( $CB_1G$ ), *para*-nitrobenzoyltrimethylgermane ( $NB_1G$ ), bisbenzoyldiethylgermane ( $B_2G$ ), bis-*para*-fluorobenzoyldiethylgermane ( $FB_2G$ ), bis-*para*-methoxybenzoyldiethylgermane ( $MB_2G$ ), tetrabenzoylgermane ( $B_4G$ ), tetramesitylgermane ( $Mes_4G$ ), tetra-*para*-methoxybenzoylgermane ( $MB_4G$ ), tetra-*ortho*-methylbenzoylgermane ( $oMeB_4G$ ), tetra-*ortho*-ethylbenzoylgermane ( $oEtB_4G$ ), and tetra-*para*-propoxybenzoylgermane ( $PrOB_4G$ ).

All initiators are labeled with  $X_jG$ , where X describes the chemical nature of j benzoyl moieties, while G is representative for germane-based groups. The nomenclature includes the following simplifications: *para*-substituted initiators have no extra label,

e.g. MB<sub>4</sub>G for tetra-*para*-methoxybenzoylgermane, while from *para*-substitution patterns-diverging moieties are labeled explicitly, e.g. oMeB<sub>4</sub>G for tetra-*ortho*-methylbenzoylgermane. The chemical nature of G varies according to the number *j* of benzoyl moieties. G reflects a trimethyl germane-group in monoacylgermanes (*j*=1), a diethyl germane-group in bisacylgermanes (*j*=2) and a central germanium in tetra-benzoylgermanes (*j*=4).

The chapter opens with the investigation of the steady-state absorption and fluorescence properties of acylgermanes, which is supported by TDDFT-calculations. Subsequently, the radical species formed by mono-, bis- and tetraacylgermanes are identified via *post-mortem* PLP-ESI-MS end group analysis of PMMA obtained from photo FRP. A comprehensive comparison of overall initiation efficiencies of *para*-fluoro and methoxy substituted mono-, bis- and tetraacylgermanes is undertaken via PLP-ESI-MS cocktail experiments. In the following, the results of fs-TA experiments with mono- and tetra-acylgermanes are presented and correlated to the findings from previous *post-mortem* methods. Parts of this chapter are published in ref. 144-146. Adapted figures and tables are labeled in accordance to the permission of the corresponding journals. Changes within the presentation of the data are pointed out in figure as well as table captions by the term “modified presentation”.

## 4.1 Steady-State Spectroscopic Properties

Steady-state UV/Vis-absorption spectroscopy provides fundamental information about the wavelength and extinction coefficient of transitions between electronic ground and excited states. Vertical excitation wavelengths calculated by TDDFT can support the evaluation of the UV/Vis spectra. In addition, luminescence spectroscopy gives insight into possible radiative relaxation pathways, which is important for the characterization of singlet-triplet channel branching within excited states. Thus, steady-state absorption and luminescence properties of acylgermanes are crucial for the development of their photophysical and -chemical mechanism. Thus, results from UV/Vis spectroscopy can guide the choice of excitation wavelength in PLP experiments as well as in fs-TA.

In the following the absorption and luminescence properties of exemplary bis- and tetraacylgermanes are presented together with results from TDDFT-calculations to investigate the influence of the number of benzoyl moieties on the electronic struc-

ture. For an in-depth UV/Vis and TDDFT-analysis of monoacylgermanes refer to Feuerstein *et al.*<sup>31</sup> Subsequently, the influence of *para*-fluoro- and methoxy-substitution patterns on  $\pi\pi^*$ -extinction coefficients of acylgermanes is analyzed for latter comparison with overall initiation efficiencies from PLP-ESI-MS cocktail experiments

#### 4.1.1 Absorption and Luminescence Properties of Exemplary Acylgermanes

UV/Vis spectra recorded in AcN and vertical excitation wavelengths calculated by TDDFT (def2-TZVPP/B3LYP) of B<sub>2</sub>G and B<sub>4</sub>G are presented in **Figure 4.3**. Similar results for MB<sub>2</sub>G, FB<sub>2</sub>G and MB<sub>4</sub>G are provided in **Figure A1**. Corresponding DFT-Cartesian coordinates and calculated vibration spectra to confirm the ground state structures are provided in **Table A1-Table A4**.

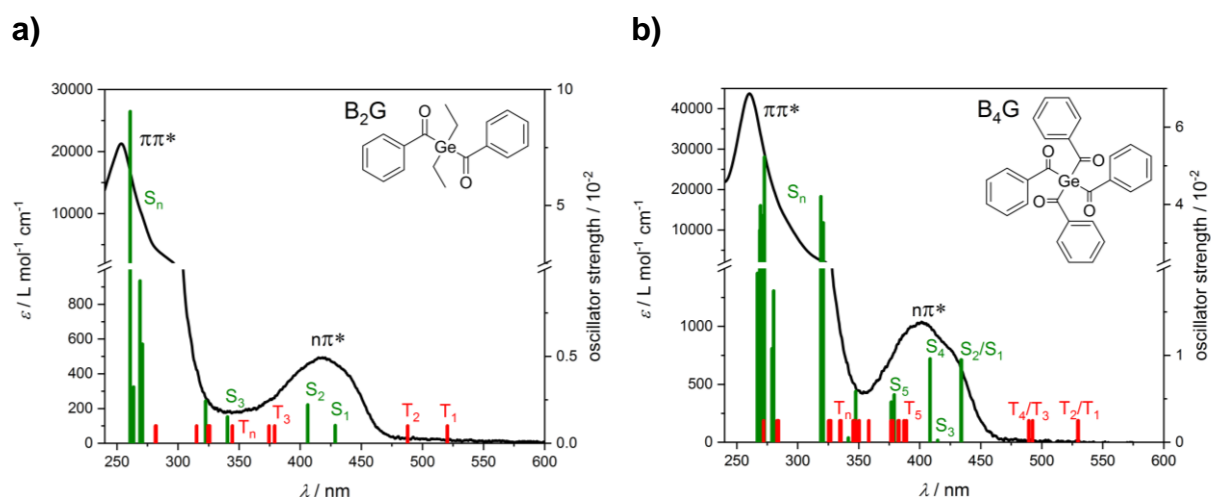


**Figure 4.3.** Steady-state UV/Vis spectra recorded in AcN together with singlet (green) and triplet (red) vertical excitation wavelength calculated by TDDFT (def2-TZVPP/B3LYP) of a) B<sub>2</sub>G and b) B<sub>4</sub>G. Adapted with permission from ref. 146. Copyright 2019 American Chemical Society. Modified presentation.

The UV/Vis spectra of B<sub>2</sub>G and B<sub>4</sub>G in AcN are exemplary for the majority of the acylgermanes derivatives, which consist of a strong band in the UV-A range, e.g.  $\epsilon_{\max}(\text{B}_2\text{G}, 254 \text{ nm}) \approx 21000 \text{ L mol}^{-1} \text{ cm}^{-1}$ ,  $\epsilon_{\max}(\text{B}_4\text{G}, 260 \text{ nm}) \approx 44000 \text{ L mol}^{-1} \text{ cm}^{-1}$  as well as a weak band in the visible range, e.g.  $\epsilon_{\max}(\text{B}_2\text{G}, 419 \text{ nm}) \approx 360 \text{ L mol}^{-1} \text{ cm}^{-1}$  and  $\epsilon_{\max}(\text{B}_4\text{G}, 402 \text{ nm}) \approx 1000 \text{ L mol}^{-1} \text{ cm}^{-1}$ . In a simplified view, the strong band can be assigned to  $\pi\pi^*$ - and the weak band to  $n\pi^*$ -transitions.<sup>31, 147</sup> In line with monoacylgermanes,<sup>31</sup> a manifold of singlet and bathochromic shifted triplet states are predicted within the  $\pi\pi^*$ -band for B<sub>2</sub>G and B<sub>4</sub>G by TDDFT-calculations.  $\pi\pi^*$ -bands of

Norrish type I initiators are known to lead to non-favored relaxation pathways due to numerous branched excited states.<sup>34-35</sup> In contrast, excitation of  $n\pi^*$ -bands feature an efficient ISC into low lying triplet states with subsequent homolytic cleavage. In accordance to the number of benzoyl moieties, one, two, and four singlet and bathochromic shifted triplet states are expected by TDDFT for  $B_1G$ ,<sup>31</sup>  $B_2G$  and  $B_4G$  within the region of their  $n\pi^*$ -bands. Thus, in a simplified picture, each  $n\pi^*$ -singlet state can be assigned to one benzoyl moiety, which is in line with an increase in the extinction coefficients from mono- to bis- to tetraacylgermanes with identical substitution patterns. However, a selective excitation of one independent benzoyl unit is unlikely due to energetically close lying transitions of the remaining moieties. For instance, the energetic separation of two  $n\pi^*$ -singlet states of  $B_2G$  amounts to 0.16 eV, while the pairs  $S_1, S_2$  and  $S_3, S_4$  of  $B_4G$  are quasi-degenerated due to a separation of 0.01 and 0.05 eV, respectively. A similar behavior is observed for the separation of calculated triplet transitions.  $T_1, T_2$  of  $B_2G$  are separated by 0.16 eV and  $B_4G$  reveals quasi-degenerated pairs of  $T_1, T_2$  and  $T_3, T_4$ . Thus, the degree of quasi-degeneration scales with the number of  $n\pi^*$ -singlet and triplet states with respect to the corresponding benzoyl moieties. In conclusion, the channel branching within excited states is expected to become more complex with increasing system size of acylgermanes. Especially, multiple branched ISC pathways can result in different ISC quantum yields for mono-, bis- and tetraacylgermanes.

### **Luminescence Properties of Mono-, Bis- and Tetraacylgermanes**

As shown in literature,<sup>31</sup> monoacylgermanes reveal a very weak fluorescence quantum yield  $\Phi_F$  of less than  $5 \cdot 10^{-4}$ . For the investigation of  $\Phi_F$  for bis- and tetraacylgermanes, a selection is quantified with steady-state fluorescence spectroscopy by using C307 in EtOH as a standard at 400 nm excitation. The fluorescence spectra used for determination of  $\Phi_F$  are provided in **Figure A2**. The obtained  $\Phi_F$  are presented in **Table 4.1**.

**Table 4.1.** Fluorescence quantum yields of a selection of bis- and tetraacylgermanes determined at an excitation wavelength of 400 nm by Dennis Haffner (Wiss. Arb. KIT 2019). C307 in EtOH was used as a standard. For the corresponding UV/Vis and fluorescence spectra refer to **Figure A2**.

derivative dissolved in AcN	fluorescence quantum yield $\Phi_F$
B <sub>2</sub> G	$1 \cdot 10^{-5}$
MB <sub>2</sub> G	$8 \cdot 10^{-6}$
B <sub>4</sub> G	$8 \cdot 10^{-6}$
oMeB <sub>4</sub> G	$5 \cdot 10^{-6}$
oEtB <sub>4</sub> G	$4 \cdot 10^{-6}$
PrOB <sub>4</sub> G	$9 \cdot 10^{-5}$

All investigated systems dissolved in AcN show a weaker  $\Phi_F < 1 \cdot 10^{-4}$  than monoacylgermanes. In conclusion, relaxation via fluorescence after light excitation of mono-, bis- and tetraacylgermanes is a very minor pathway.

#### 4.1.2 Extinction Coefficients of *Para*-Fluoro and Methoxy-substituted Mono-, Bis- and Tetraacylgermanes

According to the systematic PLP-ESI-MS study in **section 4.3**, a quantitative comparison of the extinction coefficients of *para*-fluoro and methoxy-substituted mono-, bis- and tetraacylgermanes dissolved in MMA is presented in the current section. Corresponding absorption spectra are provided in **Figure 4.4**.

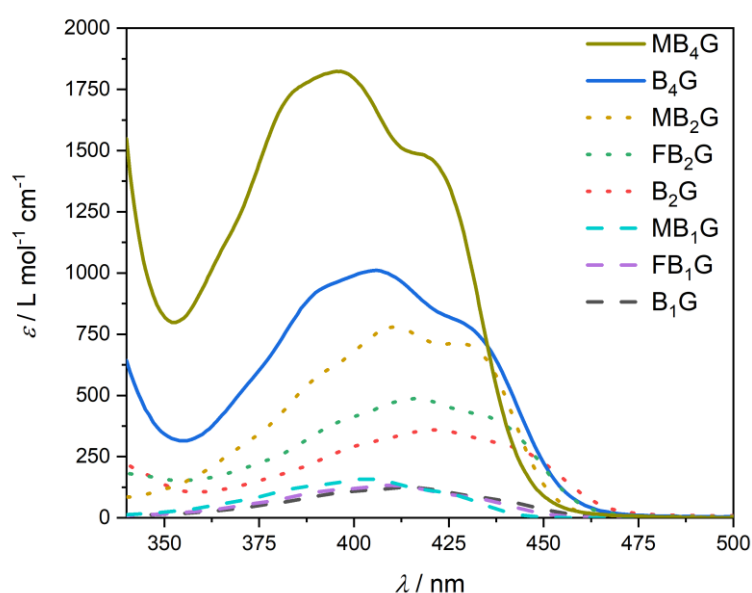


**Figure 4.4.** Steady-state UV/Vis-spectra of *para*-fluoro and methoxy-substituted mono- (dashed lines), bis- (dotted lines) and tetraacylgermanes (solid lines) dissolved in MMA and recorded in 1 cm cuvettes for determination of  $n\pi^*$ -extinction coefficients. Adapted with permission from ref. 146. Copyright 2019 American Chemical Society.

The recorded  $n\pi^*$ -bands of all initiators show significant extinction coefficients  $\epsilon$  within 360 nm and 450 nm. The overlap of absorption bands of different non-interacting acylgermane derivatives is a precondition for PLP-ESI-MS cocktail experiments, where two initiators are excited simultaneously within one sample at one wavelength. To safely exclude the influence of a wavelength-dependent cleavage mechanism, PLP-cocktail experiments are conducted at several wavelengths according to each absorption maximum of the corresponding initiator pair. However, a contribution of different  $n\pi^*$ -extinction coefficients on the overall initiation efficiency due to diverse substitution patterns cannot be neglected.

Monoacylgermanes  $B_1G$ ,  $FB_1G$ , and  $MB_1G$  reveal very weak maximal extinction coefficients  $\epsilon_{max}$  of 125, 130 and 160  $L mol^{-1} cm^{-1}$ , respectively. The influence of *para*-fluoro and methoxy substituents is more significant for bisacylgermanes, e.g.  $\epsilon_{max} \sim 360, 490, 780 L mol^{-1} cm^{-1}$  for  $B_2G$ ,  $FB_2G$  and  $MB_2G$ , respectively. Methoxy substituents show the strongest increase in the extinction coefficients of the investigated acylgermanes, e.g.  $\epsilon_{max}(MB_4G) \sim 1800 L mol^{-1} cm^{-1}$  compared to  $\epsilon_{max}(B_4G) \sim 1000 L mol^{-1} cm^{-1}$ . Remarkably, a nonstoichiometric scaling is observed for the comparison of extinction coefficients of initiators with a different number of identical substituted benzoyl moieties. A factor of  $\sim 8$  and  $\sim 11$  is obtained for  $\epsilon_{max}(B_4G)/\epsilon_{max}(B_1G)$  and  $\epsilon_{max}(MB_4G)/\epsilon_{max}(MB_1G)$ , respectively, which corresponds to a nonstoichiometric increase of 100-175 % compared to an expected factor of 4 (ratio between number of benzoyl moieties). Bis- towards mono- and tetra- towards bisacylgermanes show a nonstoichiometric increase of 30-45 % and 20-40 % compared to an expected factor of 2. The results from this chapter are used for comparison with overall initiation efficiencies obtained from PLP-ESI-MS cocktail experiments.

## 4.2 PLP-ESI-MS End Group Analysis: Initiating Radicals

PLP with 90000 pulses at  $\sim 320 \mu J/pulse$  and MMA as a monomer generates short polymers (oligomers) with 20-30 repeating units, which is ideal for the analysis with ESI-MS in mass range between  $m/z$  150-3000. Depending on its radical fragments, isotopic patterns of polymers with different end groups can be recorded for a certain initiator. Each isotopic pattern of a chemical structure is unique in its peak number and -height, due to the natural distribution of isotopes. Using an Orbitrap mass analyzer, a very high mass resolving power  $> 60000$  can be achieved, resulting in well-

resolved almost Gaussian-shaped peaks with a width at the half maximum of  $\Delta m/z \sim 0.02$ . The analysis of the isotopic pattern distribution – as a fingerprint of the molecule – via isotopic pattern simulations allows an assignment of possible species. A successful simulation of the isotopic patterns of a polymer distribution contains the information of the initiating radicals, which enables the postulation of a cleavage mechanism of the corresponding photoinitiator.

The abundance of each peak in an isotopic pattern is a measure for the quantity of the recorded species but can be affected by an ionization bias. If species are in the same mass range with overlapping isotopic pattern or have the same sum formula (isobaric overlap), the evaluation becomes challenging. For the simulation of complex mass spectra with a manifold of superimposed species, special prediction or fitting procedures are necessary.<sup>96, 148</sup>

In the present work, isotopic pattern simulations were conducted with the software package Xcalibur (Thermo Fisher) by assuming a resolution (mass resolving power) of 60000 and a Gaussian-shaped peak profile. Simple spectra, containing only a few species, are fitted by the comparison of an educated guess of species with the recorded spectrum, e.g. PMMA initiated by monoacylgermanes. Complex mass spectra with many species from polymerization of MMA initiated by bis- and tetraacylgermanes are analyzed by comparison with predicted mass spectra, which are obtained from a new developed permutation method within this thesis.

#### **4.2.1 Radical Fragments of Efficient Monoacylgermane-Derivatives**

Efficient monoacylgermanes (e.g. MB<sub>1</sub>G, FB<sub>1</sub>G and B<sub>1</sub>G) show an MMA-conversion of 4-5 % in a PLP-experiment at an excitation wavelength within the  $n\pi^*$ -band of the absorption spectra ( $\sim 320 \mu\text{J/pulse}$  and 90000 pulses, resulting in  $\sim 28 \text{ J}$  total energy per sample,  $5 \text{ mmol L}^{-1}$  initiator in a sample volume of 0.5 mL).

The cleavage mechanism of efficient monoacylgermanes is studied on the ESI-MS spectra of PMMA obtained from PLP-experiments with MB<sub>1</sub>G, FB<sub>1</sub>G and B<sub>1</sub>G. As exemplary for polymers obtained from photo FRP with efficient monoacylgermanes, the end group analysis for PMMA initiated by radical fragments originated from MB<sub>1</sub>G is presented in detail (**Figure 4.5**, for FBG and HBG refer to **Figure A3**, **Figure A4** and **Table A5** and **Table A6**).

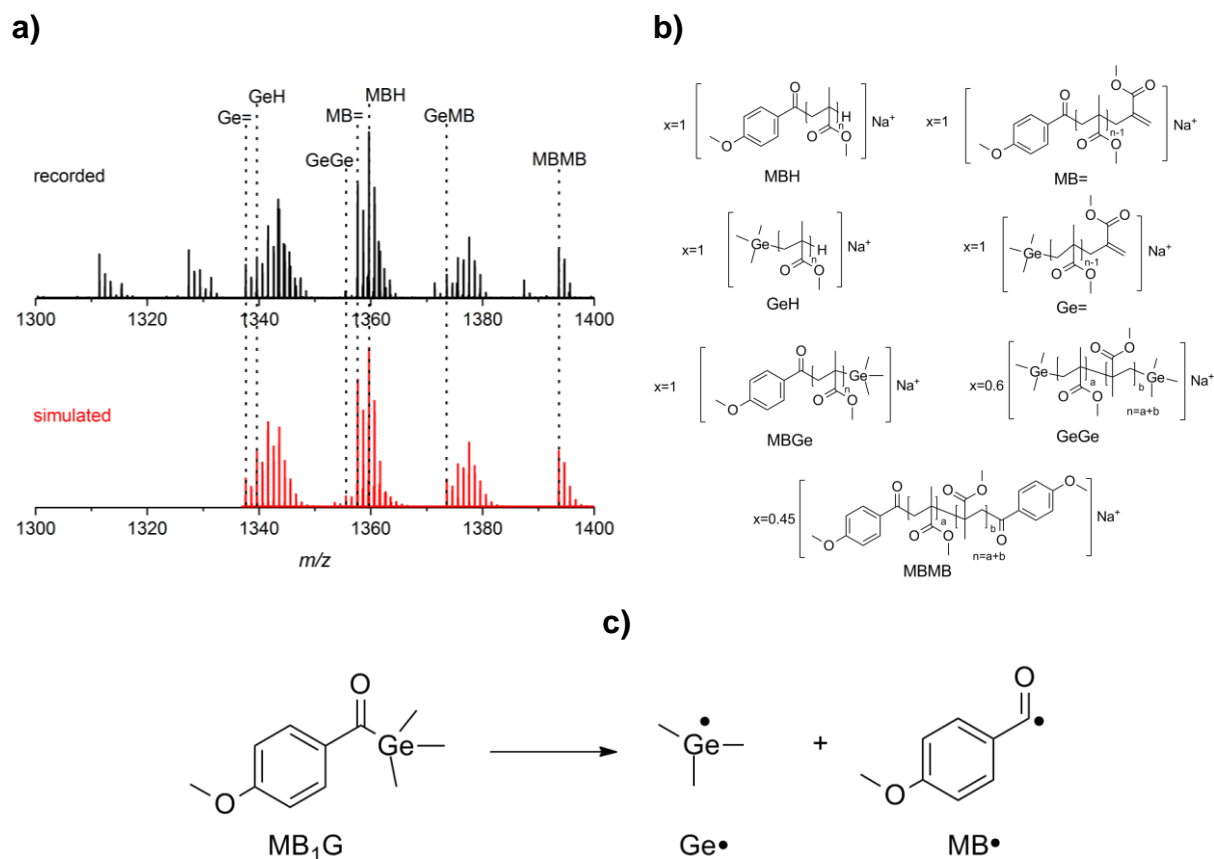


**Figure 4.5.** **a)** Recorded (black) direct infusion-ESI-MS and simulated (red) mass spectrum of PMMA-products obtained from PLP initiated by  $\text{MB}_1\text{G}$  at total irradiation energy of 27.9 J at 400 nm. **b)** Disproportionation and combination products used for simulation. **c)** Associated cleavage mechanism. Adapted with permission from ref. 144. Copyright 2017 American Chemical Society.

After PLP of MMA with  $\text{MB}_1\text{G}$  at 400 nm with 90000 pulses at 310  $\mu\text{J}/\text{pulse}$  resulting in a total energy of 27.9 J, the mass spectrum (black, **Figure 4.5a**) was recorded via direct-infusion ESI-MS. The simulated mass spectrum (red, **Figure 4.5a**) was carried out by assuming a mass resolving power of  $R = 60000$  with a Gaussian-shaped peak profile. The main species of the PLP-product distribution can be described by seven PMMA products with different end groups (**Figure 4.5b**). The quality of the simulation can be evidenced by comparing the exact mass and resolution of the recorded and the simulated isotopic patterns in **Table 4.2**.

**Table 4.2.** Exact mass and resolution of simulated and recorded spectra of the PLP-PMMA species initiated by radical fragments originated from MB<sub>1</sub>G. Adapted with permission from ref. 144. Copyright 2017 American Chemical Society. Modified presentation.

species	exact mass (recorded)	resolution (recorded)	exact mass (simulated)	resolution (simulated)
Ge=	1337.61	60118	1337.61	59947
GeH	1339.61	40577	1339.61	40114
GeGe	1357.56	59089	1357.55	57444
MB=	1357.66	56480	1357.66	59935
MBH	1359.67	56946	1359.67	55242
MBGe	1373.61	58603	1373.61	59943
MBMB	1393.66	56539	1393.66	59934

Dominantly, disproportionation products of PMMA initiated by benzoyl (MBH, MB=) and trimethylgermyl (GeH, Ge=) radical fragments are observed as expected from PLP with MMA.<sup>32</sup> In addition, the expected combination products with two methoxy-benzoyl (MBMB), two trimethylgermyl (GeGe), and one-to-one methoxy-benzoyl trimethylgermyl- (MBGe) end groups are observed. Remarkably, Ge-species exhibit broad isotopic pattern due to five natural isotopes of the germanium atom. In conclusion, the observed end groups are originating from initiation and termination processes of benzoyl- and trimethylgermyl- radical fragments as expected from an  $\alpha$ -cleavage of monoacylgermanes. The result is in line with the end group analysis of FB<sub>1</sub>G and B<sub>1</sub>G (refer to **Figure A3**, **Figure A4** and **Table A5** and **Table A6**). Further, an  $\alpha$ -cleavage for efficient monoacylgermanes with electron donating (+M-effect) methoxy and fluoro-substitution patterns is consistent with findings from literature.<sup>39</sup> However, +M-effect substituents lead to an unfavored hypsochromic shift in comparison to unsubstituted acylgermanes.<sup>31</sup>

#### 4.2.2 Radical Fragments of Weak Monoacylgermanes-Derivatives

In contrast to efficient monoacylgermanes, the initiators CB<sub>1</sub>G ( $\lambda_{\max} = 425$  nm) and NB<sub>1</sub>G ( $\lambda_{\max} = 429$  nm) reveal no MMA-conversion in a standard PLP-experiment within the red shifted  $n\pi^*$ -band of their absorption spectra ( $\sim 320$   $\mu\text{J/pulse}$  and 90000 pulses, resulting in  $\sim 28$  J total energy per sample, 5 mmol L<sup>-1</sup> initiator in a sample volume of 0.5 mL). The weak initiation performance of bathochromic shifted monoacylgermanes with electron withdrawing substitution pattern (-M-effect) NO<sub>2</sub>, and CN is consistent with expectations from theory.<sup>31</sup> However, a factor 4 higher total energy of 112 J irradiated at 425 and 429 nm, respectively, leads for CB<sub>1</sub>G to a MMA-conversion of 1 % and for NB<sub>1</sub>G to 0.1 % (**Figure 4.6**).

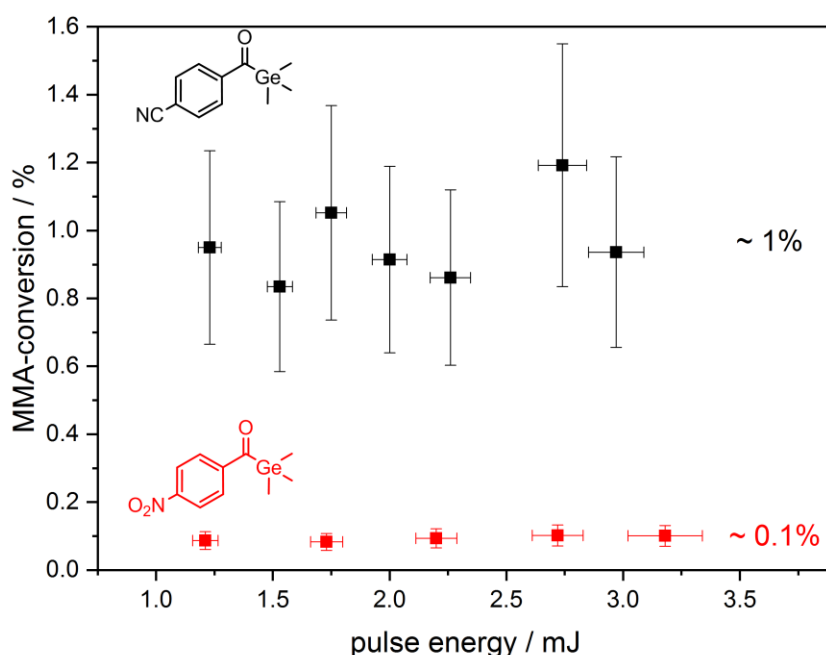


**Figure 4.6.** MMA-conversion obtained from PLP for CB<sub>1</sub>G (black) and NB<sub>1</sub>G (red) at high total irradiation energy of 112 J at different pulse energies. CB<sub>1</sub>G and NB<sub>1</sub>G are classified as weak photoinitiators due to low MMA conversion of 0.1-1 % at factor 4 higher total laser energies compared to PLP-experiments with efficient monoacylgermanes. Adapted with permission from ref. 144. Copyright 2017 American Chemical Society.

The corresponding PLP-experiment was reproduced at a constant total energy of 112 J at different pulse energies between 1-3.5 mJ/pulse and the conversion was obtained via gravimetry. A dependency on different pulse energies was not observed as indicated by constant MMA-conversion values in **Figure 4.6**. Compared to the MMA-conversion of an efficient monoacylgermane in a PLP-experiment (4-5 %) at ~28 J, an approximately 16-20 % lower initiation efficiency is observed for CB<sub>1</sub>G. In addition, the initiation efficiency estimated from PLP-conversion for NB<sub>1</sub>G is a factor 10 smaller than CB<sub>1</sub>G. Thus, CB<sub>1</sub>G and NB<sub>1</sub>G show at very high total laser energies a small MMA-conversion and can be classified by the term “weak initiators”.

In the following, the end group analysis for the ESI-MS spectra of PMMA-products initiated by the weak initiators CB<sub>1</sub>G and NB<sub>1</sub>G obtained from PLP-experiments is presented.

## Radical Fragments of CB<sub>1</sub>G

For recording the mass spectrum of CB<sub>1</sub>G, a PMMA sample from pulse energy-dependent PLP at a total irradiation energy of 112 J at 425 nm (2.7 mJ/pulse, 40900 pulses) was picked (black, **Figure 4.7a**). Multiple charged species are separated via SEC to simplify the evaluation of the complex mass spectrum due to intrinsically high isotopic pattern diversity as depicted in **Figure 4.7c**)

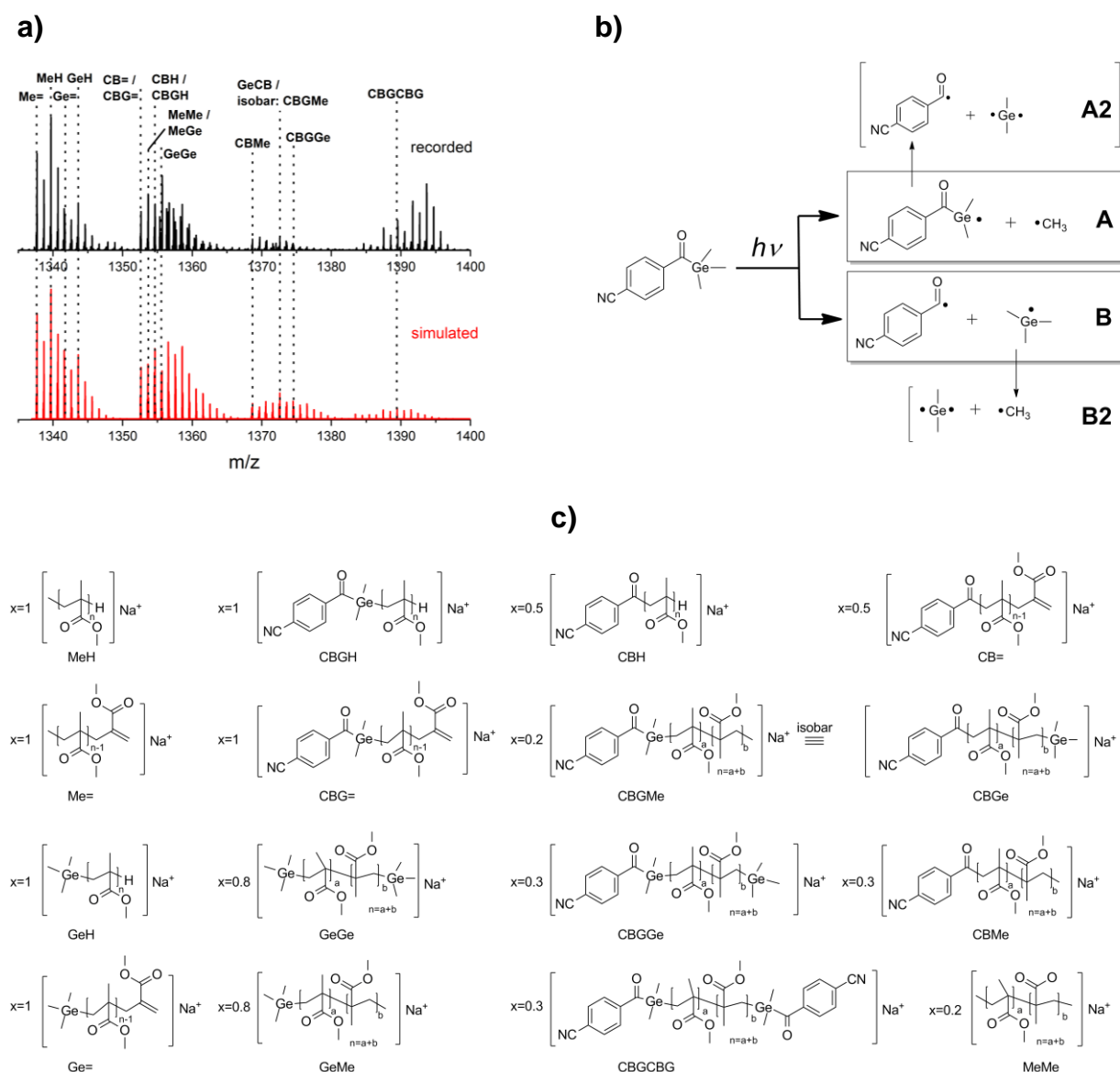


**Figure 4.7. a)** Recorded (black) SEC-ESI-MS and simulated (red) mass spectrum of PMMA-products obtained from PLP initiated by CB<sub>1</sub>G at total irradiation energy of 112 J at 425 nm. **b)** Associated cleavage mechanism. Germyl diradicals in A2, B2 are formally postulated. Presumably, a consecutive cleavage after the initiation of MMA with *para*-cyano-benzoylgermyl or trimethylgermyl radicals is more likely. **c)** Disproportionation and combination products used for simulation. *para*-cyano-benzoylgermyl species are isobaric with combination products of germane-centered 2-armed polymers (refer to **Figure 4.8**). Adapted with permission from ref. 144. Copyright 2017 American Chemical Society.

The isotopic pattern simulation of the PMMA initiated by CB<sub>1</sub>G was performed with a Gaussian-shaped peak profile and a mass resolving power  $R$  of 60000. The quality of the simulation can be seen in **Table 4.3**.

**Table 4.3.** Exact mass and resolution of simulated and recorded spectra of the PLP-PMMA species initiated by radical fragments originated from CB<sub>1</sub>G. Adapted with permission from ref. 144. Copyright 2017 American Chemical Society. Modified presentation.

species	exact mass (recorded)	resolution (recorded)	exact mass (simulated)	resolution (simulated)
Me=	1337.69	59424	1337.69	59922
MeH	1339.70	59074	1339.70	55257
Ge=	1341.61	45925	1341.61	40917
GeH	1343.62	52762	1343.62	48972
CBG=	1352.56	57920	1352.56	59591
CB=	1352.64	58934	1352.64	59942
MeGe	1353.64	57730	1353.64	56801
MeMe	1353.72	57479	1353.72	59945
CBGH	1354.57	43921	1354.56	41176
CBH	1354.66	53479	1354.65	49947
GeGe	1355.56	42933	1355.56	42225
CBMe	1368.67	58836	1368.67	59929
GeCB/ CBGMe	1372.59	57858	1372.59	56834
CBGGe	1374.51	54094	1374.51	56207
CBGCBG	1389.46	46110	1389.46	56190

Sixteen species (**Figure 4.7c**) were assumed for an appropriate simulation (**red, Figure 4.7a**) of the recorded mass spectrum (**black, Figure 4.7a**) of the PLP-experiment at 112 J with CB<sub>1</sub>G. In line with the results from efficient monoacylgermanes, *para*-cyano-benzoyl and trimethylgermyl-initiated PMMA species are observed, which are likely formed by  $\alpha$ -cleavage of CB<sub>1</sub>G (**B; Figure 4.7b**). In contrast, additional isotopic patterns of PMMA disproportionation products initiated by methyl radicals are detected. Thus, an additional cleavage pathway for the generation of methyl radicals must be assumed as depicted in **Figure 4.7b**). In a first approach, the formation of the observed species can be adequately described by initiation and termination processes resulting from initiator cleavage as depicted in reaction equation A and B in **Figure 4.7b**). However, the simulation is ambiguous due to isobaric structures. Especially *para*-cyano-benzoylgermyl initiated or terminated PMMA species are identical with germanium-centered 2-armed polymers terminated by *para*-cyano-

benzoyl radicals, e.g. isobaric structures of CBGH and CBGeH illustrated in **Figure 4.8**.

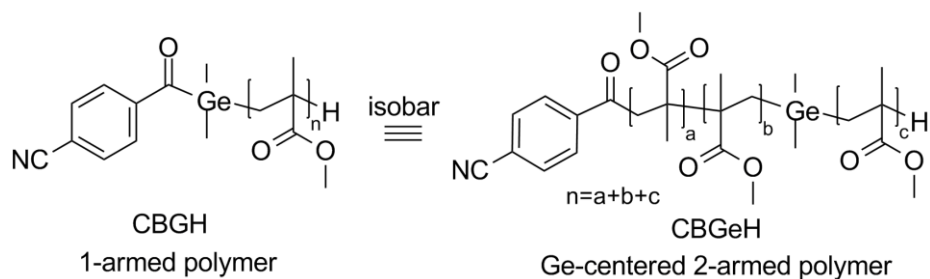


**Figure 4.8.** Isobaric structures of disproportionation product of a *para*-cyano-benzoyl-initiated polymer (CBGH) and a germanium-centered 2-armed polymer with *para*-cyano-benzoyl-combination and H-disproportionation end groups (CBGeH). Adapted with permission from ref. 144. Copyright 2017 American Chemical Society.

A scenario with germanium-centered 2-armed polymers would include a consecutive cleavage of the *para*-cyano-benzoylgermyl and/or the trimethylgermyl radical into a formal dimethylgermyl diradical as shown in reaction pathway A2 and B2 in **Figure 4.7b**). A consecutive cleavage can be induced thermally or via photons. A thermal activation for A2 and B2 is possible if, after the first cleavage, a sufficient amount of excess energy remains in a vibrational hot excited state, which may lead to a consecutive fragmentation of the radical. A photo-induced pathway is rather unlikely for B2 due to missing chromophores in trimethylgermyl-moieties. In contrast, the cyano-benzoyldimethylgermyl unit is chemically similar to the unfragmented CB<sub>1</sub>G, which has a  $n\pi^*$ -band in the visible region of the absorption spectrum.<sup>31</sup> Thus, A2 proceeds more likely via a second photo-induced activation. If the first cleavage of the initiator is considered to occur on a time scale < 1 ns, one laser pulse (pulse duration ~7 ns) may be sufficient to induce a second cleavage of the *para*-benzoyldimethylgermyl radical before the diffusion-controlled attack towards the monomer takes place. If the formation of a dimethylgermyl diradical is rather unlikely, a secondary cleavage may be favored after the initiation of a chain-growth by the *para*-cyano-benzoyldimethylgermyl radical. To summarize, a complex mechanism of CB<sub>1</sub>G is found including the formation of methyl radicals. However, a clear characterization of the fragmentation mechanism is not available from PLP-ESI-MS due to ambiguous isotopic patterns. In fact, the discussion about the appearance of possible consecutive cleavages is of high importance for the latter characterization of bis- and tetraacylgermanes (**section 4.2.3**).

## Radical Fragments of NB<sub>1</sub>G

The MMA-conversion at the same PLP-conditions ( $E_{total}=112$  J) with NB<sub>1</sub>G at 429 nm of 0.1 % was too low to record a mass spectrum. Thus, the total irradiation energy was increased to 384 J (3.2 mJ/pulse, 120000 pulses), which results in a MMA-conversion of ~0.6 % leading to the SEC-ESI-MS spectrum in black **Figure 4.9a**).

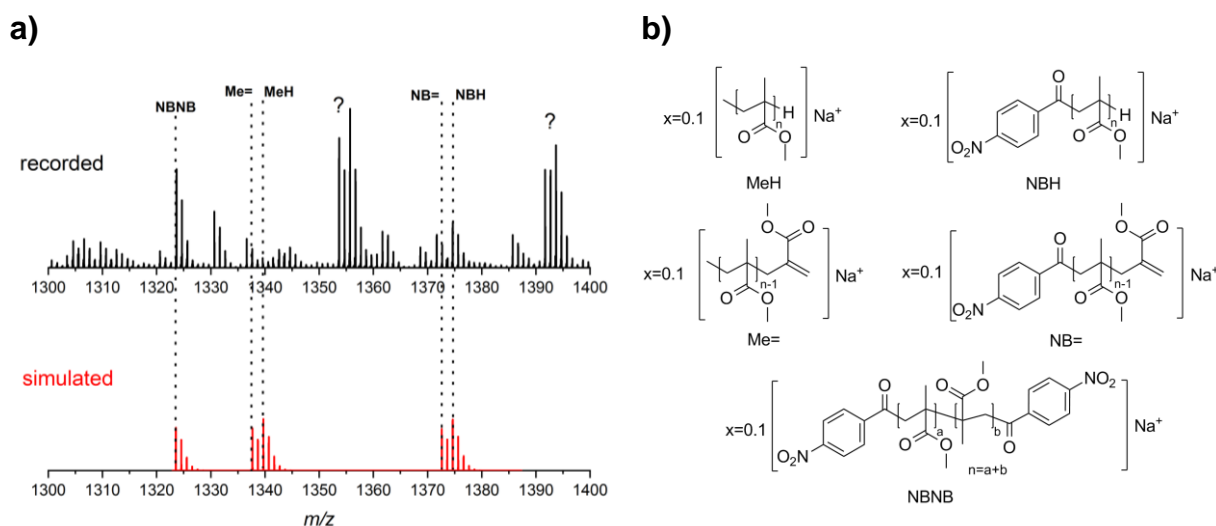


**Figure 4.9. a)** Recorded (black) SEC-ESI-MS and simulated (red) mass spectra of PMMA-products obtained from PLP initiated by NB<sub>1</sub>G at total irradiation energy of 384 J at 429 nm. **b)** Disproportionation and combination products used for simulation. Adapted with permission from ref. 144. Copyright 2017 American Chemical Society.

The recorded spectrum reveals a complex isotopic pattern distribution. A matching result between the recorded (black) and simulated mass spectrum (red,  $R=60000$ ) is found for five PMMA-species initiated by methyl and *para*-nitro-benzoyl radicals (**Figure 4.9a**) and **Table 4.4**).

**Table 4.4.** Exact mass and resolution of simulated and recorded spectra of the PLP-PMMA species initiated by radical fragments originated from NB<sub>1</sub>G. Adapted with permission from ref. 144. Copyright 2017 American Chemical Society. Modified presentation.

species	exact mass (recorded)	resolution (recorded)	exact mass (simulated)	resolution (simulated)
NBNB	1323.55	57626	1323.55	57948
Me=	1337.69	57762	1337.69	57941
MeH	1339.70	61694	1339.70	53673
NB=	1372.63	46631	1372.63	57945
NBH	1374.64	57406	1374.64	55423

Herein, most isotopic patterns including dominating disproportionation products from MMA remain unassigned. In addition, products from germyl-based counter radicals are missing for the postulation of a common  $\alpha$ -cleavage. Thus, the PLP-process at a total energy of 384 J of NB<sub>1</sub>G leads to unexpected fragmentation patterns in contrast to CB<sub>1</sub>G at 112 J. Nevertheless, weak initiators like NB<sub>1</sub>G or CB<sub>1</sub>G have a small probability to initiate polymerizations at high energy conditions ( $E_{total} = 112\text{-}384$  J) in a PLP-experiment. However, the end group distribution of obtained PMMA-products is less controlled than for efficient initiators at lower total irradiation energy of  $\sim 28$  J.

#### 4.2.3 Bis- and Tetraacylgermanes: Prediction of Germane-Centered n-Fold Star Polymers

As presented in the previous section, efficient monoacylgermanes undergo an  $\alpha$ -cleavage into benzoyl and germyl radical fragments. In comparison, bis- and tetraacylgermanes carry two, resp. four, benzoyl moieties, which are potentially available for a subsequent fragmentation of the initiator. For example, structurally similar bisacylphosphinoxides are known for the formation of secondary benzoyl radicals.<sup>149,60, 150-151</sup> In fact, only the primary cleavage of bis- and tetraacylgermanes into benzoyl- and benzoylgermyl- fragments via EPR and CIDNP studies has been reported, yet.<sup>38, 43, 147</sup> For the ESI-MS end group analysis of PMMA initiated by bis- and tetraacylgermanes, a powerful and simple method based on permutation mathematics is presented to predict the mass spectra of multifunctional initiator systems. *The a priori prediction of mass spectrometric product patterns of photoinitiated polymerizations* was published in ACS Macro Letters in 2018.<sup>145</sup> The core of the prediction is the assumption of statistically terminated star polymers formed by a multi cleavage initiation mechanism of the photoinitiator. In contrast to common end group analysis, the prediction method allows an unambiguous interpretation of isobaric structures, which is necessary for the evaluation of initiators with potentially multiple cleavage points. Independent of acylgermanes, the presented method should be generally applicable to mass spectra of linearly grown star polymers initiated by initiators with multiple cleavage points and recorded by soft ionizing spectrometric methods (e.g. MALDI-ToF). In the following, the prediction is introduced for the example of the ESI-MS spectrum of PMMA initiated by tetrabenzoylgermane B<sub>4</sub>G. Predictions for further tetraacylgermanes oMeB<sub>4</sub>G, oEtB<sub>4</sub>G, PrOB<sub>4</sub>G as well as for one bisacylgermane B<sub>2</sub>G are provided in appendix **Figure A5-Figure A12**. To anticipate the main result, bis- and tetraacylgermanes reveal clearly a quantitative multiple cleavage mechanism.

Mass spectra of PMMA initiated by bis- and tetraacylgermanes show complex product distributions resulting in broad superimposed isotopic patterns, e.g. PMMA initiated by B<sub>4</sub>G in **Figure 4.10**.

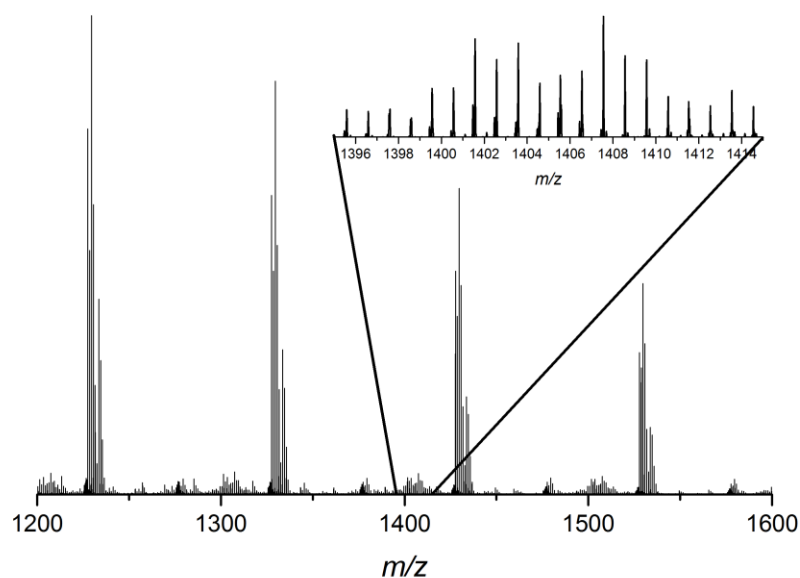


**Figure 4.10.** SEC-ESI-MS spectrum of five repeating units of PMMA initiated by B<sub>4</sub>G. Dominating peaks caused by PMMA-disproportionation and combination products initiated by benzoyl radicals. Inset: Complex PMMA isotopic patterns caused by multiple fragmentations. Adapted with permission from ref. 145. Copyright 2018 American Chemical Society.

As expected from PLP with MMA, the recorded mass spectrum reveals an isotopic pattern distribution with repeating units of  $m/z \sim 100$ . Dominantly, disproportionation products initiated by benzoyl radicals are observed, e.g.  $m/z \sim 1227$ ,  $1327$ ,  $1427$ , et cetera. Further, a much weaker and complex isotopic pattern is recorded, e.g. at  $m/z \sim 1405$  as depicted in the inset of **Figure 4.10**. Germanium-based disproportionation and combination products show broad isotopic pattern due to five natural isotopes of the Ge-atom. Thus, the complex isotopic pattern is expected to be a superposition of diverse germanium-containing PMMAs, which includes valuable information about the initiation mechanism of the photoinitiator. The quantitative evaluation of complex mass spectra is in general difficult due to the manifold of solutions for the superposition of individual peaks. In a most recently published study by De Bruycker *et al.*,<sup>148</sup> a python-based script was developed, which is able to fit complex mass spectra based on smart criteria for exclusion to reduce the number of possible

species. However, isobaric structures with equal sum formula lead to identical isotopic pattern, which limits the interpretation of ambiguous species (refer to discussion in **section 4.2.2**). In fact, the validation of the formation of star polymers via fitting-simulations of ESI-MS spectra is highly problematic. For example, a single polymer chain with  $a$  repeating units initiated by a tribenzoylgermyl radical results in the same sum formula as a germanium-centered 4-armed star polymer with  $a = b + c + d + e$  repeating units (**Figure 4.11**).

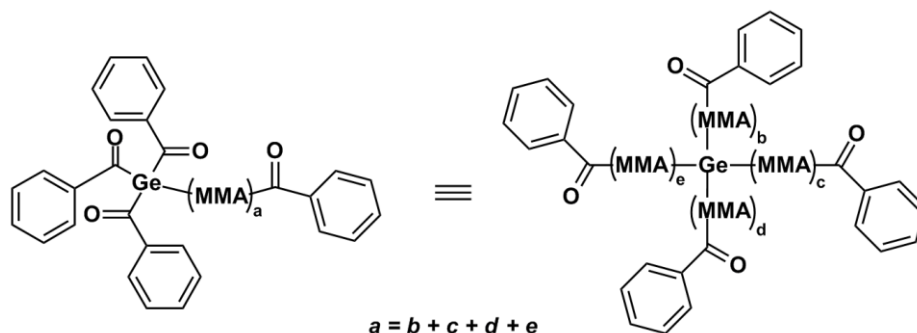


**Figure 4.11.** Isobaric structures of benzoyl combination product of germanium-centered 4-armed star polymer. For clarity reasons, the structure of MMA polymer chain with  $a$  repeating units is depicted as  $(\text{MMA})_a$ . Adapted with permission from ref. 145. Copyright 2018 American Chemical Society.

An *a priori* prediction method based on mechanistic implications is independent from limitations due to isobaric structures in fitted MS-simulations. Herein, the complete fragmentation of an initiator with  $n$  benzoyl moieties is assumed resulting in a germanium-centered  $n$ -armed star macroradical with  $n$  equivalent  $\omega$ -positions. Consequently, termination processes with  $s$  different end groups occur statistically. The statistical expectation of the termination of  $n$ -armed star macroradicals with  $s$  end groups of equal probability is given by the multinomial coefficient (**Eq 4.1**).<sup>152</sup>

$$\binom{n}{k_1 \dots k_s} = \frac{n!}{k_1! \cdot k_2! \cdot \dots \cdot k_s!} \quad \text{Eq 4.1}$$

In general, the multinomial coefficient determines the permutation possibilities of an order of  $n$  objects distinguished in  $1, 2, \dots, s$  groups from which  $k_1, \dots, k_n$  objects are identical. Regarding to  $n$ -armed star macro radicals,  $n$  is the number of possible end group positions terminated by  $s \leq n$  different end group patterns from which  $k_1, \dots, k_n$  are identical ( $k_1 \times$  end group pattern 1,  $k_2 \times$  end group pattern 2,  $\dots, k_n \times$  end group pattern  $s$ ). For example, tetraacylgermanes in MMA lead to germanium-centered 4-armed star macro radicals with  $n = 4$  termination points, which can be occupied by

different combinations selected from  $s = 3$  distinguishable end group pattern realized in one benzoyl combination (B) and two disproportionation (=,H) species. The assumption leads to four different multinomial coefficients resulting in statistical classes of species (A-D):

- A. Four identical end groups,  $\binom{4}{4\ 0\ 0} = 1$
- B. Three identical and one different end group,  $\binom{4}{3\ 1\ 0} = 4$
- C. Two times two identical end groups,  $\binom{4}{2\ 2\ 0} = 6$
- D. Two identical and two different end groups,  $\binom{4}{2\ 1\ 1} = 12$

The formulation of multinomial coefficients for the example of a tetraacylgermane is summarized in **Figure 4.12**.

#### Multinomial coefficient

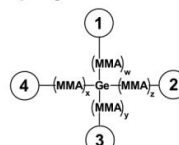
$$\binom{n}{k_1 \dots k_s} = \frac{n!}{k_1! \cdot k_2! \cdot \dots \cdot k_s!}$$

$n$ : number of possible end group positions  
 $k_1 \dots k_s$ : number of end groups 1,2,3 ...  $s$ , used for occupation

#### Example for germane-centered 4-armed PMMA star polymer:

$$\binom{4}{k_1 \ k_2 \ k_3}$$

$n=4$  possible end group positions  
 $k_1, k_2, k_3$ : choice of one combination (B) and two disproportionation (=,H) endgroups



#### Four multinomial coefficients describing all possible combinations of end groups:

<b>A.</b> $\binom{4}{4\ 0\ 0} = 1$ four identical	<b>B.</b> $\binom{4}{3\ 1\ 0} = 4$ three identical, one different	<b>C.</b> $\binom{4}{2\ 2\ 0} = 6$ two times two identical	<b>D.</b> $\binom{4}{2\ 1\ 1} = 12$ two identical, two different
---	--	--	---

#### Each coefficient can be realized by different species, illustrated on the example of D:

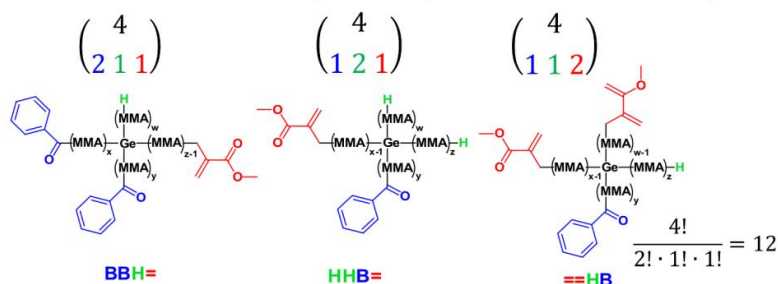


**Figure 4.12.** Instructions for the formulation of multinomial coefficients used for the prediction of isotopic pattern distributions of  $n$ -armed star polymers at the example of tetraacylgermanes. Adapted with permission from ref.145. Copyright 2018 American Chemical Society.

Each statistical class, resp. multinomial coefficient, is realized by several structures resulting in fifteen species of germanium-centered 4-armed star polymers with corresponding combinations of B, H and = end groups, as depicted in **Figure 4.13**.

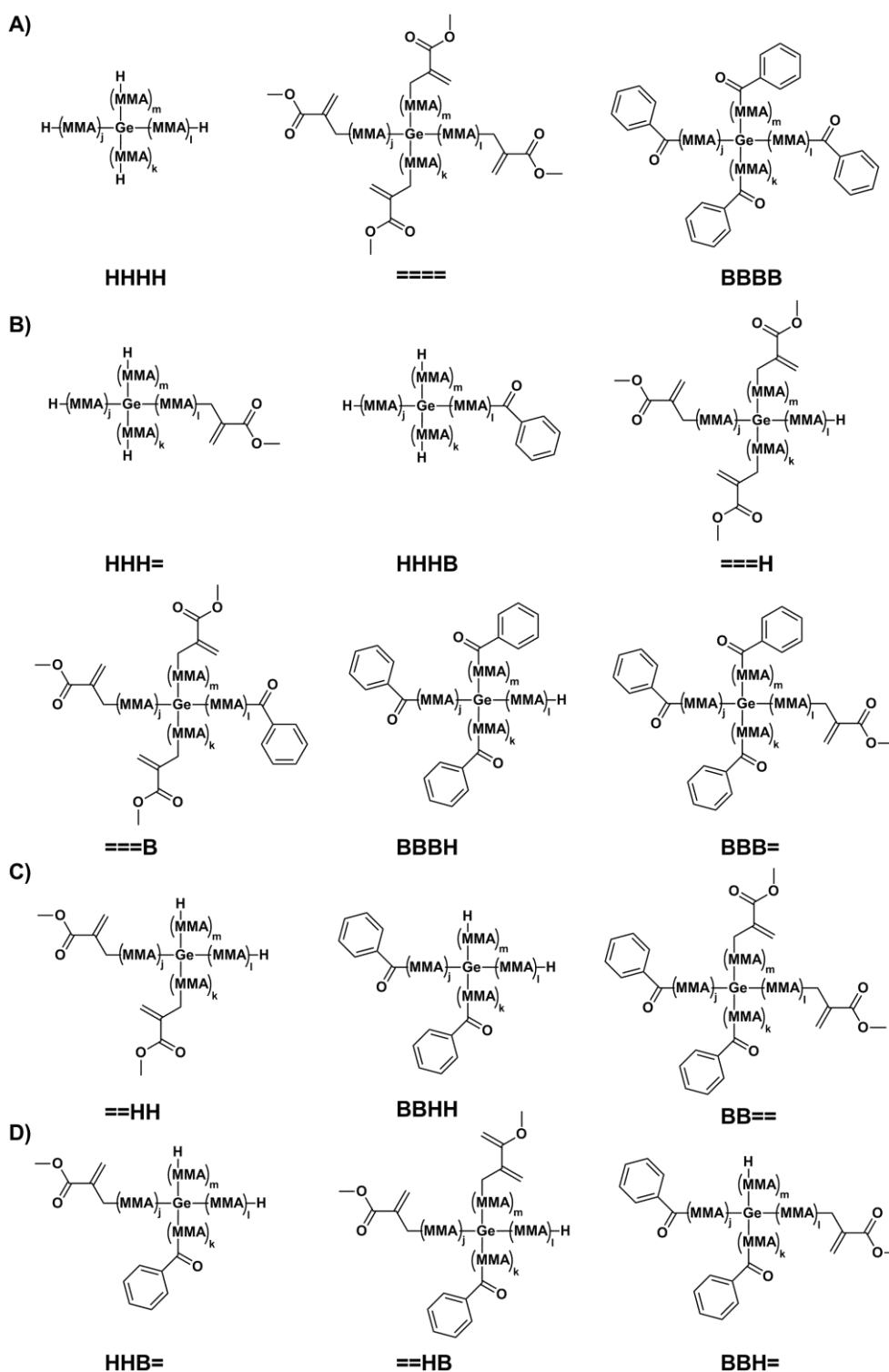


**Figure 4.13.** Fifteen germanium-centered 4-armed MMA-star polymers divided into four statistical classes A-D with distinctive multinomial coefficients. For clarity reasons, the structure of MMA polymer chain with  $j, k, l, m$  repeating units is depicted as  $(\text{MMA})_{j,k,l,m}$ . For isotopic pattern simulation and exact mass calculation, a  $\text{Na}^+$  is added to each structure. Adapted with permission from ref. 145. Copyright 2018 American Chemical Society.

The multinomial coefficients for each statistical class are normalized to class D, which lead to a ratio of 0.083 (A):0.33 (B):0.5 (C):1 (D). With respect to its class, the obtained ratio can be applied as a relative amount for an isotopic pattern simulation of each of the fifteen species (**Table 4.5**).

**Table 4.5.** Exact masses and relative amount according to the statistical classes of germanium-centered star polymers used for isotopic pattern simulation in the range of  $m/z \sim 1400$ .  $\text{Na}^+$  is added to each structure for exact mass calculation. Adapted with permission from ref. 145. Copyright 2018 American Chemical Society. Modified presentation.

statistical class	exact mass (simulated)	germyl species	sum formula	relative amount
A	1401.6233	HHHH	$\text{C}_{65}\text{H}_{108}\text{GeNaO}_{26}$	0.083
A	1393.5607	====	$\text{C}_{65}\text{H}_{100}\text{GeNaO}_{26}$	0.083
A	1417.5184	BBBB	$\text{C}_{73}\text{H}_{92}\text{GeNaO}_{22}$	0.083
B	1399.6076	HHH=	$\text{C}_{65}\text{H}_{106}\text{GeNaO}_{26}$	0.33
B	1405.5971	HHHB	$\text{C}_{67}\text{H}_{104}\text{GeNaO}_{25}$	0.33
B	1395.5763	===H	$\text{C}_{65}\text{H}_{102}\text{GeNaO}_{26}$	0.33
B	1399.5501	===B	$\text{C}_{67}\text{H}_{98}\text{GeNaO}_{25}$	0.33
B	1413.5446	BBBH	$\text{C}_{71}\text{H}_{96}\text{GeNaO}_{23}$	0.33
B	1411.5290	BBB=	$\text{C}_{71}\text{H}_{94}\text{GeNaO}_{23}$	0.33
C	1397.5920	==HH	$\text{C}_{65}\text{H}_{104}\text{GeNaO}_{26}$	0.5
C	1409.5709	BBHH	$\text{C}_{69}\text{H}_{100}\text{GeNaO}_{24}$	0.5
C	1405.5396	BB==	$\text{C}_{69}\text{H}_{96}\text{GeNaO}_{24}$	0.5
D	1403.5814	HHB=	$\text{C}_{67}\text{H}_{102}\text{GeNaO}_{25}$	1
D	1401.5658	==HB	$\text{C}_{67}\text{H}_{100}\text{GeNaO}_{25}$	1
D	1407.5552	BBH=	$\text{C}_{69}\text{H}_{98}\text{GeNaO}_{24}$	1

Disproportionation and combination PMMA-species initiated and terminated by benzoyl radicals, respectively, are introduced into the isotopic pattern simulation with a fitted factor of 6.7 (H,=) and 3.35 (B) higher than for statistical class D of the predicted germanium-centered species (**Figure 4.14** and **Table 4.6**).

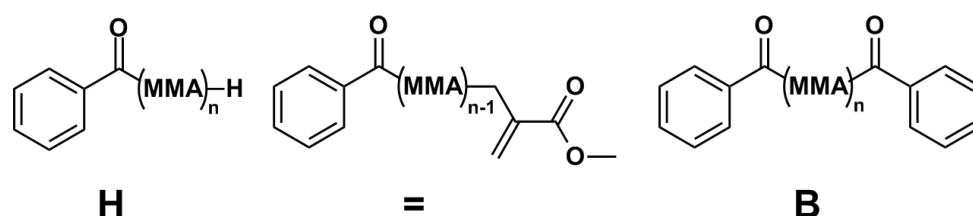


**Figure 4.14.** Disproportionation (H,=) and combination (B) products of benzoyl initiated MMA. For isotopic pattern simulation and exact mass calculation, a  $\text{Na}^+$  is added to each structure. For clarity reasons, the structure of MMA polymer chain with  $n$  repeating units is depicted as  $(\text{MMA})_n$ . Adapted with permission from ref. 145. Copyright 2018 American Chemical Society.

**Table 4.6.** Exact masses and relative amount of PMMA disproportionation (H,=) and combination (B) products initiated by benzoyl radicals used for isotopic pattern simulation in the range of  $m/z$  ~1400.  $\text{Na}^+$  is added to each structure for exact mass calculation. Adapted with permission from ref. 145. Copyright 2018 American Chemical Society. Modified presentation.

exact mass (simulated)	benzoyl species	sum formula	relative amount
1429.7127	H	$\text{C}_{72}\text{H}_{110}\text{NaO}_{27}$	6.7
1427.6970	=	$\text{C}_{72}\text{H}_{108}\text{NaO}_{27}$	6.7
1433.6865	B	$\text{C}_{74}\text{H}_{106}\text{NaO}_{26}$	3.35

The simulation of the predicted product distribution (**Table 4.5** and **Table 4.6**) was carried out with the program package Xcalibur (Thermo Fisher) at a mass resolving power of  $R = 60000$  by assuming a Gaussian-shaped peak profile. The resulting isotopic pattern simulation in comparison to the recorded mass spectrum is presented in **Figure 4.15**.

Analogous results for PLP-ESI-MS simulations of the PMMA species initiated by tetraacylgermanes  $\text{oMeB}_4\text{G}$ ,  $\text{oEtB}_4\text{G}$ , and  $\text{PrOB}_4\text{G}$  are presented in appendix **Figure A5-Figure A10** and **Table A7-Table A18**. For the prediction PMMA species initiated by bisacylgermane  $\text{B}_2\text{G}$ , six germane-centered 2-armed star polymers in two statistical groups A:B (0.5:1, refer to **Figure A11**, **Table A19**) and relatively fitted benzoyl species H:=:B (6:6:3, refer to **Table A20**) are assumed. The simulated spectrum is presented in **Figure A12**, which accuracy can be proven by inspecting **Table A21** and **Table A22**.

The predicted isotopic patterns show excellent matching results with the recorded mass spectrum of PMMA initiated by  $\text{B}_4\text{G}$  (inspect **Figure 4.15a** and **b**). Crucially, the striking accordance of the predicted with the recorded result provides evidence for the formation of 4-armed star polymers. In addition, 2-armed star polymers are observed for PMMA spectra obtained from PLP initiated by  $\text{B}_2\text{G}$  (**Figure A12**) as exemplary for efficient bisacylgermanes. Thus, bis- and tetraacylgermane photoinitiators unambiguously reveal a multiple cleavage mechanism.

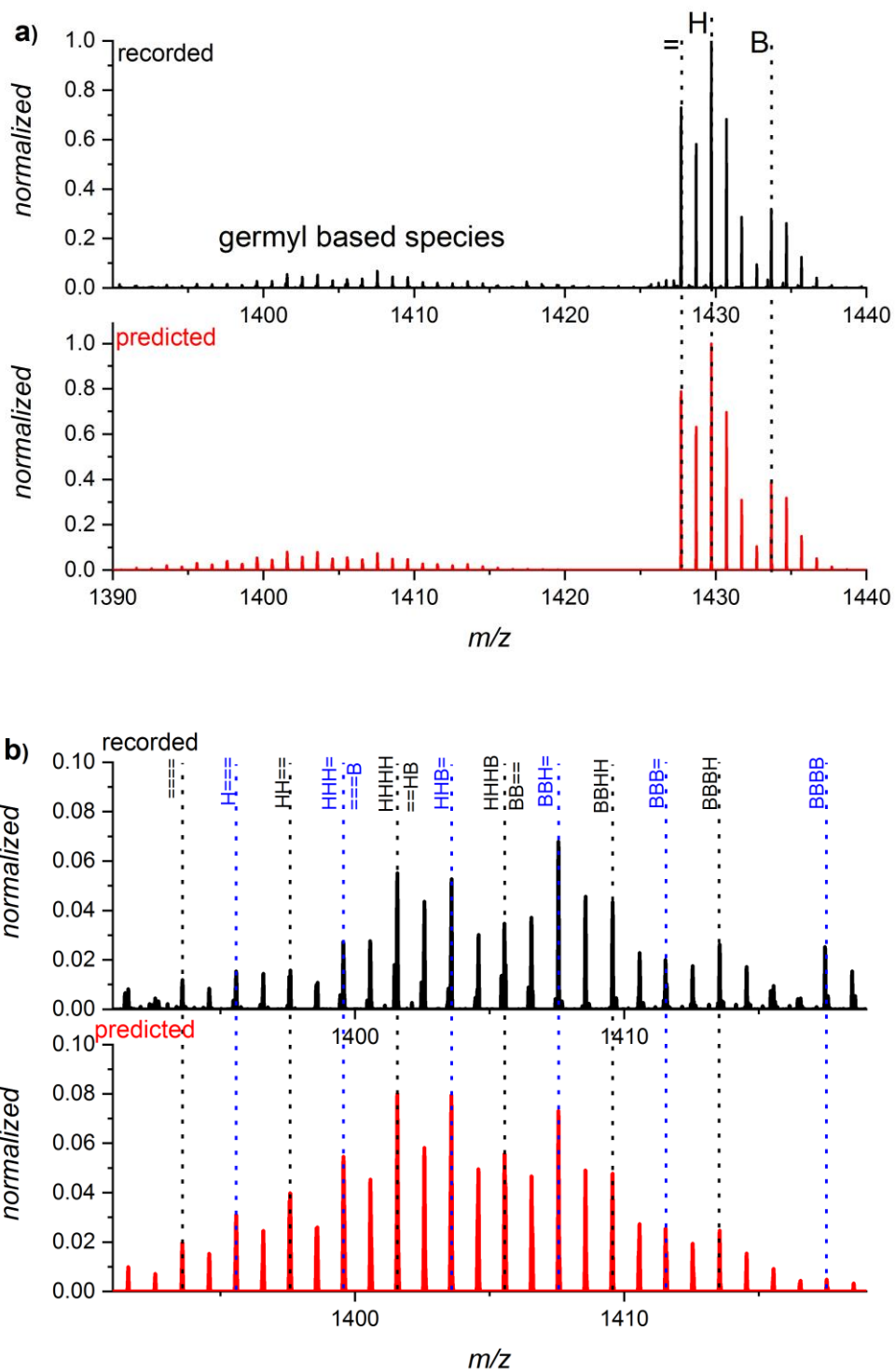


**Figure 4.15.** Recorded (black) and predicted (red) isotopic patterns of PMMA initiated by B<sub>4</sub>G. **a)** Overview of benzoyl and germyl-based species. **b)** Zoom into complex isotopic pattern distribution of germanium-centered 4-armed star polymers. Adapted with permission from ref. 145. Copyright 2018 American Chemical Society.

For testing the prediction, a peak to peak comparison of each peak maximum of predicted and recorded isotopic patterns is conducted by calculating the difference  $\Delta m/z$  and the mass accuracy  $dm/m_{sim}$  in ppm (**Table 4.7**, as well as **Table A9-Table A22**).

**Table 4.7.** Relative mass differences and mass accuracy for peak to peak comparison of predicted and recorded mass spectra of germanium-centered 4-armed star polymers. Adapted with permission from ref. 145. Copyright 2018 American Chemical Society. Modified presentation.

exact mass $(m/z)_{exp}$ (recorded)	exact mass $(m/z)_{sim}$ (simulated)	$\Delta m/z =$ $ (m/z)_{exp} - (m/z)_{sim} $	$dm/m_{sim} =$ $(\Delta m/z)/(m/z)_{sim}$ $10^6 / \text{ppm}$
1395.5860	1395.5884	0.0024	1.70
1396.5940	1396.5930	0.0011	0.75
1397.6031	1397.5931	0.0101	7.21
1398.6072	1398.5980	0.0092	6.58
1399.5626	1399.5709	0.0083	5.94
1400.5625	1400.5708	0.0083	5.93
1401.5697	1401.5714	0.0017	1.21
1402.5780	1402.5774	0.0006	0.43
1403.5873	1403.5806	0.0068	4.82
1404.5916	1404.5851	0.0065	4.61
1405.5469	1405.5546	0.0077	5.47
1406.5532	1406.5570	0.0038	2.68
1407.5543	1407.5577	0.0034	2.42
1408.5628	1408.5616	0.0013	0.89
1409.5724	1409.5661	0.0063	4.46
1410.5768	1410.5702	0.0066	4.66
1411.5319	1411.5368	0.0049	3.44
1412.5384	1412.5376	0.0008	0.59
1413.5459	1413.5443	0.0016	1.12
1414.5482	1414.5477	0.0005	0.36

Except for one ( $m/z = 1397.6031$ , 7.21 ppm), all mass differences between the maxima of predicted and recorded isotopic patterns do not exceed 0.01 and can be averaged to 0.0046 (3.26 ppm). In relation, the simulation of three benzoyl initiated species reflects an averaged mass difference of 0.0017 and mass accuracy of 1.22 ppm, respectively. Thus, a mass accuracy of 3.26 ppm is rather small compared to the number of fifteen superimposed species. For further illustration, the recorded (black) and predicted (red) isotopic patterns at  $\sim 1405.54$   $m/z$  are presented at the experimentally accessible mass resolving power of  $R = 60000$  and at a hypothetical factor 10 higher  $R = 600000$  by assuming a Gaussian peak profile.

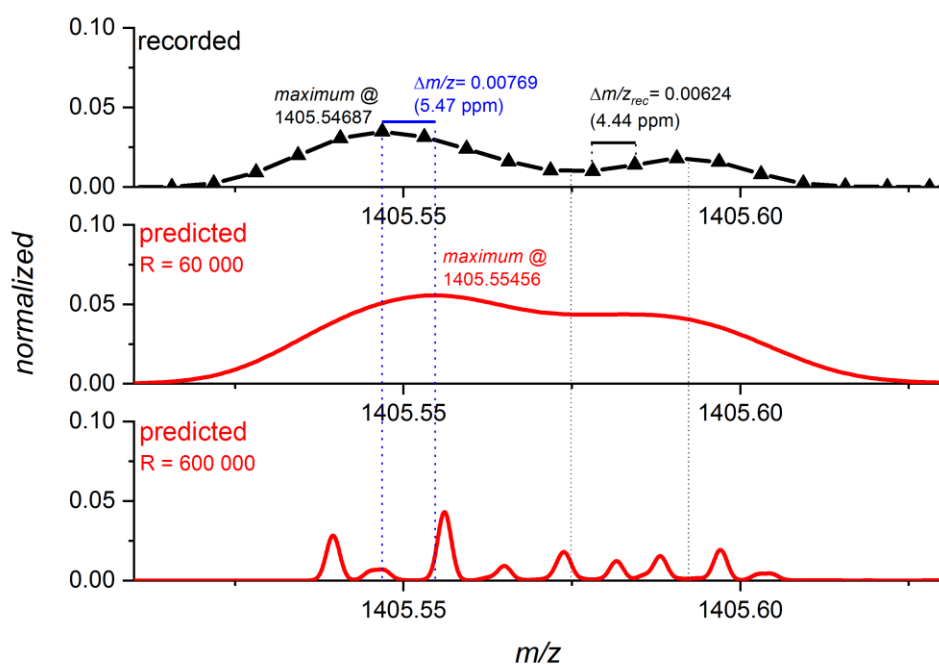


**Figure 4.16.** Zoom into recorded (black) and predicted mass spectra (red) at  $\sim 1405.54$   $m/z$ . Predicted isotopic patterns are simulated at two different resolutions as indicated. Adapted with permission from ref. 145. Copyright 2018 American Chemical Society.

At a high zoom level, the broadened peak at  $m/z \sim 1404.54$  reveals a main and a side maximum. Independently from the resolution, both peak profiles are well represented by the simulation. The prediction at a factor 10 higher resolution of  $R = 600000$  reveal nine peaks resulting from diverse species within a small mass range of  $0.08$   $m/z$ , which constitute the envelope at lower resolution of  $R = 60000$ . Hence, small differences in the peak height distribution between different species can lead to a noticeable mass shift of the maxima-position at lower resolutions. However, the maxima of the recorded ( $m/z = 1405.54687$ ) and predicted ( $m/z = 1405.55456$ ) mass spectra are shifted by  $\Delta m/z = 0.00769$  within the order of the distance of two measured points  $\Delta m/z_{rec} = 0.00624$  (cf. triangles in **Figure 4.16**). Thus, the resolution limit of the ESI-MS is one reason for deviations between the recorded and the predicted mass spectra. Further, the prediction is limited to a total statistical behavior of the termination process, which can lead to deviations due to additional reaction pathways. Integration of all peaks of the simulated, in relation to the recorded, isotopic patterns reflects a prediction of approximately 89 % of the detected species. The residual 11 % of unassigned species would need further investigations, resp. an expansion of the prediction approach. However, the excellent overall agreement of the

prediction and the experiment implies that the key reaction channels are captured by the simple statistical model. Thus, a quantitative cleavage mechanism of the initiators is expected and possible side products from a non-quantitative cleavage are only of minor importance, e.g. three- and two-armed star polymers, chain branching of two or more polymers and additional combinations of two or more germynyl-based radicals.

The development of a detailed mechanism for the radical formation in bis- and tetraacylgermanes is intrinsically not possible from *post-mortem* analysis of mass spectra. A study from literature on the dibenzoyldiethylgerman shows the formation of primary benzoyldiethylgermyl radicals within tens of nanoseconds, which is a clue for a consecutive cleavage mechanism.<sup>43</sup> According to the discussion on the mechanism of CB<sub>1</sub>G (refer to **section 4.2.2**), a consecutive cleavage can occur via subsequent excitation by photons or via a secondary activated state, e.g. vibrational hot state. Thus, a detailed mechanism development requires a time-resolved treatment from the event of excitation until the final macromolecular growth.

### **4.3 PLP-ESI-MS Cocktail Experiments: Overall Initiation Efficiency of Benzoyl-Radicals**

The PLP-ESI-MS cocktail experiment is a well-established method for the determination of the overall initiation efficiency of a radical towards a monomer originated from a distinctive pair of photoinitiators.<sup>32, 34-35, 143</sup> The approach is based on the proportionality between the relative abundance (peak height) in a mass spectrum and the number of the corresponding detected species. The overall initiation efficiency is determined by the correlation of peak height-ratios with initial molar ratios of two initiators. Due to a potential ionization bias by the ESI-source, only polymers with similar isotopic pattern can be compared in PLP-ESI-MS cocktail experiments. Thus, the method is well-suited to compare macromolecules initiated by radical fragments, which differ only in small substitution functionalities, e.g. products initiated by benzoyl vs. *para*-methoxy-benzoyl radicals. The evaluation process is developed for single charged species. Thus, for the majority of experiments, multiple charged species were separated by the use of SEC before the injection into ESI-MS.

As a special feature of the method, the overall initiation efficiency is determined from the product distribution after final macromolecular growth (*post-mortem*). As already

noted, the obtained values are the result of all critical events from the first step of light excitation until completed polymerization, e.g.  $\epsilon$ ,  $\phi_{ISC}$ ,  $\phi_{cleav.}$  and  $\phi_{escape}$ .

In the following the exact procedure for the quantification of overall initiation efficiencies from PLP-(SEC)-ESI-MS-cocktail experiments is described in detail. Subsequently, the results for a systematic comparison of the overall initiation efficiency of a library of *para*-fluoro and methoxy substituted mono- (A), bis- (B) and tetra- (C) acylgermanes (**Figure 4.17**) are presented.

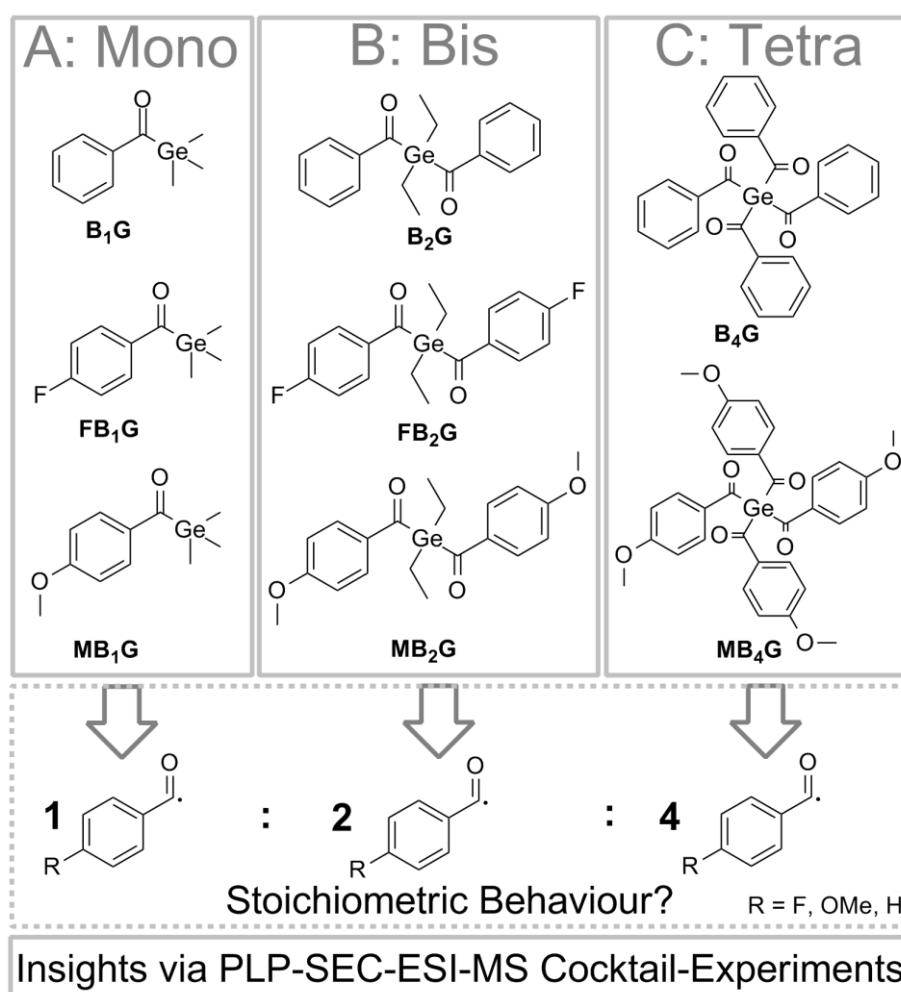


**Figure 4.17.** Overview of *para*-fluoro (F) and methoxy (M) substituted mono- (A), bis- (B) and tetra- (C) acylgermane derivatives employed for a systematic investigation on the substitution-influence and size-dependence of the overall initiation efficiencies obtained from PLP-ESI-MS cocktail experiments. Adapted with permission from ref. 146. Copyright 2019 American Chemical Society. Modified presentation.

PLP-ESI-MS cocktail experiments were conducted for acylgermanes within the same system size, and between different system sizes, to investigate the influence of substitution pattern as well as a possible size-dependence, respectively. Especially for

the size-dependence, a stoichiometric scaling is expected for the comparison of the overall initiation efficiency of mono-, bis- and tetraacylgermanes due to one, two and four benzoyl moieties as potential sources for radical formation. The experimentally obtained overall initiation efficiencies are validated via intrinsic cross-calculations. Finally, the size-dependence in the overall initiation efficiency is discussed in detail with respect to literature and UV/Vis-properties of the initiators. As a technical remark, the following quantitative PLP-ESI-MS analysis is limited to benzoyl initiated polymers due to complex isotopic patterns of germanium-containing species as shown in **section 4.2.3**.

#### **4.3.1 Quantification of Overall Initiation Efficiencies in Cocktail-Experiments**

In a PLP-ESI-MS cocktail experiment, two (acylgermane-based) initiators  $X_jG:Y_kG$  are mixed together in a defined molar ratio  $n(X_jG)/n(Y_kG)$  in MMA within one sample. X,Y describes the chemical nature of two distinctive benzoyl moieties, G reflects the germyl moiety, j and k are the number of benzoyl moieties per initiator. Disproportionation and combination products of PMMA with 20-30 repeating units are generated during the PLP process. For the exclusion of a wavelength-dependency, each cocktail experiment is conducted at excitation wavelengths close of the  $n\pi^*$ -absorption maximum of each initiator within one sample. PMMA-macroradicals prefer termination via disproportionation. Thus, using MMA as a monomer is of advantage for the determination of the overall initiation efficiency in PLP-ESI-MS cocktail experiments.<sup>32</sup> Disproportionation products are defined by the initiating radical fragment (X) of an initiator at the  $\alpha$ -chain end, and the double bond (=) or hydrogen (H) at the  $\omega$ -chain end. In contrast, the macromolecular growth of combination products were initiated and terminated by radical fragments from the initiators. Thus, the subsequent differentiation between  $\alpha$ - and  $\omega$ -chain ends is not possible. In fact, only disproportionation products enable a clear assignment to the initiation process by one radical (illustrated in **Figure 4.18**).

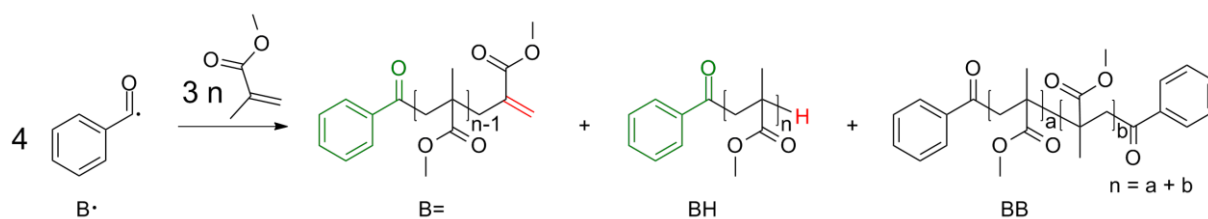


**Figure 4.18.** Exemplary disproportionation B=, BH and -combination products of MMA initiated and terminated by benzoyl radicals B. B= and BH contain the information about the initiating radical (green) due to termination via disproportionation (red). The combination product BB loses the information about which end group is related to the initiating and which to the terminating step. Adapted with permission from ref. 146. Copyright 2019 American Chemical Society.

The isotopic patterns of the two disproportionation products X= and XH occur in a mass difference of 2  $m/z$ . Thus, the first peak of the isotopic pattern of X= is free from an isobaric overlap and can be used for a quantitative evaluation. According to the proportionality between the abundance to the number of recorded polymer species in a mass spectrum, the peak-height  $h_n^{X=}$  at a repeating unit  $n$  of the disproportionation product X= can be used to count the initiation events caused by the radical fragment X. As a consequence of the electrospray mass ionization process, the abundance is not an absolute quantity for the number of X=. Thus, a quantitative evaluation is only possible for the relative comparison  $G^{X=} = \frac{h_n^{X=}}{h_n^{Y=}}$  of the peak heights of two distinctive isotopic patterns X=, Y= within the same mass spectrum. For example, the isotopic pattern of the disproportionation products initiated by benzoyl B and *para*-methoxybenzoyl MB radicals originated from the initiators B<sub>4</sub>G and MB<sub>2</sub>G used for the determination of the peak heights at the repeating unit of 8 is shown in **Figure 4.19**.

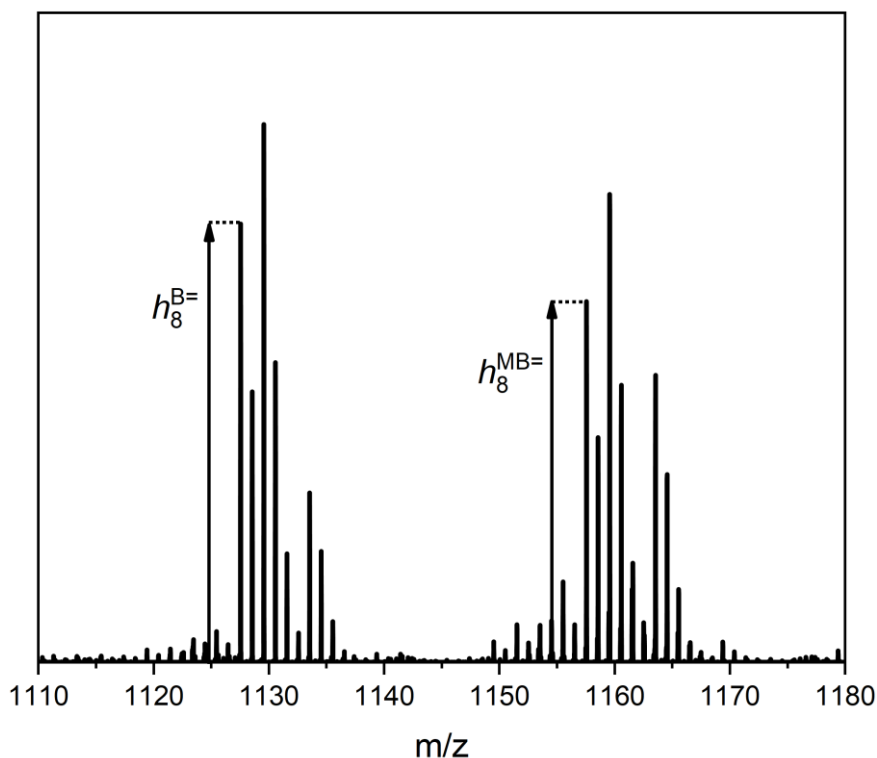


**Figure 4.19.** Extract from exemplary ESI-MS spectrum of the cocktail experiment B<sub>4</sub>G:MB<sub>2</sub>G at the initial molar ratio of 0.49, showing the determination of peak heights  $h$  of the disproportionation products B<sup>=</sup> and MB<sup>=</sup> at the repeating unit of 8. Adapted with permission from ref. 146. Copyright 2019 American Chemical Society.

For an end group-independent chain growth, one can assume equally distributed end groups over all repeating units  $n$ . The molar fraction  $F_n^{X=}$  of one disproportionation product X<sup>=</sup> at the repeating unit  $n$  is a relative quantity of the macromolecules initiated by the radical fragment X and can be described by **Eq 4.2**.<sup>34-35</sup>

$$F_n^{X=} = \frac{h_n^{X=}}{h_n^{X=} + h_n^{Y=}} \quad \text{Eq 4.2}$$

If a chain length-dependent ionization bias can be neglected, the molar fraction  $F_n^{X=}$  remains at the same value for each repeating unit  $n$ . For example, plotting  $F$  versus the degree of polymerization  $DP$  of the cocktail experiment of MB<sub>4</sub>G:B<sub>2</sub>G irradiated at 396 nm (**Figure 4.20**) reveals a slightly increasing slope, which indicates a weak chain length-dependent ionization bias.

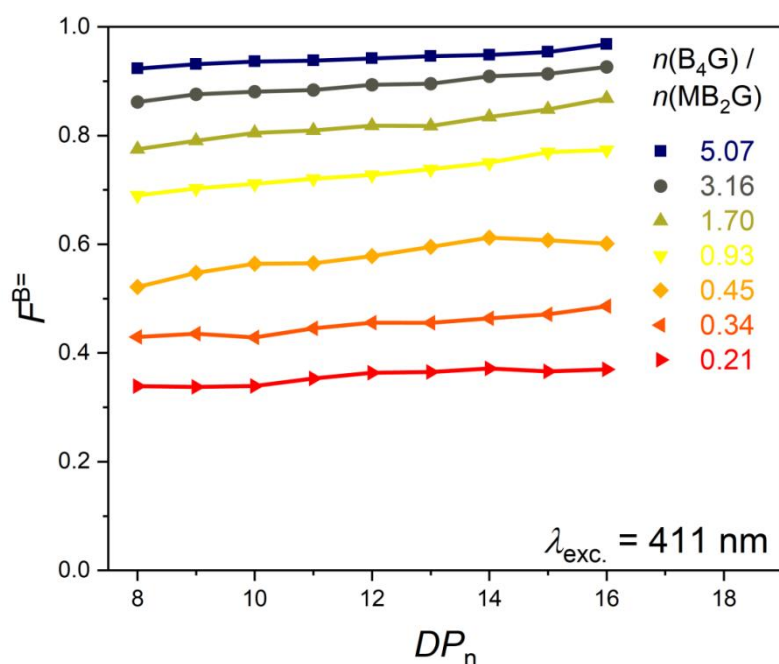


**Figure 4.20.** Exemplary  $F$  vs  $DP$ -plot of the molar fraction  $F^{B=}$  of the disproportionation product  $B=$  versus the degree of polymerization  $DP_n$  for the evaluation of a chain length-dependent ionization bias during the ESI process of the cocktail experiment  $B_4G:MB_2G$ . Excitation wavelength  $\lambda_{exc.}$  and molar ratio  $n(B_4G)/n(MB_2G)$  of each sample as indicated. Adapted with permission from ref. 146. Copyright 2019 American Chemical Society.

A weak ionization bias between the repeating units allows the averaging over all  $G_n^{X=}$ . For a further reduction of the scattering caused by a mass-biased ESI process, an established averaging method is used to obtain the mass-bias-free ratio  $G_{m/z0}^{X=}$ , which is given by **Eq 4.3**.<sup>32, 35, 143</sup>

$$G_{m/z0}^{X=} = \frac{\langle G_{n-1}^{X=} \rangle + \langle G_n^{X=} \rangle + \langle G_{n+1}^{X=} \rangle}{3}, \quad \text{Eq 4.3}$$

$$\text{with } \langle G_{n-1}^{X=} \rangle = \frac{1}{N} \sum_n \frac{h_n^{X=}}{h_{n-1}^{Y=}}, \quad \langle G_n^{X=} \rangle = \frac{1}{N} \sum_n \frac{h_n^{X=}}{h_n^{Y=}}, \quad \langle G_{n+1}^{X=} \rangle = \frac{1}{N} \sum_n \frac{h_n^{X=}}{h_{n+1}^{Y=}}.$$

$G_{m/z0}^{X=}$  is the mean value of  $\langle G_{n-1}^{X=} \rangle$ ,  $\langle G_n^{X=} \rangle$ ,  $\langle G_{n+1}^{X=} \rangle$ , which correlates the peak height  $h_n^{X=}$  of the disproportionation product  $X=$  with the compared  $h_n^{Y=}$  of  $Y=$  at the adjacent repeating units  $n - 1$ ,  $n$ , and  $n + 1$ . The presented determination of  $G_{m/z0}^{X=}$  is implemented in an in-house built Matlab-script (MathWorks) for an automated evaluation, which is described in detail in **section 4.3.2**. Plotting  $G_{m/z0}^{X=}$  against the initial molar ratios  $n(X_jG)/n(Y_kG)$  of the two photoinitiators for each cocktail experiment exhibits a linear trend, which can be evaluated via linear regression. Cocktail experiments

are conducted in MMA at excitation wavelengths of the  $n\pi^*$ -maxima for both initiators. For a negligible wavelength-dependence within the  $n\pi^*$ -maxima, the data for one cocktail experiment at different wavelengths can be plotted in a joint plot. As an example, the  $G_{m/z0}^{X=}$  vs initial molar ratios-plot is presented for the cocktail experiment MB<sub>4</sub>G:MB<sub>2</sub>G in MMA in **Figure 4.21**.

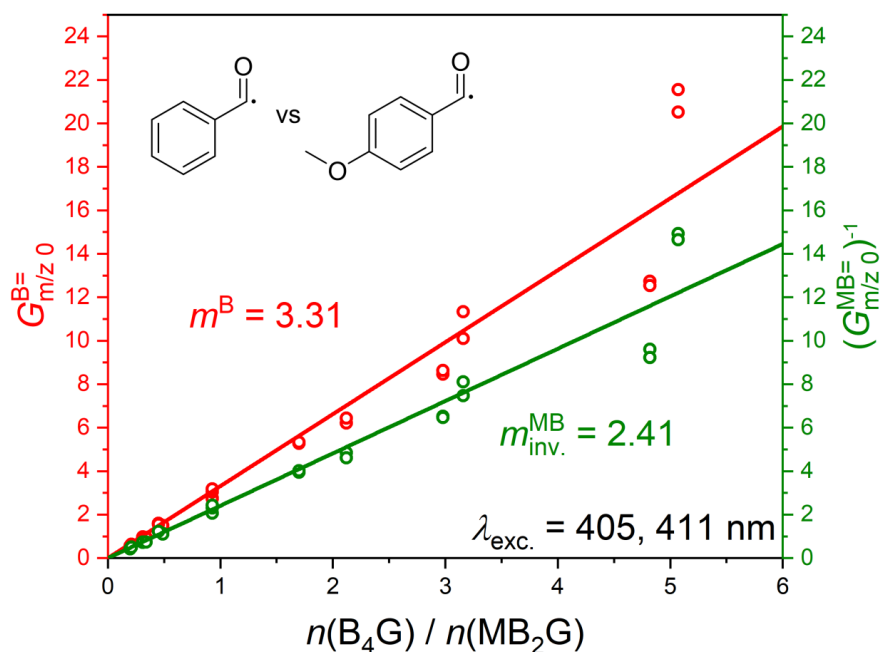


**Figure 4.21.**  $G_{m/z0}^{X=}$  vs initial molar ratios-plot of the cocktail experiment B<sub>4</sub>G:MB<sub>2</sub>G to determine the overall initiation efficiencies of the radicals B and MB at excitation wavelength as indicated. Red: Linear regression of all mass-bias-free ratios  $G_{m/z0}^{B=}$  of the disproportionation product B= initiated by the radical B originated from the initiator B<sub>4</sub>G versus the initial molar ratios  $n(B_4G)/n(MB_2G)$  resulting in an overall initiation efficiency of  $m^B=3.31$ . Green: Linear regression of all invers mass-bias-free ratios  $(G_{m/z0}^{MB=})^{-1}$  of the disproportionation product MB= initiated by the radical MB originated from the initiator MB<sub>2</sub>G versus the initial molar ratios  $n(B_4G)/n(MB_2G)$  resulting in an overall initiation efficiency of  $m_{inv.}^{MB} = 2.41$ . Deviations between  $m^B$  and  $m_{inv.}^{MB}$  reflect the scattering of the experiment. Adapted with permission from ref. 146. Copyright 2019 American Chemical Society.

Apparently, at an initial molar ratio of zero, formation of disproportionation products initiated by radical fragments is excluded. Thus, the linear fitting routine is conducted with a fixed zero intercept. At  $G_{m/z0}^{X=} = 1$ , the same amount of the disproportionation product X= compared to Y= is formed. Hence, the initial molar ratio  $x = n(X_jG) / n(Y_kG)$  at  $G_{m/z0}^{X=} = 1$  is a direct measure for the overall initiation efficiency of the two compared radical fragments X and Y originated from the initiator

pair  $X_jG:Y_kG$ . Consequently, the overall initiation efficiency of the radical fragment  $X$  originating from  $X_jG$  is defined as the slope of the linear regression with zero intercept  $m^X$  as evident from **Eq 4.4**.<sup>32, 35, 143</sup>

$$f(x) = mx \Leftrightarrow G_{m/z0}^{X=} = m \frac{n(X_jG)}{n(Y_kG)}, \quad \text{Eq 4.4}$$

$$\text{for } G_{m/z0}^{X=} = 1 \Rightarrow m^X \equiv \left( \frac{n(X_jG)}{n(Y_kG)} \right)^{-1} := \text{overall initiation efficiency.}$$

Ideally, the mass-bias-free molar ratio  $G_{m/z0}^{X=}$  is proportional to the ratio of the absolute numbers  $N^{X=}/N^{Y=}$  of the disproportionation products  $X=$  and  $Y=$ . Thus, the inverse overall initiation efficiency  $m_{\text{inv}}^Y$ , obtained from  $(G_{m/z0}^{Y=})^{-1}$  versus the initial molar ratio  $n(X_jG)/n(Y_kG)$  for the radical fragment  $Y$  originating from initiator  $Y_kG$  would be identical with  $m^X$ . In fact,  $G_{m/z0}$  is the mean value of averaged ratios of intrinsically defective peak heights, resulting in deviations between  $G_{m/z0}^{X=}$  and  $(G_{m/z0}^{Y=})^{-1}$ . Thus,  $m^X$  and  $m_{\text{inv}}^Y$  are averaged to  $m$  and its standard deviation  $\Delta m$  is interpreted as the error of the experiment. For example, the overall initiation efficiency of the cocktail experiment  $MB_4G:MB_2G$  is averaged to  $m = 2.86 \pm 0.64$ , which reflects an error of ~20 %. Potential sources of error are scattering in the laser pulse energy (~15 %), bias from uncertainties in molecular weight fractioning during the SEC process, and the ionization bias of the mass spectrometer.

An overview of all conducted cocktail experiments of *para*-fluoro- and methoxy-mono, bis and tetraacylgermanes is presented in **Table 4.8** (refer to **Figure A13-Figure A24**).

For a systematic comparison of the obtained overall initiation efficiencies of mono- (A), bis- (B) and tetra- (C) acylgermanes, cocktail experiments are sorted within the same system size A:A, B:B, C:C and between different system sizes B:A, C:B and C:A (**Table 4.8**). Only small differences within the same system size are observed. For A:A, *para*-methoxy substituted benzoyl radicals tend to a higher overall initiation efficiency compared to un- and *para*-fluoro-substituted benzoyltrimethylgermanes. As a technical remark, disproportionation products initiated by *para*-fluoro-benzoyl radicals show a small isobaric overlap with trimethylgermane-initiated species as shown in **Figure A 25**. In comparison, an alternative evaluation with y-intercept unequal zero reveals a factor of  $1.5 \pm 0.3$  for  $FB_1G:HB_1G$ .<sup>144</sup> In fact, setting the y-intercept not to

zero is physically not justified, which dismisses the overall initiation efficiency as overestimated. However, an evaluation with y-intercept takes respect to the systematic error caused by the isobaric overlap of approximately 20 %. Further, cocktail experiments within the same system size of B:B and C:C show only slight differences in their efficiencies, which are negligible according to the error margin.

**Table 4.8.** Overview of all conducted cocktail experiments (refer to **Figure A13-Figure A24**). Adapted with permission from ref. 146. Copyright 2019 American Chemical Society. Modified presentation.

type	cocktail experiment	radical fragments	$\lambda$ / nm	overall Initiation efficiency $m$	error / %
A:A	FB <sub>1</sub> G:B <sub>1</sub> G	FB:B	405, 409, 410	$1.00 \pm 0.05$	4.97
A:A	MB <sub>1</sub> G:B <sub>1</sub> G	MB:B	397, 400, 409	$1.40 \pm 0.10$	7.07
B:B	FB <sub>2</sub> G:B <sub>2</sub> G	FB:B	416, 421	$1.07 \pm 0.18$	17.18
B:B	MB <sub>2</sub> G:B <sub>2</sub> G	MB:B	411, 421	$1.14 \pm 0.25$	22.33
C:C	MB <sub>4</sub> G:B <sub>4</sub> G	MB:B	396, 405	$0.97 \pm 0.08$	8.06
B:A	FB <sub>2</sub> G:MB <sub>1</sub> G	FB:MB	416	$2.19 \pm 0.20$	9.04
B:A	MB <sub>2</sub> G:FB <sub>1</sub> G	MB:FB	410, 411	$2.40 \pm 0.42$	17.68
B:A	MB <sub>2</sub> G:B <sub>1</sub> G	MB:B	411	$3.14 \pm 0.41$	13.06
C:B	B <sub>4</sub> G:MB <sub>2</sub> G	B:MB	405, 411	$2.86 \pm 0.64$	22.25
C:B	B <sub>4</sub> G:FB <sub>2</sub> G	B:FB	405, 416	$2.61 \pm 0.29$	11.13
C:A	B <sub>4</sub> G:FB <sub>1</sub> G	B:FB	405, 410	$6.55 \pm 1.62$	24.74
C:A	MB <sub>4</sub> G:B <sub>1</sub> G	MB:B	396, 415	$5.26 \pm 0.79$	15.02

From a simple stoichiometric view, a factor 2 for B:A, C:B and factor 4 for C:A is expected due to the ratio of benzoyl moieties of a compared initiator pair. Surprisingly, a nonstoichiometric size-dependence in the overall initiation efficiency  $m$  is observed for cocktail experiments of initiators with a different number of benzoyl moieties, e.g.  $m(\text{MB}_2\text{G}:\text{B}_1\text{G}) = 3.14 \pm 0.41$  (B:A),  $m(\text{B}_4\text{G}:\text{MB}_2\text{G}) = 2.86 \pm 0.64$  (C:B),  $m(\text{B}_4\text{G}:\text{FB}_1\text{G}) = 6.55 \pm 1.62$  (C:A).

### Triple Cocktail Experiment

A special triple cocktail experiment<sup>34</sup> was conducted for an experimental validation of the observed stoichiometric increase in  $m$ . Therefore, samples were prepared in seven defined ratios of three initiators in MMA (here, B<sub>4</sub>G, FB<sub>2</sub>G, and MB<sub>1</sub>G). Each sample was irradiated with 90000 pulses (320  $\mu\text{J}/\text{pulse}$ ) at three wavelengths (397, 405, and 416 nm) with respect to the absorption maxima of the employed initiators. ESI-MS analysis and the determination of the overall initiation efficiencies were carried out analogously to regular cocktail experiments as described above. In contrast, a PLP-ESI-MS triple cocktail experiment with three initiators X<sub>j</sub>G, Y<sub>k</sub>G, and Z<sub>l</sub>G leads to

three disproportionation products X=, Y=, Z=, which are available for evaluation in three resulting cocktail-plots  $G_{m/z0}^{X=}$ ,  $(G_{m/z0}^{Y=})^{-1}$  versus  $n(X_jG)/n(Y_kG)$ ;  $G_{m/z0}^{X=}$ ,  $(G_{m/z0}^{Z=})^{-1}$  versus  $n(X_jG)/n(Z_lG)$ ; and  $G_{m/z0}^{Y=}$ ,  $(G_{m/z0}^{Z=})^{-1}$  versus  $n(Y_kG)/n(Z_lG)$ . The resulting plots for the triple cocktail experiment of B<sub>4</sub>G, FB<sub>2</sub>G, and MB<sub>1</sub>G in MMA are presented in **Figure 4.22**.

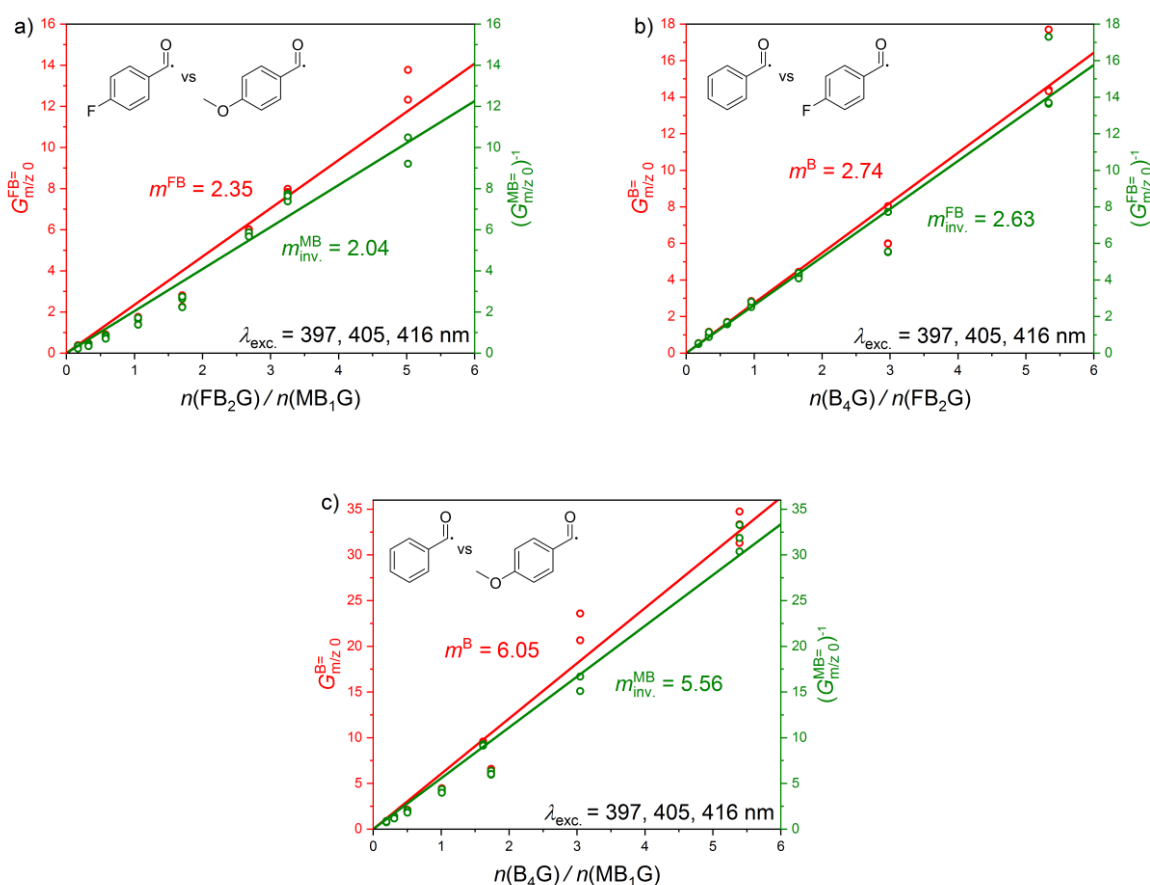


**Figure 4.22.**  $G_{m/z0}^{X=}$  vs initial molar ratios-plots resulting from triple cocktail experiment of B<sub>4</sub>G, FB<sub>2</sub>G, and MB<sub>1</sub>G in MMA for validation of the nonstoichiometric increase observed in regular cocktail experiments. Overall initiation efficiencies determined from resulting three  $G_{m/z0}^{X=}$  vs initial molar ratios-plots **a)**  $m(\text{FB}_2\text{G}:\text{MB}_1\text{G}) = 2.20 \pm 0.22$ , **b)**  $m(\text{B}_4\text{G}:\text{FB}_2\text{G}) = 2.69 \pm 0.08$ , and **c)**  $m(\text{B}_4\text{G}:\text{MB}_1\text{G}) = 5.81 \pm 0.35$ , respectively. Corresponding  $F$  versus  $DP$  plots are provided in **Figure A26**, **Figure A27**, and **Figure A28**. Adapted with permission from ref. 146. Copyright 2019 American Chemical Society.

The comparison of FB<sub>2</sub>G:MB<sub>1</sub>G within the triple cocktail experiments shows a slightly increased  $m(\text{FB}_2\text{G}:\text{MB}_1\text{G}) = 2.20 \pm 0.22$  for FB radicals originating from bisacylgermane FB<sub>2</sub>G compared to monoacylgermane MB from MB<sub>1</sub>G. However, the deviation from the stoichiometric expectation is insignificant within the error margins. Remarkably, a non-stoichiometric increase is observed for the comparison of tetra- and

bis-  $m(\text{B}_4\text{G}:\text{FB}_2\text{G}) = 2.69 \pm 0.08$  as well as tetra- and monoacylgermanes  $m(\text{B}_4\text{G}:\text{MB}_1\text{G}) = 5.81 \pm 0.35$  within the triple cocktail experiment. Further, the overall initiation efficiencies obtained from triple cocktail experiment are consistent with results from regular cocktail experiments ( $m(\text{FB}_2\text{G}:\text{MB}_1\text{G}) = 2.19 \pm 0.20$ ,  $m(\text{B}_4\text{G}:\text{FB}_2\text{G}) = 2.69 \pm 0.08$ ) as shown by small deviations of 0.5 % and 3 %, respectively. The averaged overall initiation efficiencies obtained from the triple cocktail experiment of  $\text{B}_4\text{G}$ ,  $\text{FB}_2\text{G}$ , and  $\text{MB}_1\text{G}$  in MMA are summarized in **Table 4.9**.

**Table 4.9.** Overview of Averaged overall initiation efficiencies obtained from triple cocktail experiment of  $\text{B}_4\text{G}$ ,  $\text{FB}_2\text{G}$ , and  $\text{MB}_1\text{G}$  in MMA. Adapted with permission from ref. 146. Copyright 2019 American Chemical Society. Modified presentation.

type	cocktail experiment	radical fragments	$\lambda$ / nm	overall Initiation efficiency $m$	error / %
B:A	$\text{FB}_2\text{G}:\text{MB}_1\text{G}$	FB:MB	397, 405, 416	$2.20 \pm 0.22$	9.99
C:B	$\text{B}_4\text{G}:\text{FB}_2\text{G}$	B:FB	397, 405, 416	$2.69 \pm 0.08$	2.90
C:A	$\text{B}_4\text{G}:\text{MB}_1\text{G}$	B:MB	397, 405, 416	$5.81 \pm 0.35$	5.97

#### 4.3.2 Excursus: Automated Evaluation of PLP-ESI-MS Cocktail Experiments

The manual evaluation of PLP-ESI-MS cocktail experiments is very time-consuming. For example, one cocktail experiment with seven samples leads to seven mass spectra with up to 10 repeating units for two disproportionation patterns resulting in 140 peak heights exploitable for determination of  $G_{m/z_0}^{X=}$  and  $F$ . For an efficient evaluation of the maximum peak heights for a set of mass spectra, the above described evaluation process was automated in an in-house programmed Matlab-script. As an advantage, the automated evaluation for one cocktail experiment consumes only ~2 s. Therefore, a high number of experiments can be conducted, which enables a comprehensive investigation on overall initiation efficiencies of a library of photoinitiators as presented in the previous section. In addition, a more efficient data evaluation supports a more precise error viewing by increasing the reproductions of one experiment. The core of the script is a search-routine for determination of maxima of all first mass bias-free peaks of the corresponding isotopic patterns of disproportionation products  $X=/Y=$  for all repeating units from a PLP-ESI-MS cocktail experiment. In the following the finding-routine for each maximum peak height is described in detail.

Initial input data are mass spectra and initial molar ratios of conducted cocktail experiments in txt data-sheets. The initial input parameters are  $m/z$ -values of the target end groups  $m_{X=/Y=}$  of disproportionation products  $X=$  and  $Y=$  and of the applied

monomer (e.g. MMA)  $M_{\text{MMA}}$ , further the total number of recorded spectra  $S$ , and a constant  $D$  for the definition of the  $m/z$ -interval  $[M_{X=Y,n} - D, M_{X=Y,n} + D]$ .

First, the  $m/z$ -value of the first mass bias-free peak for each repeating unit  $n$  of  $X=Y=$  is calculated via  $M_{X=Y,n} = m_{X=Y=} + n \cdot M_{\text{MMA}}$  for a given  $m/z$  of the corresponding monomer  $M_{\text{MMA}}$  and end group  $m_{X=Y=}$ . Subsequently, the maximum of all approximately Gaussian-shaped peaks is found by comparison of the data points left and right from the calculated  $m/z$   $M_{X=Y,n}$  given by the  $m/z$  interval  $[M_{X=Y,n} - D, M_{X=Y,n} + D]$ . Each approximately Gaussian-shaped peak recorded with a high-resolution ESI-Orbitrap mass spectrometer consists of 10-20 data points, which has a peak width at half-height of  $\Delta m/z \sim 0.02$ . Thus, by setting  $D$  to a constant of 0.02, differences between expected and recorded  $m/z$ -values are clearly compensated and the number of scanned data points kept small. A for-loop serially scans all data points for each repeating unit  $n$  of a mass spectrum given by the peak height as a function of  $m/z$ . A first if-condition verifies, whether the targeted data point is in the  $m/z$ -interval  $[M_{X=Y,n} - D, M_{X=Y,n} + D]$  for a given repeating unit  $n$ . A second if-condition ensures that the peak height of the targeted data point is higher than a testing-peak height, which is initially set to zero. For the first run, the target peak height substitutes the testing-peak height. In the following, the loops are repeated until the testing-peak height is substituted with the maximum peak height within the investigated  $m/z$ -interval. In addition, the corresponding  $m/z$  value is saved. The procedure runs until all data points of the mass spectrum are scanned. The procedure is repeated for each repeating unit  $n$ . Finally, maximum peak heights as a function of  $m/z$  are obtained for each repeating unit of both disproportionation products  $X=Y=$  per mass spectrum. Thus, the mass-bias-free molar ratio as well as the  $F$  vs  $DP$  plot can be calculated from the obtained data via **Eq 4.2** and **Eq 4.3**, respectively.

### 4.3.3 An Intrinsic Validation: Calculation with Overall Initiation Efficiencies

The scope of the presented data base is sufficient to prove its intrinsic consistency. If experimentally obtained overall initiation efficiencies  $m$  are valid quantities, calculations between different cocktail experiments will result in consistent calculated values  $m_{\text{calc}}$  within the estimated error margin.

In the following a new syntax is introduced, which enables the calculation with overall initiation efficiencies. Herein, the overall initiation efficiency  $m$  of a cocktail experi-

ment  $X_jG:Y_kG$  can be written in a quotient as follows in **Eq 4.5**, which allows algebraic operations.

$$m = \left( \frac{X_jG}{X_kG} \right). \quad \text{Eq 4.5}$$

For instance, by multiplying  $m(\text{FB}_2\text{G}:\text{MB}_1\text{G}) = 2.20 \pm 0.22$  and  $m(\text{B}_4\text{G}:\text{FB}_2\text{G}) = 2.69 \pm 0.08$  obtained from two initiator pairs of the triple cocktail experiment, the value for the third initiator pair can be calculated as displayed in **Eq 4.6** (error from Gaussian propagation of uncertainty).

$$\begin{aligned} \left( \frac{B_4G}{MB_1G} \right)_{calc} &= \left( \frac{FB_2G}{MB_1G} \right) \left( \frac{B_4G}{FB_2G} \right) \\ &= (2.20 \pm 0.22) \cdot (2.69 \pm 0.08) = 5.92 \pm 0.62. \end{aligned} \quad \text{Eq 4.6}$$

The calculated value of  $m_{calc}(\text{B}_4\text{G}:\text{MB}_1\text{G}) = 5.92 \pm 0.62$  shows only a small deviation of ~2% compared with the experimental value  $m(\text{B}_4\text{G}:\text{MB}_1\text{G}) = 5.81 \pm 0.34$ , which evidences the intrinsic validity of the triple cocktail experiment. In general, the cross-calculation with overall initiation efficiencies from cocktail experiments is possible in many different ways by multiplying and/or dividing two or more experimental values with each other. Thus, the determination of  $m_{calc}$  is always carried out by using as few experimental values as possible with the lowest error from uncertainty propagation. All calculated and experimentally obtained overall initiation efficiencies from cocktail experiments are summarized for a comprehensive comparison in **Figure 4.23**. The corresponding calculations are provided in appendix **Eq A1-A10**.

Except for  $m(\text{MB}_4\text{G}:\text{B}_1\text{G})$  (40 % deviation), the comparison of calculated (green) and experimental (black) overall initiation efficiencies reveals only small deviations of 0.5-15 % in **Figure 4.23**. Hence, the evaluated data base displays a high intrinsic validity within its error margin. In conclusion, the introduced calculations with overall initiation efficiencies are a powerful tool for a consistency check of a set of data obtained from PLP-ESI-MS cocktail experiments. In addition, hypothetic cocktail experiments can be calculated from experimental data with sufficient accuracy within the error margin as a base for further discussions. Well selected and highly reproduced cocktail experiments combined with calculations can reduce the total number of experiments, which is an advantage of time saving for future investigations.

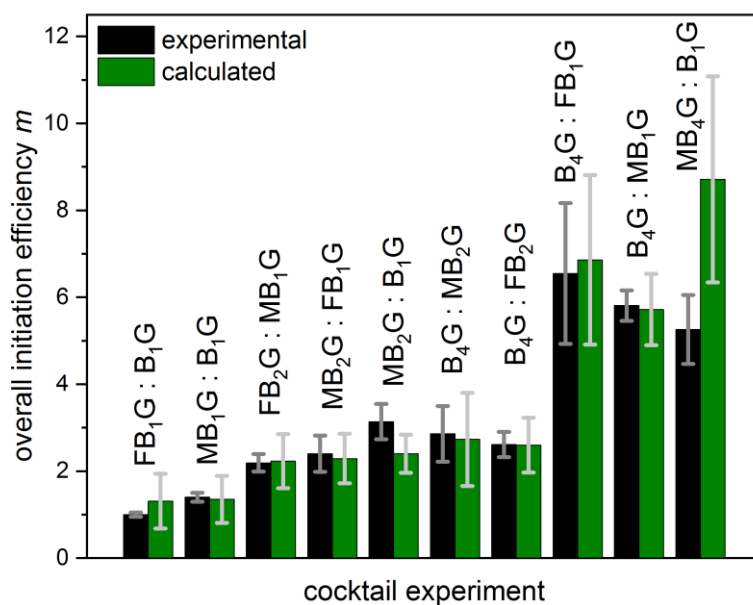


**Figure 4.23.** Comparison of calculated (green) and experimental (black) overall initiation efficiencies for proving the intrinsic validity of all conducted cocktail experiments. Adapted with permission from ref. 146. Copyright 2019 American Chemical Society. Modified presentation.

#### 4.3.4 Non-Stoichiometric Size-Dependence

As seen from the previous section, the calculation with overall initiation efficiencies based on the syntax of **Eq 4.5** leads to valid results. Thus, overall initiation efficiencies are determined for hypothetic cocktail experiments  $X_kG:X_{j<k}G$  of initiators with different numbers  $j < k$  of identical benzoyl moieties  $X$  (appendix **Eq A11-A18**). Remarkably, the comparison of initiators with same substitution patterns is only theoretically accessible due to indistinguishable PMMA-disproportionation products in PLP-ESI-MS cocktail experiments. The calculated overall initiation efficiencies (solid bars) of hypothetic cocktail experiments of bis- versus mono- (B:A), tetra- versus bis- (C:B), and tetra- versus monoacylgermanes (C:A) are presented together with the corresponding ratios of the respective  $n\pi^*$ -extinction coefficients (hatched bars; refer to **section 4.1.2** and **Table A24**) in **Figure 4.24**.

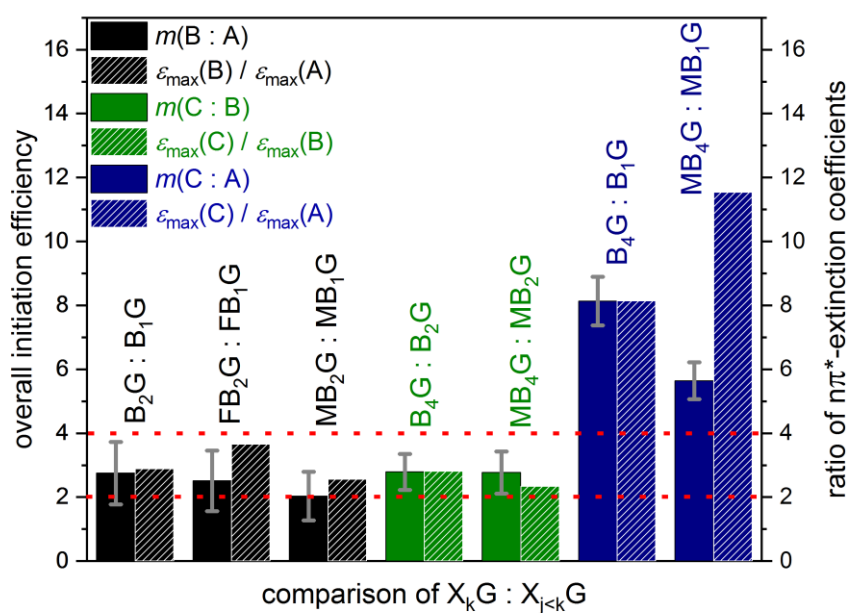


**Figure 4.24.** Calculated overall initiation efficiencies of hypothetical cocktail experiments (solid bars) and ratios of  $n\pi^*$ -extinction coefficients at the corresponding absorption maximum (hatched bars) of acylgermanes with a different number  $j < k$  of identical benzoyl moieties  $X_kG : X_{j < k}G$ . In black: Comparison of bis- towards monoacylgermanes (B:A). In green: Comparison of tetra- towards bisacylgermanes (C:B). In blue: Comparison of tetra- towards monoacylgermanes (C:A). Red dashed lines: Stoichiometric expectation. Adapted with permission from ref. 146. Copyright 2019 American Chemical Society. Modified presentation.

As represented in **Figure 4.24**, the calculated overall initiation efficiencies are exclusively a measure for the size-dependence independent from influences of substitution patterns. In general, the reactivity of identical radical fragments towards MMA is equal. Consequently, a stoichiometric factor 2 and 4 (indicated by red dashed lines in **Figure 4.24**) is expected for the comparison of B:A, C:B and C:A, respectively. In contradiction, a non-stoichiometric scaling with increasing number of identical benzoyl moieties is reflected by the calculated overall initiation efficiencies (solid bars higher than dashed red lines, **Figure 4.24**). For B:A (black solid bars, **Figure 4.24**) with  $m(B_2G : B_1G) = 2.75 \pm 0.98$ ,  $m(FB_2G : FB_1G) = 2.47 \pm 0.67$ , and  $m(MB_2G : MB_1G) = 2.03 \pm 0.76$  a nonstoichiometric increase of 0-38 % is observed. However, the result is not significant due to lower error boundaries of  $m_{\min} < 2$ . The calculated overall initiation efficiencies of C:B are significant within the estimated error boundaries and reveal a non-stoichiometric increase of ~40 % towards a factor of 2, e.g.  $m(B_4G : B_2G) = 2.79 \pm 0.56$ ,  $m(MB_4G : MB_2G) = 2.77 \pm 0.66$ . The comparison of

C:A shows a clear stoichiometric increase of ~100 % for  $m(\text{B}_4\text{G}:\text{B}_1\text{G}) = 8.13 \pm 0.76$  and 41 % for  $m(\text{MB}_4\text{G}:\text{MB}_1\text{G}) = 5.64 \pm 0.58$  towards a factor of 4. In conclusion, a significant non-stoichiometric increase of at least 40 % is estimated for benzoyl radicals originated from tetraacylgermanes. As observed from cocktail experiments within the same system size, the influence of *para*-substituents on the overall initiation efficiency is weak compared with the size-dependence, resp. tends to decrease from A:A, B:B to C:C, e.g.  $m(\text{MB}_1\text{G}:\text{B}_1\text{G}) = 1.40 \pm 0.10$ ,  $m(\text{MB}_2\text{G}:\text{B}_2\text{G}) = 1.14 \pm 0.25$ , and  $m(\text{MB}_4\text{G}:\text{B}_4\text{G}) = 0.97 \pm 0.08$  (**Table 4.8**). Thus, the extension of the system size is the dominating influence to increase the overall initiation efficiency of acylgermane-based photoinitiators.

### Discussion of Nonstoichiometric Size-Dependence: Overall Initiation Efficiencies, Extinction Coefficients and Quantum Yields

As known from earlier PLP-ESI-MS studies, the overall initiation efficiency of radical fragments is highly dependent on the structure of the corresponding initiator.<sup>32, 34-35, 143</sup> Herein, a nonstoichiometric increase as a result of the system size is a further example for the importance of the origin for radical formation. Accordingly, the overall initiation efficiency  $m$  respects all events during the polymerization process, starting from first photoexcitation step to radical formation until initiation of macromolecular chain-growth. Thus, intrinsic properties of photoinitiators, e.g.  $n\pi^*$ -extinction coefficient  $\varepsilon(\lambda)$ , ISC  $\phi_{\text{ISC}}$ , and cleavage quantum yields  $\phi_{\text{cleav}}$  of an initiator contribute to  $m$ .<sup>143</sup> Solvent-cage escape reactions  $\phi_{\text{cage}}$  are neglected due to similar sterically demanding radicals.<sup>32</sup>

Given that  $n\pi^*$ - $\varepsilon(\lambda)$  exclusively determines the overall initiation efficiency of an initiator pair  $X_j\text{G}:\text{X}_{k<j}\text{G}$ , the ratio of  $\varepsilon_{\text{max}}(X_j\text{G})/\varepsilon_{\text{max}}(\text{X}_{k<j}\text{G})$  is approximately proportional to  $m(X_j\text{G}:\text{X}_{k<j}\text{G})$ . The resulting correlation between the ratio of  $n\pi^*$ -extinction coefficients (dashed bars) and the calculated overall initiation efficiency (solid bars) of acylgermanes with a different number of identical benzoyl moieties can be derived from comparison in **Figure 4.24** and **Table A24**. Remarkably, the comparison of  $\varepsilon_{\text{max}}(X_j\text{G})/\varepsilon_{\text{max}}(\text{X}_{k<j}\text{G})$  with  $m$  obtained from calculated cocktail experiments of unsubstituted acylgermanes ( $\text{B}_2\text{G}:\text{B}_1\text{G}$ ,  $\text{B}_4\text{G}:\text{B}_2\text{G}$ ,  $\text{B}_4\text{G}:\text{B}_1\text{G}$ ) reveals only weak deviations < 7 %. In contrast,  $m$  of *para*-fluoro and methoxy-substituted acylgermanes ( $\text{MB}_2\text{G}:\text{MB}_1\text{G}$ ,  $\text{FB}_2\text{G}:\text{FB}_1\text{G}$ ,  $\text{MB}_4\text{G}:\text{MB}_2\text{G}$ ,  $\text{MB}_4\text{G}:\text{MB}_1\text{G}$ ) show higher deviations of 20-50% in comparison to the corresponding  $\varepsilon_{\text{max}}(X_j\text{G})/\varepsilon_{\text{max}}(\text{X}_{k<j}\text{G})$ . Thus,  $n\pi^*$ -

extinction coefficients are strongly correlated to the overall initiation efficiencies of unsubstituted acylgermanes, while the attachment of substitution patterns lead to higher deviations. The higher the extinction coefficient, the more excited photoinitiator molecules are generated per laser pulse, which are potentially available for a subsequent formation of initiating radical fragments after sufficient ISC. However, the extinction coefficient is a measure of the ability of the ground state molecules to absorb photons. Thus, the deviation from the correlation of the extinction coefficients and the overall initiation efficiency, especially for substituted acylgermanes, is a consequence from excited state dynamics, e.g.  $k_{ISC}$  and  $k_{cleav}$ . Herein, *para*-substitution patterns can strongly influence the ground state extinction coefficients without enhancing  $\phi_{ISC}$  and  $\phi_{cleav}$  as a possible explanation for the strong deviation between  $\epsilon_{max}(X_jG)/\epsilon_{max}(X_{k<j}G)$  and  $m$  of substituted acylgermanes. In line with the present findings, monoacylgermanes reveal weak decomposition quantum yields of 0.21-0.4.<sup>38-39</sup> However, the determination of total  $\phi_{ISC}$  and  $\phi_{cleav}$  for bis- and tetraacylgermanes is more challenging, due to complex channel branching expected from a multiple cleavage mechanism (refer **section 4.2.3**) as well as from quasi-degenerated excited singlet and triplet states estimated by TDDFT calculations (**Figure 4.3**). Hence, the development of an in-depth mechanism for mono-, bis- and tetraacylgermanes demands further investigation of the singlet-triplet channel branching after photoexcitation.

#### 4.3.5 Outlook: PLP-ESI-MS Cocktail-Experiments with Ortho-Substituted Tetraacylgermanes

The PLP-cocktail experiments of *ortho*-substituted tetraacylgermanes Mes<sub>4</sub>G and oMeB<sub>4</sub>G versus unsubstituted B<sub>4</sub>G are conducted at ~320 μJ/pulse with 90000 pulses, a repetition rate of 100 Hz, and excitation wavelengths between 400-430 nm within  $n\pi^*$ -bands of the corresponding initiators (refer to UV/Vis in **Figure A29**). The obtained  $G_{m/z0}^{X=}$  vs initial molar ratios-plots of a) oMeB<sub>4</sub>G:B<sub>4</sub>G and b) Mes<sub>4</sub>G:B<sub>4</sub>G are presented in **Figure 4.25**.

a)

b)

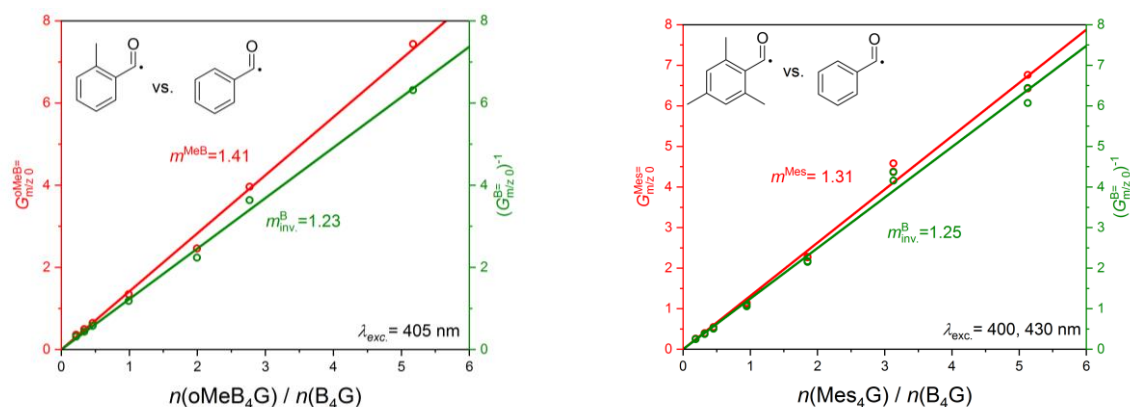


**Figure 4.25.**  $G_{m/z0}^X$  vs initial molar ratios-plots for cocktail experiments in MMA of a) oMeB<sub>4</sub>G:B<sub>4</sub>G and b) Mes<sub>4</sub>G:B<sub>4</sub>G, resulting in averaged overall initiation efficiencies of a)  $1.32 \pm 0.13$  and b)  $1.28 \pm 0.04$ , respectively. Excitation wavelength for PLP as indicated. Corresponding  $F$  versus DP plots are provided in **Figure A30** and **Figure A31**.

Both experiments reveal an increased overall initiation efficiency of  $\sim 1.3$  compared to the unsubstituted tetraacylgermane B<sub>4</sub>G. Thus, the substitution in *ortho*-position has an enhancing influence on the overall initiation efficiency of benzoyl radicals towards MMA. Possible reasons are influences of the substituents on the potential energy surfaces of the excited states, which lead to more favored reaction pathways (refer to **section 4.4.2**). In addition, steric aspects may be considered, especially for more bulky mesityl moieties.<sup>38</sup> Hence, a systematic investigation on *ortho*-substituted acylgermanes could be worthy for the future development of a more comprehensive mechanism supporting the guided design of more efficient photoinitiators.

#### 4.4 fs-TA Investigations on Acylgermanes

The aim of the present chapter is the development of an elementary mechanism for the excited state dynamics of acylgermane-initiators via time-resolved pump-probe experiments. As a special feature of the current work, mechanistic conclusions from time-resolved pump-probe experiments are related to fundamental structure/property correlations obtained from *post-mortem* PLP-ESI-MS of the previous section, e.g.  $\alpha$ -cleavage for efficient hypsochromic shifted monoacylgermanes with electron donating substitution pattern (+M-effect), weak initiation ability for bathochromic shifted monoacylgermanes with electron withdrawing substitution patterns (-M-effect), multiple cleavage mechanism of bis- and tetraacylgermanes, non-stoichiometric size-dependence in the overall initiation efficiency. The unique approach enables the characterization of behavior of initiators in photo-FRP from the first photoexcitation event to final macromolecular growth.

In the following, the results from fs-TA of mono- and tetraacylgermanes are presented to gain insight into excited state dynamics *in situ* after photo excitation. In an earlier study, B<sub>2</sub>G was investigated via fs- and ns-pump-probe spectroscopy, which shows a Norrish Type I mechanism via ISC within tens of ps and subsequent primary radical cleavage within tens of ns.<sup>43</sup>

The section opens with the investigation on the influence of substitution pattern on the electronic structure of monoacylgermanes, which leads to the development of a simple model in line with ultrafast dynamics of literature-known keto-based Norrish Type I photoinitiators.<sup>44</sup> Subsequently, the mechanism of more complex tetraacylgermanes is developed. Finally, findings from literature<sup>43</sup> for B<sub>2</sub>G are consulted for the comparison of the excited state dynamics of mono-, bis- and tetraacylgermanes.

#### 4.4.1 *para*-Substitution Pattern-Dependent Photophysics of Monoacylgermane Derivatives

The steady-state absorption spectra of FB<sub>1</sub>G, MB<sub>1</sub>G, B<sub>1</sub>G, CB<sub>1</sub>G, NB<sub>1</sub>G dissolved in MeOH and recorded in 1 mm cuvettes as used for fs-TA are presented in **Figure 4.26**.

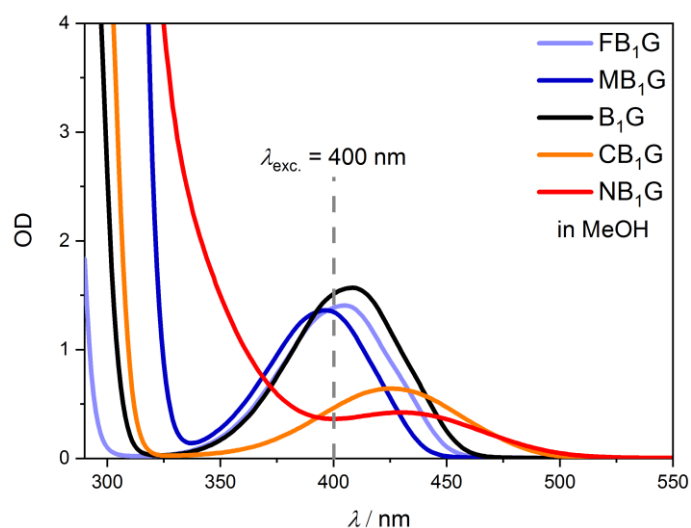


**Figure 4.26.** Steady-state UV/Vis spectra of FB<sub>1</sub>G, MB<sub>1</sub>G, B<sub>1</sub>G, CB<sub>1</sub>G, NB<sub>1</sub>G dissolved in methanol (MeOH) and recorded in 1 mm cuvettes as used for fs-TA. Transient broadband pump-probe experiments are carried out at 400 nm within the  $n\pi^*$ -bands of the investigated initiators as indicated by grey dashed line. Adapted with permission from ref. 144. Copyright 2017 American Chemical Society. Modified presentation.

As indicated by blue colors in **Figure 4.26**, FB<sub>1</sub>G ( $\lambda_{\max} = 405$  nm) and MB<sub>1</sub>G ( $\lambda_{\max} = 397$  nm) show a hypsochromic shift of  $n\pi^*$ -bands compared to B<sub>1</sub>G ( $\lambda_{\max} = 409$  nm) due to electron donating *para*-substitution patterns F and OMe (+M-effect). The electron withdrawing substitution patterns CN and NO<sub>2</sub> (-M-effect) leading to a bathochromic shift of the  $n\pi^*$ -bands in the absorption spectra of CB<sub>1</sub>G ( $\lambda_{\max} = 425$  nm) and NB<sub>1</sub>G ( $\lambda_{\max} = 429$  nm) compared to B<sub>1</sub>G ( $\lambda_{\max} = 409$  nm) is indicated by orange and red colors in **Figure 4.26**. As shown in **section 4.2.1**, B<sub>1</sub>G, FB<sub>1</sub>G and MB<sub>1</sub>G are efficient photoinitiators, while CB<sub>1</sub>G and NB<sub>1</sub>G feature only weak initiation behavior for FRP. In contrary, it is highly desired to combine the properties of a red shifted absorption with high initiation efficiency, e.g. to achieve higher penetration-depths in curing technologies. The reason for the observed substitution pattern-dependent behavior is presumed in the excited state dynamics due to similar band structure of the steady-state absorption spectra as well as in line with findings from cocktail experiments above (**section 4.3**). From a TDDFT study on the five monoacylgermanes by Feuerstein *et al.*,<sup>31</sup> a strong influence of substitution pattern on the shape and location of the potential energy surfaces is expected. In the following, the photophysics of five monoacylgermanes B<sub>1</sub>G, FB<sub>1</sub>G, MB<sub>1</sub>G, CB<sub>1</sub>G and NB<sub>1</sub>G dissolved in methanol (MeOH) are investigated via fs-TA and compared with findings from theory. All initiators are pumped at 400 nm within their  $n\pi^*$ -band (indicated by grey line in **Figure 4.26**) and probed with a CaF<sub>2</sub>-white light continuum between 350-720 nm.

### fs-TA of Efficient Monoacylgermanes B<sub>1</sub>G, FB<sub>1</sub>G and MB<sub>1</sub>G

The transient absorption (TA)-spectra of the efficient monoacylgermanes B<sub>1</sub>G, FB<sub>1</sub>G and MB<sub>1</sub>G with electron donating substituents (+M-effect) are recorded in methanol (MeOH) after excitation at 400 nm within their  $n\pi^*$ -band and probing with CaF<sub>2</sub>-white light continuum of 350-720 nm. The TA-spectrum of B<sub>1</sub>G is exemplary for the investigated efficient monoacylgermanes, which is depicted in **Figure 4.27** (TA-spectra of MB<sub>1</sub>G, FB<sub>1</sub>G in appendix Figure A33 and **Figure A34**).

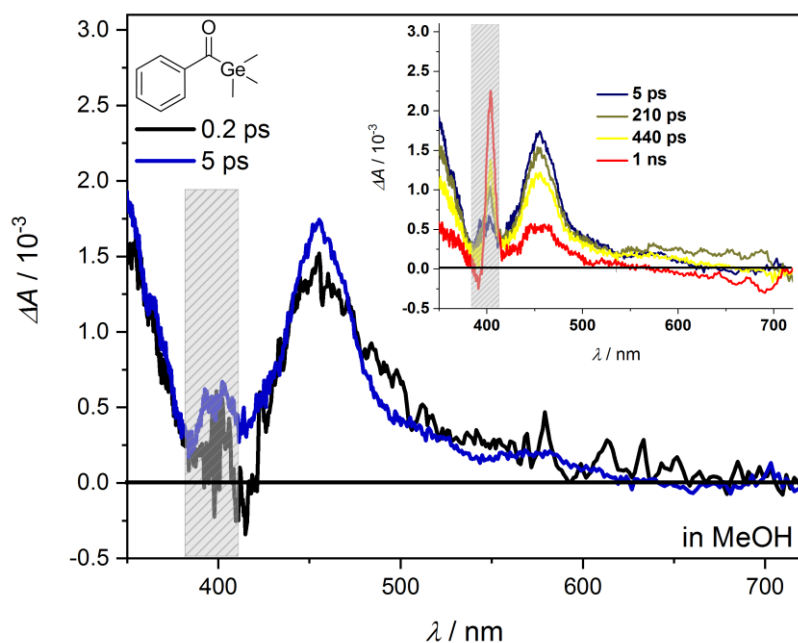


**Figure 4.27.** Transient broadband absorption spectrum of B<sub>1</sub>G for the first ps and longer delay times (inset) after excitation at 400 nm and probing with a CaF<sub>2</sub>-white light continuum from 350-720 nm. Time delays as indicated. Transient response at 400 nm omitted due to scattering from pump pulse. Adapted with permission from ref. 144. Copyright 2017 American Chemical Society. Modified presentation.

For clarity reasons, transient responses in the region of ~400 nm are omitted due to strong scattering artifacts from pump pulse with a spectral width of ~10 nm.

The TA spectrum of B<sub>1</sub>G is dominated by an ultrafast rise of an ESA-band at a center wavelength of ~450 nm within a few ps (**Figure 4.27**). Subsequently, the band decays slowly within the recorded time window (inset of **Figure 4.27**). A second strong ESA-band at ~350 nm shows a similar transient behavior of an ultrafast rise and slow decay. Thus, both transient responses are associated with the dynamics of the same excited state, which is probed into diverse higher energy levels. In line with theory,<sup>31</sup> a manifold of higher excited singlet and triplet states is accessible, which leads to a broad ESA-band between 350 to 500 nm. In fact, decreased ESA in the range of 370-425 nm is probably a result from superposition with the scattering of the pump pulse and GSB responses from depopulated ground states.

Consistent with very low fluorescence quantum yields  $< 5 \cdot 10^{-4}$ ,<sup>31</sup> no significant SE is observed within the detection limit of  $1:10^4 \Delta A$ . For instance, the apparent negative response at ~700 nm at long time scales is an artifact from white light fluctuations. In

addition, possible singlet relaxation pathways would lead to a change in the GSB in the region of the ground state absorption band of 360-440 nm. In contrast, no significant ground state recovery is observed for single transient response at 420 nm (**Figure A32**). Thus, dominant long-living singlet state dynamics can be excluded due to weak fluorescence and no complete GSB recovery. In turn, the observed ESA-band is assigned to the response of a triplet state. Consequently, the ultrafast rise reflects the ISC from excited singlet to triplet states, while the slow decay corresponds to the triplet relaxation.

An ultrafast ISC is in line with TDDFT calculations<sup>31</sup> showing two close and below lying triplet states in relation to the first excited singlet state. In addition, an energetically higher triplet manifold is accessible for broad resonant transitions. A clear differentiation between responses of  $T_1$  and  $T_2$  is not possible due to numerous similar resonant transitions into the manifold of energetically higher triplet states. Hence, the decay of ESA of the corresponding triplet states can occur via different possible relaxation pathways: (i) IC between  $T_1$  and  $T_2$ , (ii) formation of radical fragments, and (iii) additional relaxation from quenching processes. An earlier study on benzoin-based Norrish Type I initiators shows a fast triplet relaxation within tens of ps, which was interpreted as radical formation.<sup>35</sup> In contrast, the slow triplet relaxation of monoacylgermanes implies a considerably longer time scale  $> 1$  ns for the radical formation. Thus, the quantification of cleavage quantum yields by evaluation of amplitude ratios is challenging due to a not fully accessible decay of triplet states within the recorded time window.

Qualitatively, radical formation on a time scale longer than 1 ns for monoacylgermanes is consistent with low decomposition quantum yields of 0.21-0.4<sup>38-39</sup> as well as their weak performance in size-dependent PLP-ESI-MS cocktail experiments (**section 4.3**). As a possible reason, small energy barriers for dissociation of 0.31-0.39 eV within the excited triplet states of MB<sub>1</sub>G, FB<sub>1</sub>G and B<sub>1</sub>G are expected from theory,<sup>31</sup> which leads likely to a non-quantitative cleavage due to competing relaxation pathways. Nevertheless, by neglecting competing singlet relaxation pathways, a mono exponential transient behavior can be assumed for the quantification of the increase of triplet ESA according to ISC time constant  $\tau_{ISC}$ . Thus, single transient responses of B<sub>1</sub>G, FB<sub>1</sub>G and MB<sub>1</sub>G are evaluated in the range of 415-450 nm (**Figure A32-Figure A34**). The rise of triplet state-ESA between 515 to 450 nm is

superimposed by VR as depicted in **Figure A32b**). However, TA responses  $\geq 450$  nm are presumably unaffected from VR and are exploited by an exponential fitting routine. The obtained ISC time constants  $\tau_{ISC}$  for B<sub>1</sub>G, MB<sub>1</sub>G and FB<sub>1</sub>G are between 2-4 ps.

In opposition to structurally similar acylphosphine oxides,<sup>153</sup> efficient monoacylgermanes with electron donating substitution patterns are considered to undergo an efficient ultrafast ISC, while the radical formation from triplet state is in comparably slower. Consequently, the cleavage is plausibly rather inefficient due to competing radiationless relaxation pathways, e.g. T<sub>1</sub>-T<sub>1</sub> or T<sub>1</sub>-S<sub>0</sub> collision-induced relaxation on a post-ns time scale. The obtained photophysical dynamics are schematically summarized in a Jabłoński -diagram **Figure 4.28**.

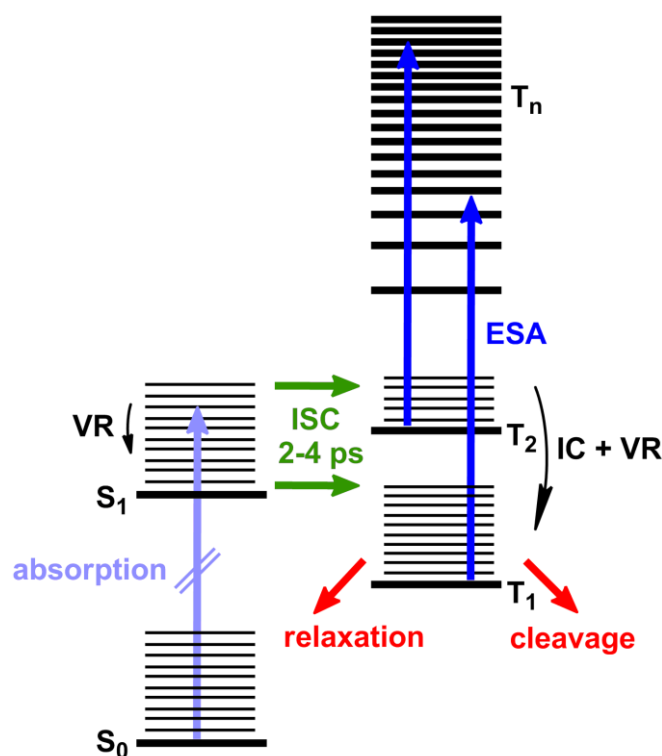


**Figure 4.28.** Jabłoński diagram depicting schematically the photophysical mechanism for efficient initiators B<sub>1</sub>G, MB<sub>1</sub>G and FB<sub>1</sub>G. After excitation into a vibrational hot excited singlet state, an ultrafast ISC occurs within 2-4 ps. Broad ESA from T<sub>1</sub> and T<sub>2</sub> into a manifold of energetically higher triplet states is observed. Decay of triplet population can proceed via  $\alpha$ -cleavage or radiationless relaxation. Adapted with permission from ref. 144. Copyright 2017 American Chemical Society. Modified presentation.

## Transient Broadband Absorption Spectroscopy of Weak Monoacylgermanes CB<sub>1</sub>G and NB<sub>1</sub>G

TA-spectra of weak monoacylgermanes with electron withdrawing substitution patterns (-M-effect) CB<sub>1</sub>G and NB<sub>1</sub>G dissolved in MeOH are conducted after excitation at 400 nm and probing with a white light continuum between 350-720 nm. In general, the TA-spectra of CB<sub>1</sub>G and NB<sub>1</sub>G show one order of magnitude higher  $\Delta A \sim 1 \cdot 10^{-2}$  at lower optical densities  $OD_{400\text{nm}} \sim 0.4$  compared to efficient monoacylgermanes MB<sub>1</sub>G, FB<sub>1</sub>G and B<sub>1</sub>G  $\sim 2 \cdot 10^{-3}$  at  $OD_{400\text{nm}} \sim 1.4$ . The recorded TA-spectra of CB<sub>1</sub>G and NB<sub>1</sub>G are presented in **Figure 4.29** and **Figure 4.31**, respectively.

### CB<sub>1</sub>G

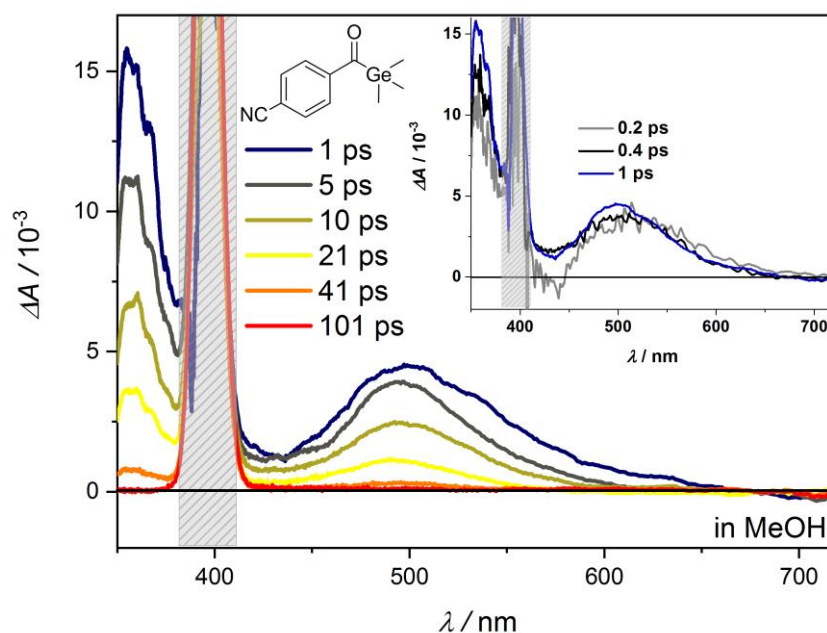


**Figure 4.29.** Transient broadband absorption spectrum of a) CB<sub>1</sub>G recorded after excitation at 400 nm and probing with a CaF<sub>2</sub>-white light continuum from 350 to 720 nm. Time delays as indicated. Transient response at 400 nm omitted due to scattering from pump pulse. Adapted with permission from ref. 144. Copyright 2017 American Chemical Society. Modified presentation.

Two broad ESA-bands are revealed for the TA spectrum of CB<sub>1</sub>G within a few hundred fs after excitation at 400 nm: The first in the UV range  $\sim 360$  nm and the second in the visible range at 500 nm (**Figure 4.29 inset**). Both ESA-bands decay to zero within  $\sim 13$  ps (refer to **Figure 4.29** and **Figure A35b, c**). In line with the discussion above, the ESA in the wavelength range close to 400 nm is superimposed by GSB

and scattering from pump pulse. Thus, both ESA-bands likely reflect the transient response of the same excited state, which is probed into different higher lying states. By inspecting the GSB response at 420 nm, a complete ground state recovery is observed (**Figure A35a**). As expected from theory, the potential energy minimum of the first excited singlet state comes relatively close to the ground state surface of CB<sub>1</sub>G and NB<sub>1</sub>G, which increases the probability for relaxation via IC in competition with an ISC.<sup>31</sup> In contrast to efficient monoacylgermanes, after ultrafast rise of ESA, no long-living contribution from a triplet state is observed. Thus, the broad ESA can be straight forwardly assigned to singlet state dynamics.

In addition, SE is revealed at ~700 nm with a short lifetime of ~8 ps (refer to exponential fitting in **Figure A35d**), which is in line with a theoretically estimated fluorescence channel of CB<sub>1</sub>G in the range of 600-800 nm with very low quantum yields.<sup>31</sup> SE is a very minor relaxation pathway due to 1-2 orders of magnitude weaker  $|\Delta A|$  in comparison to ESA at 500 and 360nm, respectively. In conclusion, the decay of ESA within 13 ps corresponds to relaxation of an excited singlet state back to ground state via dominant IC and minor fluorescence pathways. The photophysical mechanism of CB<sub>1</sub>G is depicted in a Jabłoński diagram in **Figure 4.30**.

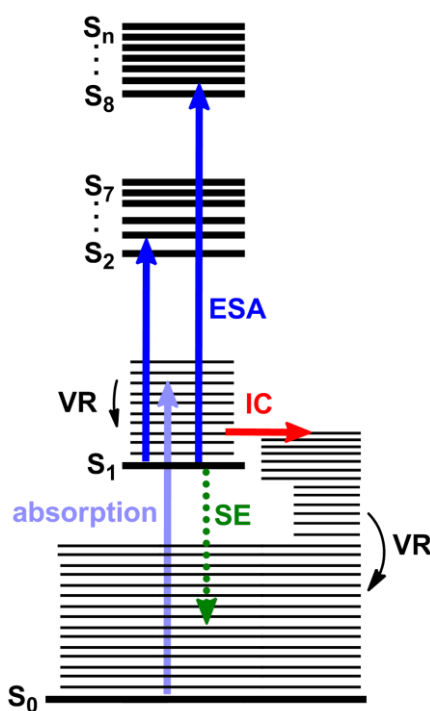


**Figure 4.30.** Jabłoński diagram depicting schematically the photophysical mechanism of the weak initiator CB<sub>1</sub>G. After excitation into a vibrational hot excited singlet state, a ground state recovery occurs within ~13 ps. The major relaxation pathway occurs via radiationless IC. A minor fluorescence pathway is observed via a very weak SE-response. Adapted with permission from ref. 144. Copyright 2017 American Chemical Society. Modified presentation.

## NB<sub>1</sub>G

Analogous to the TA-behavior of CB<sub>1</sub>G, the TA-spectrum of NBG shows a broad bi-modal ESA-band immediately after excitation peaking at ~400 and ~680 nm, which decays within a few ps (**Figure 4.31**).

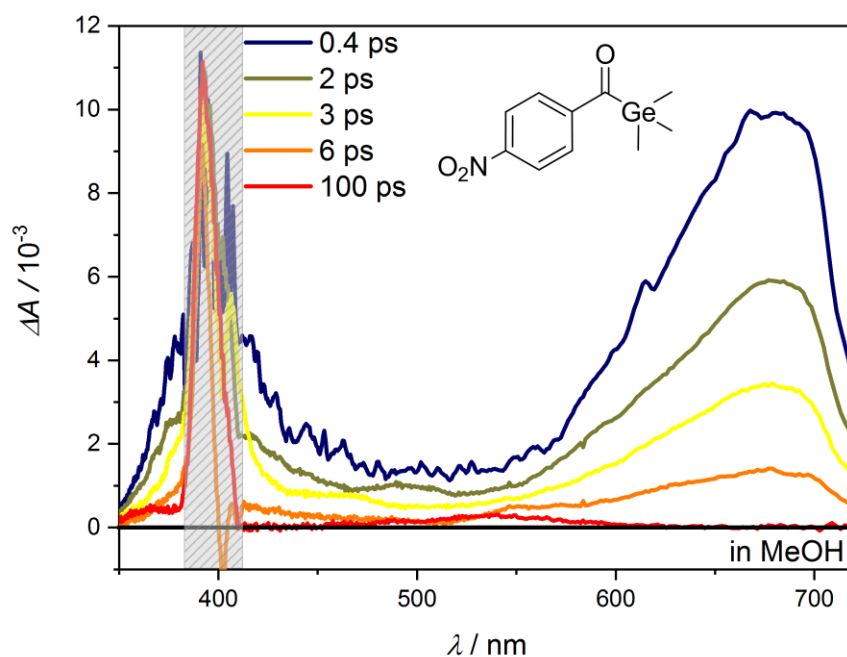


**Figure 4.31.** Transient broadband absorption spectrum of NB<sub>1</sub>G recorded after excitation at 400 nm and probing with a CaF<sub>2</sub>-white light continuum from 350-720 nm. Time delays as indicated. Transient response at 400 nm omitted due to scattering from pump pulse. Adapted with permission from ref. 144. Copyright 2017 American Chemical Society. Modified presentation.

The bimodal ESA-band corresponds to transient responses of the same excited state superimposed by GSB and scattering of the pump pulse at 400 nm, which reveal full ground state recovery in the range of expected GSB at 420 nm as indicated by **Figure A36a**). Thus, ESA of NB<sub>1</sub>G can clearly be assigned to the ultrafast decay of an excited singlet state. In contrast to a factor ~6 longer S<sub>1</sub>-lifetime for CB<sub>1</sub>G, the majority of the population in excited singlet state of NB<sub>1</sub>G decays via an ultrafast IC on a time scale within ~2 ps (estimated via a triexponential fitting routine, refer to **Figure A36b**)). Referring to a fs-study on *ortho*-nitro-phenol, an ultrafast IC within a few hundreds of fs after out-of-plane rotation of the nitro group was reported.<sup>53, 154</sup> Accordingly, motions of nitro groups have a strong influence on the potential energy surface landscape, which could result in an ultrafast relaxation pathway preferred via

conical intersection. Thus, the ultrafast  $S_1$ -relaxation of  $NB_1G$  via IC within  $\sim 2$  ps is plausibly induced by degrees of freedom of the nitro group leading to non-adiabatic phenomena.

A second ESA-band is observed for  $NB_1G$ , which peaks at 550 nm after a rise of  $\sim 10$  ps. However, this process is very minor compared to at least one order of magnitude higher IC. TDDFT-calculations from literature show that triplet transitions for  $NB_1G$  are strongly red shifted compared to  $CB_1G$ , which features up to six triplet states accessible between  $S_1$  and  $S_2$  for  $NB_1G$ . Thus, a small ISC-probability can be expected after excitation at 400 nm into the vibrational hot Franck-Condon region of  $S_1$ . However,  $NB_1G$  will not perform as an efficient initiator due to comparatively high energy barriers expected for dissociation from triplet states. Possible triplet-triplet or triplet-singlet collision induced relaxation pathways would occur on a longer time scale. Unfortunately, the latter two relaxation processes cannot be resolved within the current data set. The photophysical processes of  $NB_1G$  are summarized in **Figure 4.32**.

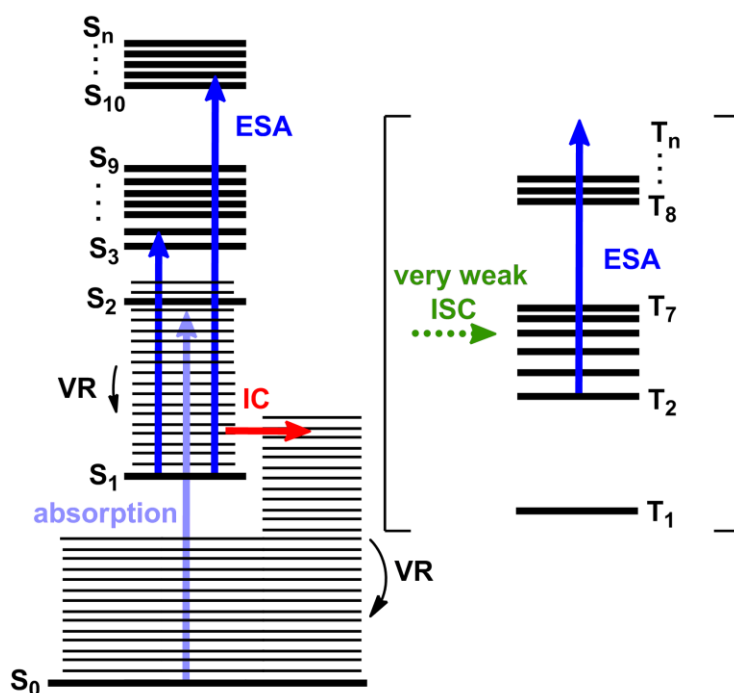


**Figure 4.32.** Jablonski diagram depicting schematically the photophysical mechanism of the weak initiator  $NB_1G$ . After excitation to an excited singlet state, the ground state recovers within  $\sim 2$  ps via ultrafast IC. A very minor relaxation pathway is featured via ISC in  $\sim 10$  ps. Adapted with permission from ref. 144. Copyright 2017 American Chemical Society. Modified presentation.

## Summary: Substitution effects on monoacylgermanes

Efficient initiators FB<sub>1</sub>G, MB<sub>1</sub>G, B<sub>1</sub>G with electron donating substituents (+M-effect) compared to weak initiators CB<sub>1</sub>G, NB<sub>1</sub>G with electron withdrawing substituents (-M-effect) show striking differences in their photophysical mechanisms. As expected for Norrish type I initiators,<sup>44</sup> efficient monoacylgermanes reveal an ultrafast ISC within 2-4 ps after photoexcitation. However, the formation of radicals occur on a much longer time scale > 1 ns, which is in line with rather low decomposition quantum yields from literature 0.2-0.4<sup>38-39</sup> as well as with the low overall initiation efficiency in PLP-cocktail experiments with bis- and tetraacylgermanes (refer to **section 4.3**). Thus, a competing radiationless relaxation pathway from triplet states is expected. In contrast, weak monoacylgermanes feature an ultrashort dominant non-radiative relaxation within 2-13 ps via IC from excited singlet to ground states. In fact, radiationless deactivation becomes more likely if excited state potential energy surfaces coming close to the ground state surface, which is in line with expectations from TDDFT calculations of CB<sub>1</sub>G, NB<sub>1</sub>G compared with FB<sub>1</sub>G, MB<sub>1</sub>G, B<sub>1</sub>G.<sup>31</sup> In summary, *para*-substitution patterns have a strong influence on the potential energy surface landscape of monoacylgermanes, which determines whether an initiator is efficient or weak. Remarkably, the crucial mechanistic steps for an efficient photo FRP occur on a ps time scale after photoexcitation, e.g. ultrafast ISC versus IC channel branching within the excited states of a photoinitiator.

### 4.4.2 Efficient Tetraacylgermanes

As expected by TDDFT-calculations (refer to **section 4.1.1**), tetraacylgermanes reveal a more complex channel branching within excited states due to higher number of benzoyl moieties. Based on a PLP-ESI-MS prediction method (refer to **section 4.2.3**), the formation of 4-armed star polymers is evidenced. Remarkably, a non-stoichiometric increase of up to 100 % is observed for the overall initiation efficiency of tetraacylgermanes. The non-stoichiometric increase is only partially correlated to ground state extinction coefficients. Especially for substituted acylgermanes higher differences are observed. As seen from the previous **section 4.4.1**, substitution patterns in *para*-position of the phenyl-ring have a strong influence on the potential energy surfaces of benzoyltrimethylgermanes. In the following, a model for the photo-physics of efficient tetraacylgermanes is developed on B<sub>4</sub>G, oMeB<sub>4</sub>G, oEtB<sub>4</sub>G and PrOB<sub>4</sub>G solved in AcN via fs-TA. Subsequently, the differences within the channel

branching of tetraacylgermanes with different substitutions are discussed quantitatively.

The UV/Vis-spectra of  $B_4G$  ( $\lambda_{\max} = 402$  nm),  $oMeB_4G$  ( $\lambda_{\max} = 404$  nm),  $oEtB_4G$  ( $\lambda_{\max} = 403$  nm) and  $PrOB_4G$  ( $\lambda_{\max} = 391$  nm) dissolved in AcN and recorded in 1 mm cuvettes as used for fs-TA are depicted in **Figure 4.33**.

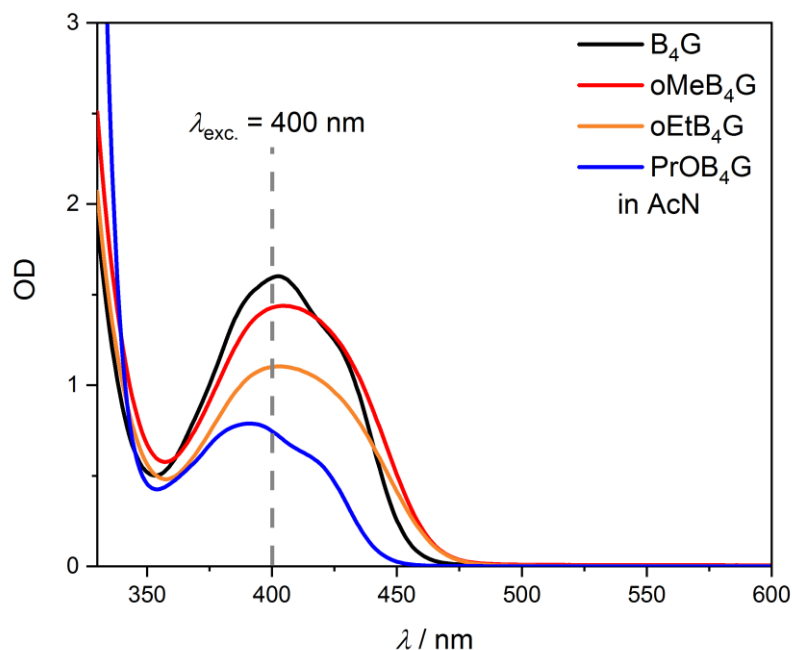


**Figure 4.33.** Steady-state UV/Vis spectra of  $B_4G$ ,  $oMeB_4G$ ,  $oEtB_4G$  and  $PrOB_4G$  dissolved in acetonitrile AcN and recorded in 1 mm cuvettes as used for fs-TA. fs-TA experiments are carried out at 400 nm pump within the  $n\pi^*$ -bands of the investigated initiators as indicated by grey dashed line.

All samples are excited at 400 nm and probed with a  $CaF_2$ -white light continuum between 350 and 720 nm. The TA-spectrum of  $B_4G$  dissolved in AcN is exemplary for the investigated tetraacylgermanes, which is presented in **Figure 4.34**. The TA-spectra of  $oMeB_4G$ ,  $oEtB_4G$  and  $PrOB_4G$  dissolved in AcN are provided in the appendix **Figure A38-Figure A40**.

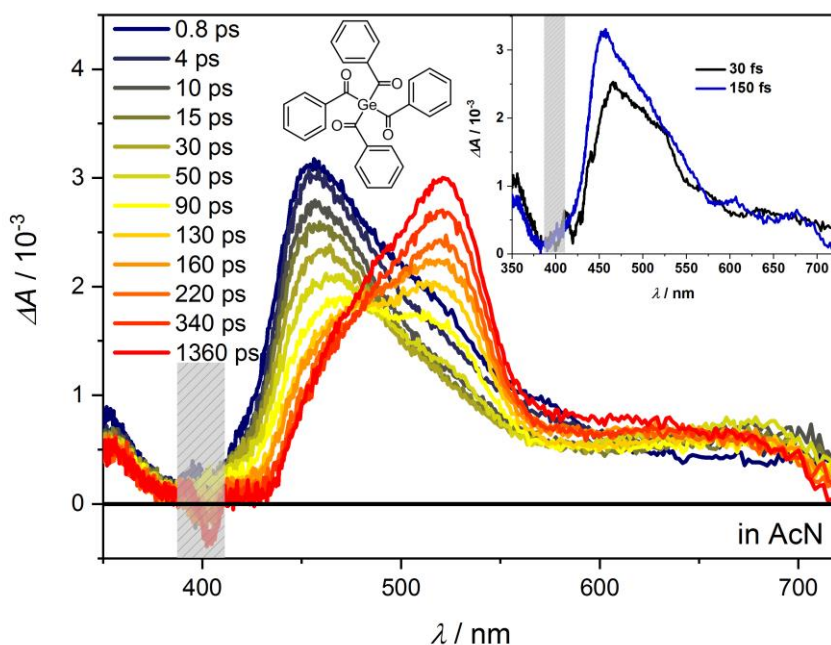


**Figure 4.34.** B<sub>4</sub>G dissolved in AcN excited at 400 nm and probed by a CaF<sub>2</sub>-white light continuum between 350-720 nm. The wavelength region at ~400 nm is omitted due to scattering from pump pulse. Time delays as indicates. Inset figure shows TA-spectra for very early times after excitation.

After excitation, an ultrafast rise of ESA within the time-resolution < 100 fs is recorded (**Figure 4.34 inset**). After 150 fs, an ESA-band at ~350 nm and a broadened ESA-band between ~430-600 nm are observed. In addition, a broad flat ESA-band without distinct peaking is revealed from 550-720 nm, which probably superimposes the entire TA-spectrum. As depicted in **Figure 4.34**, the ESA between 430 and 600 nm undergoes a fast decay within tens of ps resulting in a less broadened band peaking at ~450 nm. Subsequently, a slower decrease on a hundreds-of-ps time scale occurs, which is related to a new increasing band at ~520 nm indicated by an isosbestic point at ~480 nm. The additional band shows no decay within the recorded time window of ~1.3 ns. The band at 350 nm is dominantly a superposition of the fast decrease within tens of ps and the long-living ESA, which remains within the recorded time window. The flat band between 550-720 nm also remains within the recorded time window. However, in relation to the increase of the additional ESA-band at ~520 nm, a slight rise at ~600 nm is observed accompanied by a decrease at ~680 nm at long time scales within the flat band. Thus, a second isosbestic point is supposed at ~650 nm. In summary, the spectrum is generally dominated by three processes i) fast decay in tens of ps, ii) decay at ~450 nm correlated to an rise of

ESA at  $\sim 520$  nm, iii) long-lasting broad ESA. Hence, global analysis with three exponential functions is applied for a quantitative discussion. The resulting DAS is presented in **Figure 4.35**.

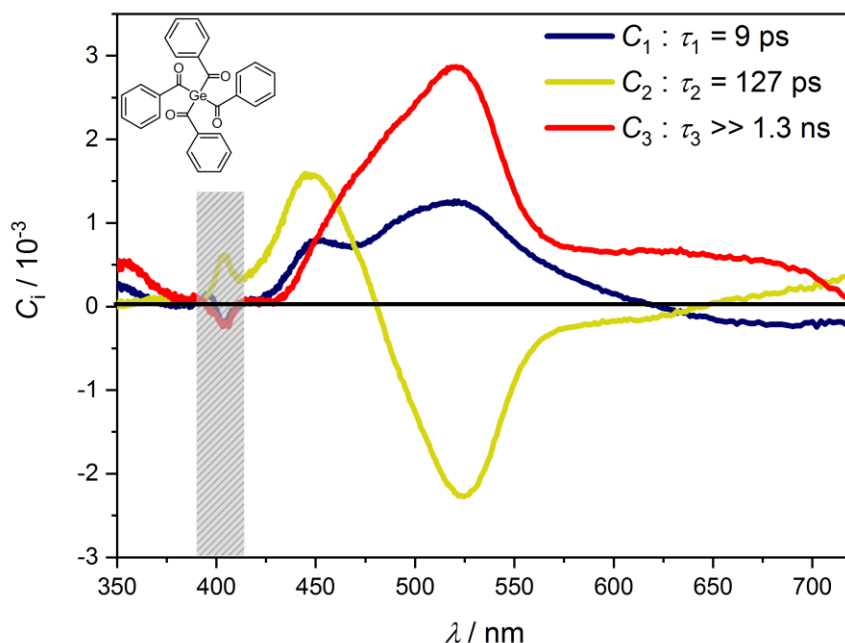


**Figure 4.35.** DAS derived from triexponential global analysis of the TA-spectrum of B<sub>4</sub>G dissolved in AcN. Time constants according to three exponential functions as indicated.

A negative amplitude  $C_i$  is related to an increasing, and a positive as a decreasing, transient response, respectively. A zero-crossing can be interpreted as an isosbestic point. In comparison, all features of the TA-spectrum of B<sub>4</sub>G in **Figure 4.34** are well represented with three exponential functions.  $C_1$  reflects the fast decay of ESA between 350 and 600 nm within 9 ps, which is correlated to an increasing TA-band at 620-720 nm. The risen ESA remains within the recorded time window as indicated by  $C_3$  (compare with single transient at 675 nm, **Figure A37**). In line with low fluorescence quantum yields of B<sub>4</sub>G, the first process can be assigned to the decay of the singlet state. As a consequence, the associated rise at 620-720 nm is interpreted as ISC into a long-living triplet state within 9 ps. In addition, no ground state recovery is observed in the region of GSB between 370 and 430 nm, which features IC and fluorescence as very minor competing relaxation pathways compared to a dominant ISC. Hence, the TA for recorded spectra after  $\sim 9$  ps can be interpreted as ESA of triplet states probed into a higher lying manifold of triplet states, which is in line with TDDFT calculations (refer to **section 4.1.1**).  $C_2$  is associated to the decrease of triplet ESA

peaking at ~450 nm, which is correlated to the rise of an additional band with its maximum at ~520 nm within 127 ps indicated by a zero-crossing, resp. isosbestic point at ~480 nm. In addition, the decrease of triplet ESA between 650 and 720 nm can be assigned to the same process, which is correlated to C<sub>2</sub> as displayed by a second isosbestic point at ~650 nm. Thus, a new species is formed from triplet states within ~127 ps, which remains on ns-time scale > 1.3 ns as indicated by C<sub>3</sub>. The comparison of TA-spectrum of B<sub>4</sub>G after 1.3 ns with the TA-spectrum of tribenzoylgermyl- (B<sub>3</sub>G·) radical, which is recorded in a recent ns-laser flash photolysis study,<sup>38</sup> features a striking accordance as shown in **Figure 4.36a**).

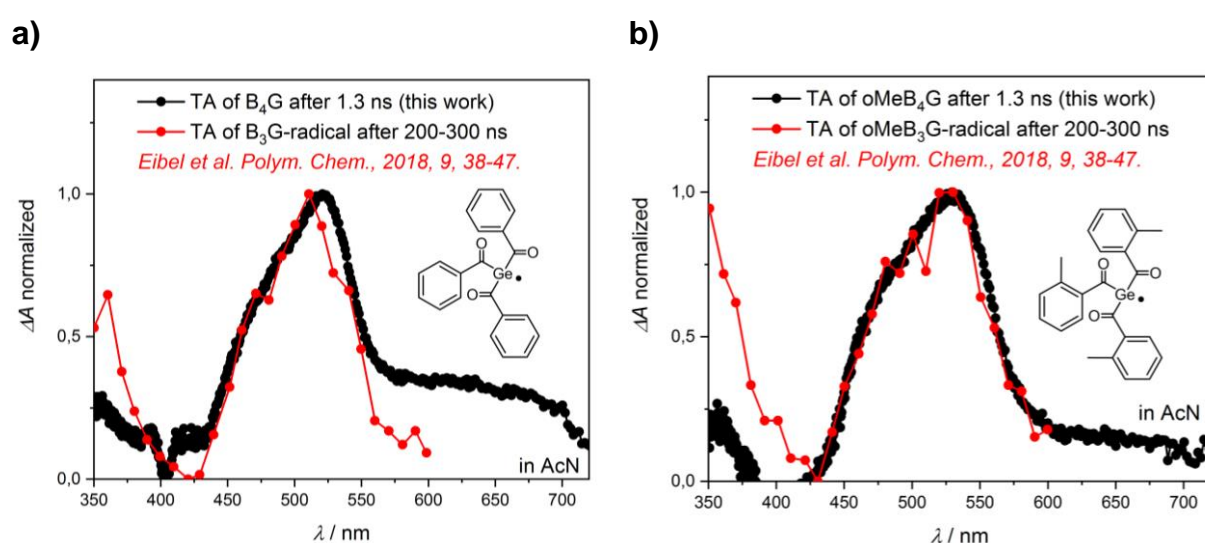


**Figure 4.36.** TA-spectra recorded in AcN after 1.3 ns in black of a) B<sub>4</sub>G and b) oMeB<sub>4</sub>G and literature-known TA-spectrum from ns-laser-flash photolysis within 200-300 ns in red<sup>38</sup> of a) of tribenzoylgermyl- (B<sub>3</sub>G·) and b) ortho-methylbenzoylgermyl- (oMeB<sub>3</sub>G·) radical. The striking accordance of the two TA-spectra for a) and b) evidence the primary radical formation within the time scale of the fs-pump-probe experiment. Data in red is reproduced from ref. 38 by permission of The Royal Society of Chemistry and the authors.

Thus, C<sub>2</sub> corresponds plausibly to the primary  $\alpha$ -cleavage of B<sub>4</sub>G within 127 ps under formation of a tribenzoyl germyl radical with a lifetime > 1.3 ns. As a further evidence, the TA-spectrum of oMeB<sub>4</sub>G in AcN reveals a similar channel branching as B<sub>4</sub>G and can analogously be discussed (refer to appendix **Figure A38**). In fact, the transient response of oMeB<sub>4</sub>G in AcN recorded after 1.3 ns is consistent with the ns-TA-spectrum of the tri-*ortho*-methylbenzoylgermyl- (oMeB<sub>3</sub>G·) radical from literature (**Figure 4.36b**). Further TA-spectra of the tetraacylgermanes oEtB<sub>4</sub>G and pPrOB<sub>4</sub>G are also in line with the discussion above (refer to appendix **Figure A39** and **Figure A40**). Unfortunately, reference spectra for evidencing the primary radicals originated from oEtB<sub>4</sub>G and pPrOB<sub>4</sub>G are not provided by literature.

The obtained photophysics of the investigated tetraacylgermanes are summarized in a Jabłoński-Diagram as follows in **Figure 4.37**.

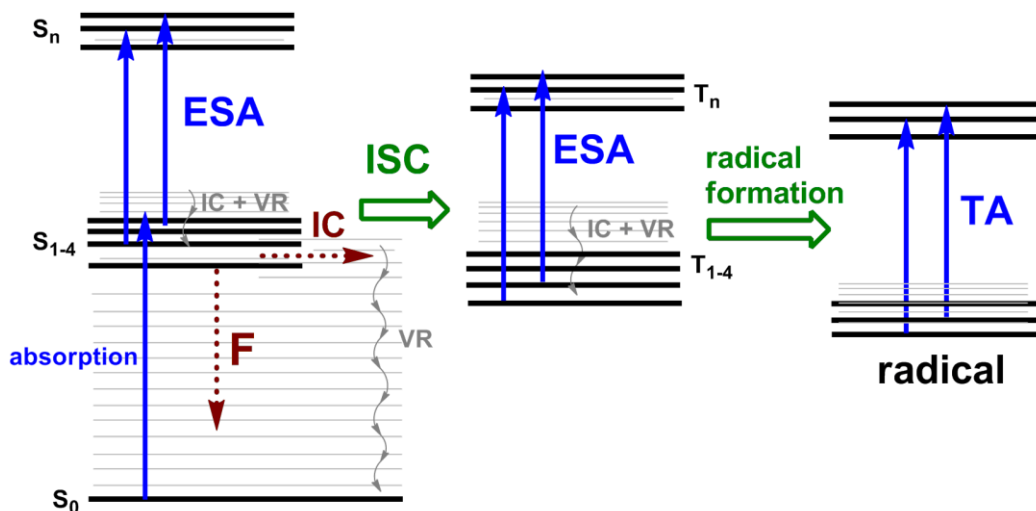


**Figure 4.37.** Jabłoński diagram depicting schematically the photophysical mechanism of the tetraacylgermanes. After excitation, the quasi-degenerated excited singlet states are depopulated dominantly via ISC into a triplet state within ~10 ps. Minor competing relaxation pathways are fluorescence and IC. After ~100 ps, radicals are formed from excited triplet states, which are probed into higher excited states.

The formation of the radical is not a quantitative process due to remaining ESA of the triplet state of  $B_4G$  at 350 nm as well as between 650 and 720 nm. At ~430 nm, the triplet ESA is free from a superposition with the transient response of the radical and decays in correlation to the radical formation to  $\Delta A$  close to zero (**Figure 4.38**).

However, the region between 370 and 430 nm is superimposed by GSB of  $B_4G$  (refer to **Figure 4.33**), which contributes with a negative  $\Delta A$ . A ground state recovery is not observed between 370 and 430 nm, which leads to the assumption of an approximately constant negative GSB offset on the triplet ESA. Herein, the TA at ~430 nm can be exploited for determination of cleavage quantum yields by comparison of the amplitudes according to the decay of the triplet ESA (related with radical formation) and the remaining ESA of the long-living triplet state. Hence, by assuming an approximately constant negative value for the GSB, the averaged ratio  $\frac{C_2}{C_2+C_3}$  from DAS between 415 and 430 nm reflects a primary cleavage quantum yield of 90 %. With respect to scattering from pump pulse, the primary cleavage quantum yields are analogously determined for oMe $B_4G$  (427-430 nm), and oEt $B_4G$  (415-430 nm). The evaluation of the primary cleavage quantum yield pPrOB $_4G$  is not accessible due to superposition with bathochromic shifted TA of the primary radical (refer to **Figure A40**).

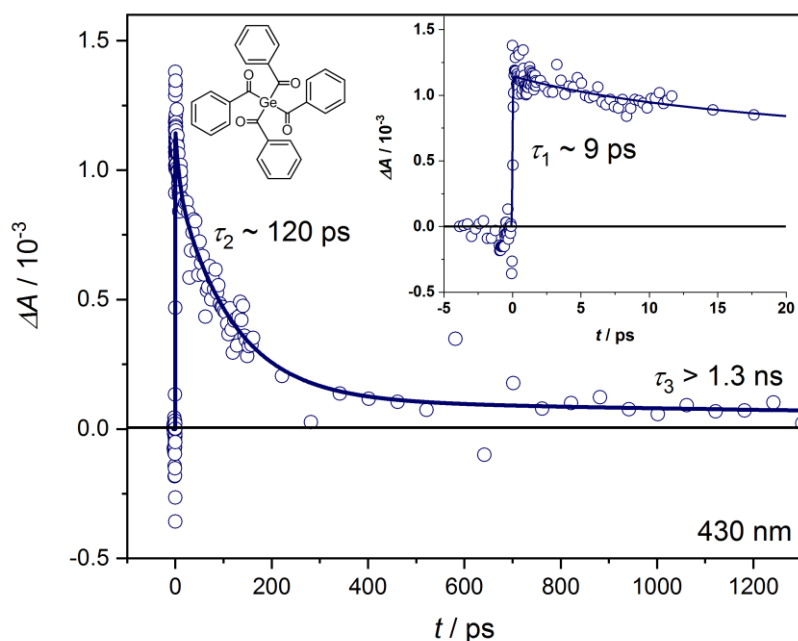


**Figure 4.38.** Example single transient response at 430 nm of B<sub>4</sub>G in AcN after excitation at 400 nm for the determination of primary cleavage quantum yields between 415 and 430 nm. Assuming a constant GSB offset due to negligible ground state recovery, the exploited wavelength reflects only the decay of triplet states. Hence,  $\tau_2$  is associated to the decay of triplet states according to primary radical formation, while  $\tau_3$  is related to the remaining long-living triplet state. Thus, the primary cleavage quantum yields can be obtained by averaging the ratio of the corresponding amplitudes given by  $\frac{c_2}{c_2+c_3}$  from DAS between 415 and 430 nm.

In **Table 4.10**, the time constants from global analysis, cleavage quantum yields, as well as estimated primary cleavage rate coefficients are summarized for the comparison of B<sub>4</sub>G, oMeB<sub>4</sub>G, oEtB<sub>4</sub>G, and pPrOB<sub>4</sub>G.

**Table 4.10.** Time constants from global analysis, primary cleavage quantum yields and rate coefficients of B<sub>4</sub>G, oMeB<sub>4</sub>G, oEtB<sub>4</sub>G, and pPrOB<sub>4</sub>G.

Initiator in AcN	$\tau_1$ / ps	$\tau_2$ / ps	$\tau_3$ / ps	$\Phi_{\text{cleav.}} / \%$	$k_{\text{cleav}} = \frac{\Phi_{\text{cleav}}}{\tau_2} / 10^9 \text{ s}^{-1}$
B <sub>4</sub> G	9	127	>> 1300	90	$7 \pm 2$
oMeB <sub>4</sub> G	4	127	>> 1300	95	$8 \pm 2$
oEtB <sub>4</sub> G	3	90	>> 1300	78	$9 \pm 3$
pPrOB <sub>4</sub> G	1	70	>> 1300	n.A.	n.A.

The first time constants decrease from 9 to 1 ps in the line of B<sub>4</sub>G > oMeB<sub>4</sub>G > oEtB<sub>4</sub>G > pPrOB<sub>4</sub>G, which are associated with the decay of the excited singlet states via competing IC, fluorescence and ISC-relaxation channels. In line with a very weak fluorescence quantum yield << 0.01 % (refer to **section 4.1.1**), a ground state-

recovery is not observed, which features IC as well as fluorescence as only minor relaxation pathways. Thus,  $\tau_1$  dominantly reflects ISC, which is in a similar order of magnitude as the ISC of efficient monoacylgermanes within 2-4 ps (refer to **section 4.4.1**). In comparison to literature,<sup>43</sup> B<sub>2</sub>G shows an ISC on a slower time scale within tens of ps, which is consistent with reproduced data as presented in appendix **Figure A41**.

Much higher differences are observed for the second time constant.  $\tau_2$  corresponds to the primary radical cleavage from excited triplet states, which decreases from 127 to 70 ps in the series of B<sub>4</sub>G = oMeB<sub>4</sub>G > oEtB<sub>4</sub>G > pPrOB<sub>4</sub>G. However, the highest primary cleavage quantum yield is observed for oMeB<sub>4</sub>G with 95 % and decreases for B<sub>4</sub>G > oEtB<sub>4</sub>G from 90 to 78 %. In conclusion, similar rate coefficients  $k_{\text{cleav}}$  between  $7$  and  $9 \cdot 10^9 \text{ s}^{-1}$  are obtained for the primary cleavage of the investigated tetraacylgermanes. In line with the overall initiation efficiency  $m(\text{oMeB}_4\text{G}:\text{B}_4\text{G}) \sim 1.3$  (**section 4.3**), oMeB<sub>4</sub>G tends to a more efficient radical formation. However, the differences in  $k_{\text{cleav}}$  for oMeB<sub>4</sub>G compared to B<sub>4</sub>G are not significant within the estimated error of 30 %. In comparison to literature-known B<sub>2</sub>G ( $k_{\text{cleav}} \sim 7 \cdot 10^7 \text{ s}^{-1}$ ),<sup>43</sup> the investigated tetraacylgermanes reveal a two magnitudes higher  $k_{\text{cleav}}$ . The primary radical formation of B<sub>2</sub>G is expected on tens of ns, which is consistent with our data (refer to **Figure A41**). In contrast to tetraacylgermanes, a long-living triplet ESA at 425 nm is observed after slow ISC within tens of ps due to missing primary radical formation within the recorded time window (**Figure A41d**). In addition, the literature-known ns-TA-spectrum of the primary benzoyldiethylgermyl radical<sup>38</sup> is not observed on the ps scale.

A comparison with efficient monoacylgermanes is not possible due to missing data on ns-time scale. However, from literature a factor 2-4 smaller cleavage quantum yield is expected for B<sub>1</sub>G compared to B<sub>2</sub>G,<sup>38-39</sup> which implies a less efficient  $k_{\text{cleav}}$  for monoacylgermanes.

## 4.5 Summary and Outlook Acylgermanes

A library of fourteen mono-, bis- and tetraacylgermane derivatives as well as one tetramesitylstannane was investigated via a special methodological combination of PLP-ESI-MS and fs-TA supported by TDDFT. The approach enables the correlation of the overall initiation efficiency of radicals originated from a photoinitiator towards a monomer after final polymerization with the ultrafast excited state dynamics immediately after photoexcitation of the molecule in a quantitative manner.

From literature suggested Norrish type I mechanism of acylgermanes is confirmed by PLP-ESI-MS end group analysis. Bis- and tetraacylgermanes are considered for a multiple cleavage mechanism, which was evidenced by a new developed prediction method for the simulation of isotopic pattern of n-armed star polymers in PLP-ESI-MS. In addition, with increasing system size a more complex channel branching due to quasi-degenerated excited states within the  $n\pi^*$ -band (400-450 nm) is suggested by TDDFT calculations. For comparison of the overall initiation efficiency of tetra-, bis- and monoacylgermanes a stoichiometric ratio is expected corresponding to the number of benzoyl moieties, e.g. factor 4 for tetra- versus bisacylgermanes, and a factor of 2 for tetra- versus bis- as well as bis- versus monoacylgermanes. Remarkably, tetraacylgermanes show a non-stoichiometric increase of 40-100 % in comparison to bis- and monoacylgermanes, e.g. maximum value of ~8 for tetrabenzoylgermane versus benzoyltrimethylgermane. In relation to fs-TA, the result is in accordance to a much faster radical formation within 70-127 ps in contrast to bis- and monoacylgermanes, which cleave on a nanosecond (ns)-time scale in line with literature.

The size-dependence in the overall initiation efficiency is correlated to the ratio of  $n\pi^*$ -extinction coefficients of unsubstituted mono-, bis and tetrabenzoylgermanes. In contrast, the overall initiation efficiency of acylgermanes with *para*-substitution pattern is less correlated to  $n\pi^*$ -extinction coefficients with deviations of 20-50 %.

The influence of substitution patterns on the overall initiation efficiency and the excited state dynamics of acylgermanes were investigated in a model study on five different *para*-substituted benzoyltrimethylgermanes (CB<sub>1</sub>G, NB<sub>1</sub>G, MB<sub>1</sub>G, FB<sub>1</sub>G, HB<sub>1</sub>G). Herein, monoacylgermanes with electron withdrawing nitro and cyano substituents show a weak initiation behavior resulting in a monomer conversion of 0.1-1 % at comparably high total irradiation energies of ~110 J. In contrast, efficient monoacyl-

germanes with electron donating fluoro and methoxy substituents (+M-effect) reveal a monomer conversion of 4-5 % at ~30 J total irradiation energy. This behavior is determined by the singlet-triplet channel branching within the excited states. In turn, weak benzoyltrimethylgermane derivatives show a fast relaxation within 2-12 ps via internal conversion (IC) to ground states after photoexcitation, while efficient initiators feature an ultrafast intersystem crossing (ISC) within 2-4 ps into a triplet state as starting point for radical formation. Thus, *para*-substitution pattern have a strong influence on the channel branching between the excited states, which determines if an initiator is efficient or weak.

The overall initiation efficiency is as well influenced by the secondary and following radical formation events, which are not observed within the time scale of the conducted fs-TA experiments. Hence, further investigations, especially on the multiple cleavage mechanism of bis- and tetraacylgermanes, are necessary, e.g. via fs-TA on a ns to ms scale for observation of long-living responses of triplet states.<sup>155</sup>

In the following, two interesting approaches for possible future investigations are presented.

#### **4.5.1 Outlook I: wavelength-dependent PLP-conversion experiments**

Within the scope of a master thesis by P.W. Kamm,<sup>156</sup> wavelength dependent PLP-conversion experiments at a constant photon count<sup>75</sup> were conducted for bisacylgermanes B<sub>2</sub>G, FB<sub>2</sub>G, and MB<sub>2</sub>G. Herein, for 5 min N<sub>2</sub>-purged samples with MMA-volume of 0.5 mL and initiator concentration of 5 mmol L<sup>-1</sup> are irradiated at different wavelengths in special quartz vials (ilmasil, transmission  $T = 92.5\%$  for wavelength >350 nm). Depending on the wavelength, the energy and number of pulses is adjusted to achieve a constant photon count following **Eq. A19**. Subsequently, the monomer conversion is determined via gravimetry. The resulting wavelength dependent MMA-conversion for the PLP-experiment with MB<sub>2</sub>G is plotted together with the corresponding UV/Vis spectra as presented in **Figure 4.39** (experiments with FB<sub>2</sub>G and B<sub>2</sub>G in **Figure A42**).

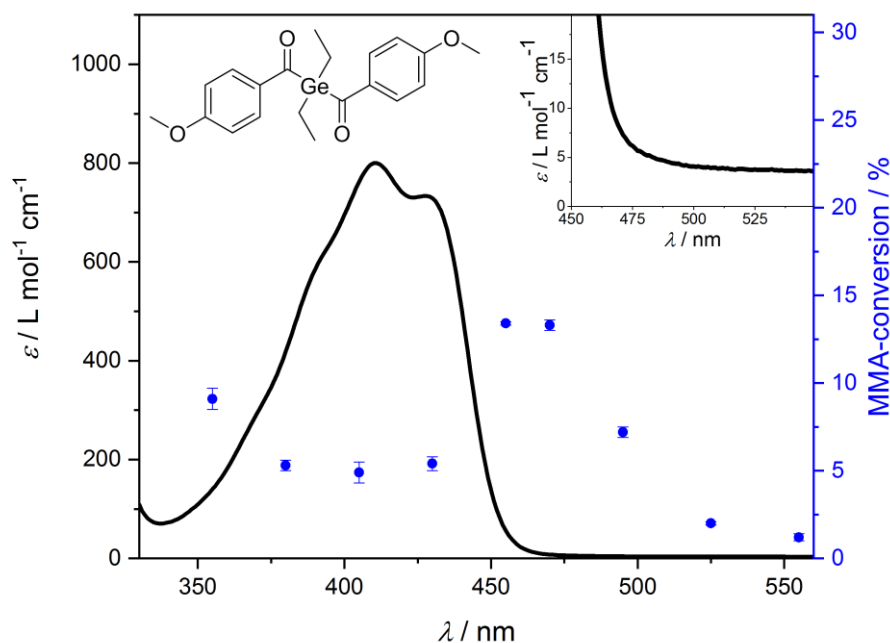


**Figure 4.39.** MMA-conversion plot of wavelength-dependent PLP-experiment of MB<sub>2</sub>G in MMA reproduced from master thesis by P.W. Kamm.<sup>156</sup> Maximum MMA-conversion is observed between 455 and 470 nm at very low extinction coefficients < 50 L mol<sup>-1</sup> cm<sup>-1</sup> of the initiator.

**Figure 4.39** shows the maximal MMA-conversion between 455 and 470 nm at very low extinction coefficients < 50 L mol<sup>-1</sup> cm<sup>-1</sup>. Thus, the conversion of a PLP-experiment is not related to the highest  $n\pi^*$ -extinction coefficient. Similar phenomena are observed for the initiation of oxime esters in photo-FRP, and dimerization of styrylpyrene.<sup>75, 157</sup> Currently, the phenomena cannot be explained via common photochemical models. However, an in-depth understanding of the underlying mechanism could open an avenue for a new generation of visible light-triggered photoinitiators.

#### 4.5.2 Outlook II: fs- vs. ns-Pulsed Laser Polymerization

Instead of tuning the chemistry of photoinitiators, an alternative approach could be the optimization of the light source used for triggering photo-FRP. To this end, a PLP-experiment with an fs-laser as light source is carried out with MB<sub>2</sub>G and B<sub>4</sub>G by using the following setup (**Figure 4.40**).

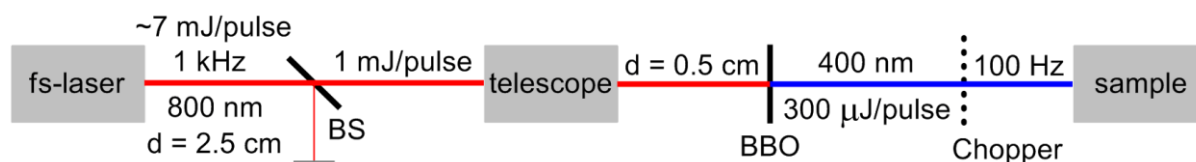


**Figure 4.40.** Schematic fs-PLP setup. d: diameter of laser mode, BS: beam splitter, BBO:  $\beta$ -barium borat for SHG. For a more detailed description refer to main text.

The output of the fs-laser system (Astrella, Coherent) was attenuated from  $\sim 7$  to  $\sim 1$  mJ/pulse via a BS. With the aid of a telescope, the laser mode is reduced from 2.5 cm to 0.5 cm, which is similar to the aperture of the ns-PLP experiment. The fundamental 800 nm-pulse was converted to 400 nm via SHG of a 0.3 mm thick BBO crystal resulting in 300  $\mu$ J/pulse. Finally, the 1 kHz repetition rate was chopped to 100 Hz (tunable chopper wheel, Thorlabs). Thus, typical PLP-conditions as used in ns-PLP experiments were achieved. In line with ns-PLP conditions, MB<sub>2</sub>G and B<sub>4</sub>G were dissolved in MMA with concentrations of 5 and 2.5 mmol L<sup>-1</sup> with a sample volume of 0.5 mL in cylindrical sample vials, which were irradiated for 15 min (90000 pulses). Samples were degassed for 5 min via N<sub>2</sub>-purging. In addition, reference ns-PLP-experiments with identical conditions are conducted for MB<sub>2</sub>G and B<sub>4</sub>G in MMA. All ns- and fs-PLP experiments were reproduced three times. After irradiation, the monomer conversion was determined via gravimetry. The resulting averaged MMA-conversion of the each two fs- and ps-PLP-experiments is presented in **Table 4.11**.

**Table 4.11.** MMA-conversion fs- and ns-PLP-experiments with identical conditions.

Sample	c / mmol L <sup>-1</sup>	fs-PLP conversion / %	ns-PLP conversion / %
MB <sub>2</sub> G in MMA	5	11.5 $\pm$ 0.2	5.0 $\pm$ 0.1
B <sub>4</sub> G in MMA	2.5	11.3 $\pm$ 0.5	6.1 $\pm$ 0.2

Remarkably, the monomer conversion of the fs-PLP-experiment is a factor 2 higher than for the ns-PLP-experiment. In the following, the result is discussed based on general considerations about differences between excitation via ns- and fs-laser pulses, which are (I) spectral width, (II) intensity, and (III) pulse duration.

(I) A ns-pulse is approximately monochromatic, while an fs-pulse shows a spectral width of  $\sim 10$  nm due to the transform limit. In general, the spectral width can be important due to a different distribution of the population within the excited states leading to a varied channel branching. However, ns-PLP-cocktail experiments show, for different excitation wavelengths within the  $\pi\pi^*$ -band of acylgermane initiators, no dif-

ference in the overall initiation efficiency in line with TDDFT-calculations. Thus, the influence by the spectral width is plausibly only of minor importance for the present experiment.

(II) Major differences are present in the peak intensities of  $1.5 \cdot 10^5 \text{ W cm}^{-2}$  and  $3 \cdot 10^{11} \text{ W cm}^{-2}$  for 10 ns- compared to 50 fs-pulses, which are calculated from the averaged pulse energy at the above presented PLP-conditions. Thus, the peak intensities of the fs-pulses are approximately 6 orders of magnitude higher than the ns-pulses resulting in many more photons per light excitation event. The high amount of photons enhances the probability for absorption, which leads to a high population of molecules in excited states. In addition, the propability for nonlinear effects increases at higher energies, e.g. two-photo absorption cannot be generally excluded anymore.

(III) A further fundamental difference between ns- and fs-laser pulses are their durations of  $\sim 10 \text{ ns}$  and  $\sim 50 \text{ fs}$ . Herein, pulse durations in the order of fs are shorter than the time scale for most photophysical processes of a molecule<sup>3</sup> featuring a temporally defined excitation. In contrast, ns-pulses of 10 ns are in the order of radical cleavage, which reflects a quasi-continuous irradiation compared to the time scale of photophysical processes, e.g. ISC within tens of ps. Thus, the quasi-continuous irradiation can plausibly interfere with the excited state relaxation processes of the photoinitiators, e.g. repeated ESA into higher excited states instead of the population of a triplet via ISC from lower excited singlet states.

In conclusion, the increased conversion for fs-PLP experiment is plausibly a result of temporally defined as well as efficient excitation caused by very intensive (II) and short pulses (III). Herein, it is shown that fs-PLP experiments are feasible and show promising results in comparison to ns-PLP experiments. Hence, an in-depth investigation on fs-PLP with respect to temporal controlled initiation events could be a future perspective within the FRP-research.

## 5. Tin-Based Visible Light Initiators

In the previous chapter, the photophysical and -chemical properties of acylgermanes were analyzed. Especially, approaches for increasing the initiation efficiency could be shown, e.g. non-stoichiometric size-dependence. However, a systematic approach for increasing the bathochromic shift in the absorption spectrum is challenging, e.g. electron withdrawing substitution patterns for monoacylgermanes, which lead to a red shift accompanied by very weak initiation efficiency. A promising path could be the substitution of the germanium with a tin-atom as shown for the example of tetramesitylstannane ( $\text{Mes}_4\text{T}$ ) in a recent publication of the Liska group.<sup>41</sup> For a closer look, the steady-state UV/Vis spectra of  $\text{Mes}_4\text{T}$  and  $\text{B}_4\text{G}$  dissolved in MMA are provided in **Figure 5.1**.

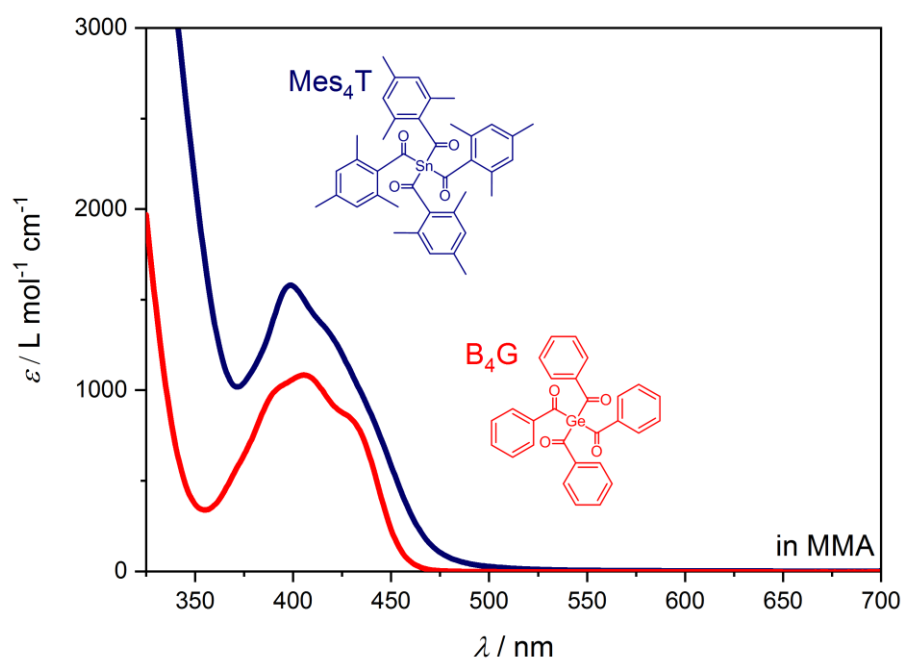


**Figure 5.1.** Steady-state UV/Vis-spectra of  $\text{Mes}_4\text{G}$  and  $\text{B}_4\text{G}$  illustrating the red shift of the tin-compound.

In comparison, both spectra reveal an absorption band with similar extinction coefficients of  $1000\text{--}1500\text{ L mol}^{-1}\text{ cm}^{-1}$  peaking at  $\sim 400\text{ nm}$ , which can plausibly be assigned to  $n\pi^*$ -transition into  $S_{1-4}$  due to four mesityl-moieties (refer to **section 4.1.1**). Remarkably, the right wing of the absorption band of  $\text{Mes}_4\text{T}$  in MMA shows a stronger broadening than  $\text{B}_4\text{G}$  up to  $\sim 500\text{ nm}$ . In addition, the efficient decomposition, surprisingly low toxicity and good bleaching properties of  $\text{Mes}_4\text{T}$  are reported.<sup>158</sup>

However, organo-tin-compounds are, in general, less stable than their germanium-substitute due to weaker Sn-C bond energy leading to a higher possibility for intermolecular interactions.<sup>42, 159</sup>

In the following, the photophysical and -chemical properties of two acylstannane-derivatives are investigated. Herein, the stability is studied by combination of solvent-dependent steady-state UV/Vis-, nuclear magnetic spin resonance (NMR) and solid state X-ray photoelectron spectroscopy (XPS). As a consequence, a special sample preparation for PLP-ESI-MS studies on Mes<sub>4</sub>T dissolved in MMA is introduced. Subsequently, wavelength-dependent PLP-MMA-conversion-plots are conducted. PLP-ESI-MS experiments are carried out to characterize the cleavage mechanism and to quantify the initiation efficiency in cocktail experiments. Finally, the TA-spectrum of Mes<sub>4</sub>T is presented as a first approach for the development of a possible photophysical mechanism.

## 5.1 Stability of Triphenylbenzoyl- and Tetramesitylstannane

In the current chapter, the chemical stability of Mes<sub>4</sub>T and triphenylbenzoylstannane (TPBT) are investigated in solid state via XPS and in solution via NMR and steady-state UV/Vis-spectroscopy. Solid-state XPS-spectra of Mes<sub>4</sub>T and TPBT were conducted by Lukas Michalek and are presented in **Figure B1**. As a general remark, XPS on photoinitiators is limited to a characterization of the overview spectrum, which includes the atomic ratios of a compound. A more detailed characterization via peak-deconvolution is not possible due to photodamages from X-ray excitation. In contrast to Mes<sub>4</sub>T, TPBT decomposes already in the solid state, which dismisses TPBT for further experiments. In fact, TPBT changes its macroscopic appearance from crystalline powder to high viscosity grease within a day under exclusion of light. Mes<sub>4</sub>T is sufficiently stable in the solid state, which is reflected by a weak deviation between the recorded and expected atomic ratio of the compound (**Figure B1a**). However, Mes<sub>4</sub>T decomposes in solution under light-exclusion as shown in **Figure 5.2**. The decomposition in solution is in line with NMR-measurements done by Marcus Zieger, which show significant decomposition already after 15 min, which is further increased after 18 h (**Figure B2**).

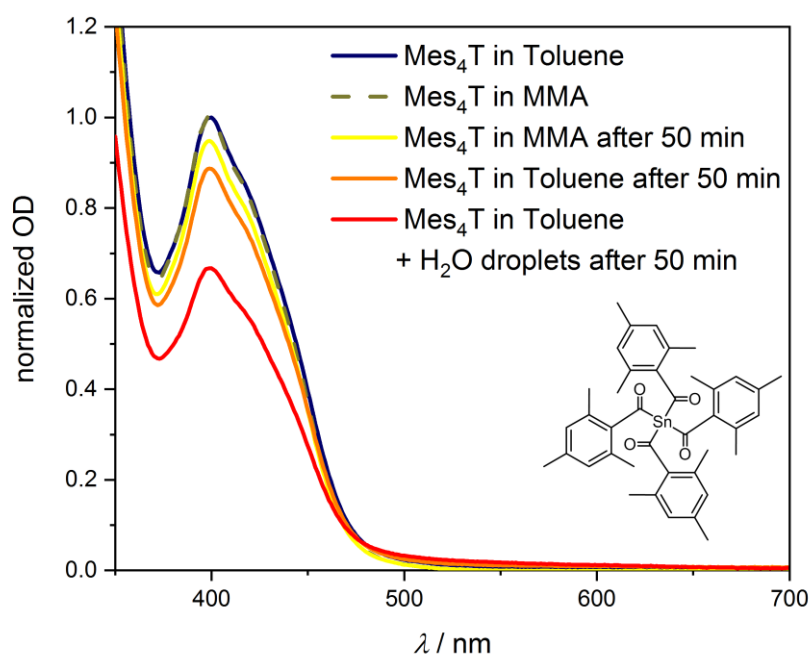


**Figure 5.2.** Steady-state UV/Vis-spectra of Mes<sub>4</sub>T dissolved in MMA, toluene, and toluene with water droplets for comparison of the decay of OD before and after 50 min waiting time under light-exclusion.

The OD of all absorption spectra is normalized to the absorption spectra of Mes<sub>4</sub>T dissolved in toluene and in MMA, respectively. All spectra were recorded immediately after sample preparation. After 50 min waiting time with light-exclusion, a significant decay of all spectra was observed. Remarkably, the addition of water droplets to toluene leads to a very strong decay, which is plausibly an evidence for hydrolysis reactions, as known for organo-tin-compounds.<sup>159</sup> Especially, the results in MMA are important for further PLP-ESI-MS investigations, which show already a decay of 2 % after 15 min (refer to **Figure B3**). Thus, special conditions are chosen to minimize the non-photo-induced decomposition of Mes<sub>4</sub>G in MMA in PLP-experiments.

With respect to possible hydrolysis reactions, PLP-cocktail- and wavelength-dependent PLP-experiments were conducted with water-free MMA, which was received after stirring overnight with CaH<sub>2</sub> and subsequent distillation. Further, the sample preparation was conducted in less than 6 min from solvent addition inclusive N<sub>2</sub>-purging until light irradiation. Fs-experiments with Mes<sub>4</sub>T are carried out in toluene without further purification.

## 5.2 PLP-ESI-MS Investigations on Tetramesitoylstannane

In the following, the radical fragments of Mes<sub>4</sub>T are investigated via PLP-ESI-MS end group analysis. Subsequently, the overall initiation efficiency of the cocktail experiment Mes<sub>4</sub>T:MB<sub>2</sub>G is quantified under special conditions with respect to the instability of Mes<sub>4</sub>T as described above (**section 5.1**).

### 5.2.1 PLP-ESI-MS End Group Analysis of Tetramesitylstannane

The SEC-ESI-MS-spectrum of the PMMA-products obtained from PLP is analyzed for identification of crucial initiating and terminating radicals originated from Mes<sub>4</sub>T. Herein, PLP-experiments of 2.5 mmol L<sup>-1</sup> Mes<sub>4</sub>T in MMA are conducted with 90000 pulses at 400 nm and ~320 μJ/pulse. The corresponding recorded (black) and predicted (red) SEC-ESI-MS-spectra are presented in **Figure 5.3**.

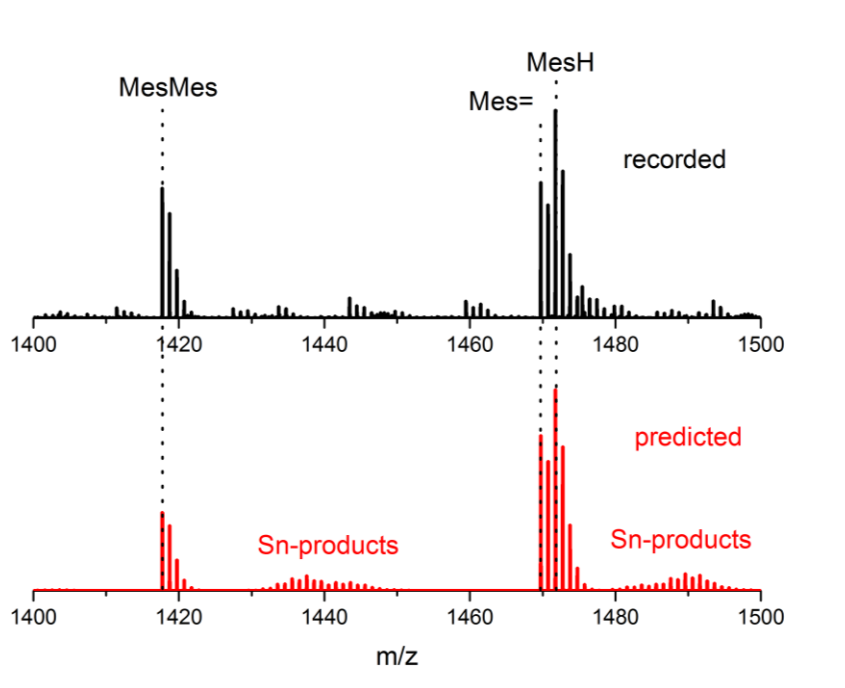


**Figure 5.3.** Recorded (black) SEC-ESI-MS and predicted (red) mass spectra of PMMA-products obtained from PLP initiated by Mes<sub>4</sub>T at 400 nm. From comparison with predicted spectrum, no Sn-containing species are observed.

Dominantly, disproportionation (Mes=, MesH) and combination products (MesMes) initiated and terminated by mesityl radicals are obtained, which are expected from an  $\alpha$ -cleavage of the Sn-CO bond. For analyzing possible Sn-containing products, the PLP-ESI-MS spectrum of 4-armed tin-centered star polymers, analogous to germane-centered species (refer to **section 4.2.3**), are predicted by using the above presented multinomial coefficient approach (**Figure 5.3**, red spectrum, species in **Figure B4**). In comparison of predicted Sn-products with the recorded spectrum, an

evidence for the formation of Sn-containing species is missing. Thus, it can be assumed that competing reaction channels of Sn-radicals impede an efficient initiation of polymerization. However, a weak ionization ability of Sn-containing polymer products cannot be safely excluded, which could hamper the subsequent detection.

In summary, Mes<sub>4</sub>T reveal a common α-cleavage mechanism, but no evidence for the formation of 4-armed star polymers is observed. In contrary to acylgermanes, the tin-containing radicals must not lead to a statistical formation of star polymers, which may be a consequence of competing reaction channels introduced by tin.

### 5.2.2 PLP-ESI-MS Cocktail Experiment of Tetramesitoylstannane

The PLP-ESI-MS cocktail experiment of Mes<sub>4</sub>T:MB<sub>2</sub>G in water-free MMA was conducted at analogous conditions to the acylgermane study above, e.g. 7 samples, 5 mmol L<sup>-1</sup>, ~320 μJ/pulse, 100 Hz, 15 min within the nπ\*-maxima at 398 and 411 nm. In addition, the evaluation of the recorded mass spectra was carried out as described in **section 4.3**. The corresponding  $G_{m/z0}^{X=}$  vs initial molar ratio-plot is presented in **Figure 5.4**. A weak chain length dependent ionization-bias can be inspected in **Figure B6** (for further explanation refer to **section 4.3**)

The averaged overall initiation efficiency of Mes<sub>4</sub>T:MB<sub>2</sub>G in water-free MMA is obtained to  $1.4 \pm 0.08$ , which is smaller than a factor of 2 as expected by stoichiometry as well as by the ratio of the maximal nπ\*-extinction coefficients ( $\epsilon_{\max}(\text{Mes}_4\text{T}) = 1579 \text{ L mol}^{-1} \text{ cm}^{-1}$   $\epsilon_{\max}(\text{MB}_2\text{G}) = 779 \text{ L mol}^{-1} \text{ cm}^{-1}$ ). Thus, the overall initiation efficiency of Mes<sub>4</sub>T:MB<sub>2</sub>G is likely decreased by decomposition channels, which do not lead to an initiation of polymerization as expected from UV/Vis and NMR studies above. By considering  $m(\text{B}_4\text{G}:\text{MB}_2\text{G})=2.86 \pm 0.64$  (refer to **Table 4.8**), the overall initiation efficiency of the cocktail experiment Mes<sub>4</sub>T:B<sub>4</sub>G can be calculated to  $\sim 0.49 \pm 0.37$ , which shows a factor 3 higher efficiency as measured in a cocktail experiment in MMA without further purification (refer to **Figure B5**). Thus, water clearly has an influence on the overall initiation efficiency of Mes<sub>4</sub>T, which is in line with a presumed hydrolysis.<sup>42, 159</sup>

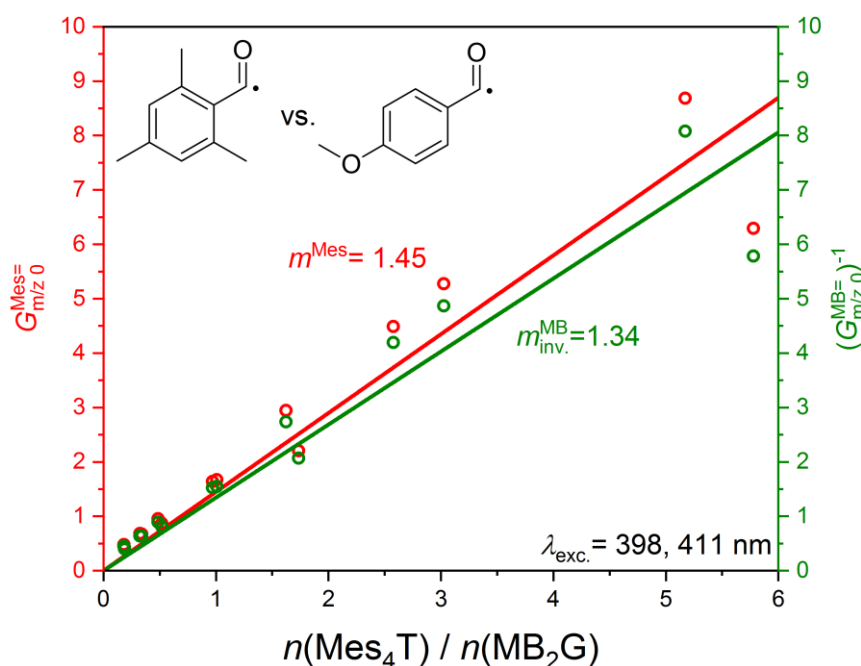


**Figure 5.4.**  $G_{m/z0}^{X=}$  vs initial molar ratios-plot of the cocktail experiment Mes<sub>4</sub>T:MB<sub>2</sub>G in water-free MMA to determine the overall initiation efficiencies of the radicals Mes and MB at excitation wavelength as indicated. Red: Linear regression of all mass-bias-free ratios  $G_{m/z0}^{B=}$  of the disproportionation product Mes= initiated by the radical Mes originated from the initiator Mes<sub>4</sub>T versus the initial molar ratios  $n(\text{Mes}_4\text{T})/n(\text{MB}_2\text{G})$  resulting in an overall initiation efficiency of  $m^{\text{Mes}}=1.45$ . Green: Linear regression of all inverse mass-bias-free ratios  $(G_{m/z0}^{\text{MB}=\text{}})^{-1}$  of the disproportionation product MB= initiated by the radical MB originated from the initiator MB<sub>2</sub>G versus the initial molar ratios  $n(\text{B}_4\text{G})/n(\text{MB}_2\text{G})$  resulting in an overall initiation efficiency of  $m_{\text{inv.}}^{\text{MB}}=1.34$ . Deviations between  $m^{\text{Mes}}$  and  $m_{\text{inv.}}^{\text{MB}}$  reflect the scattering of the experiment.

In conclusion, the overall initiation efficiency of Mes<sub>4</sub>T is significantly lower than for B<sub>4</sub>G and MB<sub>2</sub>G as reflected by a factor of 0.5 and 1.4, respectively. However, the obtained factor is plausibly a lower boundary for the estimation of the overall initiation efficiency due to possible degradation of the tin-compound before starting the PLP-experiment. A further improvement could be achieved by working in a yellow/red light-laboratory under inert conditions, e.g. oxygen- and water-free glove box.

### 5.3 fs-TA Investigation on Tetramesitoylstannane

In this section, the photophysical dynamics of Mes<sub>4</sub>T are studied in toluene via fs-TA. The corresponding steady-state spectrum of Mes<sub>4</sub>T dissolved in toluene as used for fs-TA is shown in **Figure 5.5**.

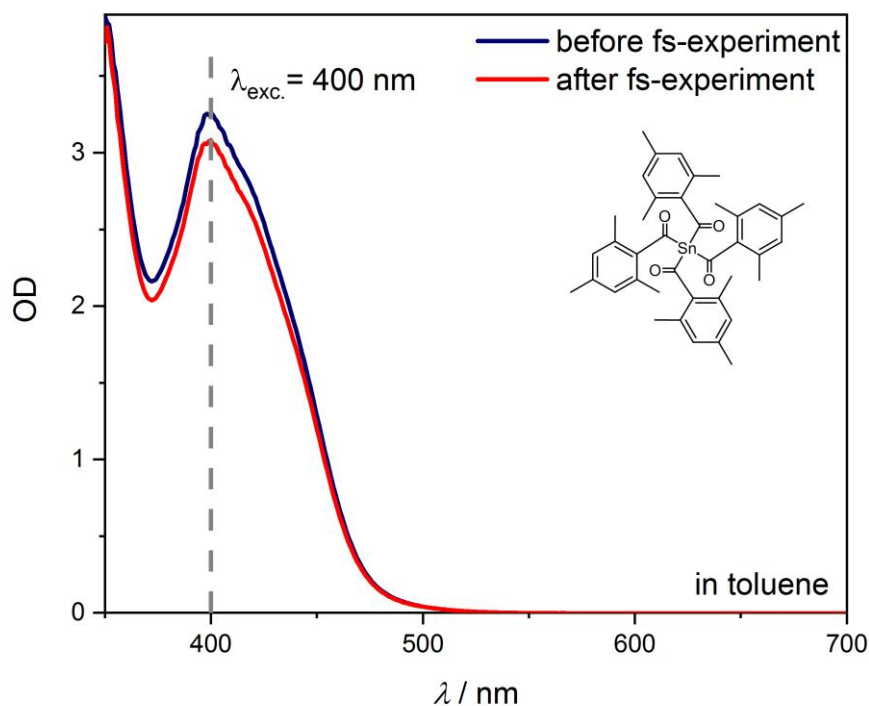


**Figure 5.5.** UV/Vis-spectrum of Mes<sub>4</sub>T in Toluene as used for fs-TA. Excitation wavelength of 400 nm (grey dashed line) results in a sample OD  $\sim$  3.2 in a 1 mm cuvette (blue spectrum). Spectrum in red indicates the decomposition of the initiator during the fs-experiment.

The samples for fs-TA are prepared at very high OD of  $\sim$ 3 at the excitation wavelength of 400 nm due to very weak transient responses of the system. After excitation at 400 nm, the transient responses of Mes<sub>4</sub>T in toluene are probed with a CaF<sub>2</sub>-white light continuum between 350 and 720 nm. The resulting TA-spectrum is presented in **Figure 5.6**.

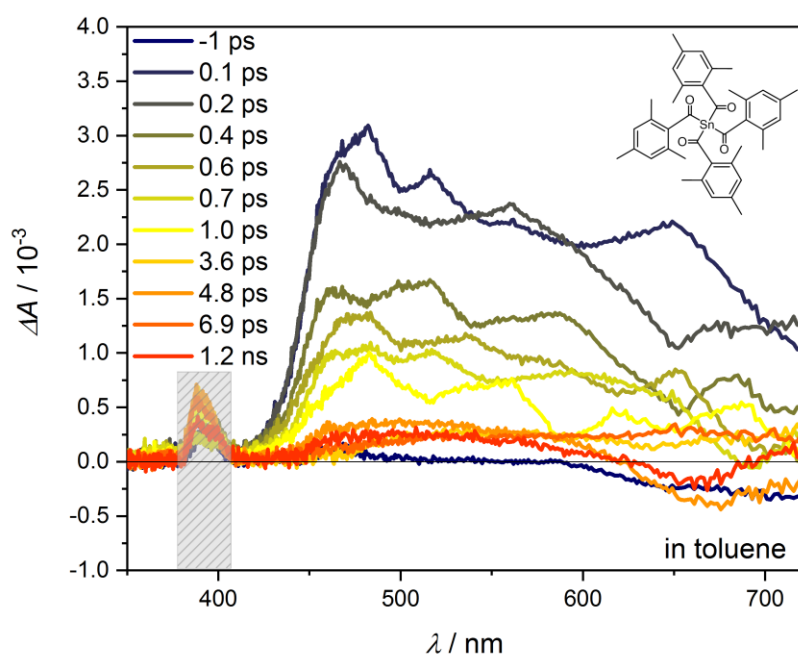


**Figure 5.6.** Transient Spectra of Mes<sub>4</sub>T dissolved in toluene pumped at 400 nm and probed by CaF<sub>2</sub>-white light continuum between 350-720 nm. Time delays as indicated.

The region at 400 nm is omitted due to scattering from pump pulse. Transient responses at wavelength < 420 nm are vanished by high sample OD > 2. Immediately after excitation, a broad ESA-absorption is observed from 420 to 720 nm, which decays in ~500 fs to a very weak ESA remaining on a time scale > 1.2 ns (time constants are obtained from biexponential fitting routine of single transient response at 480 nm as presented in **Figure B8.** ). The apparently negative response in the region of 700 nm is caused by white light fluctuations within the resolution of the experiment of  $1:10^4$ , which can be seen from comparison with the TA-spectrum recorded for delay times before zero (-1 ps). In line with a more efficient bleaching behavior<sup>41, 158</sup> compared to acylgermanes, as well as the weak stability of Mes<sub>4</sub>T in solution (refer to **section 5.1**), the major depopulation is plausibly caused by ultrafast singlet-decay via IC. In comparison to a negligible fluorescence quantum yield (**Figure B7**), the weak long-living ESA can be assigned to the transient response of a triplet state, which is probed into higher lying excited triplet states. The formation of triplet states is crucial for the radical formation via  $\alpha$ -cleavage as expected from PLP-ESI-MS end group analysis. In line with the reduced overall initiation efficiency of Mes<sub>4</sub>T compared to acylgermanes, the dominant singlet decay is likely associated to competing channels, which do not lead to initiation of polymerizations. By evaluating the relative ampli-

tudes  $\frac{c_1}{c_1+c_2}$  of the biexponential fit at 480 nm, the channel branching is roughly estimated by 88 % singlet decay and 12 % remaining triplet ESA (refer to **Figure B8**). However, the obtained ratio is probably defective due to low signal-to-noise ratio of the experiment. The channel branching between a competing singlet decay and ISC is sketched in **Figure 5.7**.

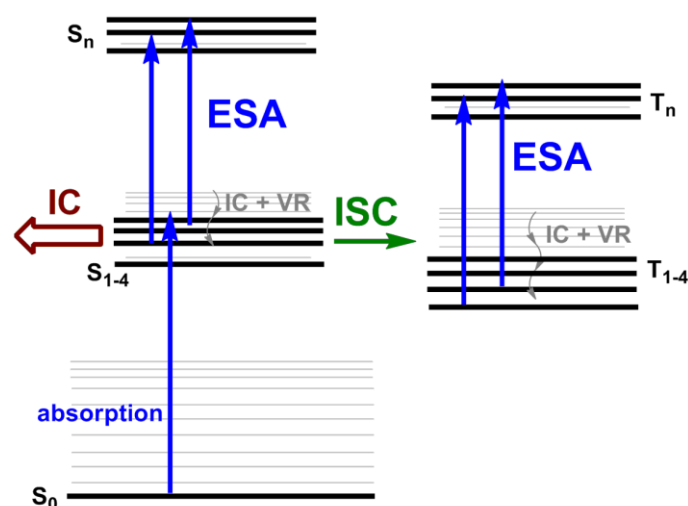


**Figure 5.7.** Jabłoński diagram depicting the photophysical mechanism of Mes<sub>4</sub>T. After excitation, the quasi-degenerated excited singlet states are depopulated dominantly by IC as a competing pathway to ISC in less than 1 ps. ISC into triplet states is expected to be crucial for the radical formation.

## 5.4 Summary Tetramesitoylstannane

The substitution of the germanium-centered atom with a tin-atom of a tetraacyl-system leads to a strong bathochromic shift, which could be a promising direction for the development of new visible light initiators. However, the investigated systems decompose already from ground state without light excitation, which is plausibly caused by longer C-Sn in comparison to C-Ge-bonds.<sup>42</sup> In line with literature,<sup>159</sup> a possible decomposition pathway is the intermolecular interaction with water. Consequently, the overall initiation efficiency of Mes<sub>4</sub>T is reduced by a factor of 0.5 compared to structurally similar tetraacylgermanes as a result of decomposition without radical formation. In addition, no stannyl-initiated PMMA products are observed via PLP-ESI-MS, which could be an evidence for a competing reaction pathway. The results are in line with data from fs-TA. Herein, dominating ultrafast singlet decay (~88%) within ~500 fs is observed, while only a small long-living triplet population can be considered for radical formation. The excellent bleaching behavior of Mes<sub>4</sub>T as reported by literature<sup>41, 158</sup> is, in turn, not necessarily related to an efficient initiation behavior due to dominant singlet decay without radical formation.



The section begins with the steady-state properties of the investigated tetrazole systems. Accordingly, the fluorescence quantum yields of BiphTet and PyTet as well as the corresponding quenching-effects of IEt in DCM were assessed via steady-state spectroscopy. Subsequently, the transient spectra of Tet, PyTet and BiphTet in DCM and in DCM:IEt mixtures are presented allowing the evaluation of their ultrafast dynamics. The results will be compared with known reactivity properties to develop a photophysical and -chemical mechanism for NITEC-precursors. Furthermore, the applied method is carefully analyzed via concentration-dependent fs-pump-probe experiments to show the possibilities and limits of fluorescence quenching studies in fs-TA for the presented chromophores.

## 6.1 Steady-State Fluorescence Spectra of Tet, PyTet, BiphTet in DCM and Quenching Effects of IEt

In the present section, the fluorescence properties of Tet, PyTet, and BiphTet in DCM and DCM:IEt mixtures are compared. If possible, their fluorescence quantum yields  $\Phi_F$  are determined.

Tet shows no significant fluorescence within the resolution of the spectrometer after excitation at its absorption maximum of  $\sim 280$  nm (**Figure C1**). Thus,  $\Phi_F$  is expected to be smaller than  $< 10^{-4}$ . Hence, a competing radiative relaxation pathway can be excluded, which makes Tet an ideal non-fluorescent reference system for the following fs-pump-probe experiments.

The fluorescence spectra of a) PyTet and b) BiphTet are presented in **Figure 6.2**. PyTet and BiphTet dissolved in DCM reveal distinct fluorescence bands peaking at 430 and 520 nm after excitation at 395 nm, respectively, which is consistent with fluorescence spectra presented in literature.<sup>21, 30</sup> Evidences for dimer- or excimer-formation are not observed, e.g. additional bands in UV/Vis absorption spectra or bimodal fluorescence bands as known for pyrene.<sup>160-161, 163</sup>

Excitation at 395 nm within the red tail of the absorption spectra of PyTet and BiphTet presumably leads to transitions into low vibrational levels of the first excited singlet state  $S_1$ .<sup>30</sup> The conditions are chosen for later comparison with fs-TA, which was conducted at an excitation wavelength of 400 nm. In addition,  $\Phi_F$  was quantified at an excitation wavelength of 395 nm by using C307 (reference spectrum in **Figure C2**) in ethanol as a reference system ( $\Phi_F(\text{C307}, 395 \text{ nm}) = 56 \%$ )<sup>135</sup>. Herein,  $\Phi_F$  of PyTet

and BiphTet dissolved in DCM are estimated by  $\sim 8$  and  $\sim 11$  %, respectively. In addition, the corresponding fluorescence lifetimes of PyTet and BiphTet in DCM are  $\sim 1.3$  and  $\sim 1.8$  ns, which were obtained via TCSPC (refer to **Figure C3**). In comparison,  $\Phi_F$  of PyTet and BiphTet in DCM are very similar. Thus, the radiative singlet relaxation channel is plausibly not the main reason for the weak reactivity of BiphTet compared to PyTet, which features efficient NITEC.

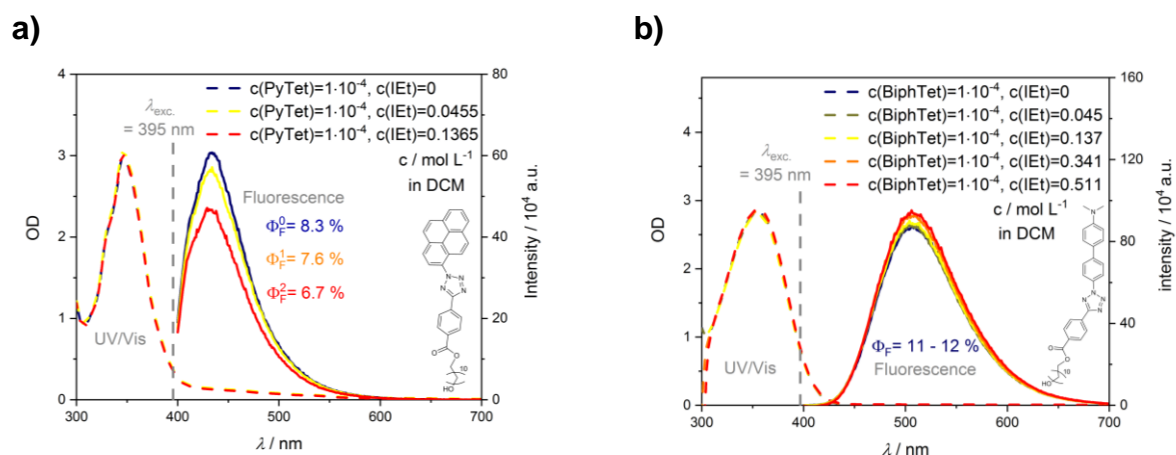


**Figure 6.2.** Steady-state UV/Vis (dashed lines) and fluorescence spectra (solid lines) recorded at excitation wavelength 395 nm in DCM (blue) as well as diverse DCM:IET mixtures (green/yellow to red) of a) PyTet b) BiphTet. Fluorescence quantum yields  $\Phi_F$  determined by using coumarin 307 in ethanol as a literature-known standard (refer to **Figure C2**).<sup>135</sup> Concentrations of PyTet, BiphTet, IET as indicated.

The quenching influence of IET is quantified by determining  $\Phi_F$  from recorded UV/Vis and fluorescence spectra of PyTet and BiphTet in diverse DCM:IET-mixtures at exact defined sample concentrations (**Figure 6.2**). Importantly, UV/Vis spectra are not influenced in the presence of IET excluding chemical interactions between the investigated tetrazole and quencher systems. With increasing IET-concentration,  $\Phi_F$  of PyTet is linearly decreased from 8.3 to 6.7 % (**Figure 6.2a**), **Figure C4**) as expected from the HAE of IET.<sup>11-12, 161, 164-165</sup> In contrast, the fluorescence of BiphTet is not quenched in the presence of IET as evidenced by a slight increase of  $\Phi_F$  from 11 to 12 % in **Figure 6.2b**). Remarkably, the absence of a quenching effect on the fluorescence of BiphTet, in contrast to PyTet in DCM:IET mixtures, is most likely caused by different branched excited states.

As a technical remark, the quantification of  $\Phi_F$  of PyTet and BiphTet in DCM:IET mixture is challenging due to sample preparation with very exact concentrations. The quenching processes can be disturbed by the presence of  $O_2$ .<sup>161, 166</sup> However, de-

gassing of samples dissolved in DCM without solvent loss is complicated due to the low vapor pressure, which can lead to slight concentration changes. Hence, DCM (molecular sieve) without further degassing is used for the quencher-dependent steady-state fluorescence measurements, which could have led to overestimated  $\Phi_F$  of PyTet in the presence of IEt.

## 6.2 fs-TA: Investigation on Diaryl-Tetrazoles in DCM

The excited state dynamics of Tet, PyTet and BiphTet in DCM and DCM:IEt mixtures are investigated via fs-TA. The results will be compared to the findings of steady-state spectroscopy and literature-known TDDFT-calculations as well as reactivity properties.<sup>21, 30, 46</sup>

### 6.2.1 Tet in DCM

In the following, a simple model for the excited state dynamics of Tet is developed, which can support the subsequent characterization of more complex photophysics and -chemistry of fluorescent PyTet and BiphTet. Tet is an example for efficient UV-triggered NITEC precursors exhibiting negligible fluorescence properties (**Figure C1**). Thus, Tet is an ideal reference system to study the singlet-triplet branching via fs-TA. The UV/Vis spectrum of Tet dissolved in DCM recorded in a 1 mm cuvette as used for fs-TA is presented in **Figure 6.3**.

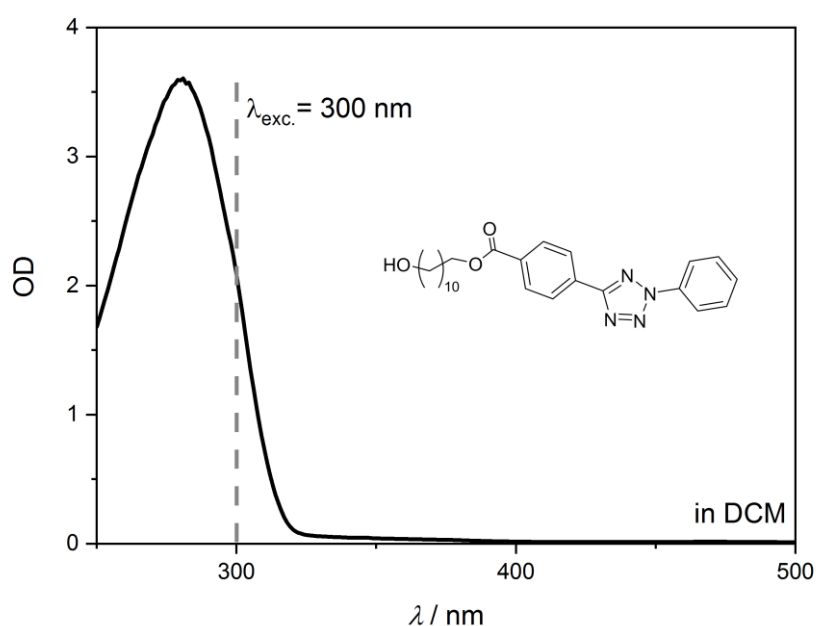


**Figure 6.3.** UV/Vis-spectrum of Tet in DCM as used for fs-TA. Excitation wavelength of 300 nm (grey dashed line) results in a sample OD ~2 in a 1 mm cuvette.

The sample for pump-probe experiments with Tet in DCM is prepared at a relatively high OD  $\sim 2$  due to weak transient responses within the excited states. The corresponding TA-spectrum of Tet dissolved in DCM is recorded after excitation at 300 nm (4.1 eV) and probing with a CaF<sub>2</sub>-white light continuum between 350-720 nm as shown in **Figure 6.4**.

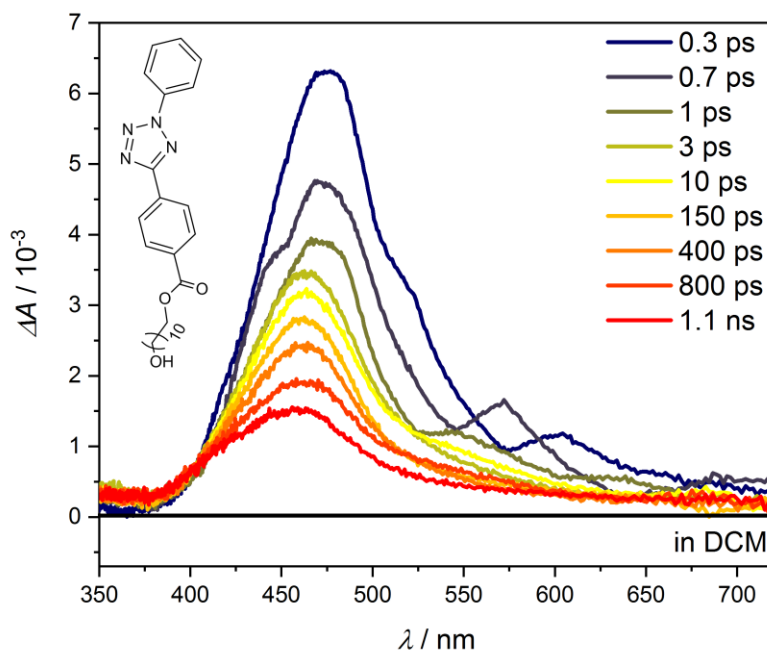


**Figure 6.4.** Transient spectra of Tet dissolved in DCM, pumped at 300 nm (4.1 eV), and probed by CaF<sub>2</sub>-white light continuum between 350-720 nm. Time delays as indicated.

After excitation at 300 nm into the right wing of the S<sub>1</sub>-absorption band (refer to **Figure 6.3** and ref. 30), the TA-spectrum of Tet reveals instantaneously a broad ESA from 400-720 nm peaking at  $\sim 475$  nm (**Figure 6.4**). The broad ESA decays in a few ps from  $\sim 6.5$  to  $3.5 \Delta mA$ , which is accompanied by a hypsochromic shift from  $\sim 475$  to  $\sim 460$  nm. As indicated by an isosbestic point at  $\sim 410$  nm, the ultrafast decay is related to an increasing ESA at  $\sim 370$  nm (**Figure C5**). Subsequently, the broad ESA decreases on a longer time scale, which remains within the recorded time window. The remaining ESA with a maximum at  $\sim 460$  nm is broadened over the entire recorded wavelength range from 350-720 nm.

GSB is expected in the region  $< 325$  nm due to the ground state absorption spectrum of Tet (refer to **Figure 6.3**), which is not accessible within the probing region of 350-720 nm. The assumption of a long-living singlet state would likely lead to a

strong fluorescence pathway. In contrast, neither a negative transient response from SE nor significant steady-state fluorescence are observed (refer to **Figure C1**). In addition, the ultrafast decay of ESA at  $\sim 475$  nm is accompanied by a hypsochromic shift to  $\sim 460$  nm and rise of ESA at  $\sim 375$  nm, which emphasizes the formation of a triplet state. In conclusion, the ultrafast decay is assigned to VR within  $S_1$  accompanied by an ISC into long-living triplet states. In comparison with TDDFT-calculations,<sup>30</sup> the long-living broad ESA-band corresponds to the first three triplet states, which are probed into a triplet manifold. Obtained from biexponential global analysis (for corresponding DAS refer to **Figure C6**), ISC occurs within 600 fs, which is convoluted with VR from vibrational hot  $S_1$ . The decay of triplet ESA occurs on a time scale  $> 1.3$  ns, which is associated with IC and VR within the first three triplet states. In addition, ring-opening accompanied by  $N_2$ -release is another plausible reason for the decay of triplet ESA.<sup>30, 46, 82</sup> However, a significant wavelength-shift or a rise of additional species is not observed within the recorded wavelength-range. A summary of the photophysical and -chemical processes is given in **Figure 6.5**.

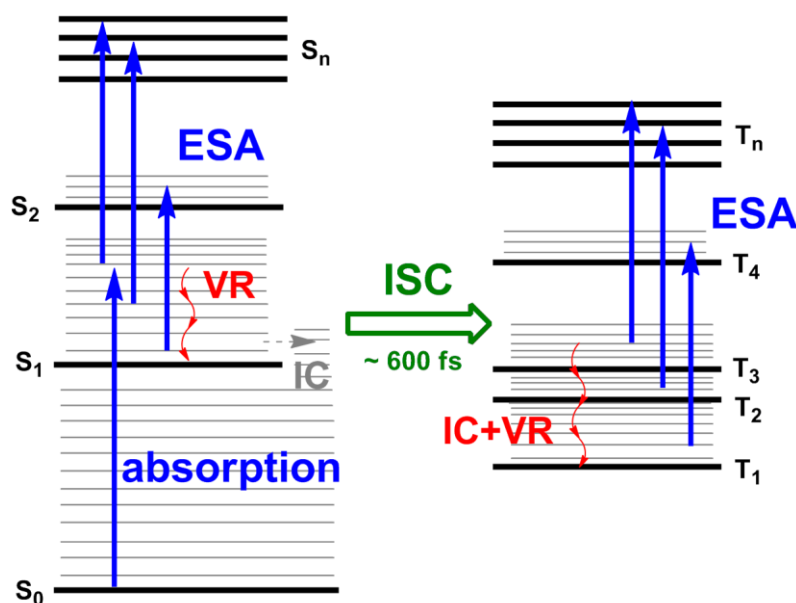


**Figure 6.5.** Jablonski diagram schematically depicting the photophysical mechanism of Tet.

### 6.2.2 PyTet in DCM

In this section, the singlet-triplet branching of PyTet in DCM is investigated via fs-TA. Herein, fluorescence quenchers IET and TEMPO are utilized to elucidate excited triplet state absorption in TA-spectra, which are highly superimposed by transient responses of excited singlet dynamics. Subsequently, an approach for quantifying the

influence of fluorescence quenchers on the TA-spectrum of PyTet in DCM:IEt mixtures is presented, which shows the possibilities and limitations of the method.

The UV/Vis spectrum of PyTet dissolved in DCM recorded in a 1 mm cuvette as used for fs-TA is presented in **Figure 6.6**.

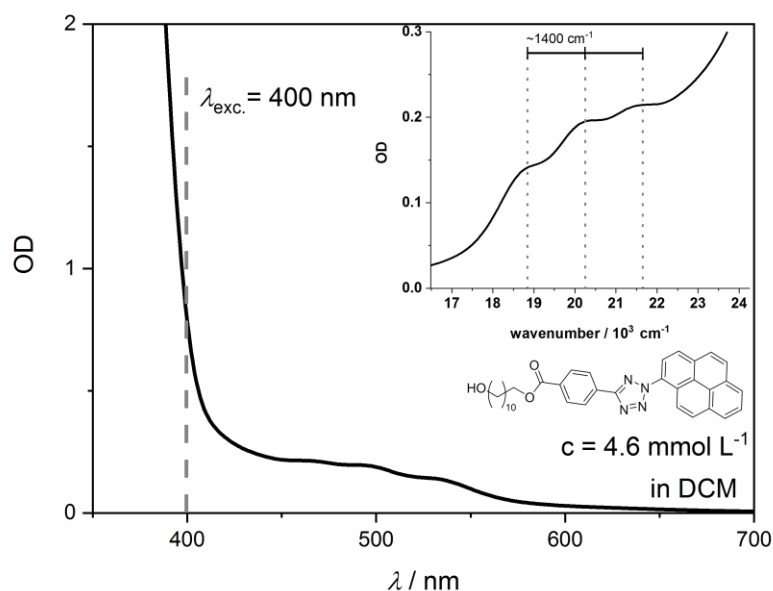


**Figure 6.6.** UV/Vis spectra of PyTet dissolved in DCM as used for fs-TA. Excitation wavelength of 400 nm (grey dashed line) results in a sample OD of ~0.7 in a 1 mm cuvette. Inset: OD-wavenumber-plot of structured absorption tail between 400 and 600 nm reveals a vibrational progression of ~1400 cm<sup>-1</sup>.

PyTet dissolved in DCM is excited within its right absorption wing at 400 nm (3.1 eV) of the first absorption band, which is in the region of the S<sub>1</sub>-transition.<sup>30</sup> Remarkably, a structured absorption tail between 400 and 600 nm can be observed. Plotting the OD versus wavenumbers reveals a vibrational progression of ~1400 cm<sup>-1</sup> (inset of **Figure 6.6**), which is in the order of a C-C stretching mode of S<sub>0</sub> or S<sub>1</sub> of pyrene of 1410 and 1397 cm<sup>-1</sup>, respectively.<sup>167</sup> Thus, the absorption tail reaching up to 600 nm can be plausibly assigned to a vibronic transition into S<sub>1</sub> of PyTet due to sufficient overlapping of Franck-Condon factors according to the presumed C-C stretching mode of the pyrene moiety.

After excitation at 400 nm, PyTet dissolved in DCM is probed by a CaF<sub>2</sub>-white light continuum between 350 and 720 nm. The corresponding TA-spectrum of PyTet in DCM is presented in **Figure 6.7**.

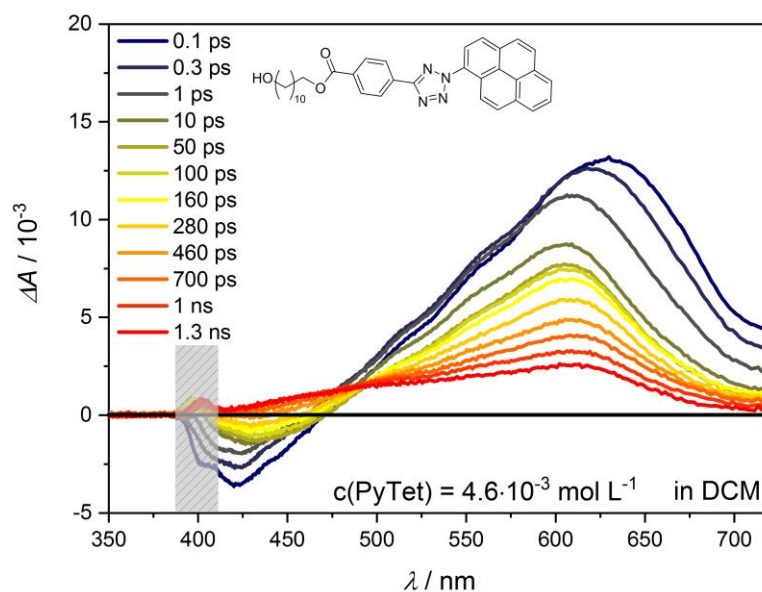


**Figure 6.7.** Transient spectra of PyTet dissolved in DCM pumped at 400 nm (3.1 eV) and probed with a CaF<sub>2</sub>-white light continuum between 350 and 720 nm with a fixed concentration and varying time delays as indicated. Region at 400 nm omitted due to scattering from pump pulse. Zero  $\Delta A$  within the UV-A range is caused by sample OD > 2 for wavelengths smaller than 390 nm (refer to **Figure 6.6**).

PyTet in DCM reveals, immediately after excitation, a broad TA-band of the excited states peaking at  $\sim 630$  nm as well as a broad negative transient response at  $\sim 420$  nm. Within a few ps, the ESA undergoes an ultrafast decay to  $\sim 85\%$  from the initial  $\Delta A$  ( $\sim 13 \cdot 10^{-3}$  to  $\sim 11 \cdot 10^{-3}$ ), which is accompanied by a strong hypsochromic shift of  $\sim 30$  to  $\sim 600$  nm. In addition, the negative response shifts from  $\sim 420$  to  $430$  nm during an ultrafast recovery within a few ps to  $\sim 60\%$  of the initial  $\Delta A$  ( $-3.5 \cdot 10^{-3}$  to  $-2 \cdot 10^{-3}$ ). In comparison, the ultrafast recovery of the negative transient response and the ESA decay are likely correlated. However, the differences in  $\Delta A$  as well as the wavelength shifts indicate superposition of photophysical processes on an ultrashort time scale. Subsequently, the ESA-band decreases further with a slight red shift from  $600$  to  $\sim 610$  nm within hundreds of ps. As indicated by an isosbestic point at  $\sim 490$  nm, the recovery of the broad negative response with a minimum at  $\sim 420$  nm is linearly correlated to the decay of the ESA-band. Remarkably, the transient response at  $\sim 440$  nm increases to positive  $\Delta A$ , which could be an evidence for a superimposed long-lasting ESA within this wavelength region. Finally, the entire TA spectrum from  $\sim 400$  to  $\sim 720$  nm is dominated by ESA, which persists longer than the recorded time window of 1.3 ns.

In accordance with the fluorescence maximum at  $\sim 430$  nm of PyTet ( $\Phi_F \sim 8\%$ , **Figure 6.2**), the negative transient response can be assigned to dominant SE. Consequently, the linearly correlated decay of the broad ESA within hundreds of ps can be interpreted as the corresponding singlet state, which is depopulated via SE. By comparison with the steady state UV/Vis spectrum as shown in **Figure 6.6**, GSB of PyTet is mainly expected at wavelengths  $< 400$  nm. Unfortunately, the region at  $\sim 400$  nm is superimposed by scattering of the pump pulse, while the TA  $< 390$  nm is vanished by the strong absorption of the sample. However, superposition with GSB cannot be safely excluded within the region of the SE due to the absorption tail up to 600 nm (refer to inset **Figure 6.6**). In conclusion, the entire TA-spectrum of PyTet in DCM is dominated by ESA and SE according to relaxation of singlet states via fluorescence. In contrast to the non-fluorescent reference system Tet, the characterization of triplet states in PyTet is complex due to superposition with dominant singlet state dynamics.

In the following, a striking evidence for triplet states will be given by analyzing the influence of fluorescence quenching processes on the TA-spectra of PyTet. For this purpose, the transient pump-probe broadband spectra of PyTet in a DCM:IEt mixture as well as in DCM with TEMPO are presented in **Figure 6.8** and **Figure C8** (corresponding steady-state UV/Vis spectrum in **Figure C7**), respectively.

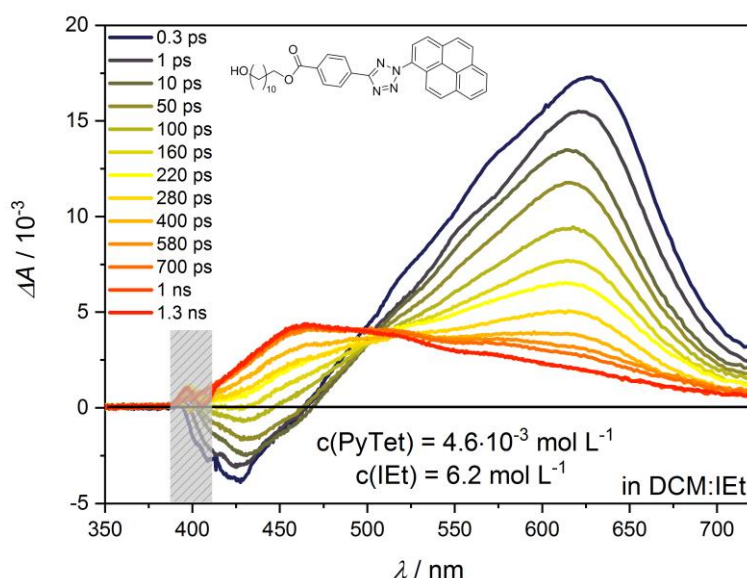


**Figure 6.8.** TA-spectrum of PyTet dissolved in a DCM:IEt mixture, which was excited at 400 nm and probed with a  $\text{CaF}_2$ -white light continuum between 350 and 720 nm. Significant increase of ESA at  $\sim 450$  nm is an evidence for a triplet state. Time delays and concentrations of PyTet and IEt as indicated. Transient responses at  $\sim 400$  nm are omitted due to scattering from pump pulse.

The TA-spectrum of PyTet was recorded in a DCM:IEt-mixture featuring a quencher concentration of  $c(\text{IEt}) = 6.2 \text{ mol L}^{-1}$  with an excitation wavelength centered at 400 nm and probed with a  $\text{CaF}_2$ -white light continuum between 350 and 720 nm (for further TA-spectra in other DCM:IEt-mixtures refer to **Figure C9**).

In comparison to the TA-spectrum of PyTet in DCM (**Figure 6.7**), all dominant features of the spectra are represented as well in the presence of IEt, e.g. strong singlet ESA at  $\sim 600 \text{ nm}$  and corresponding SE  $\sim 430 \text{ nm}$  immediately after excitation. In contrast, the recovery of SE proceeds on a shorter time scale, which is correlated to the decay of the corresponding singlet ESA peaking at  $615 \text{ nm}$  indicated by an isosbestic point at  $514 \text{ nm}$ .

For long delay times of  $\sim 1.3 \text{ ns}$ , the ESA-band reveals no distinct maximum within the region of  $600 \text{ nm}$  anymore. However, a distinct ESA-band peaking at  $\sim 460 \text{ nm}$  is observed with a lifetime exceeding the recorded time window of  $\sim 1.3 \text{ ns}$ . The faster SE-recovery as well as the decay of singlet ESA are in accordance with a decreased  $\Phi_F$  (8.3 to 6.7 %) originating from the quenching effect of IEt on PyTet in steady state fluorescence spectroscopy (refer to **section 6.1**). The additional band at  $\sim 460 \text{ nm}$  indicates a long-living process being unaffected by the presence of IEt.

The quenching mechanism of IEt can be explained by the HAE, enhancing the SOC.<sup>11</sup> SOC is resulting from interactions between spin and orbital angular momenta, leading to a higher probability for spin-forbidden transitions.<sup>10</sup> Thus – as a consequence of the presence of IEt –  $\Phi_F$  is reduced, while singlet relaxation via ISC is favored. Hence, the additional TA-band at  $\sim 460 \text{ nm}$  in the presence of IEt is a striking evidence for ESA of triplet states. The triplet ESA superimposes the entire transient spectrum, which is in accordance with TDDFT calculations from literature.<sup>30</sup> Herein, three energetically low-lying triplet states are accessible from the Franck-Condon region of  $S_1$ , from which a manifold of higher lying triplet states is available for triplet ESA.

The quenching-effect is validated by the transient spectrum of PyTet in DCM in the presence of TEMPO ( $c = 4 \cdot 10^{-3} \text{ mol L}^{-1}$ ), which is known for an alternative fluorescence quenching mechanism via interactions with the paramagnetic doublet states.<sup>9, 62, 168</sup> In fact, a similar TA-spectrum is observed, which exhibits a faster SE-recovery revealing a strong ESA-band within the same wavelength region (refer to **Figure C8**).

Thus, the change in the ratio between SE and triplet ESA is clearly an effect of a fluorescence quenching mechanism.

The steady-state UV/Vis- and TA-reference spectra of TEMPO and IET are provided in **Figure C10** and **Figure C11**, respectively. Both quencher molecules show only a very weak OD < 0.01 at the pump wavelength of 400 nm. TEMPO reveals no transient response in fs-TA after excitation at 400 nm (**Figure C10b, c**). IET in bulk reveals a very weak, long-living transient response peaking at ~500 nm (**Figure C11b**). However, the intrinsic transient response of IET has an insignificant influence on the progression of the transient response from superimposed SE and triplet ESA for PyTet in DCM:IET-mixtures (**Figure C11c, d**). Thus, influences by intrinsic dynamics of the quencher molecules are not relevant for the presented discussion. A more detailed view on the dynamics of IET is given in the caption of **Figure C11** in the appendix.

The clear evidence for a long-living triplet state in PyTet enables a quantitative analysis of the TA-spectrum of PyTet in DCM (**Figure 6.7**). Hence, a global analysis with four exponential functions is applied featuring 20 nm steps from 420 to 680 nm. The resulting amplitudes  $C_i(\lambda, \tau_i)$  of the DAS are presented in **Figure 6.9**.

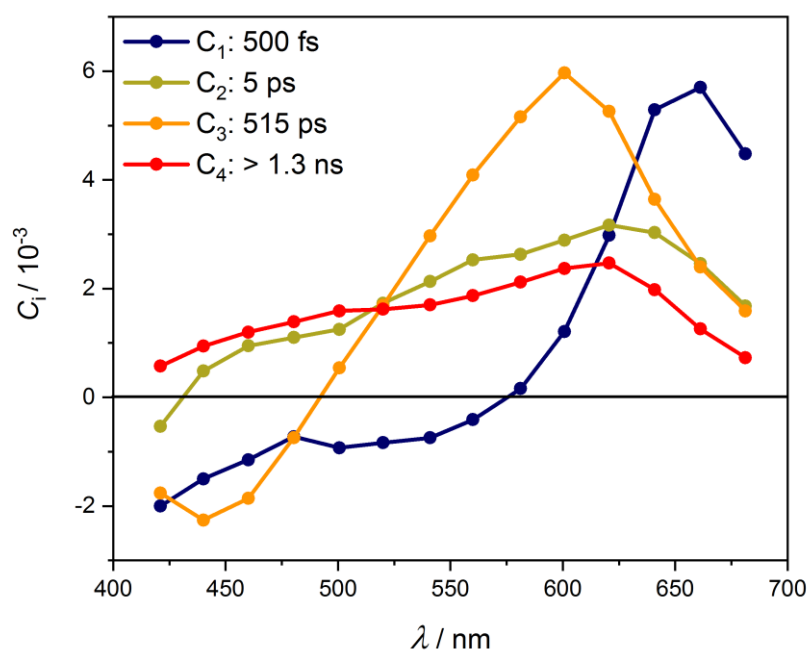


**Figure 6.9.** DAS obtained from multiexponential global analysis of the TA-spectrum of PyTet dissolved in DCM. Time constants  $\tau_i$  according to amplitudes  $C_i(\lambda, \tau_i)$  of four exponential functions as indicated.

Four time constants  $\tau_{1-4}$  are obtained from multiexponential fitting of single transient responses between 420 and 680 nm of PyTet in DCM. A negative amplitude  $C_i(\lambda, \tau_i) < 0$  reveals a rising and a positive  $C_i(\lambda, \tau_i) > 0$  a decaying transient response, respectively. A zero-crossing indicates an isosbestic point.

The dominant radiative singlet relaxation observed for TA-spectrum of PyTet (**Figure 6.7**) is represented by  $C_3(\lambda, \tau_3)$ , reflecting the correlation of the decay of ESA  $\sim 600$  nm with SE-recovery at  $\sim 430$  nm within 515 ps. The fourth process is associated with a slow decay of ESA exceeding the recorded time window of  $> 1.3$  ns observed on the entire spectrum from 420-680 nm. Thus, the recovery of SE is clearly superimposed by a long-living ESA, which is consistent with an increase to positive  $\Delta A$  within the region of the SE at  $\sim 430$  nm (**Figure 6.7**). Demonstrated by results from pump-probe experiments with PyTet in DCM:IEt-mixtures, the increase to positive  $\Delta A$  at  $\sim 430$  nm can be interpreted as a superposition of SE from radiative singlet relaxation and ESA from triplet states. Consequently, the ultrafast decay of the ESA shifting from 630 to 600 nm as well as the nonlinearly correlated SE recovery shifting from 420 to 430 nm originate from triplet state dynamics, reflected by  $C_1(\lambda, \tau_1)$ , and  $C_2(\lambda, \tau_2)$  (**Figure 6.9**).

$C_1(\lambda, \tau_1)$  is associated to an ultrafast decay within  $\sim 500$  fs between 575 and 680 nm, which is correlated with a broad rise in the region from 420 to 575 nm. Since SE is immediately observed after excitation (**Figure 6.7**), the ultrafast rise in 500 fs within the range of 420-575 nm is presumably not resulting from IC and VR of excited singlet states due to Kasha's rule.<sup>9</sup> Thus, the increase within 500 fs most likely stems from ISC into excited triplet states, which is consistent with the ultrafast ISC within 600 fs of Tet in DCM (refer to **section 6.2.1**).

The ultrafast ISC is also correlated to the decay of ESA between 575 and 680 nm (**Figure 6.9**), which is associated with the blue shift from 630 to 600 nm in the TA-spectrum (**Figure 6.7**). Consequently, the band shifting from 630 to 600 nm is a superposition of the increasing ESA from triplet and decreasing ESA from singlet states as indicated by the zero-crossing of  $C_1(\lambda, \tau_1)$  at  $\sim 575$  nm. The second process ( $C_2(\lambda, \tau_2)$ ) proceeds from VR and IC within triplet states, which is reflected by a fast decay within 5 ps on the entire TA-spectrum.

In accordance with TDDFT-calculations,<sup>30</sup> the broad TA-band from 400 to 720 nm observed in  $C_4(\lambda, \tau_4)$  is likely dominated by the transient responses of long-living triplet states, which are probed into a manifold of higher triplet states for long delay times. Thus, the ESA-band at 600 nm is a superposition of the decay of singlet states and the long-living ESA of triplet states. Herein, the decay of singlet state-ESA is accompanied by a slight red shift from 600 to 610 nm (**Figure 6.7**) as a plausible result of overlaying transient responses. In this scenario, the time constant  $\tau_3 \sim 515$  ps of the radiative singlet relaxation is superimposed with the slow decay of the long-living triplet ESA, which is possibly a reason for the deviation from singlet-lifetime of  $\sim 1.3$  ns recorded in TCSPC (**Figure C3**). The presented photophysical processes of PyTet in DCM are summarized in **Figure 6.10**.

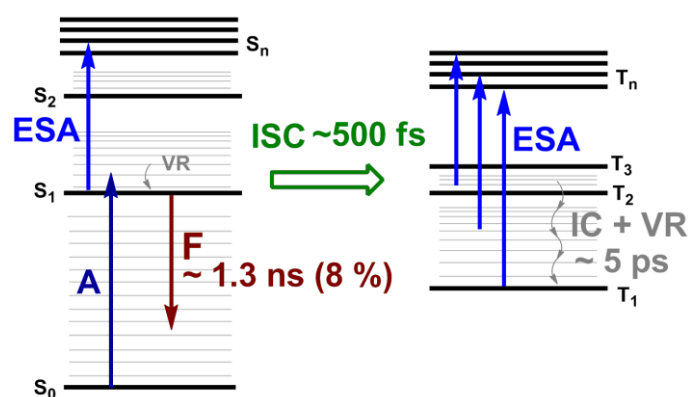


**Figure 6.10.** Jabłoński diagram schematically depicting the photophysical mechanism of PyTet.

In fact, triplet relaxation is not observed within the recorded time window. However, a clear evidence for the ultrafast ISC into a long-living triplet state is found, which is in line with expectations from theory.<sup>30, 46</sup> Subsequently, a ring-opening via triplet states would be expected, which leads to  $N_2$ -release and subsequent nitrile imine intermediate formation.<sup>46</sup> An ultrafast formation of a triplet state with diradical character is in accordance to a fs-study on structurally similar tetrazolium salts, which reveal diradical species within 1 ps.<sup>169</sup> However, a ring-opening leading to diradical states of PyTet in DCM is not observed within the presented set of data. Hence, the decomposition occurs on a longer time scale, which is in line with an observed decay of OD in steady-state UV/Vis spectroscopy before and after fs-experiments (**Figure C17a**). As a consequence, further investigations on the decomposition from triplet states are of high interest, e.g. anisotropy pump-probe<sup>170-171</sup>, pump-dump-probe<sup>172-173</sup> spectroscopy as well as time-resolved spectroscopy on ps to  $\mu$ s time scale.<sup>155, 174-175</sup>

## Towards Quantification of Fluorescence Quenching on PyTet in DCM:IEt-Mixtures

In general, the bimolecular fluorescence quenching mechanism based on HAE occurs by inducing SOC via an external perturbation. This depends on the overlap of free p-orbital electrons of a heavy-atom (iodine of IEt) and the  $\pi$ -system of the target.<sup>10-11</sup> Therefore, inducing SOC via HAE is a short-range interaction possessing a  $R^3$  dependency of the spin-orbital-operator for a Coulomb-field.<sup>10</sup> Thus, an efficient overlap of orbitals of quencher and target molecules depends on the concentration ratio, resulting in two scenarios: 1) diffusion-controlled perturbation by collisions, called dynamic quenching, or 2) frequently repeated perturbations within a molecular cage, known as static quenching.<sup>11</sup> Consequently, a concentration dependent screening is necessary for the characterization of the quenching mechanism of PyTet in DCM:IEt mixtures.

Herein, single transient responses of PyTet in different DCM:IEt mixtures as well as the reference experiment with TEMPO are analyzed at 450 nm by a multiexponential fitting routine as presented in **Figure 6.11** (corresponding TA and UV/Vis-spectra in **Figure C7**, **Figure C8** and **Figure C9**). The corresponding time constants are provided in **Table 6.1**. In agreement with global analysis,  $\tau_1$  and  $\tau_2$  are determined to a few ps for all samples. However, the TA-spectra of PyTet in DCM:IEt mixtures are convoluted with the transient response of IEt within the first ps (refer to **Figure C11**), rendering quantitative comparison of  $\tau_1$  challenging. Differences in  $\tau_2$  accord to a varied VR due to the influence of the specific solvent mixtures, e.g. caused by the influence of a collision-complex with the quencher molecule.  $\tau_3$  reflects the SE-recovery superimposed by triplet ESA featuring a decreasing trend from ~430 to ~220 ps for an increasing concentration of the quencher. In addition, the relative amplitudes scale from 0.35 to 0.50 with increasing quencher amount (**Table 6.1**). Thus, a decrease of  $\tau_3$  accompanied by an increase of  $A_3^{rel}$  results in a stronger and faster SE-recovery, which is consistent with the decreasing trend of  $\Phi_F$  with higher IEt-concentration obtained from steady-state spectroscopy (**Figure 6.2**, **Figure C4**).  $\tau_3$  of PyTet in DCM:IEt mixtures (II) and (III) are very similar indicating saturation of collisions between quencher and target molecules.

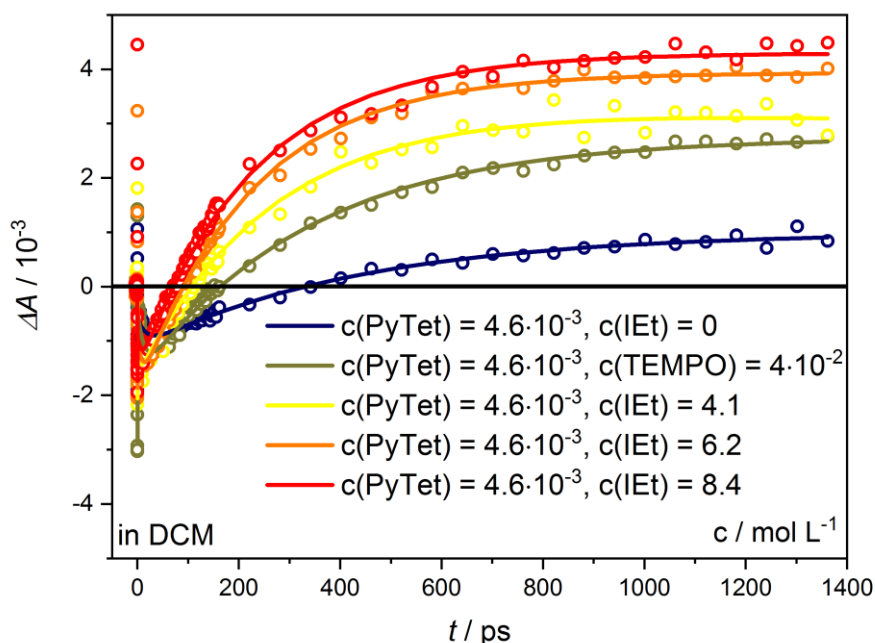


**Figure 6.11.** Transient response of PyTet dissolved in various DCM:IEt mixtures at 450 nm for analyzing SE-quenching influence of IEt. In addition, reference experiment of PyTet dissolved in DCM with TEMPO as quencher for validation purposes (olive line). PyTet, TEMPO, and IEt concentrations as indicated. Obtained time constants  $\tau_3$  from multiexponential fitting routine as depicted from blue to red are between 430-220 ps (refer to **Table 6.1**).

**Table 6.1.** Time constants are obtained from multiexponential fitting routine with four time constants. The concentration of PyTet is constant in all experiments (  $4.6 \cdot 10^{-3} \text{ mol L}^{-1}$  ). The concentration of TEMPO in the reference experiment of PyTet in DCM was  $c(\text{TEMPO}) = 4 \cdot 10^{-2} \text{ mol L}^{-1}$ . PyTet dissolved in DCM:IEt mixtures with increasing  $c(\text{IEt})$  from top to bottom, e.g. (I) 4.1, (II) 6.2, and (III) 8.4  $\text{mol L}^{-1}$ .

solvent (PyTet)	$\tau_1 /$ ps	$ A_1^{rel} $ (rise)	$\tau_2 /$ ps	$ A_2^{rel} $ (decay)	$\tau_3 /$ ps	$ A_3^{rel} $ (rise)	$\tau_4 /$ ns	$ A_4^{rel} $ (decay)
DCM	0.2	0.30	17	0.14	433	0.35	>1.3	0.20
DCM+TEMPO	0.3	0.28	13	0.11	337	0.38	>1.3	0.23
(I) DCM:IEt	0.2	0.14	4	0.06	269	0.48	>1.3	0.32
(II) DCM:IEt	0.4	0.09	9	0.09	222	0.49	>1.3	0.33
(III) DCM:IEt	0.2	0.09	8	0.05	228	0.50	>1.3	0.36

Quenching with TEMPO reveals an increase of  $\tau_3$  by a factor 1.5 compared to DCM:IEt (II). Regarding two orders of magnitude smaller TEMPO-concentration, the quench efficiency per TEMPO-molecule is by a factor of  $\sim 70$  higher compared to IEt. In fact, the quenching mechanism of TEMPO is presumably more complex in comparison to HAE of IEt due to additional relaxation pathways via doublet states. For example, in a recently published work, the intramolecular fluorescence quenching mechanism of stabilized nitroxide radicals is described by a dominant relaxation pathway via a dark doublet state, while ISC is only a minor side process.<sup>168</sup> Thus, the higher fluorescence quenching efficiency is most likely a result of additional relaxation pathways. Consequently, the assignment of a triplet state by using TEMPO in fs-TA experiments is not straightforwardly possible due to a more complex channel branching, which has to be considered. In comparison, the quenching mechanism of IEt is simply based on increasing the singlet-triplet transitions via HAE, which exactly corresponds to the purpose of uncovering the weak transient responses of a triplet state in the presence of dominating singlet dynamics. Apart from that, TEMPO suffers from low solubility in DCM, while IEt can be utilized as a solvent leading to very high quencher concentrations. High quencher concentrations are important to enable quencher experiments in fs-TA as described in the following.

Diffusion-controlled bimolecular interactions occur in the order of  $k_{\text{Diffusion}} \sim 10^{10} \text{ s}^{-1} \text{ M}^{-1}$ .<sup>176</sup> Thus, very high quencher concentrations (here 4-8 mol L<sup>-1</sup>) are necessary to observe bimolecular interactions in fs-TA experiments within tens of ps. However, at high concentrations additional undesired processes can occur, e.g. molecular stacking leading to self-quenching, or dimer/excimer formation.<sup>160-161, 163</sup> Hence, reference transient pump-probe spectra of PyTet in DCM:IEt mixtures at low concentrations are conducted (refer to **Figure C12**). The TA-spectra of PyTet in DCM at one order of magnitude lower concentration ( $c(\text{PyTet}) = 2.2 \cdot 10^{-4} \text{ mol L}^{-1}$ ) is presented in **Figure 6.12**.

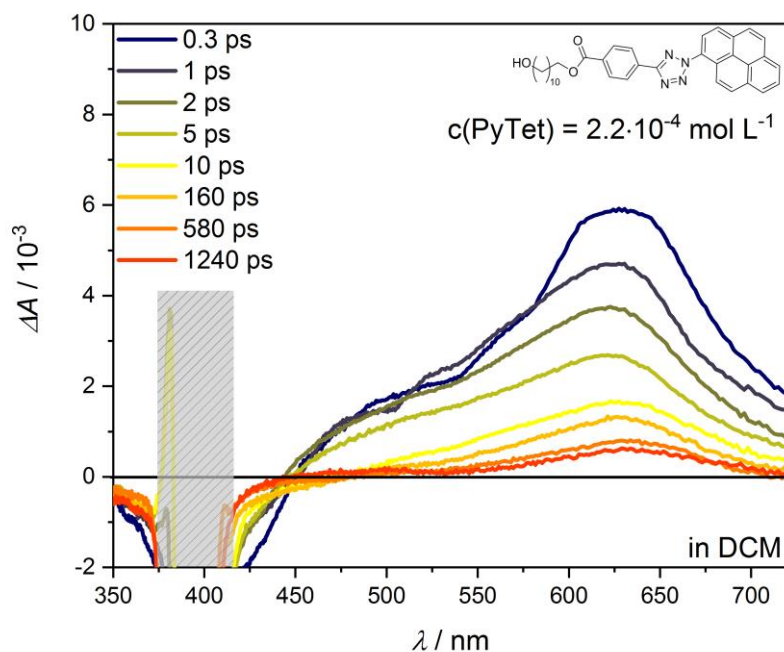


**Figure 6.12.** Transient spectrum of PyTet dissolved in DCM pumped at 400 nm (3.1 eV) and probed with a CaF<sub>2</sub>-white light continuum between 350 and 720 nm. Time delays and concentration of PyTet as indicated. Region at 400 nm omitted due to scattering from pump pulse.

In principle, the recorded TA-spectra of PyTet in DCM at low concentrations are in-line with the discussion above at higher  $c(\text{PyTet}) = 2.6 \cdot 10^{-3} \text{ mol L}^{-1}$ . Herein, the TA-spectrum is strongly dominated by SE and corresponding ESA of the decaying singlet state at  $\sim 430$  and  $\sim 600$  nm, respectively. Thus, undesired concentration-dependent side-reactions of PyTet are not observed within the resolution of the experiment, e.g. dimer or excimer formation. In contrast to the TA-spectrum of PyTet in DCM at higher concentrations, the TA-spectrum for lower concentrations reveals a much stronger superposition of GSB and scattering from pump pulse in the region of the SE. GSB at  $\sim 350$  nm does not recover back to zero within the recorded time window, which is characteristic for ultrafast singlet depopulation via ISC into long-living triplet states (**Figure C13**). However, absence of GSB recovery could also be the result of a long-living singlet state, which is the dominant response in the TA-spectrum. In addition, a significant triplet ESA-band in the region of the SE is not observed. Thus, the transient response of the triplet state is not resolved within the sensitivity of the conducted experiments at low PyTet-concentrations due to the much stronger transient responses of the corresponding singlet dynamics.

To access the quencher influence on the superposition of SE and triplet ESA, single transient responses are analyzed at 430 nm for low and high quencher concentrations (refer to **Figure 6.13**, corresponding TA- and UV/Vis-spectra in **Figure C12**).

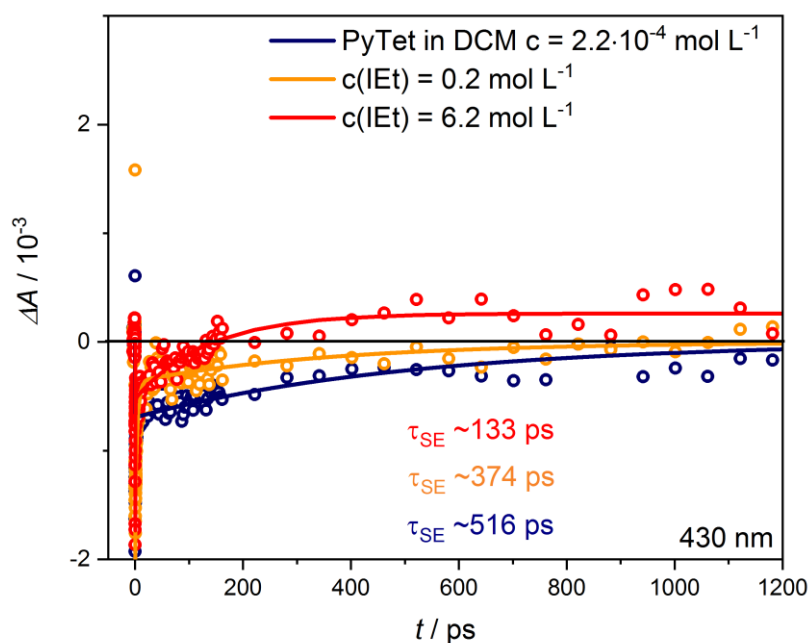


**Figure 6.13.** Transient response of PyTet dissolved in various DCM:IET mixtures at 430 nm for analysis of SE-quenching influence of IET at low concentrations. Time constants obtained from multiexponential analysis with two (blue), three (orange), and four (red) exponential functions.

As expected for a low  $c(\text{IET}) = 0.2 \text{ mol L}^{-1}$  resulting in an estimated  $\tau_{\text{Diffusion}}$  of  $\sim 500 \text{ ps}$ , the quenching effect of IET on the SE of PyTet for low concentration is comparably weak. The determined time constants for the SE-recovery are consistent with  $\tau_3$  (refer to **Table 6.1**). Herein, a decreasing trend is observed for an increasing quencher concentration. However, a significant increasing ESA  $> 0$  is only observed for high IET concentrations and, in turn, the comparably weak triplet ESA is not well-resolved within the limits of the experiment  $\sim 1:10^4$ . A better signal-to-noise ratio could be achieved in the future using an additional detector (CCD camera) to record zero-reference spectra.

In conclusion, investigation of fluorescence quenching of IET on PyTet in DCM is in principle possible with ultrafast pump-probe techniques. However, the in-depth characterization and quantification of fluorescence quenching effects is challenging. HAE

of IET is a diffusion controlled process, which can only be recorded on a ps-time scale at very high sample concentrations. Based on the current set of data, a distinction between a static and a dynamic quench mechanism is not possible, which would require further concentration- and especially temperature-dependent investigations. Undesired concentration-dependent processes are not observed, e.g. dimer or excimer formation of PyTet. However, the sensitivity of the fs-TA experiment at low concentrations of PyTet is not sufficient enough to resolve the comparably small transient response, e.g. triplet ESA. An alternative approach to elucidate singlet-triplet branching in singlet-dominated TA-spectra is pump-dump-probe spectroscopy.<sup>172-173</sup> An advantage of this method is the deactivation of the SE-channel without introducing an additional quencher molecule, excluding undesired bias on the excited state dynamics of the investigated system.

### 6.2.3 BiphTet in DCM

In the following the excited state dynamics of BiphTet in DCM are investigated by fs-TA. The corresponding steady-state UV/Vis spectrum of BiphTet in DCM is presented in **Figure 6.14**.

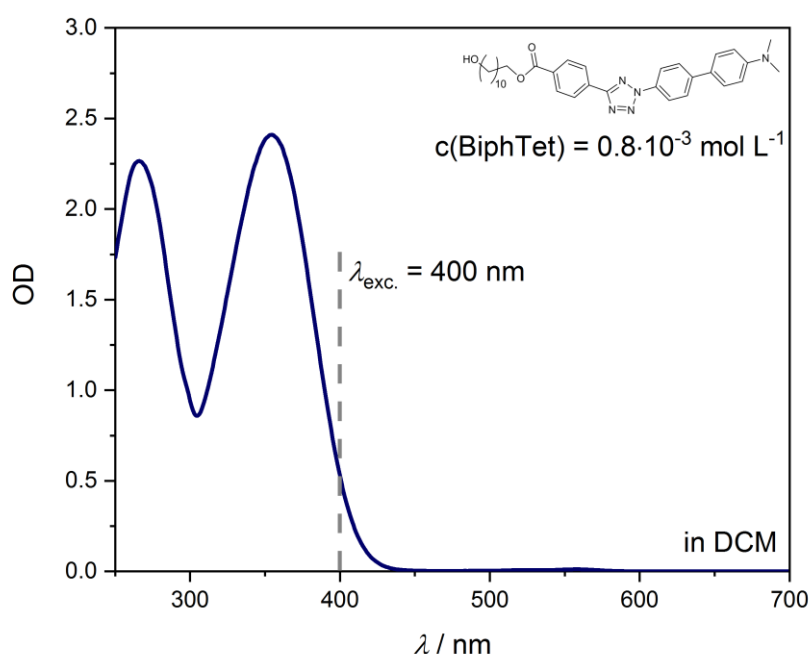


**Figure 6.14.** UV/VIS spectrum of BiphTet dissolved in DCM as used for fs-TA at an excitation wavelength of 400 nm as indicated by the grey dashed line.

In comparison to theory, excitation at 400 nm within the red wing of the absorption maximum leads to low vibrational states corresponding to  $S_1$ . The TA-spectrum of BiphTet dissolved in DCM ( $c(\text{BiphTet}) = 0.8 \cdot 10^{-3} \text{ mol L}^{-1}$ ) is presented in **Figure 6.15**.

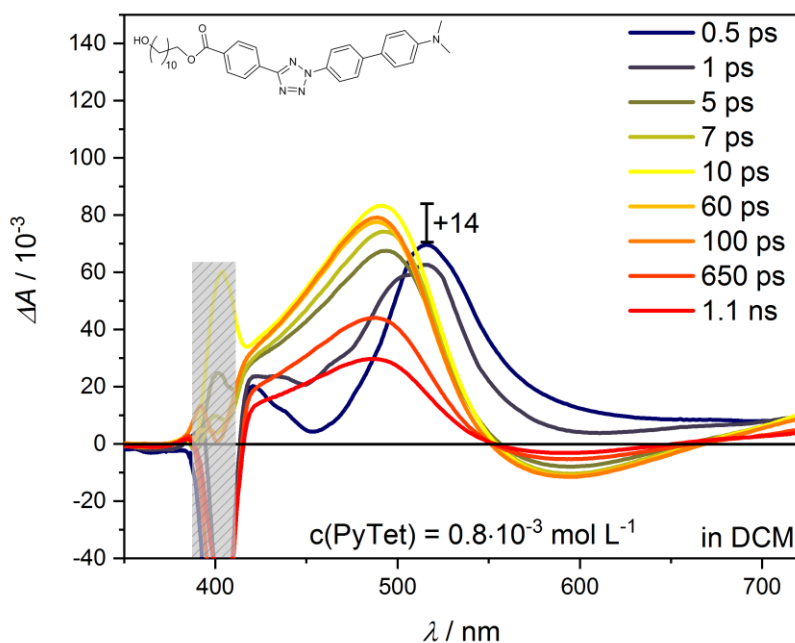


**Figure 6.15.** Transient spectra of BiphTet dissolved in DCM pumped at 400 nm (3.1 eV) and probed with a  $\text{CaF}_2$ -white light continuum between 350 and 720 nm. Time delays and concentration of PyTet as indicated. Region at 400 nm omitted due to scattering from pump pulse. Black line indicates the change in  $\Delta A$  of  $14 \cdot 10^{-3}$  after blue shift of ESA.

The region at 400 nm is omitted due to scattering of the pump pulse. Transient responses at wavelengths  $< 390 \text{ nm}$  are vanished by the strong absorption of the sample. After excitation at 400 nm, the excited state dynamics of BiphTet in DCM are probed with a  $\text{CaF}_2$ -white light continuum between 350 and 720 nm. Remarkably, very high  $\Delta A$  are recorded, reflecting very high oscillator strengths for transitions into higher excited states for BiphTet in DCM. However, to exclude a concentration-dependence, TA-spectra of BiphTet in DCM at lower concentrations ( $c(\text{BiphTet}) = 3 \cdot 10^{-4} \text{ mol L}^{-1}$ ) were recorded (refer to **Figure C15**), revealing the same behavior as discussed in the following.

Immediately after excitation, a broad ESA-band from 410 to 720 nm peaking at  $\sim 520 \text{ nm}$  is observed, which undergoes a blue shift to  $\sim 490 \text{ nm}$  accompanied by an increase of  $\Delta A$  ( $+14 \cdot 10^{-3}$ ) within a few ps. In addition, two local minima at  $\sim 600 \text{ nm}$

and ~455 nm indicate a negative response, which are superimposed with the broad ESA-band at early times.

In comparison to the steady-state UV/Vis spectrum of BiphTet in DCM, GSB is mainly expected below 400 nm, which is in line with TA-spectra of BiphTet in DCM at low concentrations (refer to **Figure C15**). In addition, superposition with GSB up to 420 nm cannot be excluded.

Steady-state fluorescence spectroscopy of BiphTet in DCM reveals a very broad emission band between 420 and 700 nm, which is peaking at ~520 nm (refer to **Figure 6.2b**). Thus, both local minima at ~455 and 600 nm are most likely superimposed by SE according to a strong fluorescence channel ( $\Phi_F \sim 11\%$ ). Consequently, the ultrafast blue shift of the ESA within a few ps results from superposition of SE and (vibrational) relaxation processes of ESA, which makes the assignment of the exact position of the SE minimum and the ESA maximum cumbersome.

On longer time scales, the ESA peaking at 490 nm decays correlating to the recovery of SE at ~600 nm as indicated by an isosbestic point at 490 nm. A relatively weak ESA-band at ~700 nm is a residuum of the broad ESA-band corresponding to the ESA-decay and SE-recovery as suggested by a second isosbestic point at 690 nm. In line with TDDFT-calculations from literature,<sup>30</sup> the ESA-band can be assigned to a long-living  $S_1$ , which is probed into a manifold of higher excited singlet states. The main relaxation channel occurs via SE according to the strong fluorescence pathway. The ESA-band peaking at 440 and 720 nm is clearly correlated to the SE at 600 nm as revealed by biexponential global analysis (**Figure 6.16**).

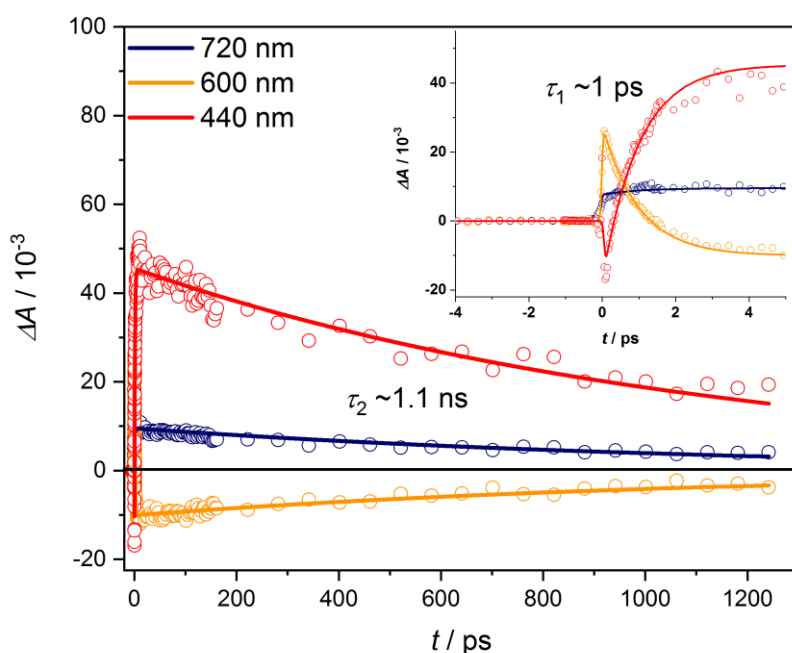


**Figure 6.16.** Transient response of BiphTet dissolved in DCM recorded at 720, 600 and 440 nm after excitation at 400 nm (3.1 eV). Transient response at 720 and 440 correspond to the same ESA-band, which is superimposed by SE at 600 nm. Decay of ESA-band is correlated to SE-recovery within  $\sim 1.1$  ns. Inset figure: Ultrafast VR within singlet states corresponding to strong blue shift (refer to **Figure 6.15**).

The first time-constant from global analysis reflects the ultrafast relaxation process from ESA accompanied by a blue shift within 1 ps. The second time-constant of  $\sim 1.1$  ns can be assigned to the decay of singlet ESA, which is correlated to the SE-recovery associated to a radiative relaxation pathway. Hence, the SE-lifetime is in a similar order of magnitude with the fluorescence lifetime of  $\sim 1.8$  ns measured in TCSPC (refer to **Figure C3**). The findings are in accordance with GSB-recovery observed for BiphTet in DCM at low concentrations, which is correlated to the decay of excited singlet state dynamics (refer to **Figure C16**). In addition, no evidence for an additional process is observed. Thus, the TA-spectrum of BiphTet shows dominant singlet dynamics. In consequence, the first time constant of  $\sim 1$  ps can be assigned to VR within singlet states. Steady-state UV/Vis spectra of BiphTet in DCM recorded before and after fs-experiments show a decomposition of BiphTet as indicated by a decreased OD after fs-TA experiment (refer to **Figure C17b**). However, this process is not observed within the recorded time window and has to occur in a post-ns regime. As known from literature,<sup>30</sup> BiphTet is incapable to induce an efficient NITEC.

Consequently, the decomposition of BiphTet leads to undesired products without significant NITEC-reactivity.

In fact, the striking evidence for the absence of an ISC into triplet states is given by recording the transient spectrum of BiphTet in DCM:IEt mixtures as showed in **Figure 6.17** (for further DCM:IEt mixtures refer to **Figure C15**).

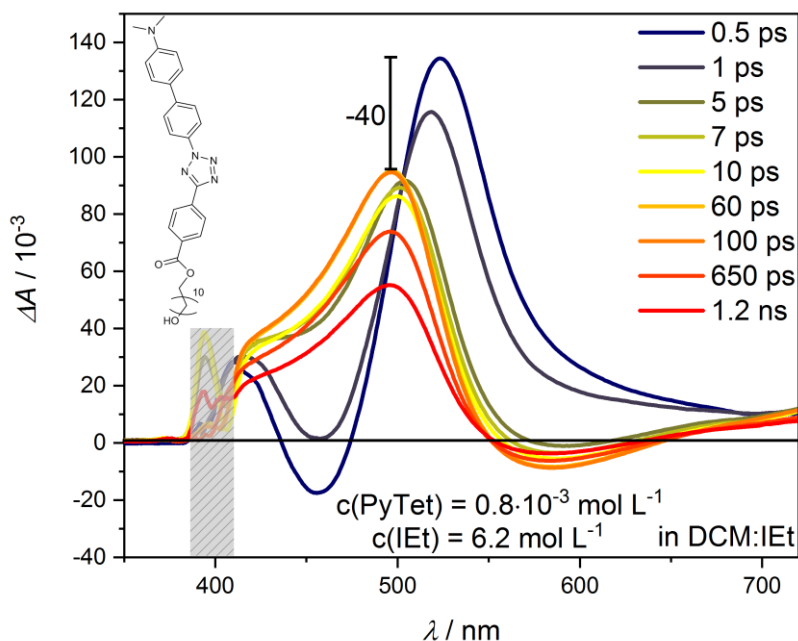


**Figure 6.17.** Transient spectra of BiphTet dissolved in DCM:IEt mixture pumped at 400 nm (3.1 eV) and probed with a CaF<sub>2</sub>-white light continuum between 350 and 720 nm. Time delays and concentration of PyTet and IEt as indicated. Region at 400 nm omitted due to scattering from pump pulse.

All main features of the TA-spectrum of BiphTet in DCM are reflected in the DCM:IEt mixture ( $c(\text{PyTet}) = 0.8 \cdot 10^{-3} \text{ mol L}^{-1}$ ,  $c(\text{IEt}) = 6.2 \text{ mol L}^{-1}$ ) as well. For instance, an ultrafast blue shift of ESA from 520 to 490 nm as well as a slow decay of ESA peaking at 490 and 700 nm are observed, which correlate to the SE-recovery with a minimum at ~600 nm. In contrast, the ultrafast blue shift is accompanied by a decrease in  $\Delta A$  ( $-40 \cdot 10^{-3}$ ). In addition, the change in  $\Delta A$  depends on the quencher-concentration as reflected by an decrease of -11 at  $c(\text{IEt}) = 3.1 \text{ mol L}^{-1}$  depicted in **Figure C14**. In contrary to the quencher studies on PyTet (refer to **section 6.2.2**), the TA-spectrum of BiphTet in DCM:IEt mixtures reveals no additional ESA-band, which would be expected for an ISC into triplet states. Thus, no quenching effect of IEt is observed,

which is in accordance with results of  $c(\text{IEt})$ -dependent steady-state fluorescence spectroscopy (refer to **section 6.1**). In addition, the absence of ISC is in agreement with expectations from TDDFT-calculations predicting unfavorable energy gaps between singlet and triplet states due to symmetry reasons.<sup>30</sup> However, IEt influences the potential energy surfaces of the excited states of BiphTet in DCM indicated by differences in  $\Delta A$  before and after VR within singlet states compared to BiphTet in DCM without additional quencher. Thus, the contour-plots for early times of BiphTet in a) DCM and b) DCM:IEt-mixture are presented in **Figure 6.18**, which show the influence of IEt on VR within  $S_1$ .

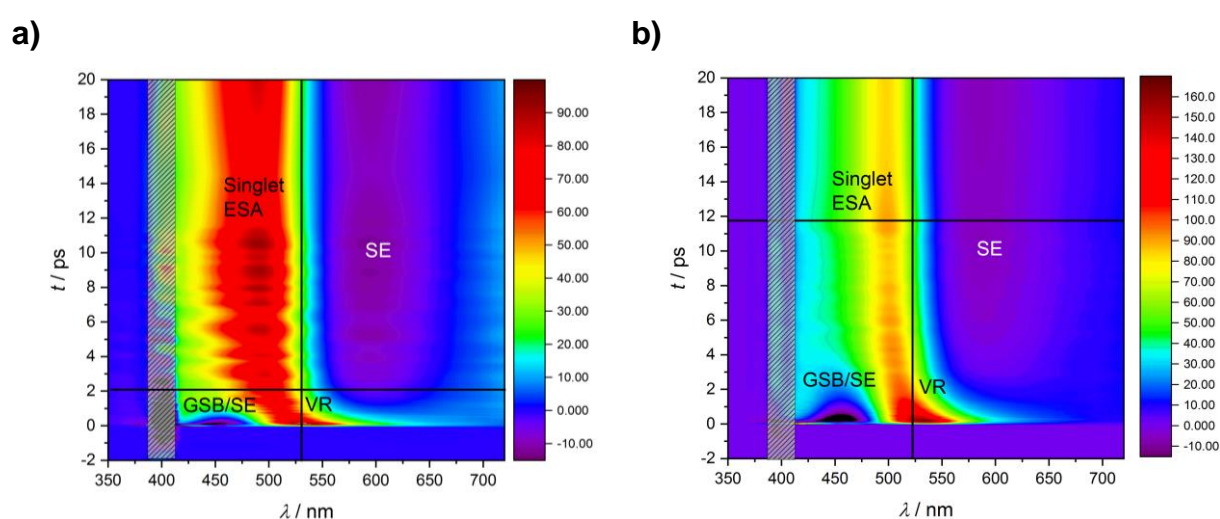


**Figure 6.18.** Contour-plot of BiphTet dissolved in a) DCM and b) DCM-IEt mixture revealing differences in VR in the presence of IEt. For quantitative analysis refer to **Figure C16**.

Despite of changes in the  $\Delta A$ -scale, the blue shift according to VR within  $S_1$  of BiphTet occurs on a longer time scale in the presence of IEt indicated by the temporally delayed crossing of black lines for **Figure 6.18b**) in comparison to **a**). As a consequence of the slower shift, the superposition with GSB/SE-response possessing a minimum at  $\sim 450$  nm is more pronounced. By inspecting the single transients at 720, 600 and 440 nm an additional time constant of 7 ps is observed (**Figure C16**). Thus, the change in the VR of  $S_1$  is plausibly caused by in-cage-solvent interactions with IEt due to the high concentrations of  $6.2 \text{ mol L}^{-1}$ . In conclusion, IEt interacts with BiphTet without quenching the fluorescence. Consequently, HAE of IEt has no influence on the singlet-triplet branching of BiphTet clearly demonstrating that ISC is quite unlikely process, as confirmed from TDDFT-calculations.<sup>30</sup> The photophysics of BiphTet in DCM are summarized in **Figure 6.19**.

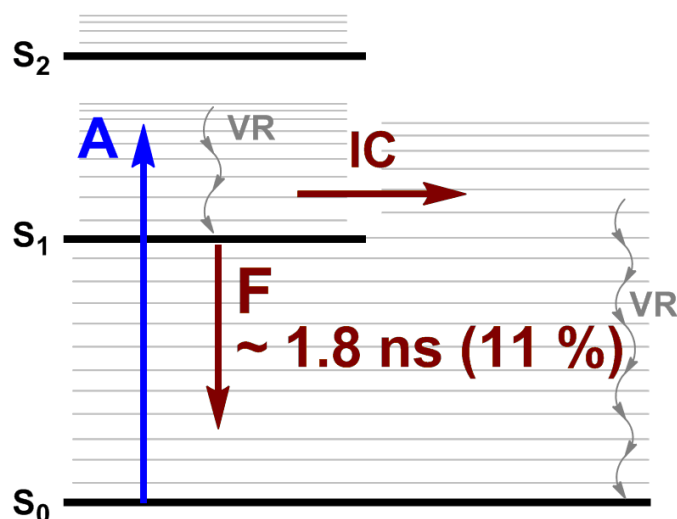


**Figure 6.19.** Jabłoński diagram depicting schematically the photophysical mechanism of BiphTet.

#### 6.2.4 Summary and Outlook: Visible Light-Triggered Diaryl-Tetrazoles

Visible light-triggered PyTet and BiphTet dissolved in DCM are investigated via fs-TA, TCSPC, and steady-state UV/Vis absorption as well as fluorescence spectroscopy. Efficient UV-triggered Tet in DCM was used as reference system. Depending on the chromophore, PyTet is an efficient precursor for NITEC, while BiphTet is known for weak NITEC-reactivity. PyTet and BiphTet dissolved in DCM show strong fluorescence relaxation pathways from excited singlet states after excitation at  $\sim 400$  nm with lifetimes of 1.3 and 1.8 ns with quantum yields  $\Phi_F$  of 8 and 11 %, respectively.

By using the heavy-atom effect (HAE) of iodoethane (IEt) as a fluorescence quencher,  $\Phi_F$  of PyTet is reduced to 6.7 % at an IEt-concentration of  $\sim 0.1$  mol L<sup>-1</sup>, while BiphTet reveals no change in  $\Phi_F$ . For utilizing fluorescence quenching in fs-TA experiments much higher IEt-concentrations (4-8 mol L<sup>-1</sup>) are necessary to achieve a sufficient probability for collision-induced HAE. Herein, fs-TA spectra of PyTet in DCM reveal a reduced stimulated emission (SE) due to singlet relaxation via fluorescence in the presence of IEt, while an additional unaffected excited triplet state absorption is elucidated. This finding is confirmed by using tetramethylpiperidineoxyl (TEMPO) as an alternative quencher molecule. ISC is estimated to occur on a time scale shorter than 1 ps, which is in line with findings for the UV reference system Tet. In contrast, the SE due to fluorescence of BiphTet in DCM remains unaffected in the presence of IEt. In summary, PyTet as well as Tet featuring an efficient NITEC reac-

tivity and reveal an ultrafast ISC, while inefficient BiphTet is clearly dominated by singlet relaxation. The findings are in accordance with TDDFT calculations.<sup>30, 46</sup>

The investigation has demonstrated that utilizing fluorescence quenchers (IEt, TEMPO) in fs-TA presents an efficient approach to investigate the channel branching between long-living singlet and triplet states. However, a quantitative approach is sophisticated due to the need of very high quencher concentrations to observe bimolecular processes on a ps-time scale. High concentrations can lead to undesired molecular stacking, which could change the quenching-effect. Thus, the distinction between static and dynamic quenching processes would require further investigations, e.g. more comprehensive temperature- and concentration-dependent screenings. A quantitative time-resolved characterization on the quenching mechanism of IEt could be achieved by fluorescence up-conversion experiments, which enables the interference-free detection of fluorescence relaxation pathways.<sup>177-178</sup> An alternative to elucidate the singlet-triplet branching in strongly SE-dominated molecules without using a quencher would be a pump-dump-probe experiment, whereby the singlet population is depleted by SE induced by a third laser pulse.<sup>172-173</sup>

## 7. Outlook: Visible Light-Triggered Precursor Molecules

The presented approach clearly shows that relating reactivity with ultrafast dynamics is of striking importance for the mechanistic understanding of photo (visible light-) triggered precursor molecules. The fate of the investigated visible light-triggered precursors is determined immediately after photoexcitation. Remarkably, a sufficient ISC is important for efficient acylgermanes as well as diaryl-tetrazole systems, which depends highly on the relative position of potential energy surfaces within the relevant excited states. Based on the findings of the present thesis, the major possibilities and challenges for the design of visible light precursor molecules are emphasized in the following.

### Towards the Ideal Potential Energy Surface Topology of Visible Light-Triggered Precursor Molecules

Bathochromic absorption properties of a molecule are achieved for small energy gaps between the ground and the first excited singlet state, which increases the probability for deactivation via IC, e.g. ultrafast relaxation of NB<sub>1</sub>G within 2 ps. On the other hand, visible light chromophores with stabilized excited singlet states do not necessarily lead to a sufficient reactivity due to a probable fluorescence relaxation pathway, e.g. BiphTet. Further, unfavored decomposition of the precursor molecule can compete with the intermediate formation, e.g. decomposition of Mes<sub>4</sub>T from singlet states competing with ISC. Thus, a sufficient interaction between the excited singlet state and the potential energy surface of the desired intermediate state is crucial. The intermediate formation for efficient acylgermanes and diaryl-tetrazoles is considered to occur from excited triplet potential energy surfaces. In comparison to literature,<sup>30-31, 35</sup> ISC is sufficient for small energy gaps between excited singlet and triplet states.

In particular, mono-, bis-, and tetraacylgermanes reveal a non-stoichiometric size dependence in the overall initiation efficiency. In a simplified picture, each benzoyl moiety contributes with one singlet state within the  $n\pi^*$ -band and one lower lying triplet state to the excited state topology. Thus, the result of a non-stoichiometric size dependence suggests a more complex mechanism than expected solely from an additive effect of the  $n\pi^*$ -contributions. Instead, it seems to be a synergetic effect be-

tween the benzoyl moieties, i.e. more than just the sum of four moieties, which deserve further investigations.

Finally, an ultrafast ISC is not necessarily a guarantee for an efficient intermediate formation. For instance, monoacylgermanes reveal a factor  $\sim 0.5$  lower overall initiation efficiency compared to bisacylgermanes, despite of a factor 10-20 faster ISC. In fact, the highest overall initiation efficiency of tetraacylgermanes (factor of  $\sim 8$  for  $B_4G$  versus  $B_1G$ ) can be correlated to much faster radical formation within 70-127 ps from triplet states in comparison to bis- and monoacylgermanes (radical formation on a post ns-scale). Thus, the potential energy surface of the triplet state must feature a sufficiently low energy barrier along the coordinates leading to radical formation.

In conclusion, efficient visible light-triggered precursor systems provide an energy surface topology with a suitable relaxation pathway leading to the formation of the desired intermediates. This pathway must not necessarily be the major contribution to the channel branching. In fact, a sufficient ISC from a low singlet state into a close adjacent triplet state with a low energy barrier is an efficient pathway for intermediate formation despite the competition with IC or fluorescence. Future investigations should focus on the question of whether a general concept for time scales can be found which lead to an efficient mechanism for visible light-triggered precursor molecules.

### **Possible Future Investigations on Photophysical and -Chemical Properties**

The intermediate formation from triplet states can occur on time scales longer than the recorded temporal window of  $\sim 1$  ns of the applied fs-TA experiment, e.g. mono- and bisacylgermanes as well as  $N_2$ -release of diaryl-tetrazoles. Thus, extending the assessable time window from fs to ms<sup>179</sup> would enable the observation of the photophysical and -chemical dynamics starting from light absorption to final product formation, e.g. for investigation of the (multiple) cleavage mechanism of mono-, bis- and tetraacylgermanes. In addition, fluorescence upconversion<sup>177-178</sup> and transient NIR-spectroscopy<sup>180</sup> could enable a more quantitative investigation of competing fluorescence pathways and the detection of far red shifted responses of triplet states as well as radical fragments, respectively. Pump-dump-probe experiments<sup>172</sup> are a promising alternative to triplet dynamics uncovering via external HAE, which circumvents unde-

sired concentration effects due to the very high quencher concentrations of 4-8 mol L<sup>-1</sup>.

### **Systematic Synthesis for Supporting the Development of Photophysical and -Chemical Mechanisms**

As a task for synthesis, the development of a photophysical and -chemical mechanism gains from the systematic analysis of as simple as possible designed model systems, which can iteratively be increased in their degree of complexity, e.g. non-fluorescent UV-tetrazole as a reference system for fluorescent visible light systems PyTet and BiphTet, or acylgermanes bearing one, two or four benzoyl moieties.

Within the present thesis, a remarkable non-stoichiometric increase scaling with the number of benzoyl moieties in acylgermanes was observed. Thus, a further proof of concept could be achieved by synthesis of photoinitiators bearing a higher number than four benzoyl moieties.

Further, mainly *para*-substituted acylgermanes were investigated, which reveal high overall initiation efficiencies but suffer from hypsochromic shifts. In contrast, acylgermanes with substitution patterns in *ortho*-position show an increased overall initiation efficiency in comparison to unsubstituted acylgermanes as shown for one experiment  $m(oMeB_4G:B_4G) \sim 1.3$  (refer to **section 4.3.5**), while the absorption spectrum is slightly bathochromic shifted compared to B<sub>4</sub>G (refer to **Figure 4.33**). In addition, fs-TA experiments reveal a faster ISC and primary radical formation for oEtB<sub>4</sub>G of 3 and 90 ps than for B<sub>4</sub>G of 9 and 127 ps, respectively. Thus, a systematic investigation on the influence of *ortho*-substituents on the overall initiation efficiency of acylgermane derivatives via PLP-ESI-MS cocktail experiments would be interesting.

### **Studying Wavelength-Dependent Photochemistry via PLP( $\lambda$ )-ESI-MS and fs-TA Experiments**

Within the present thesis, the overall initiation efficiencies of photoinitiators is obtained at the  $n\pi^*$ -maxima of the applied initiator pair. However, a comprehensive screening of the wavelength-dependence of photoreactions can enable a new approach for the design of visible light photoinitiators as shown by promising results of a red shifted highest monomer conversion compared to the wavelength of the corresponding absorption maximum for bisacylgermanes (refer to **section 4.5.1**) as well as for exam-

ples from literature.<sup>14</sup> Thus, the PLP-ESI-MS cocktail experiments could be conducted dependent on the wavelength. In addition, a wavelength-dependent investigation of ultrafast dynamics via fs-TA would be feasible by a more sophisticated combination of frequency conversion processes, e.g. NOPA combined with SFM.

### **Investigations on the Light Source: PLP with fs-Lasers**

Finally, feasible PLP-studies conducted with a fs-Laser on MB<sub>2</sub>G and B<sub>4</sub>G show a factor 2 higher MMA-conversion compared to common ns-PLP experiments. Thus, a further future perspective could be the investigation on the influence of the light source on the initiation efficiency and channel branching of visible light-triggered initiators (for further details refer to **section 4.5.2**).

## A. Appendix of Chapter 4

### Comparison of Time-Dependent Density Functional Theory of Bis- and Tetraacylgermanes and UV/Vis absorption spectra

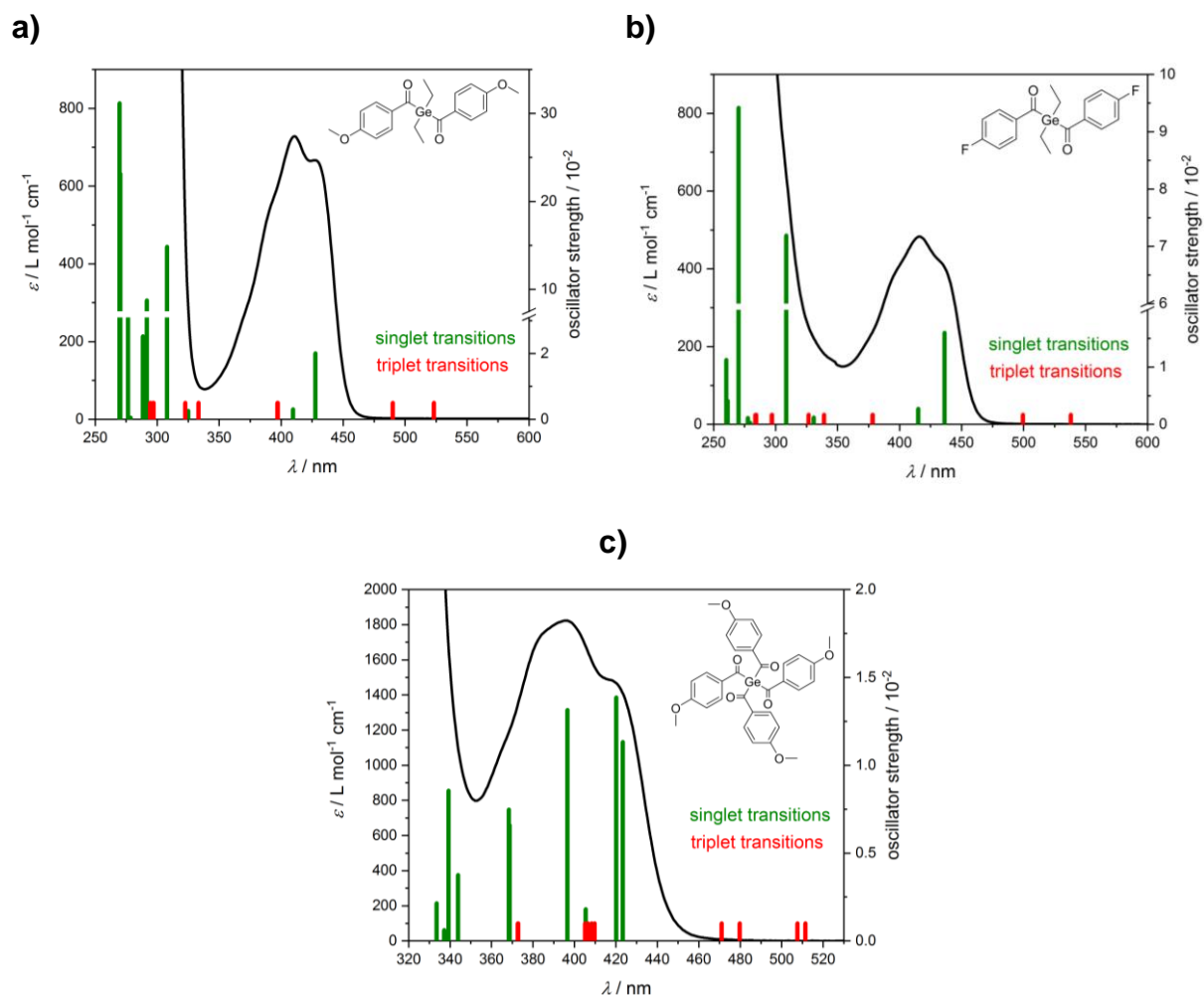


**Figure A1.** Absorption spectra (black) recorded in MMA as solvent. Singlet (green) and triplet (red) transitions calculated by TDDFT (def2-TZVPP/B3LYP) for a) MB<sub>2</sub>G, b) FB<sub>2</sub>G, and c) MB<sub>4</sub>G in gas-phase. Adapted with permission from ref. 146. Copyright 2019 American Chemical Society. Modified presentation.

**Table A1.** Optimized DFT (def2-TZVPP/B3LYP) Gas-phase geometries of ground states of B<sub>2</sub>G and MB<sub>2</sub>G used for vertical excited energies calculations via TDDFT. Adapted with permission from ref. 146. Copyright 2019 American Chemical Society. Modified presentation.

B <sub>2</sub> G (Cartesian coordinates)				MB <sub>2</sub> G (Cartesian coordinates)			
C	0.1328548	0.5498954	-0.8160597	C	-0.3294238	0.4997140	-0.1348476
C	1.4051805	0.8835420	-1.2698486	C	0.6733666	1.3332645	-0.5749271
C	2.5198483	0.6014938	-0.4902505	C	1.1166736	1.2593210	-1.9045926
C	2.3667771	-0.0153761	0.7521308	C	0.5384312	0.3372023	-2.7783024
C	1.1028827	-0.3463544	1.2085219	C	-0.4666671	-0.5037684	-2.3155528
C	-0.0264680	-0.0662919	0.4248756	C	-0.9177379	-0.4404721	-0.9983324
H	-0.7334058	0.7730623	-1.4255345	H	-0.6825520	0.5530908	0.8861314
H	1.5225633	1.3634808	-2.2327089	H	1.1364027	2.0561993	0.0832778
H	3.5092333	0.8604287	-0.8456856	O	2.1048717	2.1206534	-2.2430481

H	3.2364765	-0.2343416	1.3583041	H	0.8578704	0.2667806	-3.8069036
H	0.9626599	-0.8231246	2.1690327	H	-0.9079731	-1.2076250	-3.0089562
C	-1.3670376	-0.4365940	0.9506714	C	-2.0002666	-1.3215521	-0.4965818
Ge	-3.2338096	-0.2771538	0.0996089	O	-2.4830461	-1.1655963	0.6120453
O	-1.4922515	-0.9324555	2.0559016	Ge	-2.7674826	-2.8642033	-1.6086050
C	-3.8722891	-2.1593339	0.1665337	C	-3.7055236	-2.1624266	-3.2913726
C	-4.2036403	0.8518028	1.4194759	C	-4.0018699	-3.8102480	-0.3776716
C	-3.4999435	0.5036108	-1.7974909	C	-1.3761734	-4.1049125	-2.2851525
H	-3.9772233	0.4097780	2.3915316	C	-4.8259547	-4.9176976	-1.0394373
H	-5.2768150	0.7316047	1.2586170	H	-4.6486466	-3.0682487	0.0904002
C	-3.8202311	2.3335346	1.3967525	H	-3.3851035	-4.2162080	0.4273969
H	-4.9593311	-2.1636668	0.0699624	H	-4.1918577	-5.6821672	-1.4926975
H	-3.6417169	-2.5011538	1.1771223	H	-5.4670475	-5.4206181	-0.3113480
C	-3.2379865	-3.0854460	-0.8742996	H	-5.4737676	-4.5255682	-1.8259573
H	-3.6043989	-4.1090071	-0.7666223	H	-0.8287858	-3.5982433	-3.0799823
H	-3.4623607	-2.7659389	-1.8938573	H	-1.9061758	-4.9285797	-2.7681841
H	-2.1515489	-3.1191043	-0.7731085	C	-0.4217154	-4.6319167	-1.2104391
H	-2.7553800	2.4757138	1.5899577	H	-0.9532632	-5.1609792	-0.4169302
H	-4.0418552	2.7972991	0.4335043	H	0.3026113	-5.3313321	-1.6350987
H	-4.3655053	2.8928214	2.1604525	H	0.1434996	-3.8251123	-0.7400799
O	-2.5645994	1.0109537	-2.3878540	O	-3.2327326	-2.5138042	-4.3587640
C	-4.8432348	0.4461418	-2.4633044	C	-4.8971139	-1.2816349	-3.2257823
C	-4.9385431	0.8073475	-3.8136338	C	-5.5851049	-0.9518971	-4.4063058
C	-6.1594339	0.7703216	-4.4666995	C	-6.6899151	-0.1317003	-4.3751445
C	-7.3076260	0.3806676	-3.7788487	C	-7.1401876	0.3955891	-3.1547551
C	-7.2268114	0.0264165	-2.4375340	C	-6.4655169	0.0840999	-1.9733434
C	-5.9944469	0.0545001	-1.7856528	C	-5.3568379	-0.7526291	-2.0209991
H	-4.0389797	1.1133626	-4.3295806	H	-5.2267051	-1.3590250	-5.3420876
H	-6.2222118	1.0451296	-5.5117142	H	-7.2292061	0.1238246	-5.2773765
H	-8.2618373	0.3537086	-4.2892366	O	-8.2315986	1.1935390	-3.2262705
H	-8.1169032	-0.2724773	-1.8996522	H	-6.7888060	0.4835290	-1.0242196
H	-5.9517565	-0.2219686	-0.7422278	H	-4.8424655	-0.9770304	-1.0958095
				C	-8.7462692	1.7651540	-2.0311825
				C	2.6037246	2.1081730	-3.5739091
				H	-8.0101198	2.4159583	-1.5529889
				H	-9.6082750	2.3550627	-2.3308964
				H	-9.0625529	0.9929498	-1.3256802
				H	3.0401198	1.1384339	-3.8253725
				H	3.3765058	2.8713683	-3.6089354
				H	1.8194686	2.3525210	-4.2943132

**Table A2.** DFT (def2-TZVPP/B3LYP) Gas-phase geometries of ground states of FB<sub>2</sub>G and B<sub>4</sub>G used for vertical excited energies calculations via TDDFT. Adapted with permission from ref. 146. Copyright 2019 American Chemical Society. Modified presentation.

<b>FB<sub>2</sub>G (Cartesian coordinates)</b>				<b>B<sub>4</sub>G (Cartesian coordinates)</b>			
C	-0.3161353	0.4959526	-0.1285054	C	-0.7047910	-1.1329022	-0.9213042
C	0.6851374	1.3437063	-0.5672412	C	0.3990685	-1.7110202	-1.5353257
C	1.0928789	1.2550544	-1.8914938	C	1.6269737	-1.7225823	-0.8840511
C	0.5388826	0.3518816	-2.7817256	C	1.7518791	-1.1588015	0.3852118
C	-0.4587634	-0.4976190	-2.3225103	C	0.6507124	-0.5874680	1.0002340
C	-0.8987467	-0.4360586	-0.9980819	C	-0.5899844	-0.5687994	0.3498077
H	-0.6673259	0.5387370	0.8933999	H	-1.6530695	-1.1249156	-1.4417505
H	1.1505888	2.0666627	0.0883597	H	0.3012315	-2.1472286	-2.5204103
F	2.0633439	2.0805131	-2.3246695	H	2.4883740	-2.1694607	-1.3637926
H	0.8852230	0.3228174	-3.8050901	H	2.7094110	-1.1685651	0.8896869
H	-0.9014617	-1.2018095	-3.0140410	H	0.7252235	-0.1483291	1.9855686
C	-1.9820296	-1.3252816	-0.4916215	C	-1.7557929	0.0453707	1.0412530
O	-2.4567615	-1.1667801	0.6177284	Ge	-3.6140164	0.1294030	0.1624522

Ge	-2.7583097	-2.8670592	-1.5993005	O	-1.6770690	0.4761186	2.1731414
C	-3.6759286	-2.1318756	-3.2796434	C	-4.2999200	-1.7803683	-0.1795136
C	-4.0044534	-3.7985852	-0.3716700	C	-4.9323967	1.0958008	1.4103309
C	-1.3760707	-4.1102242	-2.2849462	C	-3.4625294	1.1702349	-1.6044440
C	-4.8531079	-4.8842196	-1.0387942	O	-5.9416140	0.4830421	1.6910444
H	-4.6337194	-3.0497759	0.1091520	O	-4.4830920	-2.0870669	-1.3395300
H	-3.3898035	-4.2243350	0.4246939	O	-2.3888629	1.6977636	-1.8118530
H	-4.2365485	-5.6550588	-1.5049754	C	-4.6092475	1.3245633	-2.5384115
H	-5.4963848	-5.3825967	-0.3099561	C	-4.4142867	2.0181157	-3.7401779
H	-5.5012664	-4.4728437	-1.8150731	C	-5.4641923	2.1838961	-4.6272123
H	-0.8242253	-3.6009069	-3.0748824	C	-6.7225582	1.6657718	-4.3223476
H	-1.9127082	-4.9252268	-2.7753754	C	-6.9256382	0.9805801	-3.1303000
C	-0.4274150	-4.6549197	-1.2139256	C	-5.8709360	0.8068494	-2.2431635
H	-0.9639040	-5.1866169	-0.4257173	H	-3.4320317	2.4159873	-3.9551098
H	0.2900903	-5.3565304	-1.6456658	H	-5.3089312	2.7158977	-5.5568978
H	0.1456893	-3.8580043	-0.7363638	H	-7.5428621	1.7963874	-5.0165851
O	-3.1754760	-2.4388525	-4.3458828	H	-7.9010908	0.5774379	-2.8933892
C	-4.8901360	-1.2702568	-3.2208951	H	-6.0388644	0.2643243	-1.3229629
C	-5.5600458	-0.9507203	-4.4096568	C	-4.4937795	-2.7516395	0.9311966
C	-6.6867773	-0.1484058	-4.3932282	C	-4.9471526	-4.0426059	0.6298081
C	-7.1323923	0.3398178	-3.1723658	C	-5.1274955	-4.9718501	1.6401645
C	-6.4941860	0.0532645	-1.9782020	C	-4.8535977	-4.6256073	2.9628853
C	-5.3704872	-0.7615616	-2.0118314	C	-4.4020834	-3.3476844	3.2706259
H	-5.1768223	-1.3454534	-5.3405910	C	-4.2258433	-2.4130092	2.2581654
H	-7.2214364	0.1059225	-5.2979160	H	-5.1504534	-4.2922539	-0.4025015
F	-8.2264669	1.1225212	-3.1517595	H	-5.4800478	-5.9674134	1.4035182
H	-6.8738421	0.4623638	-1.0526339	H	-4.9935356	-5.3535109	3.7518401
H	-4.8621962	-0.9860248	-1.0837088	H	-4.1901869	-3.0771976	4.2963830
				H	-3.8804509	-1.4201622	2.5125094
				C	-4.6941438	2.4844185	1.8874502
				C	-5.6341486	3.0771629	2.7409380
				C	-5.4435463	4.3703402	3.1969149
				C	-4.3155388	5.0891802	2.8026823
				C	-3.3800103	4.5100230	1.9535628
				C	-3.5669662	3.2102266	1.5002295
				H	-6.5037369	2.5037695	3.0315046
				H	-6.1699658	4.8238094	3.8587796
				H	-4.1676250	6.1004006	3.1596459
				H	-2.5042600	5.0665709	1.6475605
				H	-2.8280192	2.7690705	0.8452788

**Table A3.** DFT (def2-TZVPP/B3LYP) Gas-phase geometries of ground states of MB<sub>4</sub>G used for vertical excited energies calculations via TDDFT. Adapted with permission from ref. 146. Copyright 2019 American Chemical Society. Modified presentation.

<b>MB<sub>4</sub>G (Cartesian coordinates)</b>							
C	-0.5345320	-0.9735946	-1.1089055	C	-3.8643550	-3.2514125	3.2100643
C	0.5563680	-1.5532339	-1.7245435	C	-3.8105769	-2.3338646	2.1803925
C	1.8043051	-1.5409786	-1.0925437	H	-4.6193556	-4.3452169	-0.4123121
C	1.9418543	-0.9407931	0.1649451	H	-4.7310638	-6.0058409	1.4027292
C	0.8371936	-0.3657399	0.7698530	O	-4.2247278	-5.4118610	4.0140451
C	-0.4161577	-0.3706797	0.1493652	H	-3.6571855	-2.9619843	4.2309424
H	-1.4870772	-0.9908821	-1.6211712	H	-3.5584897	-1.3082247	2.4135325
H	0.4706112	-2.0187808	-2.6965540	C	-4.6901881	2.4772985	1.7289678
O	2.8162640	-2.1320768	-1.7713113	C	-5.6819666	3.0311721	2.5580049
H	2.8964502	-0.9210837	0.6691288	C	-5.5881783	4.3309971	2.9986104
H	0.9285581	0.0996004	1.7420034	C	-4.4943133	5.1240250	2.6177895
C	-1.5676175	0.2520706	0.8406896	C	-3.5020658	4.5902627	1.7940881
Ge	-3.4543009	0.1976664	0.0218413	C	-3.6080390	3.2746516	1.3618536

O	-1.4607789	0.7695279	1.9362757	H	-6.5214841	2.4116946	2.8427341
C	-4.0209600	-1.7592695	-0.2682872	H	-6.3433792	4.7663272	3.6391244
C	-4.8303676	1.0803193	1.2686090	O	-4.4913312	6.3893780	3.0994128
C	-3.3927784	1.2416174	-1.7475640	H	-2.6509909	5.1805605	1.4907101
O	-5.7965111	0.3972206	1.5524351	H	-2.8244702	2.8775608	0.7311262
O	-4.2473953	-2.0989521	-1.4146772	C	-8.9588512	1.0607075	-5.1093718
O	-2.3548874	1.8405720	-1.9618628	H	-8.8499254	-0.0258221	-5.0714718
C	-4.5528420	1.3252800	-2.6579689	H	-9.5824727	1.3316708	-5.9570776
C	-4.4515057	2.0900611	-3.8337342	H	-9.4276661	1.4122277	-4.1870242
C	-5.5143755	2.1946161	-4.7007624	C	-4.5542847	-6.7803707	3.8211165
C	-6.7207602	1.5360545	-4.4152952	H	-5.5617015	-6.8934874	3.4127521
C	-6.8390861	0.7757952	-3.2509328	H	-4.5117533	-7.2380145	4.8058261
C	-5.7556981	0.6761598	-2.3879207	H	-3.8360800	-7.2737007	3.1613661
H	-3.5180644	2.5947910	-4.0424508	C	-3.4146153	7.2527221	2.7598506
H	-5.4472155	2.7774864	-5.6095263	H	-3.3572649	7.4102907	1.6800480
O	-7.7073507	1.6978454	-5.3278991	H	-3.6255709	8.1985129	3.2517621
H	-7.7558848	0.2588833	-3.0124197	H	-2.4615532	6.8598453	3.1217101
H	-5.8618689	0.0734790	-1.4967991	C	4.1149436	-2.1524285	-1.1954472
C	-4.0802591	-2.7150691	0.8602764	H	4.4954350	-1.1404027	-1.0359395
C	-4.4108256	-4.0503299	0.6072773	H	4.7497319	-2.6666656	-1.9120889
C	-4.4722177	-4.9823621	1.6291846	H	4.1220182	-2.6978729	-0.2485991
C	-4.1961877	-4.5838376	2.9427644				

**Table A4.** Vibrational spectra in wavenumbers  $\tilde{\nu}$  /  $\text{cm}^{-1}$  of the optimized DFT (def2-TZVPP/B3LYP) gas-phase geometries of ground states of  $\text{B}_2\text{G}$ ,  $\text{MB}_2\text{G}$ ,  $\text{FB}_2\text{G}$ ,  $\text{B}_4\text{G}$ , and  $\text{MB}_4\text{G}$  according to **Table A1**, **Table A2**, and **Table A3**.

$\tilde{\nu}(\text{B}_2\text{G}) / \text{cm}^{-1}$		$\tilde{\nu}(\text{MB}_2\text{G}) / \text{cm}^{-1}$		$\tilde{\nu}(\text{FB}_2\text{G}) / \text{cm}^{-1}$		$\tilde{\nu}(\text{B}_4\text{G}) / \text{cm}^{-1}$		$\tilde{\nu}(\text{MB}_4\text{G}) / \text{cm}^{-1}$	
5.78	9.97	4.72	14.75	7.27	16.52	3.90	7.90	4.72	14.75
29.84	36.08	18.51	32.14	17.59	34.56	13.20	18.85	18.51	32.14
43.69	52.39	34.38	42.18	35.97	40.03	19.48	27.99	34.38	42.18
60.28	83.16	50.13	64.68	52.39	74.54	33.38	34.46	50.13	64.68
86.88	106.49	70.33	76.95	75.48	96.98	47.45	66.73	70.33	76.95
130.90	145.54	82.18	105.44	101.01	111.07	68.35	71.06	82.18	105.44
149.29	152.18	105.97	131.00	122.38	143.59	73.04	97.93	105.97	131.00
159.40	222.74	133.56	139.82	149.34	208.17	120.64	122.03	133.56	139.82
234.33	237.29	146.96	198.54	221.36	223.32	139.08	147.51	146.96	198.54
264.96	272.35	208.42	221.91	233.92	271.40	148.23	151.79	208.42	221.91
277.29	319.94	225.37	229.48	275.87	296.40	154.24	195.00	225.37	229.48
349.46	413.54	235.01	255.01	298.15	319.03	258.51	258.76	235.01	255.01
414.30	430.70	259.88	276.81	340.09	401.00	279.28	295.11	259.88	276.81
436.18	468.03	280.86	299.66	402.24	425.96	321.36	334.76	280.86	299.66
485.11	548.04	301.20	316.76	426.90	456.48	337.98	409.69	301.20	316.76
550.02	606.66	340.35	427.42	457.44	504.98	409.83	412.54	340.35	427.42
624.85	632.21	428.41	439.99	512.47	539.41	412.78	428.19	428.41	439.99
632.90	686.21	440.28	492.49	572.47	587.62	428.78	429.06	440.28	492.49
688.10	699.01	492.80	513.82	621.65	622.44	437.22	464.81	492.80	513.82
710.16	712.14	520.71	538.86	632.49	648.28	473.86	474.34	520.71	538.86
712.21	789.62	571.42	590.78	649.39	682.94	484.42	599.34	571.42	590.78
794.85	867.85	627.06	628.20	715.91	741.75	601.27	630.14	627.06	628.20
880.20	890.49	635.89	656.35	745.67	825.32	630.83	630.90	635.89	656.35
911.92	959.55	657.24	682.44	826.61	838.97	631.30	635.45	657.24	682.44
974.38	975.42	715.80	753.57	840.28	870.05	640.38	687.11	715.80	753.57
979.05	981.94	756.49	802.46	871.63	903.68	687.47	687.64	756.49	802.46
985.16	1005.49	803.71	832.24	913.28	961.67	689.74	703.90	803.71	832.24
1017.18	1020.25	832.37	867.95	976.64	978.42	704.49	704.60	832.37	867.95
1020.36	1020.89	869.02	900.83	982.81	984.19	705.59	788.58	869.02	900.83
1024.47	1030.11	910.63	960.12	991.24	1007.32	788.79	792.69	910.63	960.12

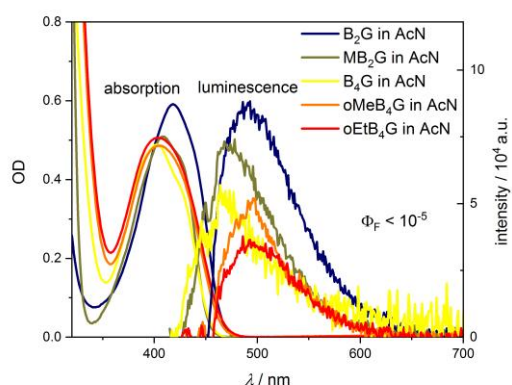
---

1047.02	1049.05	976.02	977.82	1008.25	1028.21	793.04	864.58	976.02	977.82
1049.33	1106.86	979.57	981.27	1029.44	1034.03	865.08	866.02	979.57	981.27
1108.52	1183.28	990.17	1011.86	1035.16	1123.06	866.25	892.84	990.17	1011.86
1183.81	1189.37	1012.35	1022.29	1123.33	1172.21	893.76	897.70	1012.35	1022.29
1204.63	1211.71	1023.87	1033.57	1175.53	1213.16	909.99	961.72	1023.87	1033.57
1225.97	1244.70	1034.76	1056.63	1218.92	1253.87	962.00	963.17	1034.76	1056.63
1253.09	1263.81	1057.18	1135.89	1257.12	1260.21	963.79	1005.10	1057.18	1135.89
1270.32	1336.46	1136.50	1172.77	1260.49	1262.27	1005.19	1005.88	1136.50	1172.77
1340.93	1357.58	1173.07	1183.26	1263.48	1325.34	1006.33	1018.07	1173.07	1183.26
1368.42	1419.33	1190.13	1205.13	1325.65	1341.34	1019.69	1020.10	1190.13	1205.13
1421.43	1459.52	1205.97	1229.85	1341.83	1418.91	1020.28	1020.46	1205.97	1229.85
1463.43	1481.76	1234.25	1253.07	1419.06	1441.07	1020.62	1021.04	1234.25	1253.07
1482.99	1498.98	1256.52	1259.99	1441.38	1458.85	1021.50	1047.19	1256.52	1259.99
1499.59	1506.27	1262.33	1286.34	1463.04	1499.42	1047.36	1047.62	1262.33	1286.34
1506.30	1522.58	1287.58	1334.24	1501.38	1506.15	1047.69	1108.29	1287.58	1334.24
1526.86	1618.38	1335.39	1353.32	1507.26	1536.44	1108.60	1108.81	1335.39	1353.32
1619.00	1634.24	1353.68	1417.55	1536.63	1622.42	1108.98	1183.54	1353.68	1417.55
1636.26	1681.85	1417.90	1452.90	1623.92	1635.11	1183.99	1184.49	1417.90	1452.90
1688.80	3019.73	1453.29	1458.72	1635.53	1686.45	1185.01	1193.52	1453.29	1458.72
3020.41	3036.14	1461.92	1478.69	1691.04	3020.49	1194.29	1195.89	1461.92	1478.69
3039.97	3069.80	1478.97	1495.65	3020.62	3041.12	1200.41	1218.74	1478.97	1495.65
3071.37	3073.82	1495.70	1499.41	3041.84	3071.12	1219.28	1222.32	1495.70	1499.41
3074.74	3092.16	1501.48	1504.46	3072.50	3075.53	1223.54	1337.86	1501.48	1504.46
3093.54	3163.43	1505.80	1506.07	3076.53	3095.26	1338.00	1338.14	1505.80	1506.07
3166.92	3172.69	1507.13	1538.73	3096.97	3186.89	1338.46	1358.63	1507.13	1538.73
3177.88	3178.41	1539.16	1603.17	3187.93	3192.03	1358.79	1358.95	1539.16	1603.17
3188.29	3188.39	1604.63	1637.26	3192.51	3203.99	1359.23	1482.38	1604.63	1637.26
3197.52	3200.63	1637.58	1678.72	3204.52	3205.86	1482.67	1482.90	1637.58	1678.72
3204.30		1682.50	3013.00	3206.37		1482.96	1523.50	1682.50	3013.00
		3013.72	3018.23			1523.70	1524.06	3013.72	3018.23
		3018.39	3040.03			1524.23	1619.26	3018.39	3040.03
		3041.45	3068.17			1619.27	1619.91	3041.45	3068.17
		3069.67	3072.73			1620.07	1635.02	3069.67	3072.73
		3073.61	3073.98			1635.28	1635.54	3073.61	3073.98
		3075.00	3094.17			1636.39	1689.76	3075.00	3094.17
		3095.86	3136.12			1692.59	1693.92	3095.86	3136.12
		3136.54	3182.32			1703.17	3167.03	3136.54	3182.32
		3182.41	3184.91			3167.11	3167.12	3182.41	3184.91
		3185.18	3198.77			3167.12	3178.60	3185.18	3198.77
		3199.09	3212.66			3178.97	3179.01	3199.09	3212.66
		3213.25				3179.40	3185.19	3213.25	
						3186.17	3186.32		
						3187.08	3195.82		
						3196.66	3196.75		
						3197.98	3199.45		
						3199.56	3199.66		
						3199.83			

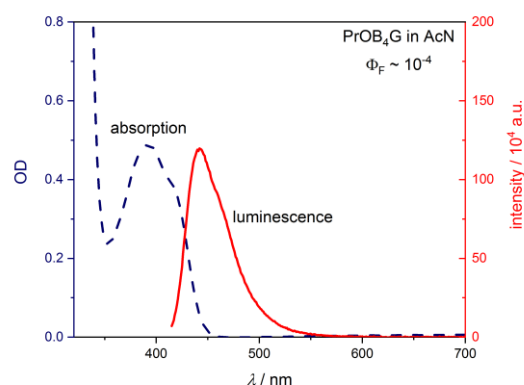
---

## Fluorescence Spectroscopy of Bis- and Tetraacylgermanes

a)



b)



c)

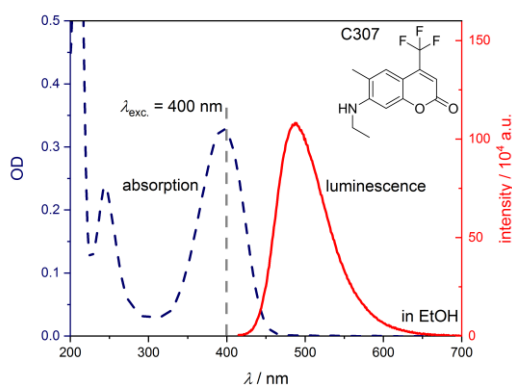
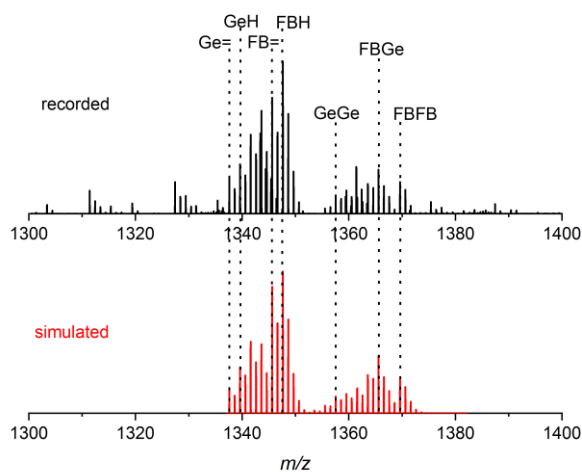


**Figure A2.** a) Steady-state UV/Vis and fluorescence spectra of B<sub>2</sub>G, MB<sub>2</sub>G, B<sub>4</sub>G, oMeB<sub>4</sub>G, and oEt<sub>4</sub>G dissolved in AcN. b) Steady-state UV/Vis and fluorescence spectra of PrOB<sub>4</sub>G dissolved in AcN. c) Reference steady-state UV/Vis and fluorescence spectra of coumarin 307 in ethanol recorded at excitation of 400 nm. The C307-sample is further diluted by a factor of 5000, to obtain non-saturated fluorescence spectrum at a slit size of 5 nm. Thus, a corrected OD of  $6.5 \cdot 10^{-5}$  was used for the determination of fluorescence quantum yields  $\Phi_F$  of acylgermanes. The reference quantum yield of 56 % is taken from literature.<sup>135</sup> All investigated bis- and tetraacylgermanes reveal very low  $\Phi_F < 10^{-5}$ . As an exception, PrOB<sub>4</sub>G features a  $\Phi_F$  of  $\sim 10^{-4}$ . All obtained values are provided in **Table 4.1**. The fluorescence spectra of bis- and tetraacylgermanes were conducted by Dennis Haffner (Wiss. Arb. KIT, 2019).

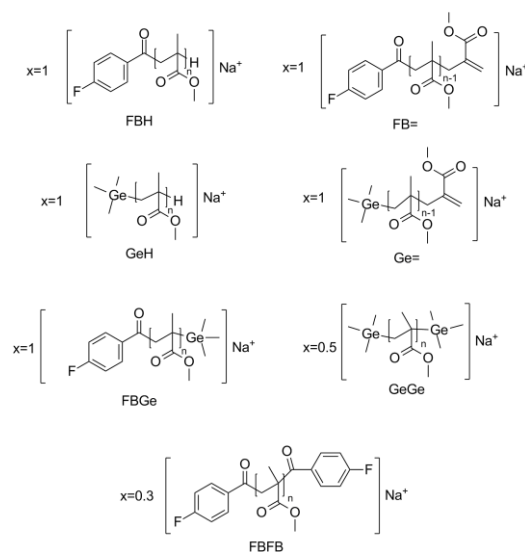
## Isotopic Pattern Simulations of Monoacylgermanes

### FB<sub>1</sub>G

a)



b)



c)

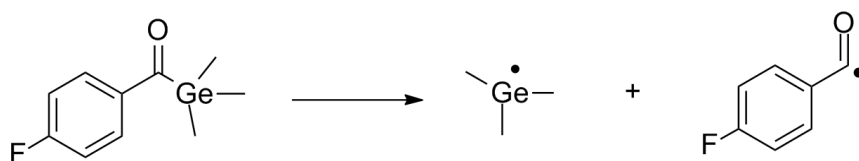


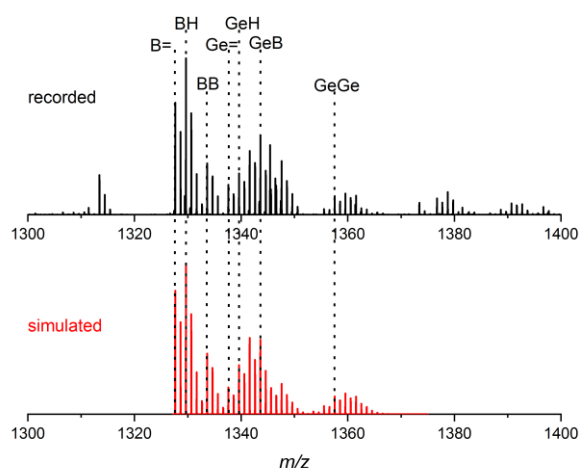
**Figure A3.** a) Recorded (black) direct infusion-ESI-MS and simulated (red) mass spectrum of PMMA-products obtained from PLP initiated by FB<sub>1</sub>G at total irradiation energy of 27.9 J at 400 nm. b) Disproportionation and combination products used for simulation. c) Associated cleavage mechanism. Adapted with permission from ref. 144. Copyright 2017 American Chemical Society.

**Table A5.** Exact mass and resolution of simulated and recorded spectra of the PLP-PMMA species initiated by radical fragments originated from  $B_1G$ . Adapted with permission from ref. 144. Copyright 2017 American Chemical Society. Own representation.

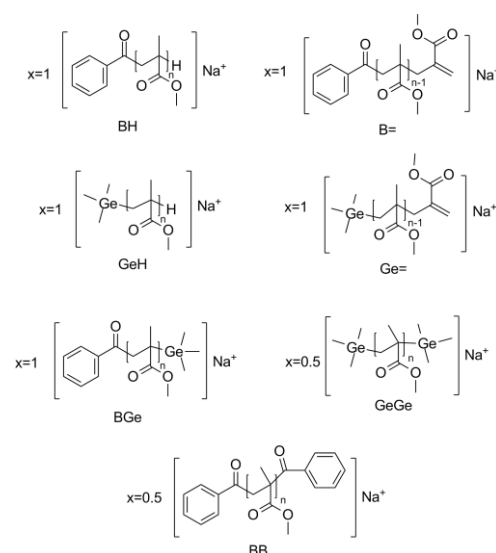
species	exact mass (recorded)	Resolution (recorded)	exact mass (simulated)	resolution (simulated)
Ge=	1337.61	60176	1337.61	59947
GeH	1339.61	42370	1339.61	40114
FB=	1345.64	53914	1345.63	54458
FBH	1347.65	57984	1347.65	54721
GeGe	1357.55	58289	1357.55	57444
FBGe	1365.59	57263	1365.58	56578
FBFB	1369.62	59688	1369.61	58043

### $B_1G$

a)



b)



c)

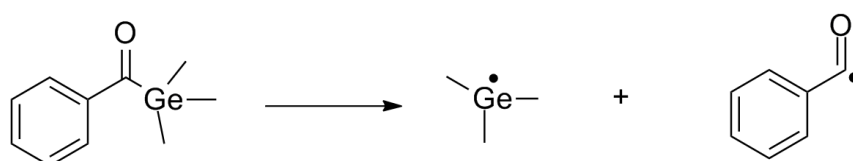


**Figure A4.** a) Recorded (black) direct infusion-ESI-MS and simulated (red) mass spectrum of PMMA-products obtained from PLP initiated by  $B_1G$  at total irradiation energy of 27.9 J at 400 nm. b) Disproportionation and combination products used for simulation. c) Associated cleavage mechanism. Adapted with permission from ref. 144. Copyright 2017 American Chemical Society.

**Table A6.** Exact mass and resolution of simulated and recorded spectra of the PLP-PMMA species initiated by radical fragments originated from B<sub>1</sub>G. Adapted with permission from ref. 144. Copyright 2017 American Chemical Society. Modified presentation.

species	exact mass (recorded)	resolution (recorded)	exact mass (simulated)	resolution (simulated)
B=	1327.65	60253	1327.64	59947
BH	1329.66	58931	1329.66	55157
BB	1333.64	60522	1333.63	59879
Ge=	1337.61	60553	1337.61	59916
GeH	1339.61	41849	1339.61	40109
BGe	1343.62	50481	1343.61	43285
GeGe	1357.56	56679	1357.55	57442

## Isotopic Pattern Simulations of Bis- and Tetraacylgermanes

### Isotopic pattern simulation of oMeB<sub>4</sub>G

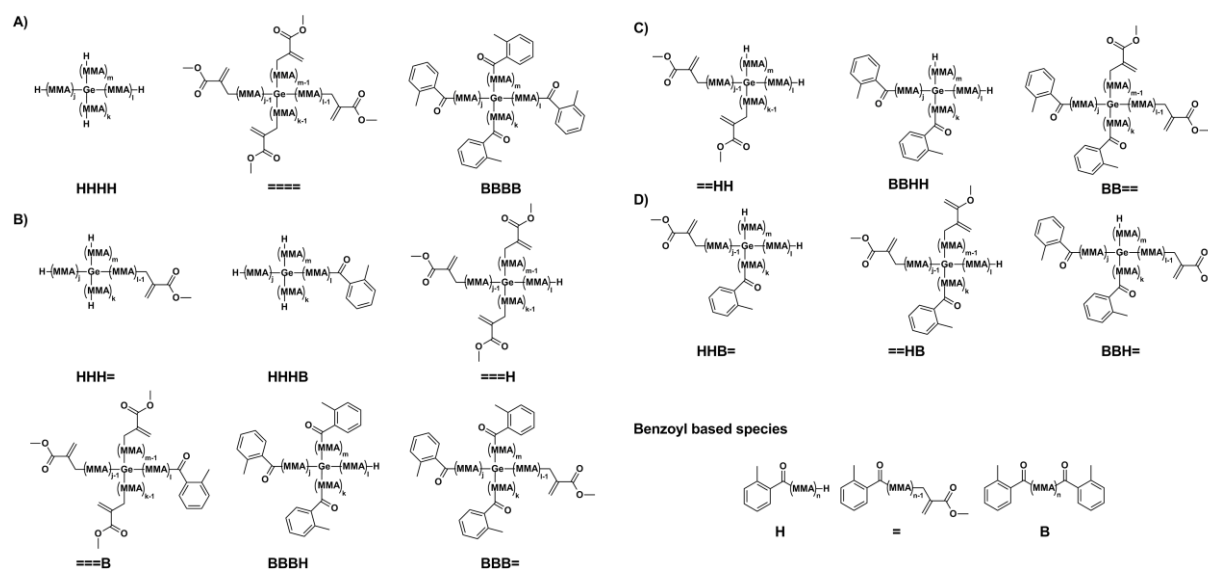


**Figure A5.** oMeB<sub>4</sub>G: Fifteen germanium-centered 4-armed MMA star polymers divided in four statistical groups A,B,C,D with relative propabilities of 0.083:0.33:0.5:1 and three benzoyl based PMMA species for isotopic pattern simulation. A Na<sup>+</sup> is added to each structure for exact mass calculation. Adapted with permission from ref. 145. Copyright 2018 American Chemical Society.

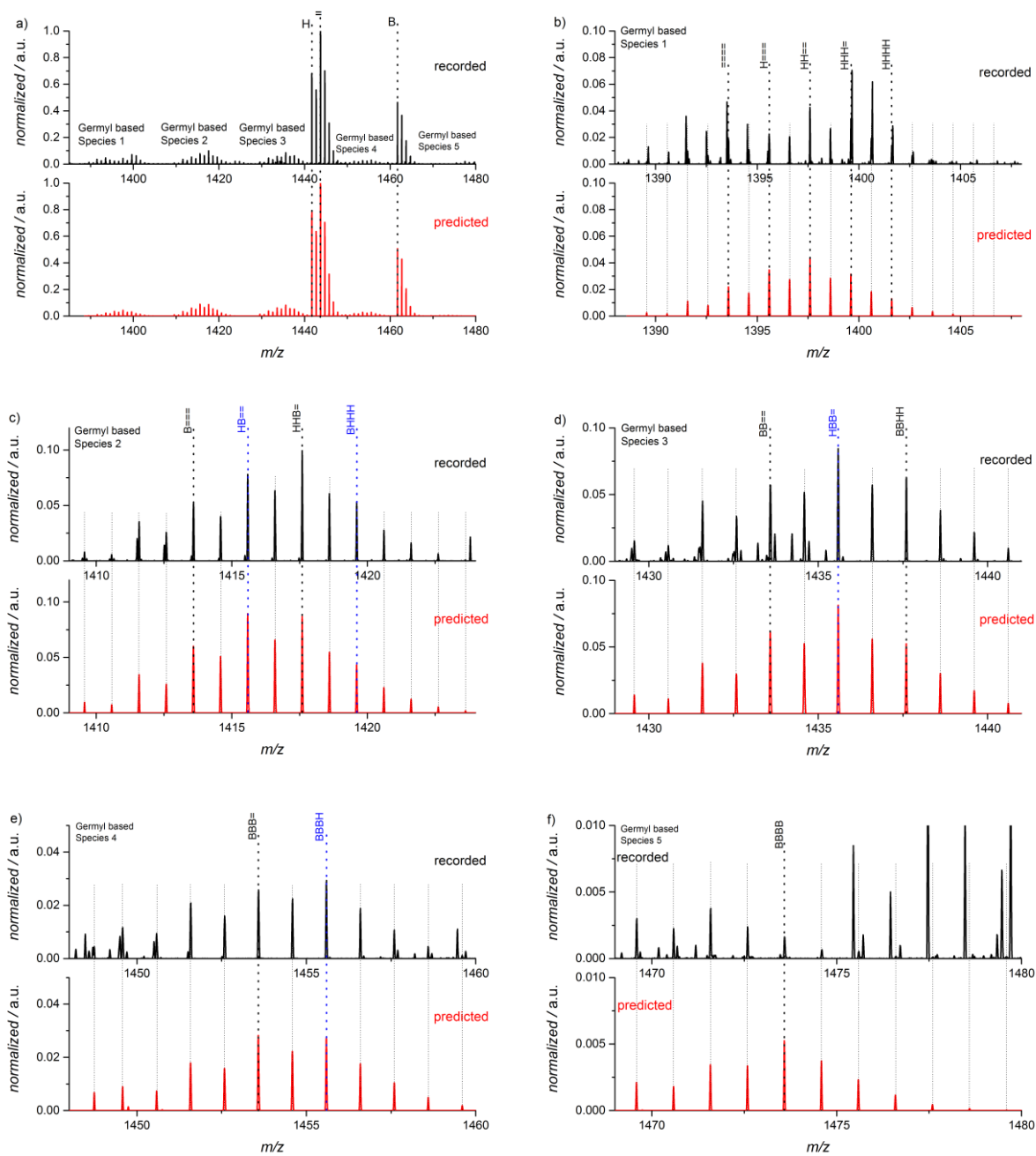


**Figure A6.** Mass spectra (black) and isotopic pattern simulations (red) of oMeB<sub>4</sub>G: **a)** Overview spectrum with all gernyl and benzoyl based species shown in **Figure A5**. **b)-f)** Gernyl based species 1-5 as depicted in a). Adapted with permission from ref. 145. Copyright 2018 American Chemical Society.

**Table A7.** oMeB<sub>4</sub>G: Exact masses of germanium-centered MMA star polymers used for isotopic pattern simulation in the range of  $m/z \sim 1400$ . Na<sup>+</sup> is added to each structure for exact mass calculation. Adapted with permission from ref. 145. Copyright 2018 American Chemical Society. Modified presentation.

exact mass (simulated)	germyl species	sum formula	relative amount
1393.5607	====	C <sub>65</sub> H <sub>100</sub> GeNaO <sub>26</sub>	0.083
1395.5763	H===	C <sub>65</sub> H <sub>102</sub> GeNaO <sub>26</sub>	0.33
1397.5920	HH==	C <sub>65</sub> H <sub>104</sub> GeNaO <sub>26</sub>	0.5
1399.6076	HHH=	C <sub>65</sub> H <sub>106</sub> GeNaO <sub>26</sub>	0.33
1401.6233	HHHH	C <sub>65</sub> H <sub>108</sub> GeNaO <sub>26</sub>	0.083
1413.5658	B===	C <sub>68</sub> H <sub>100</sub> GeNaO <sub>25</sub>	0.33
1415.5814	HB==	C <sub>68</sub> H <sub>102</sub> GeNaO <sub>25</sub>	1
1417.5971	HHB=	C <sub>68</sub> H <sub>104</sub> GeNaO <sub>25</sub>	1
1419.6127	BHHH	C <sub>68</sub> H <sub>106</sub> GeNaO <sub>25</sub>	0.33
1433.5709	BB==	C <sub>71</sub> H <sub>100</sub> GeNaO <sub>24</sub>	0.5
1435.5865	HBB=	C <sub>71</sub> H <sub>102</sub> GeNaO <sub>24</sub>	1
1437.6022	BBHH	C <sub>71</sub> H <sub>104</sub> GeNaO <sub>24</sub>	0.5
1453.5759	BBB=	C <sub>74</sub> H <sub>100</sub> GeNaO <sub>23</sub>	0.33
1455.5916	BBBH	C <sub>74</sub> H <sub>102</sub> GeNaO <sub>23</sub>	0.33
1473.5810	BBBB	C <sub>77</sub> H <sub>100</sub> GeNaO <sub>22</sub>	0.083

**Table A8.** oMeB<sub>4</sub>G: Benzoyl initiated PMMA species used for the isotopic pattern simulation in the mass range of  $m/z \sim 1400$ . Na<sup>+</sup> is added to each structure for exact mass calculation. Adapted with permission from ref. 145. Copyright 2018 American Chemical Society. Modified presentation.

exact mass (simulated)	benzoyl species	sum formula	relative amount
1443.7283	H	C <sub>73</sub> H <sub>112</sub> NaO <sub>27</sub>	6
1441.7127	=	C <sub>73</sub> H <sub>110</sub> NaO <sub>27</sub>	6
1461.7178	B	C <sub>76</sub> H <sub>110</sub> NaO <sub>26</sub>	4

**Table A9.** oMeB<sub>4</sub>G: Relative mass difference and mass accuracy of simulated and recorded mass spectra of benzoyl based PMMA species. Adapted with permission from ref. 145. Copyright 2018 American Chemical Society. Modified presentation.

exact mass ( $m/z$ ) <sub>exp</sub> (recorded)	exact mass ( $m/z$ ) <sub>sim</sub> (simulated)	$\Delta m/z =$ $  (m/z)_{exp} - (m/z)_{sim}  $	$dm/m_{sim} =$ $(\Delta m/z) / (m/z)_{sim}$ $10^6 / \text{ppm}$
1441.70957	1441.71291	0.00334	2.32
1442.71601	1442.71645	0.00044	0.30
1443.72351	1443.72610	0.00259	1.79
1444.73206	1444.73105	0.00101	0.70
1445.73515	1445.73428	0.00087	0.60
1446.73928	1446.73821	0.00107	0.74
1461.71568	1461.71783	0.00215	1.47
1462.71662	1462.72128	0.00466	3.19

1463.72522	1463.7242	0.00102	0.70
1464.72822	1464.72841	0.00019	0.13
1465.73226	1465.7321	0.001734	1.18

**Table A10.** oMeB<sub>4</sub>G: Relative mass difference and mass accuracy of simulated and recorded mass spectra of germyl based PMMA species. Strong deviations (> 10 ppm) occur only at very small peak intensities close to the detection limit. Adapted with permission from ref. 145. Copyright 2018 American Chemical Society. Modified presentation.

species Number as depicted in <b>Figure A5</b>	exact mass ( $m/z$ ) <sub>exp</sub> (recorded)	exact mass ( $m/z$ ) <sub>sim</sub> (simulated)	$\Delta m/z =$ $ (\mathbf{m/z})_{\text{exp}} - (\mathbf{m/z})_{\text{sim}} $	$dm/m_{\text{sim}} =$ $(\Delta m/z)/(\mathbf{m/z})_{\text{sim}}$ $10^6 / \text{ppm}$
1	1389.5628	1389.5643	0.0016	1.12
	1390.5704	1390.5681	0.0023	1.68
	1391.5730	1391.5783	0.0053	3.83
	1392.5829	1392.5801	0.0028	2.00
	1393.5938	1393.5866	0.0072	5.18
	1394.5873	1394.5851	0.0022	1.59
	1395.5819	1395.5878	0.0059	4.23
	1396.5899	1396.5930	0.0031	2.21
	1397.5928	1397.5948	0.0020	1.43
	1398.5968	1398.5997	0.0029	2.06
	1399.6081	1399.6059	0.0022	1.58
	1400.6081	1400.6110	0.0030	2.13
	1401.6153	1401.6152	0.0001	0.09
	1402.6236	1402.6218	0.0019	1.32
	1403.6206	1403.6227	0.0021	1.49
	1404.5812	1404.6284	0.0472	33.62
	1405.5740	1405.6301	0.0562	39.95
	1406.6679	1406.6408	0.0271	19.26
	2	1409.5682	1409.5696	0.0014
1410.5726		1410.5731	0.0005	0.38
1411.5843		1411.5821	0.0023	1.62
1412.5846		1412.5852	0.0007	0.47
1413.5922		1413.5850	0.0072	5.07
1414.5882		1414.5866	0.0016	1.12
1415.5853		1415.5872	0.0019	1.33
1416.5961		1416.5932	0.0029	2.05
1417.5954		1417.5976	0.0022	1.57
1418.6020		1418.6015	0.0005	0.37
1419.6097		1419.6067	0.0030	2.13
1420.6121		1420.6114	0.0007	0.51
1421.6156		1421.6139	0.0017	1.22
3	1422.6138	1422.6183	0.0044	3.12
	1423.6194	1423.6222	0.0027	1.92
	1429.5730	1429.5746	0.0016	1.13
	1430.5796	1430.5781	0.0015	1.08

	1431.5872	1431.5846	0.0027	1.86
	1432.5895	1432.5859	0.0037	2.56
	1433.5864	1433.5848	0.0016	1.12
	1434.5908	1434.5887	0.0021	1.48
	1435.5898	1435.5891	0.0007	0.52
	1436.5963	1436.5931	0.0032	2.21
	1437.6039	1437.5991	0.0048	3.30
	1438.6060	1438.6028	0.0032	2.24
	1439.6027	1439.6048	0.0020	1.42
	1440.6070	1440.6068	0.0001	0.09
4	1448.7442	1448.7433	0.0008	0.57
	1449.5813	1449.5790	0.0023	1.58
	1449.7056	1449.7469	0.0413	28.49
	1450.5829	1450.5826	0.0003	0.21
	1450.7074	1450.7524	0.0451	31.08
	1451.5921	1451.5838	0.0082	5.68
	1452.5892	1452.5840	0.0052	3.61
	1453.5874	1453.5830	0.0044	3.03
	1454.5931	1454.5875	0.0056	3.86
	1455.5933	1455.5909	0.0024	1.66
	1456.5946	1456.5944	0.0002	0.12
	1457.5968	1457.5955	0.0013	0.90
	1458.5935	1458.5974	0.0038	2.62
	1459.5979	1459.6005	0.0026	1.79
5	1469.5917	1469.5841	0.0077	5.21
	1470.5874	1470.5874	0.0000	0.01
	1471.5908	1471.5835	0.0073	4.97
	1472.5885	1472.5857	0.0028	1.88
	1473.5872	1473.5831	0.0041	2.78
	1474.6004	1474.5855	0.0149	10.08
	1475.5944	1475.5867	0.0077	5.22
	1476.6029	1476.5880	0.0149	10.10
	1477.5990	1477.5899	0.0090	6.11
	1479.5941	1479.6021	0.0079	5.36

---

## Isotopic pattern simulation of oEtB<sub>4</sub>G

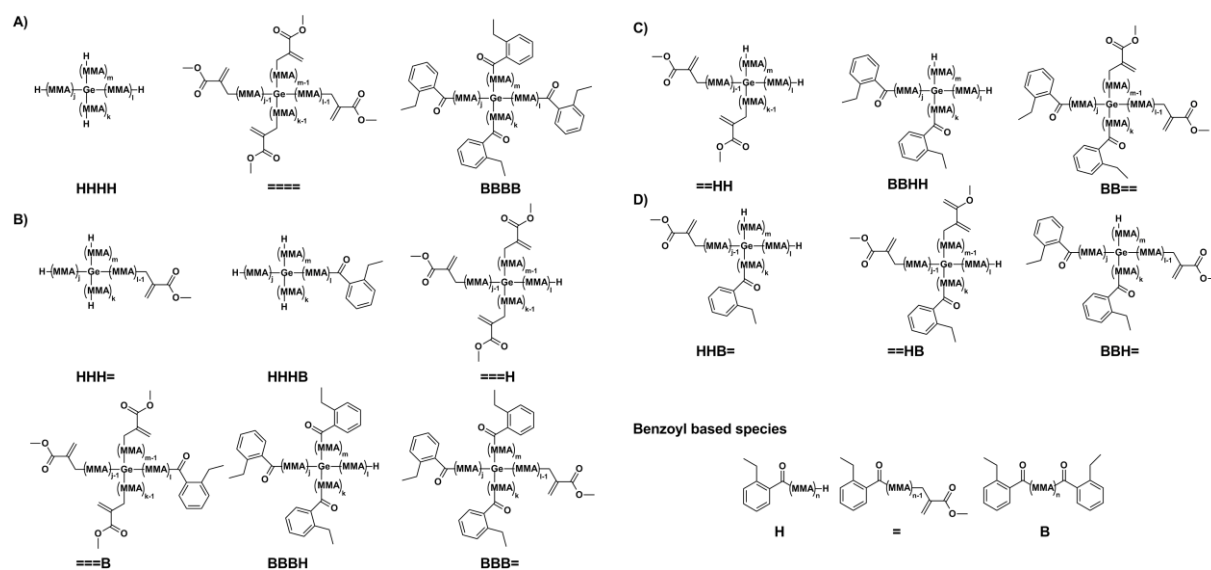


**Figure A7.** oEtB<sub>4</sub>G: Fifteen germanium-centered 4-armed MMA star polymers divided in four statistical groups A,B,C,D with relative propabilities of 0.083:0.33:0.5:1 and three benzoyl based PMMA species for isotopic pattern simulation. A Na<sup>+</sup> is added to each structure for exact mass calculation. Adapted with permission from ref. 145. Copyright 2018 American Chemical Society.

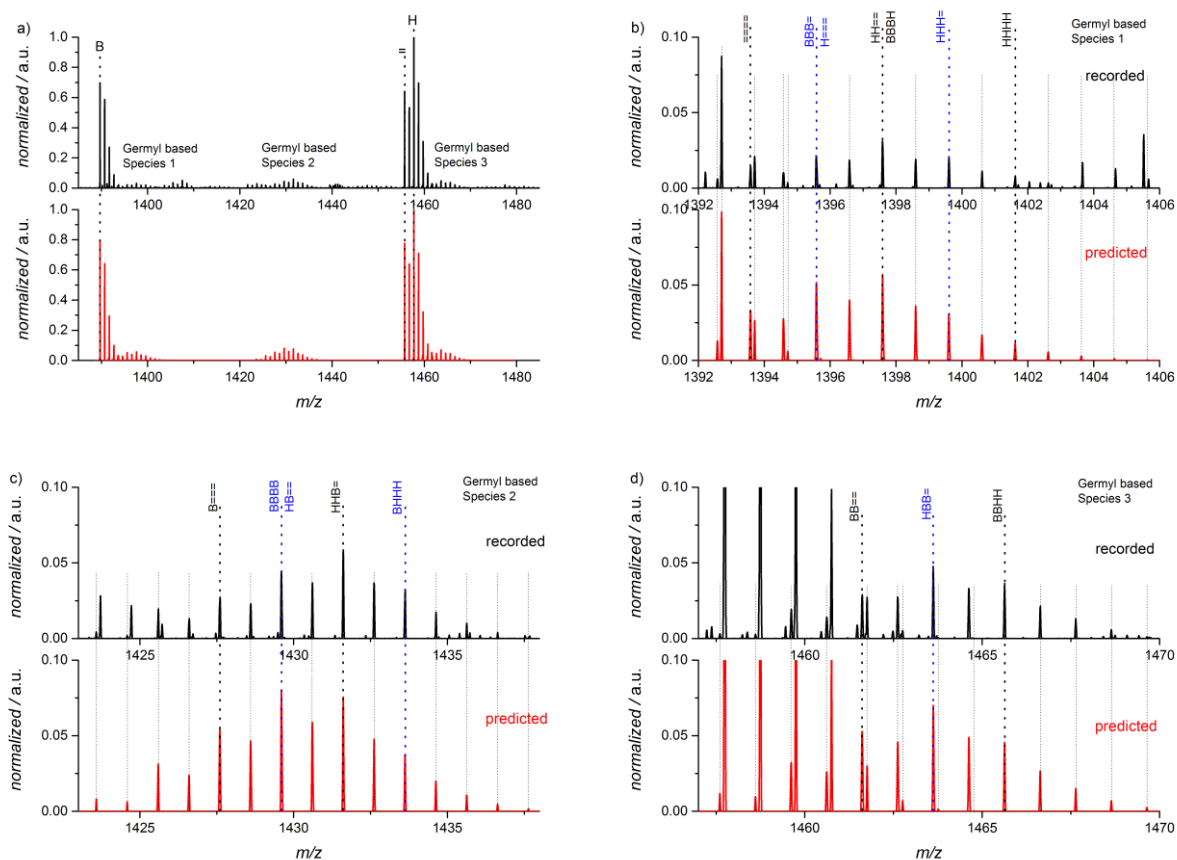


**Figure A8.** Mass spectra (black) and isotopic pattern simulations (red) of oEtB<sub>4</sub>G: a) Overview spectrum with all gernyl and benzoyl based species shown in **Figure A7**. b)-d) Gernyl based species 1-3 as depicted in **a)**. Adapted with permission from ref. 145. Copyright 2018 American Chemical Society.

**Table A11.** oEtB<sub>4</sub>G: Exact masses of germanium-centered MMA star polymers used for isotopic pattern simulation in the range of  $m/z \sim 1400$ . Na<sup>+</sup> is added to each structure for exact mass calculation. Adapted with permission from ref. 145. Copyright 2018 American Chemical Society. Modified presentation.

exact mass (simulated)	germyl species	sum formula	relative amount
1393.5607	====	C <sub>65</sub> H <sub>100</sub> GeNaO <sub>26</sub>	0.083
1395.5705	BBB=	C <sub>72</sub> H <sub>98</sub> GeNaO <sub>21</sub>	0.33
1395.5763	H===	C <sub>65</sub> H <sub>102</sub> GeNaO <sub>26</sub>	0.33
1397.5861	BBBH	C <sub>72</sub> H <sub>100</sub> GeNaO <sub>21</sub>	0.33
1397.5920	HH==	C <sub>65</sub> H <sub>104</sub> GeNaO <sub>26</sub>	0.5
1399.6076	HHH=	C <sub>65</sub> H <sub>106</sub> GeNaO <sub>26</sub>	0.33
1401.6233	HHHH	C <sub>65</sub> H <sub>108</sub> GeNaO <sub>26</sub>	0.083
1427.5814	B===	C <sub>69</sub> H <sub>102</sub> GeNaO <sub>25</sub>	0.33
1429.5912	BBBB	C <sub>76</sub> H <sub>100</sub> GeNaO <sub>20</sub>	0.083
1429.5971	HB==	C <sub>69</sub> H <sub>104</sub> GeNaO <sub>25</sub>	1
1431.6127	HHB=	C <sub>69</sub> H <sub>106</sub> GeNaO <sub>25</sub>	1
1433.6284	BHHH	C <sub>69</sub> H <sub>108</sub> GeNaO <sub>25</sub>	0.33
1461.6022	BB==	C <sub>73</sub> H <sub>104</sub> GeNaO <sub>24</sub>	0.5
1463.6178	HBB=	C <sub>73</sub> H <sub>106</sub> GeNaO <sub>24</sub>	1
1465.6335	BBHH	C <sub>73</sub> H <sub>108</sub> GeNaO <sub>24</sub>	0.5

**Table A12.** oEtB<sub>4</sub>G: Benzoyl initiated PMMA species used for the isotopic pattern simulation in the mass range of  $m/z \sim 1400$ . Na<sup>+</sup> is added to each structure for exact mass calculation. Adapted with permission from ref. 145. Copyright 2018 American Chemical Society. Modified presentation.

exact mass (simulated)	benzoyl species	sum formula	relative amount
1457.7440	H	C <sub>74</sub> H <sub>114</sub> NaO <sub>27</sub>	9
1455.7283	=	C <sub>74</sub> H <sub>112</sub> NaO <sub>27</sub>	9
1389.6966	B	C <sub>73</sub> H <sub>106</sub> NaO <sub>24</sub>	9

**Table A13.** oEtB<sub>4</sub>G: Relative mass difference and mass accuracy of simulated and recorded mass spectra of benzoyl based PMMA species. Adapted with permission from ref. 145. Copyright 2018 American Chemical Society. Modified presentation.

exact mass ( $m/z$ ) <sub>exp</sub> (recorded)	exact mass ( $m/z$ ) <sub>sim</sub> (simulated)	$\Delta m/z =$ $ (\mathbf{m/z})_{\text{exp}} - (\mathbf{m/z})_{\text{sim}} $	$dm/m_{\text{sim}} =$ $(\Delta m/z)/(\mathbf{m/z})_{\text{sim}}$ $10^6 / \text{ppm}$
1389.69751	1389.69693	0.00058	0.42
1390.69915	1390.70019	0.00104	0.75
1391.70188	1391.70301	0.00113	0.81
1392.70570	1392.70656	0.00086	0.62
1455.72461	1455.72857	0.00396	2.72
1456.73258	1456.73215	0.00043	0.30
1457.74160	1457.7419	0.0003	0.21
1458.74506	1458.74687	0.00181	1.24
1459.74956	1459.7501	0.00054	0.37
1460.75509	1460.75342	0.00167	1.14

**Table A14.** oEtB<sub>4</sub>G: Relative mass difference and mass accuracy of simulated and recorded mass spectra of germyl based PMMA species. Strong deviations (> 10 ppm) occur only at very small peak intensities close to the detection limit. Adapted with permission from ref. 145. Copyright 2018 American Chemical Society. Modified presentation.

species Number as depicted in <b>Figure A7</b>	exact mass ( $m/z$ ) <sub>exp</sub> (recorded)	exact mass ( $m/z$ ) <sub>sim</sub> (simulated)	$\Delta m/z =$ $ (\mathbf{m/z})_{\text{exp}} - (\mathbf{m/z})_{\text{sim}} $	$dm/m_{\text{sim}} =$ $(\Delta m/z)/(\mathbf{m/z})_{\text{sim}}$ $10^6 / \text{ppm}$
1	1392.5825	1392.5789	0.0036	2.56
	1392.7057	1392.7060	0.0003	0.20
	1393.5872	1393.5813	0.0059	4.23
	1393.7106	1393.7091	0.0015	1.08
	1394.5808	1394.5810	0.0003	0.19
	1394.7104	1394.7123	0.0019	1.38
	1395.5753	1395.5826	0.0072	5.19
	1395.6804	1395.7146	0.0342	24.48
	1396.5833	1396.5883	0.0050	3.57
	1397.5862	1397.5907	0.0045	3.22
	1398.5964	1398.5945	0.0020	1.42
	1399.6077	1399.6030	0.0048	3.39
	1400.6139	1400.6081	0.0058	4.11
	1401.6211	1401.6146	0.0066	4.67
	1402.6233	1402.6200	0.0032	2.31
1403.6202	1403.6250	0.0048	3.42	
2	1423.5808	1423.5854	0.0045	3.19
	1424.5875	1424.5882	0.0007	0.48
	1425.6016	1425.5970	0.0045	3.18
	1426.6040	1426.6000	0.0039	2.75
	1427.6074	1427.5996	0.0078	5.46

	1428.6055	1428.6011	0.0045	3.12
	1429.6047	1429.6020	0.0026	1.85
	1430.6113	1430.6079	0.0034	2.39
	1431.6125	1431.6126	0.0001	0.06
	1432.6149	1432.6169	0.0020	1.42
	1433.6247	1433.6225	0.0022	1.53
	1434.6291	1434.6269	0.0021	1.49
	1435.6281	1435.6297	0.0016	1.13
	1436.6347	1436.6332	0.0014	0.98
	1437.6810	1437.6362	0.0448	31.15
3	1457.6096	1457.6059	0.0038	2.60
	1458.6064	1458.6095	0.0032	2.16
	1459.6173	1459.6163	0.0010	0.71
	1460.6227	1460.6177	0.0050	3.44
	1461.6159	1461.6167	0.0008	0.55
	1461.7550	1461.7562	0.0012	0.79
	1462.6168	1462.6195	0.0028	1.88
	1462.7560	1462.7591	0.0031	2.09
	1463.6186	1463.6205	0.0019	1.30
	1463.7182	1463.7632	0.0450	30.77
	1464.6215	1464.6247	0.0032	2.16
	1465.6321	1465.6295	0.0026	1.76
	1466.6370	1466.6338	0.0032	2.21
	1467.6364	1467.6363	0.0000	0.02
	1468.6367	1468.6383	0.0016	1.10
	1469.6448	1469.6429	0.0019	1.30

### Isotopic pattern simulation of PrOB<sub>4</sub>G

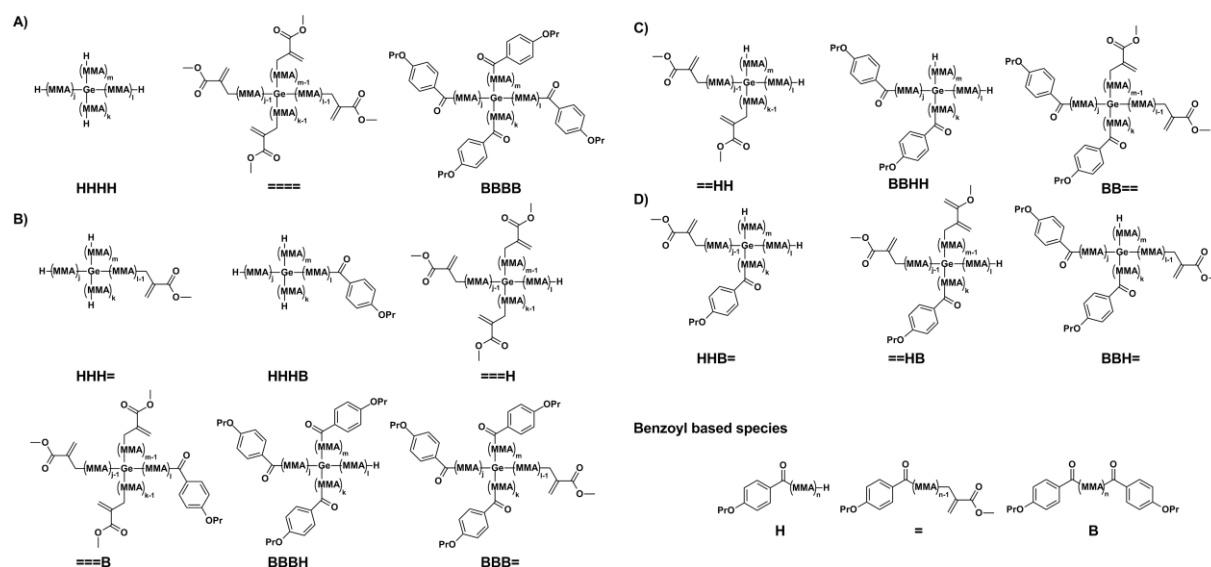


**Figure A9.** PrOB<sub>4</sub>G: Fifteen germanium-centered 4-armed MMA star polymers divided in four statistical groups A,B,C,D with relative propabilities of 0.083:0.33:0.5:1 and three benzoyl based PMMA species for isotopic pattern simulation. A Na<sup>+</sup> is added to each structure for exact mass calculation. Adapted with permission from ref. 145. Copyright 2018 American Chemical Society.

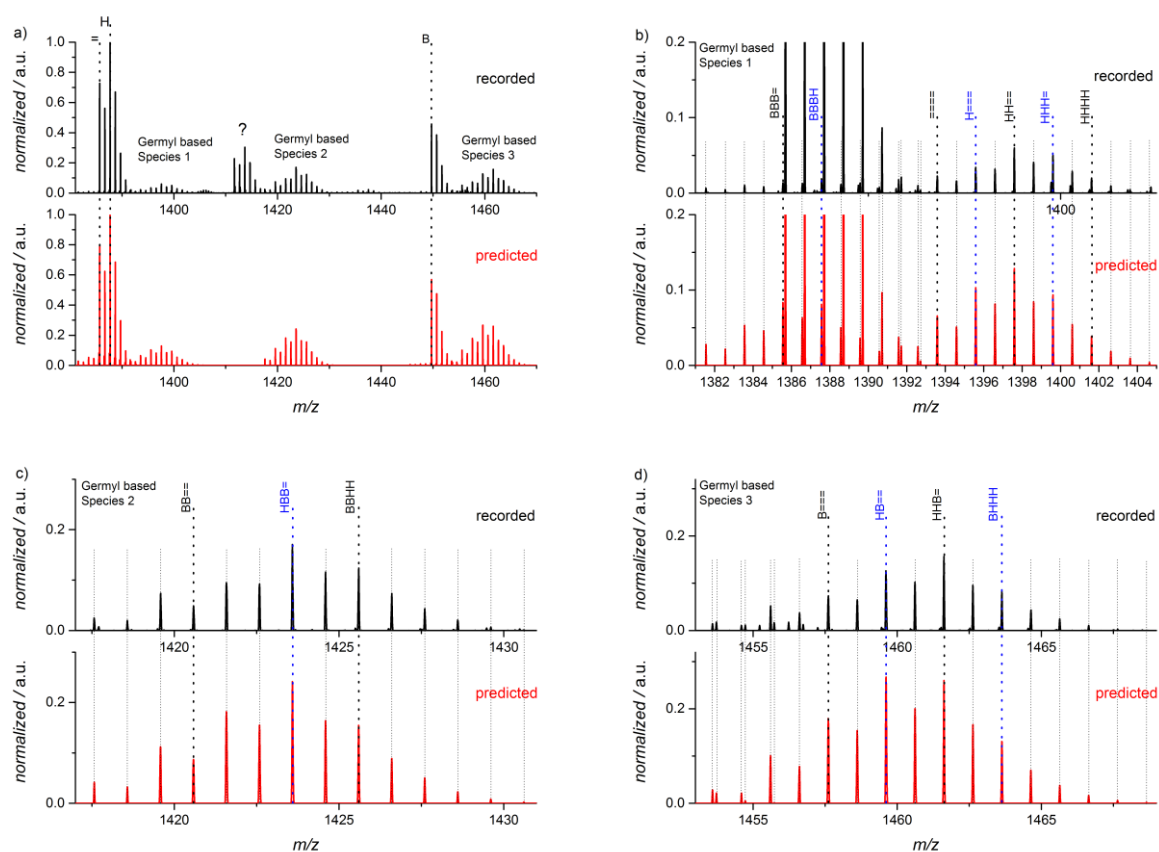


**Figure A10.** Mass spectra (black) and isotopic pattern simulations (red) of PrOB<sub>4</sub>G: **a)** Overview spectrum with all gerymyl and benzoyl based species shown in **Figure A9**. **b)-d)** Gerymyl based species 1-3 as depicted in **a)**. Adapted with permission from ref. 145. Copyright 2018 American Chemical Society.

**Table A15.** PrOB<sub>4</sub>G: Exact masses of germanium-centered MMA star polymers used for isotopic pattern simulation in the range of  $m/z$ ~1400. Na<sup>+</sup> is added to each structure for exact mass calculation. Adapted with permission from ref. 145. Copyright 2018 American Chemical Society. Modified presentation.

exact mass (simulated)	germyl species	sum formula	relative amount
1385.5497	BBB=	C <sub>70</sub> H <sub>96</sub> GeNaO <sub>22</sub>	0.33
1387.5654	BBBH	C <sub>70</sub> H <sub>98</sub> GeNaO <sub>22</sub>	0.33
1393.5607	====	C <sub>65</sub> H <sub>100</sub> GeNaO <sub>26</sub>	0.083
1395.5763	H===	C <sub>65</sub> H <sub>102</sub> GeNaO <sub>26</sub>	0.33
1397.5920	HH==	C <sub>65</sub> H <sub>104</sub> GeNaO <sub>26</sub>	0.5
1399.6076	HHH=	C <sub>65</sub> H <sub>106</sub> GeNaO <sub>26</sub>	0.33
1401.6233	HHHH	C <sub>65</sub> H <sub>108</sub> GeNaO <sub>26</sub>	0.083
1421.5709	BB==	C <sub>70</sub> H <sub>100</sub> GeNaO <sub>24</sub>	0.5
1423.5865	HBB=	C <sub>70</sub> H <sub>102</sub> GeNaO <sub>24</sub>	1
1425.6022	BBHH	C <sub>70</sub> H <sub>104</sub> GeNaO <sub>24</sub>	0.5
1449.5810	BBBB	C <sub>75</sub> H <sub>100</sub> GeNaO <sub>22</sub>	0.083
1457.5920	B===	C <sub>70</sub> H <sub>104</sub> GeNaO <sub>26</sub>	0.33
1459.6076	HB==	C <sub>70</sub> H <sub>106</sub> GeNaO <sub>26</sub>	1
1461.6233	HHB=	C <sub>70</sub> H <sub>108</sub> GeNaO <sub>26</sub>	1
1463.6389	BHHH	C <sub>70</sub> H <sub>110</sub> GeNaO <sub>26</sub>	0.33

**Table A16.** PrOB<sub>4</sub>G: Benzoyl initiated PMMA species used for the isotopic pattern simulation in the mass range of  $m/z$ ~1400. Na<sup>+</sup> is added to each structure for exact mass calculation. Adapted with permission from ref. 145. Copyright 2018 American Chemical Society. Modified presentation.

exact mass (simulated)	benzoyl species	sum formula	relative amount
1387.7021	H	C <sub>70</sub> H <sub>108</sub> NaO <sub>26</sub>	2.5
1385.6865	=	C <sub>70</sub> H <sub>106</sub> NaO <sub>26</sub>	2.5
1449.7178	B	C <sub>75</sub> H <sub>110</sub> NaO <sub>26</sub>	1.75

**Table A17.** PrOB<sub>4</sub>G: Relative mass difference and mass accuracy of simulated and recorded mass spectra of benzoyl based PMMA species. Adapted with permission from ref. 145. Copyright 2018 American Chemical Society. Modified presentation.

exact mass ( $m/z$ ) <sub>exp</sub> (recorded)	exact mass ( $m/z$ ) <sub>sim</sub> (simulated)	$\Delta m/z =$ $  (m/z)_{exp} - (m/z)_{sim}  $	$dm/m_{sim} =$ $(\Delta m/z)/(m/z)_{sim}$ $10^6 / \text{ppm}$
1385.68375	1385.68636	0.00261	1.88
1386.68718	1386.69019	0.00301	2.17
1387.69783	1387.69995	0.00212	1.53
1388.70345	1388.70466	0.00121	0.87
1389.71016	1389.70836	0.00180	1.30

1390.71182	1390.71163	0.00019	0.14
1449.71864	1449.71778	0.00086	0.59
1450.72038	1450.72085	0.00047	0.32
1451.72316	1451.72461	0.00145	1.00
1452.72697	1452.72786	0.00089	0.61

**Table A18.** PrOB<sub>4</sub>G: Relative mass difference and mass accuracy of simulated and recorded mass spectra of germyl based PMMA species. Strong deviations (> 10 ppm) occur only at very small peak intensities close to the detection limit. Adapted with permission from ref. 145. Copyright 2018 American Chemical Society. Modified presentation.

species number as depicted in Figure A9	exact mass (m/z) <sub>exp</sub> (recorded)	exact mass (m/z) <sub>sim</sub> (simulated)	$\Delta m/z =  (m/z)_{exp} - (m/z)_{sim} $	$dm/m_{sim} = (\Delta m/z)/(m/z)_{sim} 10^6 / \text{ppm}$
1	1381.5530	1381.5534	0.0003	0.24
	1382.5581	1382.5565	0.0016	1.14
	1383.5642	1383.5575	0.0067	4.86
	1384.5592	1384.5575	0.0018	1.27
	1385.5615	1385.5565	0.0050	3.61
	1386.5648	1386.5619	0.0028	2.04
	1387.5630	1387.5647	0.0016	1.18
	1388.5685	1388.5681	0.0004	0.27
	1389.5689	1389.5677	0.0013	0.90
	1390.5704	1390.5691	0.0013	0.96
	1390.7118	1390.7111	0.0008	0.55
	1391.5792	1391.5776	0.0015	1.11
	1391.7146	1391.7145	0.0001	0.08
	1392.5828	1392.5805	0.0023	1.69
	1392.7122	1392.7192	0.0069	4.99
	1393.5876	1393.5864	0.0012	0.85
	1394.5873	1394.5844	0.0029	2.11
	1395.5819	1395.5877	0.0058	4.14
	1396.5899	1396.5928	0.0029	2.11
	1397.5928	1397.5947	0.0019	1.33
1398.5968	1398.5996	0.0027	1.97	
1399.6081	1399.6063	0.0018	1.26	
1400.6080	1400.6103	0.0023	1.62	
1401.6153	1401.6156	0.0003	0.24	
1402.6174	1402.6187	0.0013	0.94	
1403.6206	1403.6243	0.0037	2.64	
1404.7060	1404.6271	0.0789	56.18	
2	1417.5700	1417.5744	0.0044	3.08
	1418.5766	1418.5783	0.0016	1.16
	1419.5906	1419.5846	0.0060	4.23
	1420.5867	1420.5858	0.0009	0.63
	1421.5838	1421.5853	0.0015	1.05
	1422.5883	1422.5885	0.0001	0.10

	1423.5875	1423.5894	0.0018	1.29
	1424.5942	1424.5934	0.0008	0.58
	1425.6019	1425.5992	0.0027	1.87
	1426.6043	1426.6029	0.0014	1.01
	1427.6077	1427.6048	0.0029	2.06
	1428.6059	1428.6075	0.0016	1.12
	1429.6114	1429.6126	0.0012	0.83
	1430.6116	1430.6149	0.0032	2.26
3	1453.5939	1453.5961	0.0023	1.56
	1453.7318	1453.7318	0.0000	0.02
	1454.5996	1454.5995	0.0002	0.11
	1454.7312	1454.7364	0.0053	3.63
	1455.6130	1455.6083	0.0047	3.21
	1455.7315	1455.7357	0.0042	2.87
	1456.6143	1456.6112	0.0030	2.08
	1457.6166	1457.6112	0.0054	3.70
	1458.6133	1458.6124	0.0009	0.60
	1459.6110	1459.6137	0.0027	1.84
	1460.6164	1460.6194	0.0029	2.02
	1461.6229	1461.6239	0.0010	0.71
	1462.6237	1462.6279	0.0042	2.86
	1463.6322	1463.6326	0.0004	0.25
	1464.6418	1464.6373	0.0044	3.02
	1465.6390	1465.6397	0.0007	0.46
	1466.6440	1466.6440	0.0000	0.01
	1467.6500	1467.6490	0.0010	0.67

### Isotopic pattern simulation of B<sub>2</sub>G

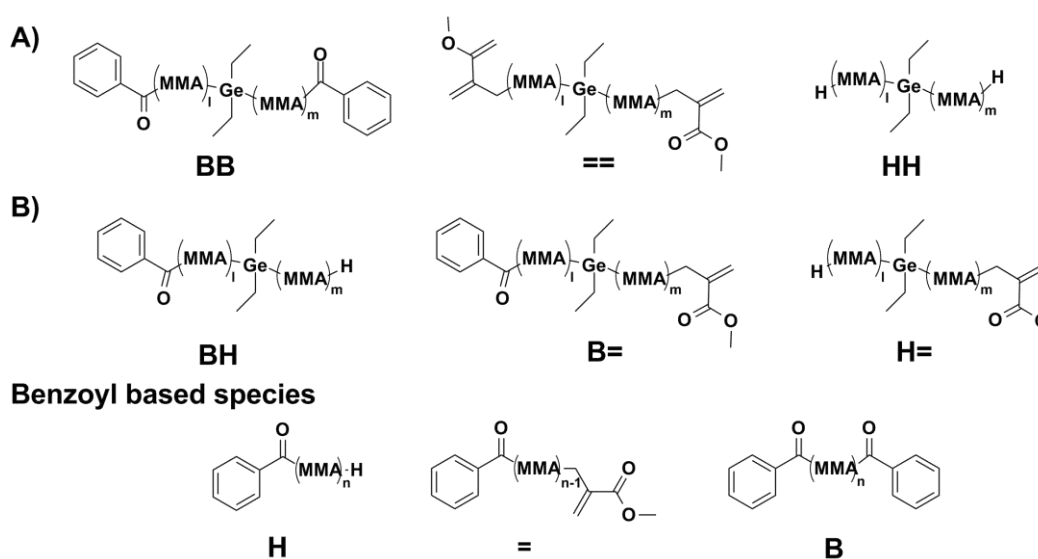


**Figure A11.** B<sub>2</sub>G: Six germanium-centered 2-armed MMA star polymers divided in two statistical groups A,B with relative propabilities 0.5:1 and three benzoyl based PMMA species for isotopic pattern simulation. A Na<sup>+</sup> is added to each structure for exact mass calculation. Adapted with permission from ref. 145. Copyright 2018 American Chemical Society.

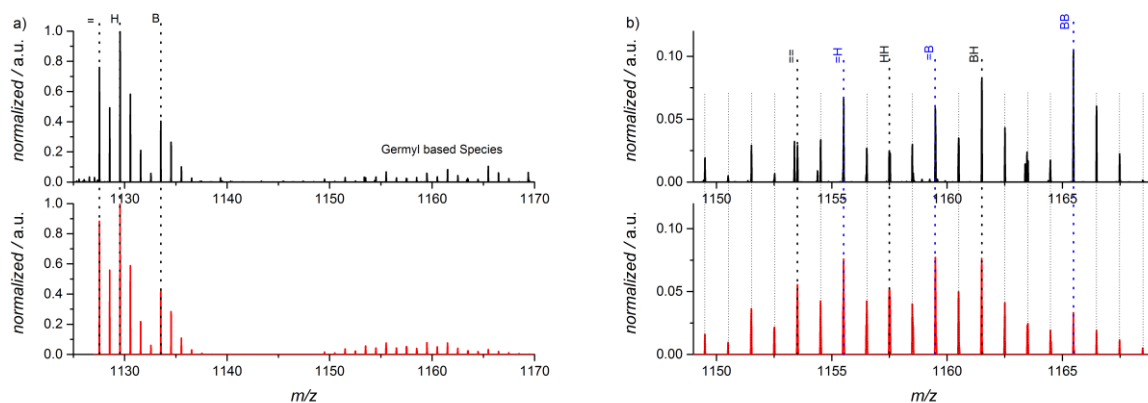


**Figure A12.** Mass spectra (black) and isotopic pattern simulations (red) of  $B_2G$ : a) Overview spectrum with all germyl and benzoyl based species shown in **Figure A11**. b) Germyl based species as depicted in a). Adapted with permission from ref. 145. Copyright 2018 American Chemical Society.

**Table A19.**  $B_2G$ : Exact masses of germanium-centered MMA star polymers used for isotopic pattern simulation in the range of  $m/z$ ~1400.  $Na^+$  is added to each structure for exact mass calculation. Adapted with permission from ref. 145. Copyright 2018 American Chemical Society. Modified presentation.

exact mass (simulated)	germyl species	sum formula	relative amount
1153.4973	= =	$C_{54}H_{88}GeNaO_{20}$	0.5
1155.5129	= H	$C_{54}H_{90}GeNaO_{20}$	1
1157.5286	HH	$C_{54}H_{92}GeNaO_{20}$	0.5
1159.4867	= B	$C_{56}H_{86}GeNaO_{19}$	1
1161.5024	BH	$C_{56}H_{88}GeNaO_{19}$	1
1165.4762	BB	$C_{58}H_{84}GeNaO_{18}$	0.5

**Table A20.**  $B_2G$ : Benzoyl initiated PMMA species used for the isotopic pattern simulation in the mass range of  $m/z$ ~1400.  $Na^+$  is added to each structure for exact mass calculation. Adapted with permission from ref. 145. Copyright 2018 American Chemical Society. Modified presentation.

exact mass (simulated)	benzoyl species	sum formula	relative amount
1129.5554	H	$C_{57}H_{86}NaO_{21}$	6
1127.5397	=	$C_{57}H_{84}NaO_{21}$	6
1133.5292	B	$C_{59}H_{82}NaO_{20}$	3

**Table A21.** B<sub>2</sub>G: Relative mass difference and mass accuracy of simulated and recorded mass spectra of benzoyl based PMMA species. Adapted with permission from ref. 145. Copyright 2018 American Chemical Society. Modified presentation.

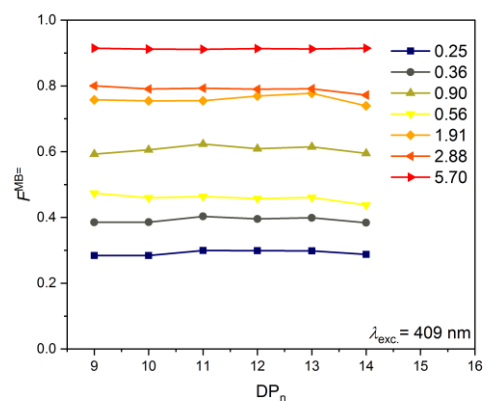
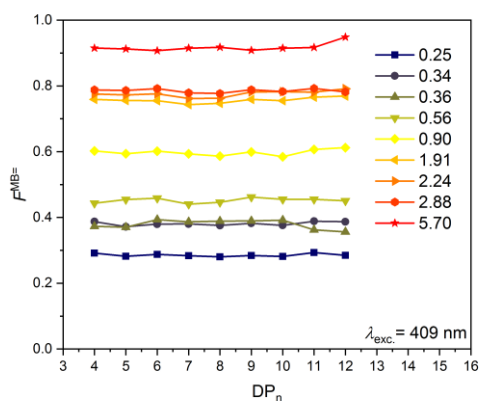
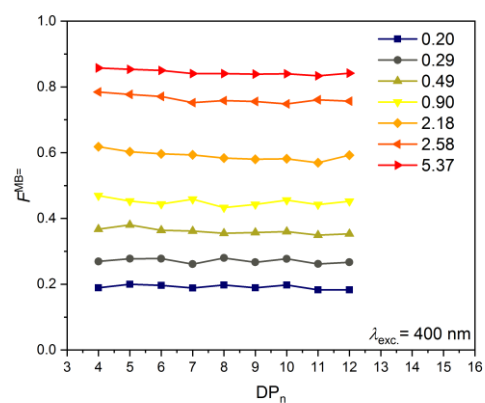
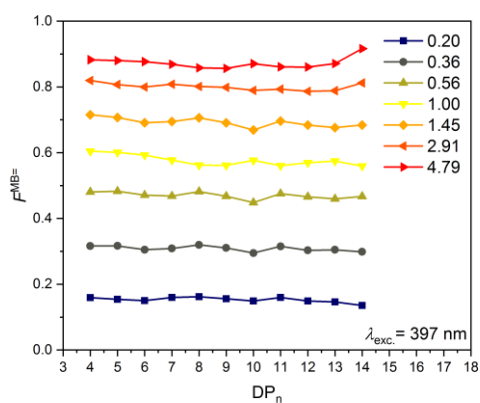
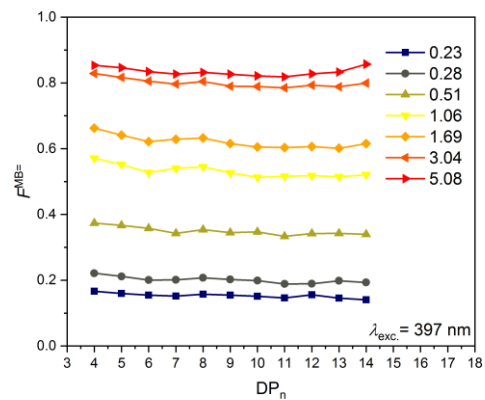
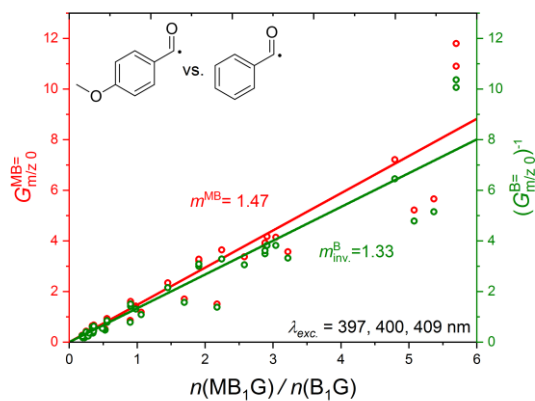
exact mass ( $m/z$ ) <sub>exp</sub> (recorded)	exact mass ( $m/z$ ) <sub>sim</sub> (simulated)	$\Delta m/z =$ $  (m/z)_{exp} - (m/z)_{sim}  $	$dm/m_{sim} =$ $(\Delta m/z)/(m/z)_{sim}$ $10^6 / \text{ppm}$
1127.53947	1127.53973	0.00026	0.23
1128.54562	1128.54322	0.00240	2.13
1129.55763	1129.55419	0.00344	3.05
1130.56198	1130.55852	0.00346	3.06
1131.56315	1131.56140	0.00175	1.55
1132.56566	1132.56516	0.00050	0.44
1133.52878	1133.52919	0.00041	0.36
1134.53390	1134.53281	0.00109	0.96
1135.53582	1135.53637	0.00055	0.48
1136.53907	1136.53940	0.00033	0.29

**Table A22.** B<sub>2</sub>G: Relative mass difference and mass accuracy of simulated and recorded mass spectra of germyl based PMMA species. Strong deviations (> 10 ppm) occur only at very small peak intensities close to the detection limit. Adapted with permission from ref. 145. Copyright 2018 American Chemical Society. Modified presentation.

exact mass ( $m/z$ ) <sub>exp</sub> (recorded)	exact mass ( $m/z$ ) <sub>sim</sub> (simulated)	$\Delta m/z =$ $  (m/z)_{exp} - (m/z)_{sim}  $	$dm/m_{sim} =$ $(\Delta m/z)/(m/z)_{sim}$ $10^6 / \text{ppm}$
1149.5045	1149.5006	0.0039	3.39
1150.5078	1150.5045	0.0034	2.92
1151.5171	1151.5140	0.0031	2.68
1152.5231	1152.5172	0.0058	5.05
1153.5164	1153.5127	0.0037	3.23
1154.5203	1154.5157	0.0046	4.01
1155.5162	1155.5143	0.0019	1.68
1156.5181	1156.5181	0.0000	0.00
1157.4886	1157.4914	0.0028	2.44
1158.4931	1158.4921	0.0009	0.79
1159.4894	1159.4913	0.0018	1.60
1160.5059	1160.5005	0.0054	4.63
1161.5095	1161.5018	0.0077	6.62
1162.5098	1162.5055	0.0043	3.69
1163.4643	1163.4790	0.0147	12.64
1164.4813	1164.4806	0.0007	0.63
1165.4807	1165.4776	0.0031	2.66
1166.4814	1166.4803	0.0011	0.91
1167.4834	1167.4805	0.0028	2.43
1168.4866	1168.4826	0.0041	3.50

# Overall initiation efficiencies of *para*-Fluor- and Methoxy-Substituted Mono-, Bis- and Tetraacylgermanes obtained by PLP-SEC-ESI-MS-Cocktail Experiments

## MB<sub>1</sub>G:B<sub>1</sub>G



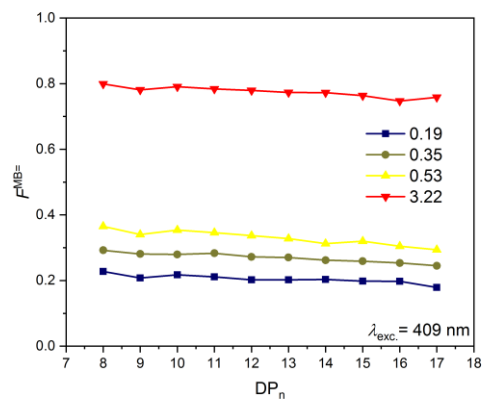


**Figure A13.**  $G$  versus molar ratio-plot and corresponding  $F$  versus  $DP$ -plots of the cocktail experiment  $MB_1G:B_1G$  conducted at 397, 400 and 409 nm. The overall initiation efficiency results in  $1.40 \pm 0.10$  via averaging of  $m$  and  $m_{inv.}$ . For further details refer to **chapter 4.3**. Adapted with permission from ref. 144. Copyright 2017 American Chemical Society. New evaluation.

## FB<sub>1</sub>G:B<sub>1</sub>G

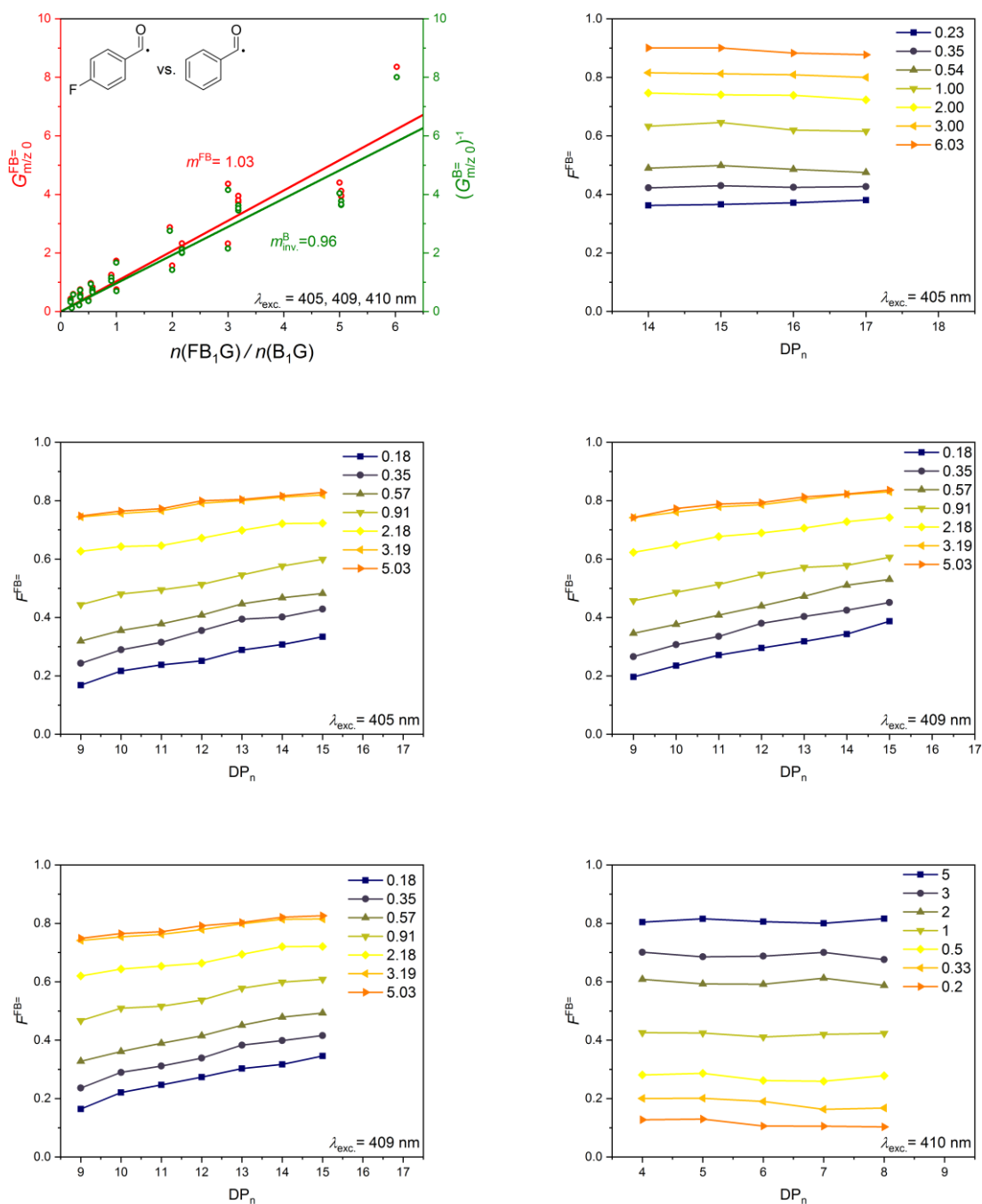


**Figure A14.**  $G$  versus molar ratio-plot and corresponding  $F$  versus  $DP_n$ -plots of the cocktail experiment FB<sub>1</sub>G, B<sub>1</sub>G conducted at 405, 409 and 410 nm. The overall initiation efficiency results in  $1.00 \pm 0.05$  via averaging of  $m$  and  $m_{\text{inv.}}$ . For further details refer to **chapter 4.3**. Adapted with permission from ref. 144. Copyright 2017 American Chemical Society. New evaluation.

## FB<sub>2</sub>G:B<sub>2</sub>G

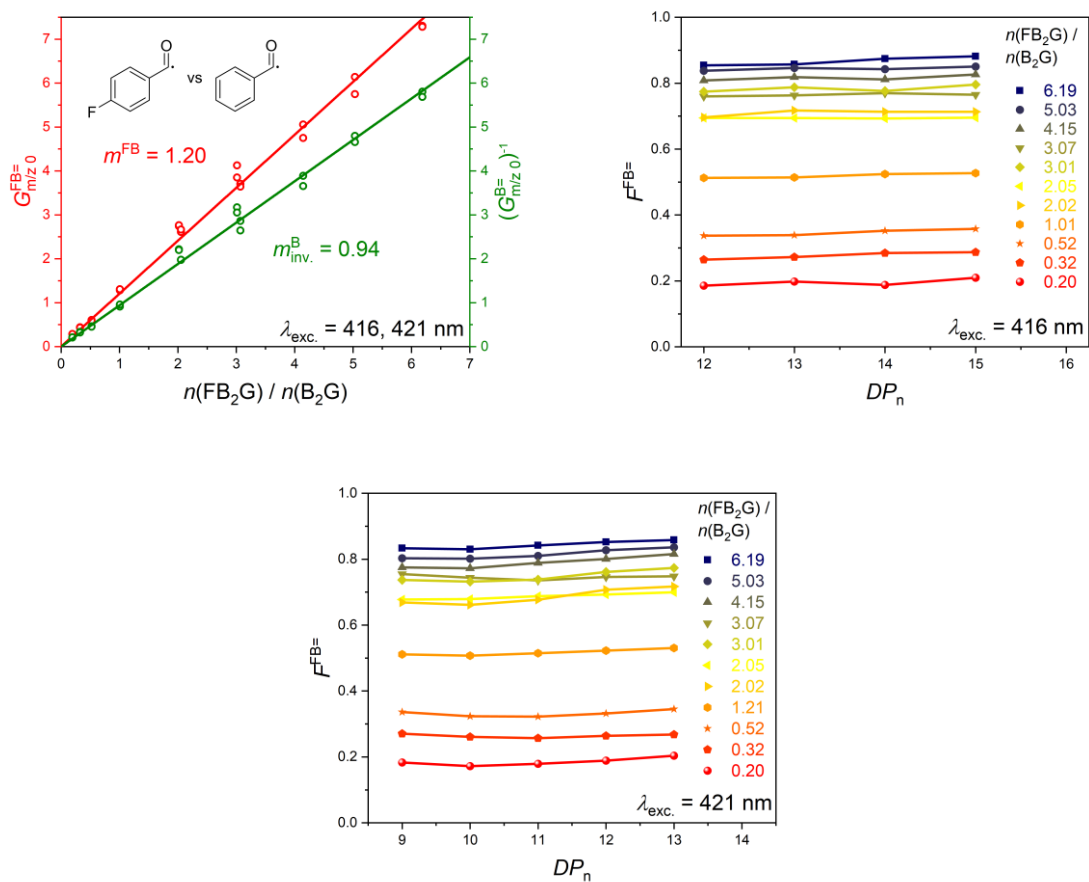


**Figure A15.** G versus molar ratio-plot and corresponding F versus DP-plots of the cocktail experiment FB<sub>2</sub>G, B<sub>2</sub>G conducted at 416 and 421 nm. The overall initiation efficiency in  $1.07 \pm 0.18$  results via averaging of  $m$  and  $m_{\text{inv.}}$ . For further details refer to **chapter 4.3**. Adapted with permission from ref. 146. Copyright 2019 American Chemical Society.

## MB<sub>2</sub>G:B<sub>2</sub>G

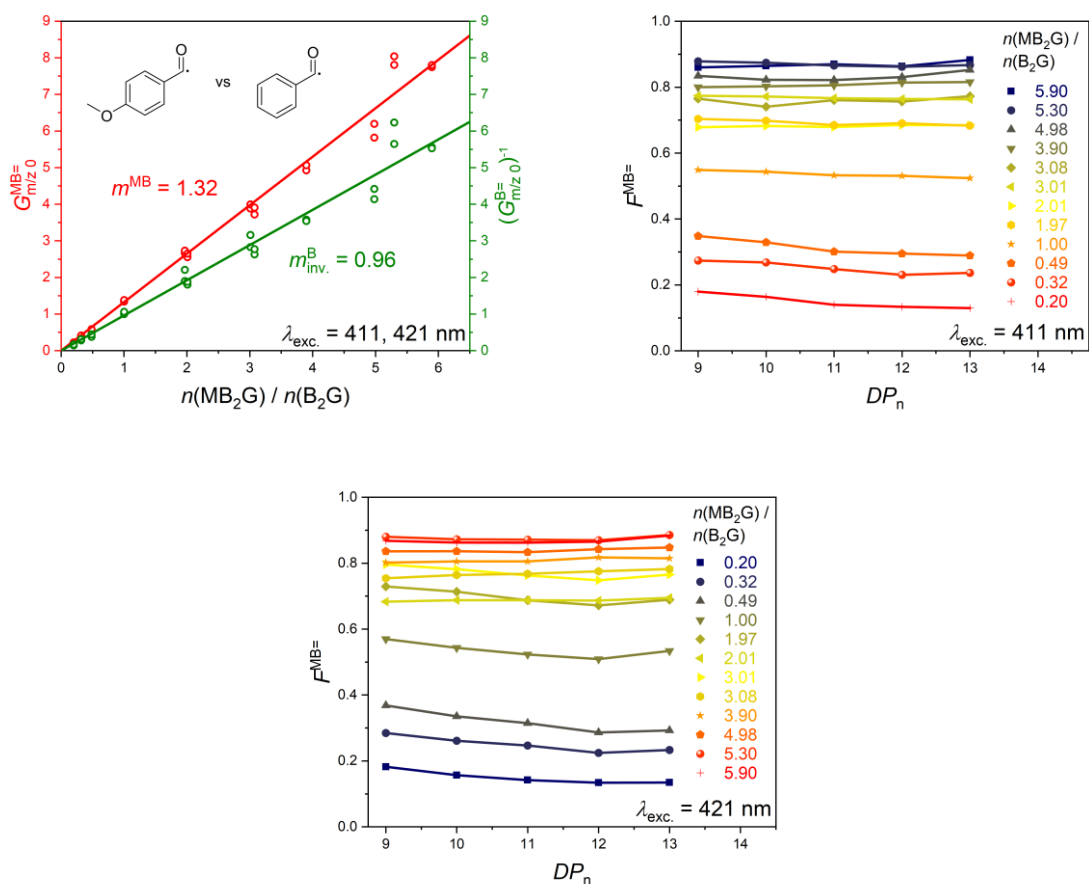


**Figure A16.** G versus molar ratio-plot and corresponding F versus DP-plots of the cocktail experiment MB<sub>2</sub>G, B<sub>2</sub>G conducted at 411 and 421 nm. The overall initiation efficiency results in  $1.14 \pm 0.25$  via averaging of  $m$  and  $m_{\text{inv.}}$ . For further details refer **chapter 4.3**. Adapted with permission from ref. 146. Copyright 2019 American Chemical Society.

## MB<sub>4</sub>G:B<sub>4</sub>G

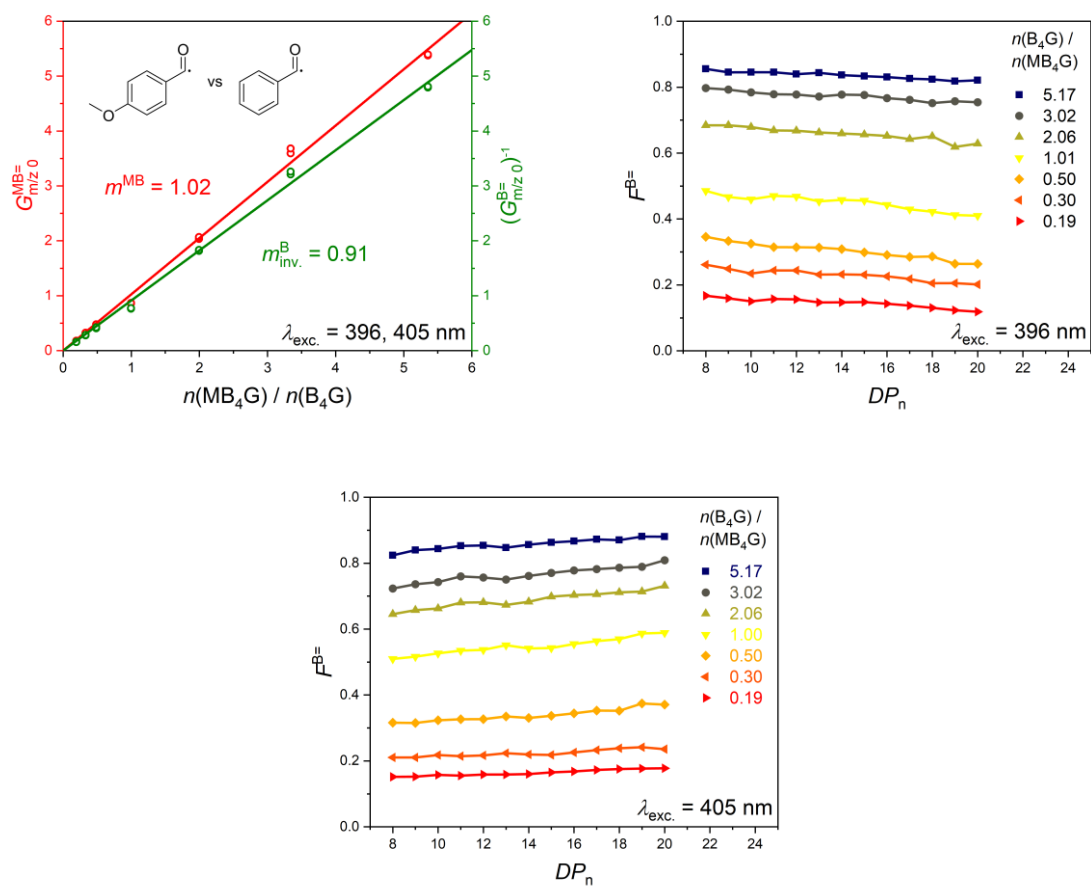


**Figure A17.** G versus molar ratio-plot and corresponding  $F$  versus  $DP$ -plots of the cocktail experiment MB<sub>4</sub>G, B<sub>4</sub>G conducted at 396 and 405 nm. The overall initiation efficiency results in  $0.97 \pm 0.08$  via averaging of  $m$  and  $m_{\text{inv.}}$ . For further details refer **chapter 4.3**. Adapted with permission from ref. 146. Copyright 2019 American Chemical Society.

## FB<sub>2</sub>G:MB<sub>1</sub>G

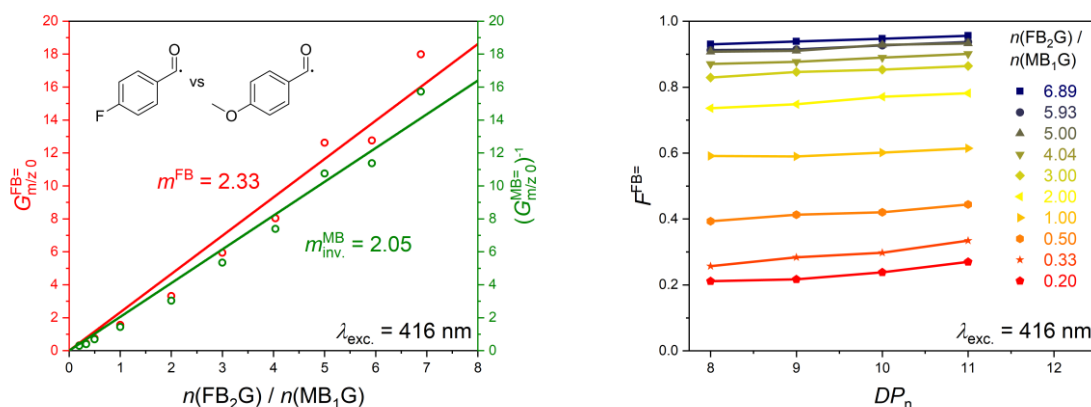


**Figure A18.** G versus molar ratio-plot and corresponding  $F$  versus  $DP_n$ -plots of the cocktail experiment FB<sub>2</sub>G, MB<sub>1</sub>G conducted at 416 nm. The overall initiation efficiency results in  $2.19 \pm 0.20$  via averaging of  $m$  and  $m_{\text{inv.}}$ . For further details refer to **chapter 4.3**. Adapted with permission from ref. 146. Copyright 2019 American Chemical Society.

## MB<sub>2</sub>G:B<sub>1</sub>G

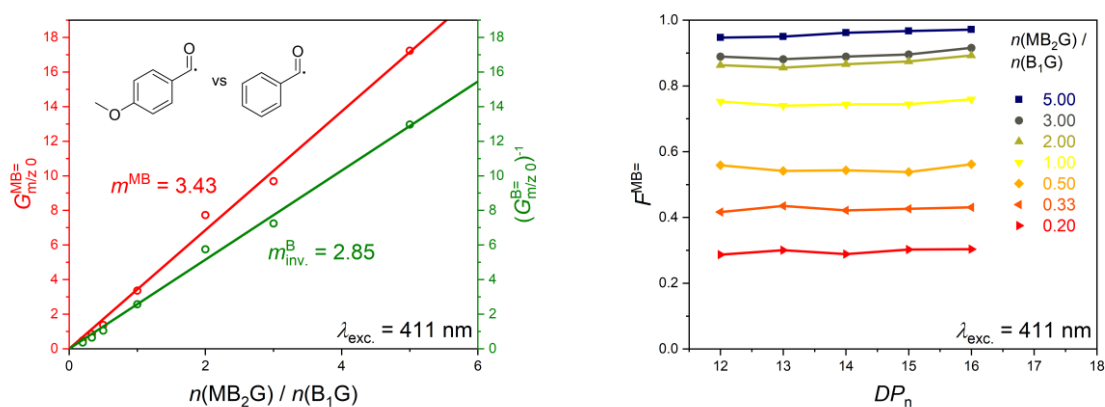


**Figure A19.** G versus molar ratio-plot and corresponding  $F$  versus  $DP_n$ -plots of the cocktail experiment MB<sub>2</sub>G, B<sub>1</sub>G conducted at 411 nm. The overall initiation efficiency results in  $3.14 \pm 0.41$  via averaging of  $m$  and  $m_{\text{inv.}}$ . For further details refer to **chapter 4.3**. Adapted with permission from ref. 146. Copyright 2019 American Chemical Society.

## MB<sub>2</sub>G:FB<sub>1</sub>G

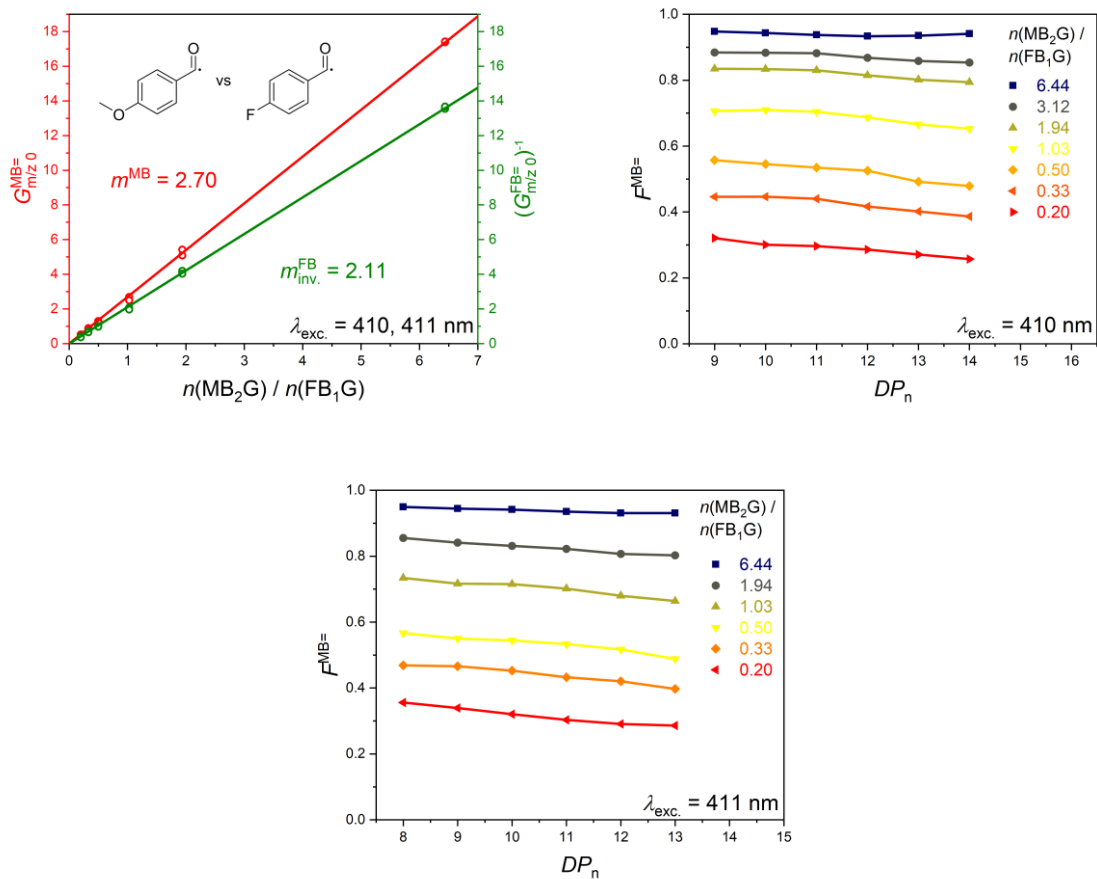


**Figure A20.**  $G$  versus molar ratio-plot and corresponding  $F$  versus  $DP$ -plots of the cocktail experiment MB<sub>2</sub>G, FB<sub>1</sub>G conducted at 410 and 411 nm. The overall initiation efficiency results in  $2.40 \pm 0.42$  via averaging of  $m$  and  $m_{\text{inv.}}$ . For further details refer to **chapter 4.3**. Adapted with permission from ref. 146. Copyright 2019 American Chemical Society.

## B<sub>4</sub>G:MB<sub>2</sub>G

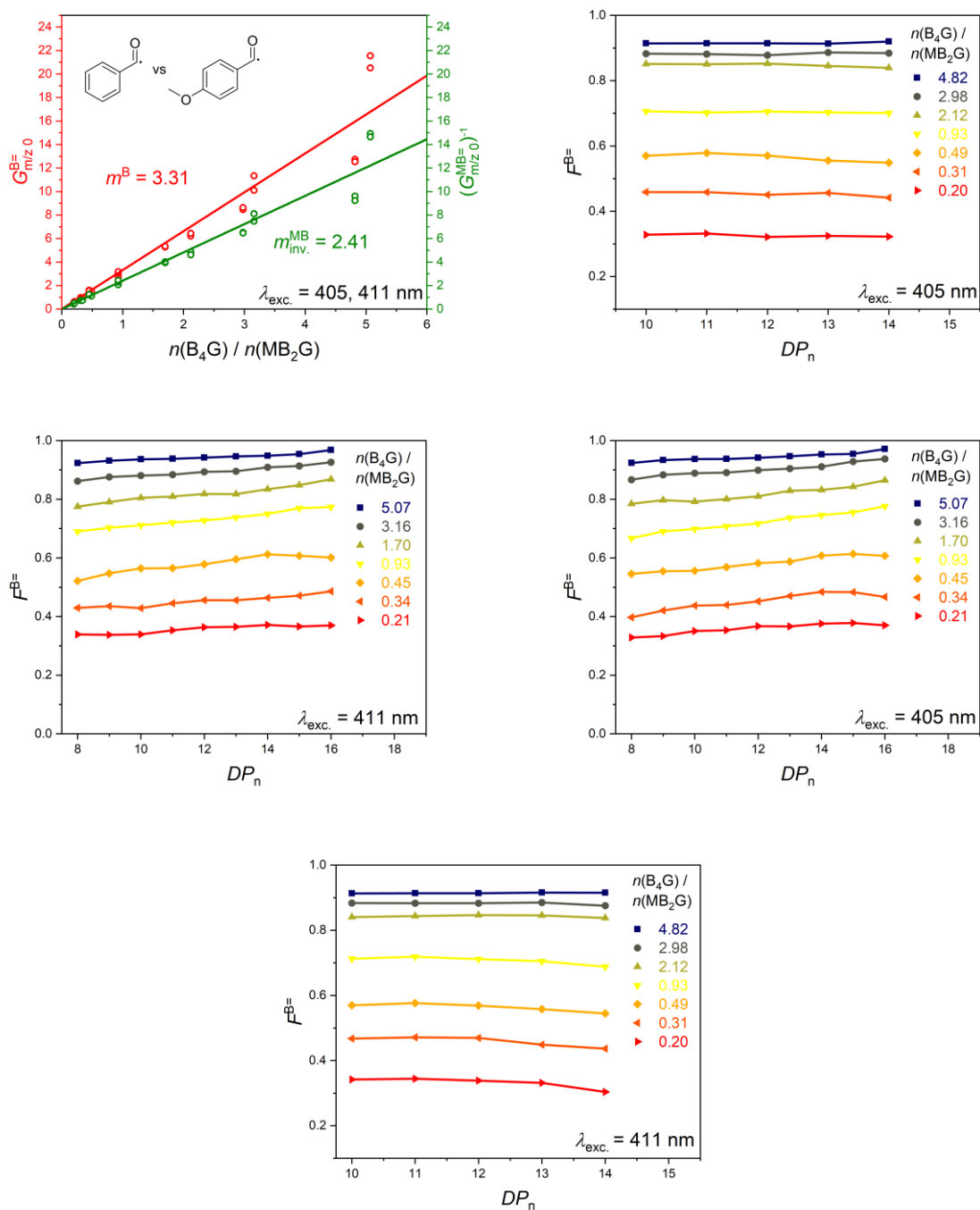


**Figure A21.** G versus molar ratio-plot and corresponding F versus DP-plots of the cocktail experiment B<sub>4</sub>G, MB<sub>2</sub>G conducted at 405 and 411 nm. The overall initiation efficiency results in  $2.86 \pm 0.64$  via averaging of  $m$  and  $m_{\text{inv.}}$ . For further details refer to **chapter 4.3**. Adapted with permission from ref. 146. Copyright 2019 American Chemical Society.

## B<sub>4</sub>G:FB<sub>2</sub>G

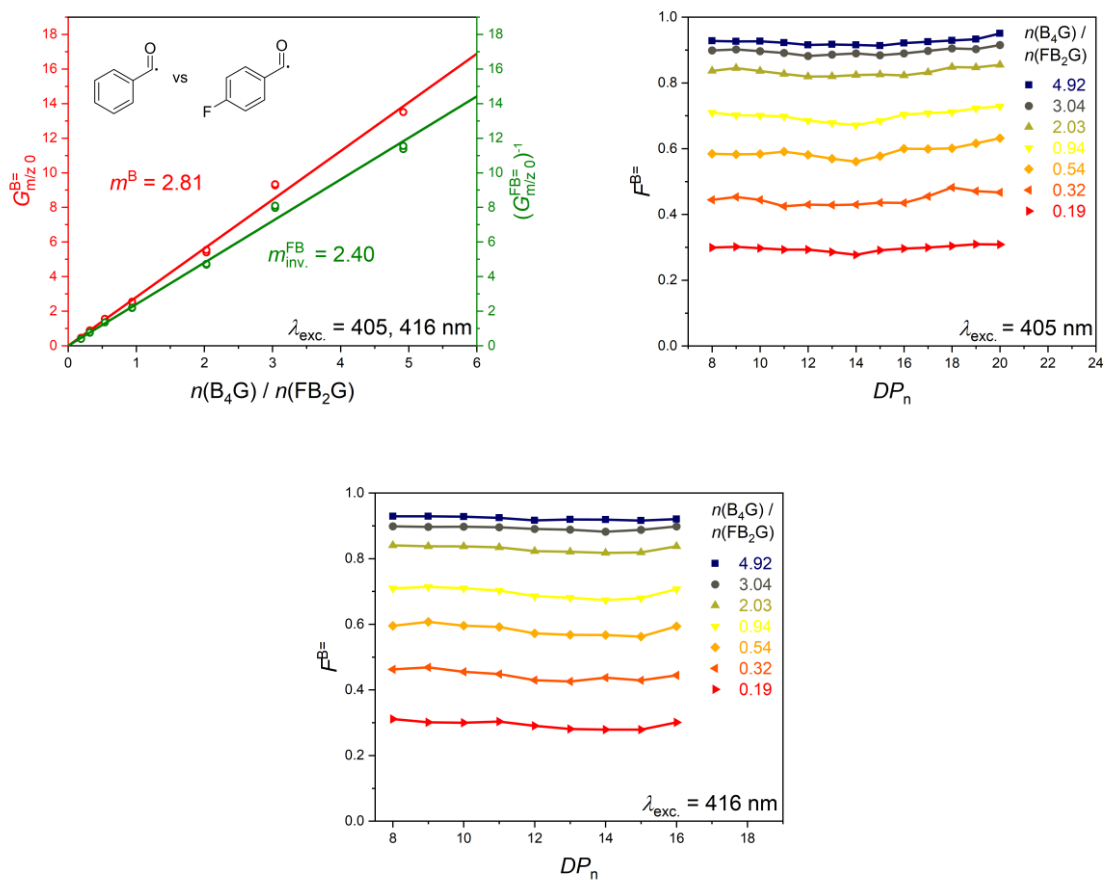


**Figure A22.** G versus molar ratio-plot and corresponding F versus DP-plots of the cocktail experiment B<sub>4</sub>G, FB<sub>2</sub>G conducted at 405 and 416 nm. The overall initiation efficiency results in  $2.61 \pm 0.29$  via averaging of  $m$  and  $m_{inv.}$ . For further details refer to **chapter 4.3**. Adapted with permission from ref. 146. Copyright 2019 American Chemical Society.

## B<sub>4</sub>G : FB<sub>1</sub>G

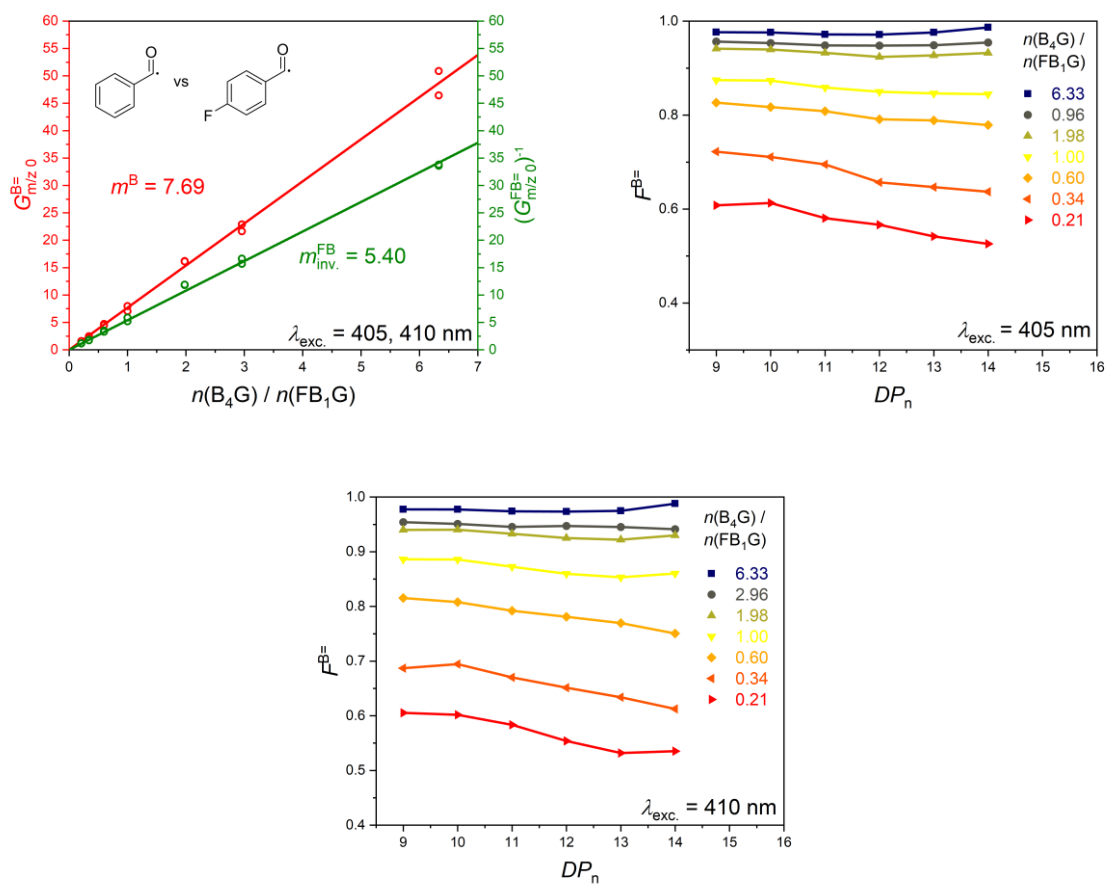


**Figure A23.** G versus molar ratio-plot and corresponding F versus DP-plots of the cocktail experiment B<sub>4</sub>G, FB<sub>1</sub>G conducted at 405 and 410 nm. The overall initiation efficiency results in  $6.55 \pm 1.62$  via averaging of  $m$  and  $m_{inv.}$ . For further details refer to **chapter 4.3**. Adapted with permission from ref. 146. Copyright 2019 American Chemical Society.

## MB<sub>4</sub>G : B<sub>1</sub>G

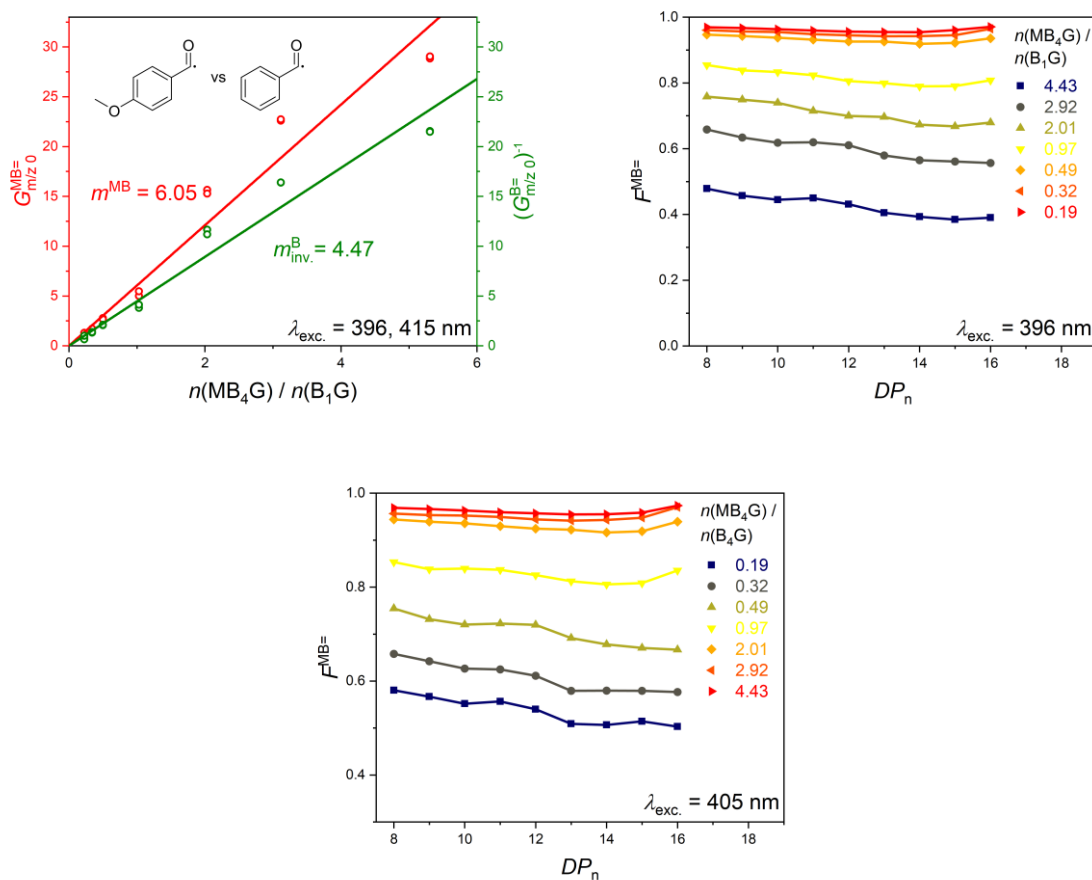


**Figure A24.** G versus molar ratio-plot and corresponding F versus DP-plots of the cocktail experiment MB<sub>4</sub>G, B<sub>1</sub>G conducted at 396 and 415 nm. The overall initiation efficiency results in  $5.26 \pm 0.79$  via averaging of  $m$  and  $m_{inv.}$ . For further details refer to **chapter 4.3**. Adapted with permission from ref. 146. Copyright 2019 American Chemical Society.

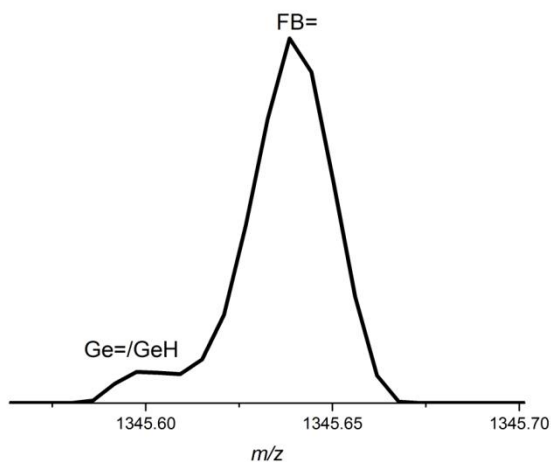


**Figure A 25.** Slight intrinsic isobaric overlap of disproportionation products initiated by fluoro-substituted benzoyl- and trimethylgermane-radicals leading to a systematic error for cocktail experiments including FB<sub>1</sub>G. Adapted with permission from ref. 144. Copyright 2017 American Chemical Society.

## Triple Cocktail Experiment of B<sub>4</sub>G, FB<sub>2</sub>G, MB<sub>1</sub>G

### FB<sub>2</sub>G:MB<sub>1</sub>G Corresponding to Triple Cocktail Experiment with B<sub>4</sub>G, FB<sub>2</sub>G, MB<sub>1</sub>G

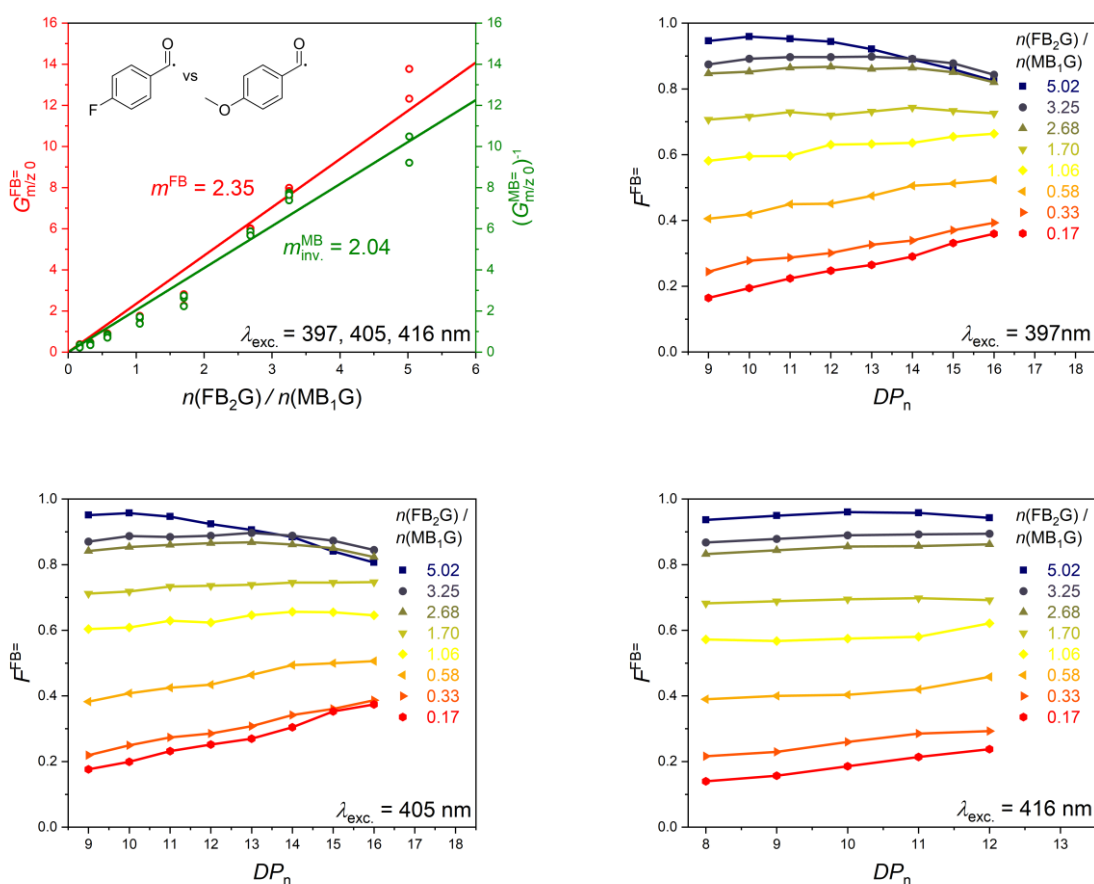


**Figure A26.** G versus molar ratio-plot and corresponding F versus DP-plots of FB<sub>2</sub>G, MB<sub>1</sub>G according to the triple cocktail experiment conducted at 397, 405, and 416 nm. The overall initiation efficiency results in  $2.20 \pm 0.22$  via averaging of  $m$  and  $m_{inv.}$ . For further details refer to **chapter 4.3**. Adapted with permission from ref. 146. Copyright 2019 American Chemical Society.

## B<sub>4</sub>G:FB<sub>2</sub>G Corresponding to Triple Cocktail Experiment with B<sub>4</sub>G, FB<sub>2</sub>G, MB<sub>1</sub>G

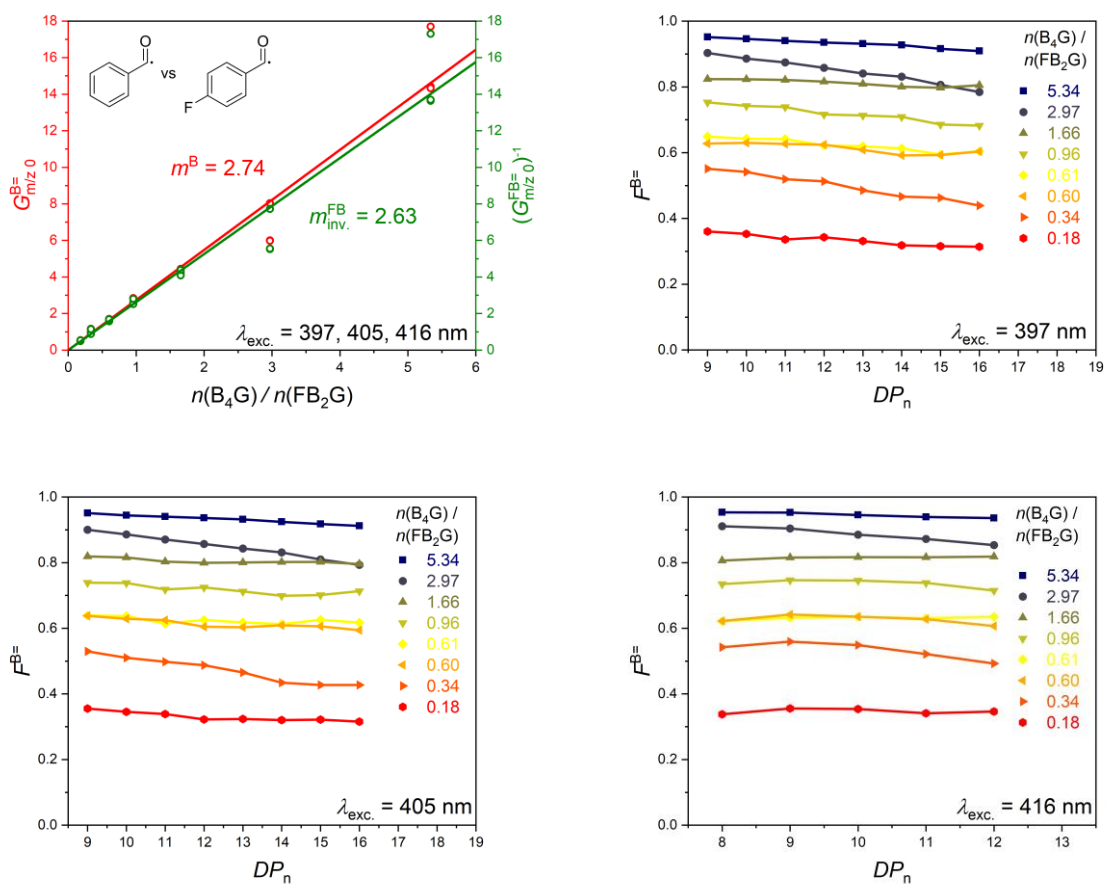


**Figure A27.** G versus molar ratio-plot and corresponding  $F$  versus  $DP$ -plots of B<sub>4</sub>G, FB<sub>2</sub>G according to the triple cocktail experiment conducted at 397, 405, and 416 nm. The overall initiation efficiency results in  $2.69 \pm 0.08$  via averaging of  $m$  and  $m_{\text{inv.}}$ . For further details refer to **chapter 4.3**. Adapted with permission from ref. 146. Copyright 2019 American Chemical Society.

## B<sub>4</sub>G:MB<sub>1</sub>G Corresponding to Triple Cocktail Experiment with B<sub>4</sub>G, FB<sub>2</sub>G, MB<sub>1</sub>G

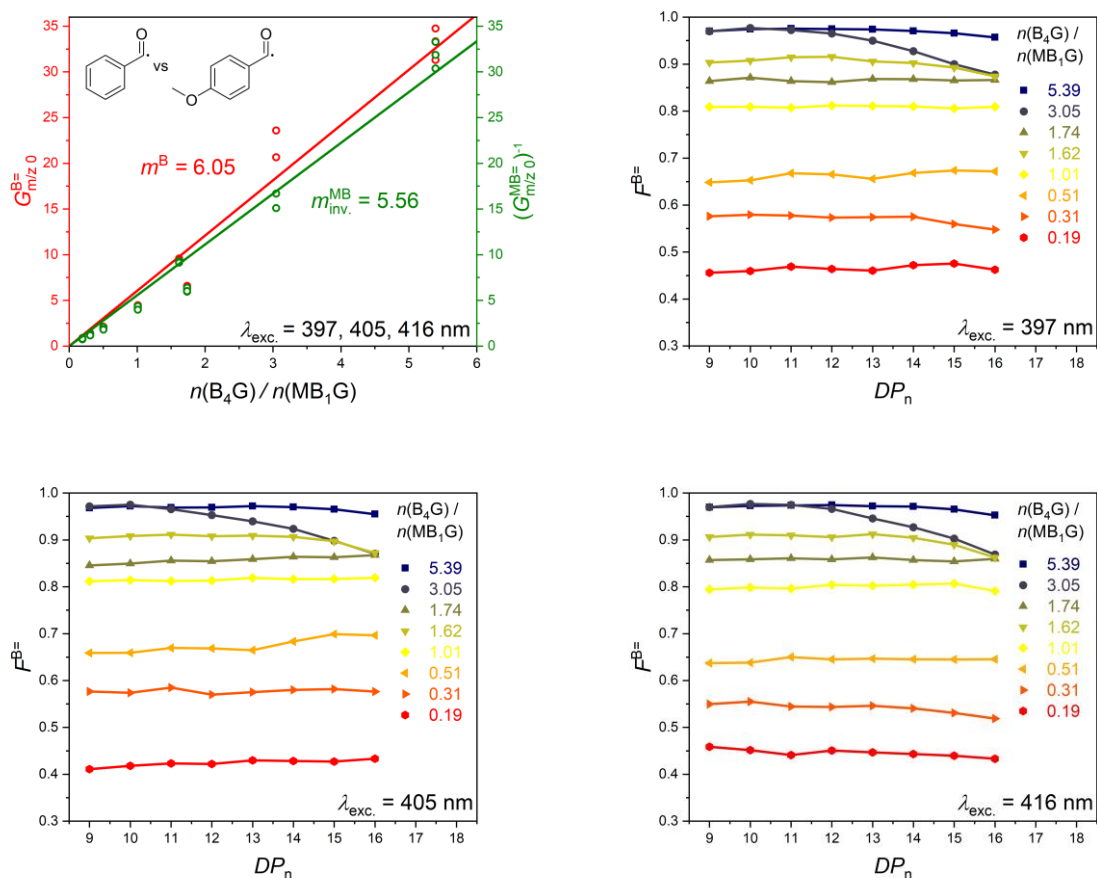


**Figure A28.** G versus molar ratio-plot and corresponding  $F$  versus  $DP$ -plots of B<sub>4</sub>G, MB<sub>1</sub>G according to the triple cocktail experiment conducted at 397, 405, and 416 nm. The overall initiation efficiency results in  $5.81 \pm 0.35$  via averaging of  $m$  and  $m_{inv.}$ . For further details refer to **chapter 4.3**. Adapted with permission from ref. 146. Copyright 2019 American Chemical Society.

## PLP-ESI-MS Cocktail-Experiments with *Ortho*-Substituted Tetraacylgermanes

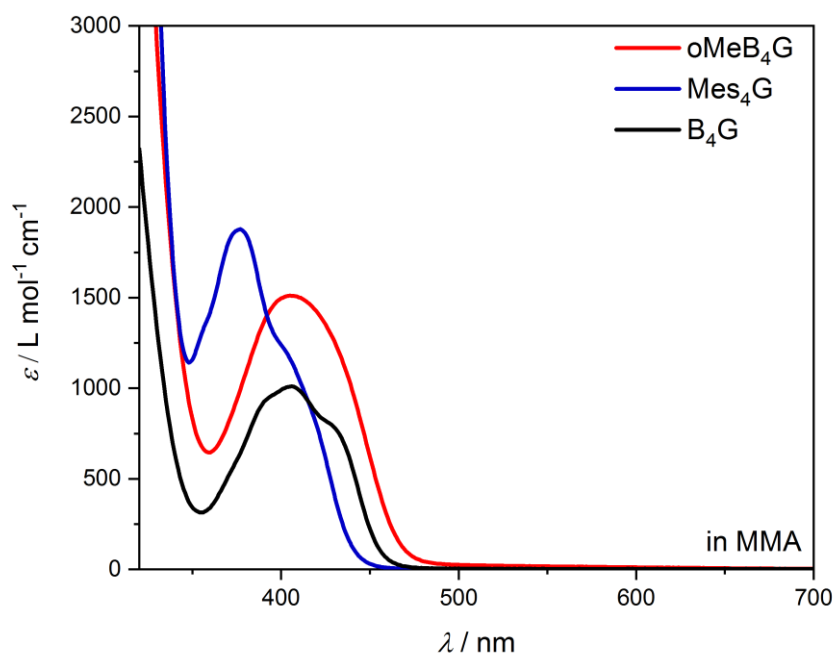


**Figure A29.** Steady-state UV/Vis-spectra of  $o\text{MeB}_4\text{G}$  (red) and  $\text{Mes}_4\text{G}$  (blue) compared with  $\text{B}_4\text{G}$  (black) dissolved in MMA and recorded in 1 cm cuvettes for determination of  $n\pi^*$ -extinction coefficients.

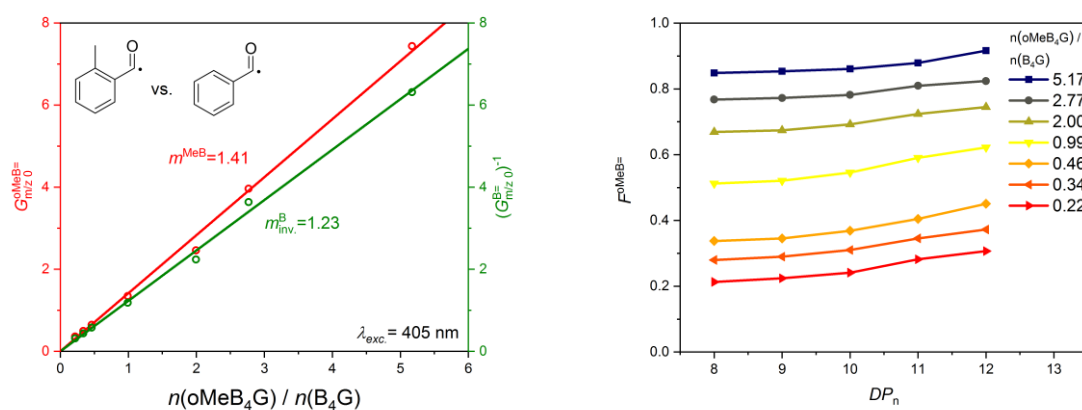


**Figure A30.**  $G$  versus molar ratio-plot and corresponding  $F$  versus  $DP$ -plots of the cocktail experiment  $o\text{MeB}_4\text{G}:\text{B}_4\text{G}$  conducted at 405 nm. The overall initiation efficiency results in  $1.32 \pm 0.13$  via averaging of  $m$  and  $m_{\text{inv.}}$ . For further details refer to **chapter 4.3**.

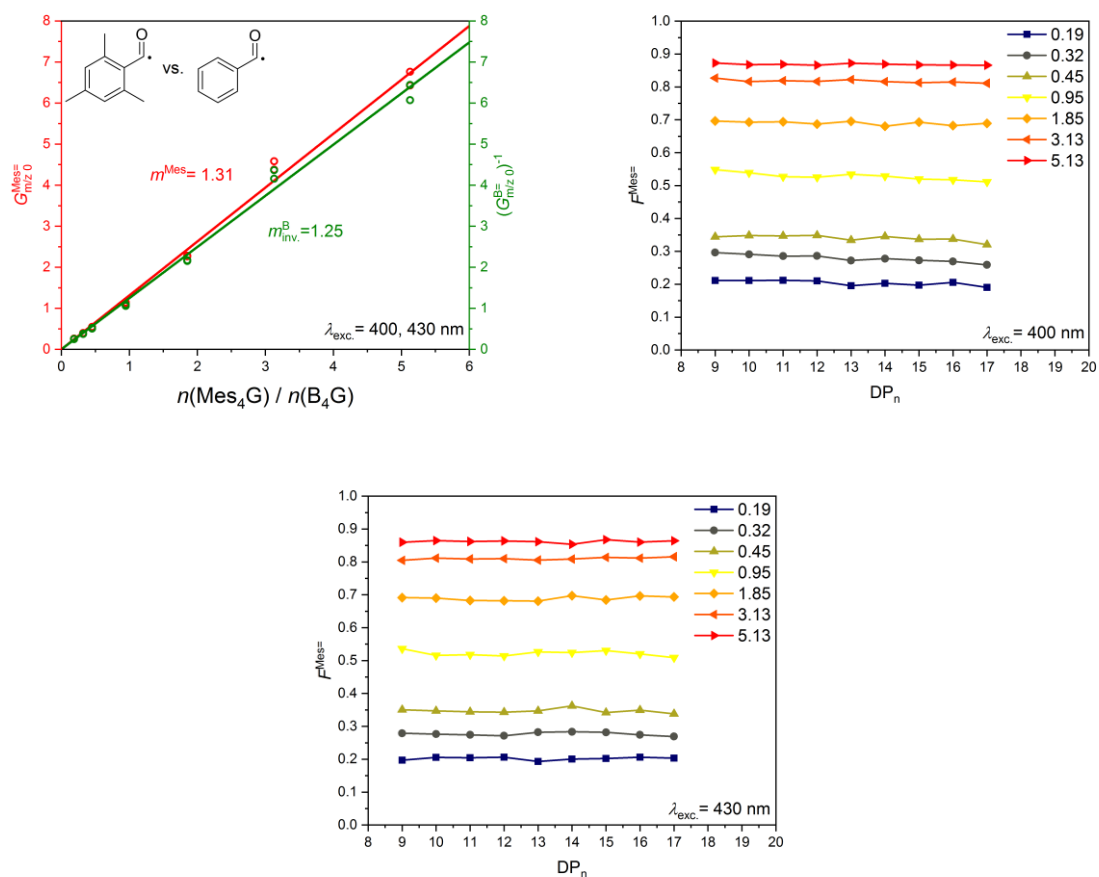


**Figure A31.** *G* versus molar ratio-plot and corresponding *F* versus *DP*-plots of the cocktail experiment Mes<sub>4</sub>G:B<sub>4</sub>G conducted at 400 and 430 nm. The overall initiation efficiency results in  $1.28 \pm 0.04$  via averaging of *m* and *m*<sub>inv.</sub>. For further details refer to **chapter 4.3**.

### Validity of the Overall Initiation Efficiencies Data Base

**Equations A1-A10.** Adapted with permission from ref. 146. Copyright 2019 American Chemical Society. Modified presentation:

$$\left(\frac{\text{FB}_1\text{G}}{\text{B}_1\text{G}}\right)_{\text{calc.}} = \left(\frac{\text{MB}_2\text{G}}{\text{B}_1\text{G}}\right) \left(\frac{\text{MB}_2\text{G}}{\text{FB}_1\text{G}}\right)^{-1} = \frac{3.14 \pm 0.41}{2.40 \pm 0.42} = 1.31 \pm 0.44 \text{ (34 \%)}$$

$$\begin{aligned} \left(\frac{\text{MB}_1\text{G}}{\text{B}_1\text{G}}\right)_{\text{calc.}} &= \left(\frac{\text{FB}_2\text{G}}{\text{B}_2\text{G}}\right) \left(\frac{\text{MB}_2\text{G}}{\text{B}_1\text{G}}\right) \left(\frac{\text{MB}_2\text{G}}{\text{B}_2\text{G}}\right)^{-1} \left(\frac{\text{FB}_2\text{G}}{\text{MB}_1\text{G}}\right)^{-1} \\ &= \frac{(1.07 \pm 0.18) \cdot (3.14 \pm 0.41)}{(1.14 \pm 0.25) \cdot (2.19 \pm 0.20)} = 1.35 \pm 0.54 \text{ (40 \%)} \end{aligned}$$

$$\left(\frac{\text{FB}_2\text{G}}{\text{MB}_1\text{G}}\right)_{\text{calc.}} = \left(\frac{\text{B}_4\text{G}}{\text{MB}_1\text{G}}\right) \left(\frac{\text{B}_4\text{G}}{\text{FB}_2\text{G}}\right)^{-1} = \frac{5.81 \pm 0.35}{2.61 \pm 0.29} = 2.23 \pm 0.62 \text{ (28 \%)}$$

$$\left(\frac{\text{MB}_2\text{G}}{\text{FB}_1\text{G}}\right)_{\text{calc.}} = \left(\frac{\text{B}_4\text{G}}{\text{FB}_1\text{G}}\right) \left(\frac{\text{B}_4\text{G}}{\text{MB}_2\text{G}}\right)^{-1} = \frac{6.55 \pm 1.62}{2.86 \pm 0.64} = 2.29 \pm 0.57 (25 \%)$$

$$\left(\frac{\text{MB}_2\text{G}}{\text{B}_1\text{G}}\right)_{\text{calc.}} = \left(\frac{\text{MB}_2\text{G}}{\text{FB}_1\text{G}}\right) \left(\frac{\text{FB}_1\text{G}}{\text{B}_1\text{G}}\right) = (2.40 \pm 0.42) \cdot (1.00 \pm 0.05) = 2.40 \pm 0.44 (28 \%)$$

$$\left(\frac{\text{B}_4\text{G}}{\text{MB}_2\text{G}}\right)_{\text{calc.}} = \left(\frac{\text{B}_4\text{G}}{\text{FB}_1\text{G}}\right) \left(\frac{\text{MB}_2\text{G}}{\text{FB}_1\text{G}}\right)^{-1} = \frac{6.55 \pm 1.62}{2.40 \pm 0.42} = 2.73 \pm 1.07 (39 \%)$$

$$\left(\frac{\text{B}_4\text{G}}{\text{FB}_2\text{G}}\right)_{\text{calc.}} = \left(\frac{\text{B}_4\text{G}}{\text{MB}_1\text{G}}\right) \left(\frac{\text{FB}_2\text{G}}{\text{MB}_1\text{G}}\right)^{-1} = \frac{5.81 \pm 0.35}{2.19 \pm 0.20} = 2.60 \pm 0.63 (24 \%)$$

$$\left(\frac{\text{B}_4\text{G}}{\text{FB}_1\text{G}}\right)_{\text{calc.}} = \left(\frac{\text{B}_4\text{G}}{\text{MB}_2\text{G}}\right) \left(\frac{\text{MB}_2\text{G}}{\text{FB}_1\text{G}}\right) = (2.86 \pm 0.64) \cdot (2.40 \pm 0.42) = 6.86 \pm 1.62 (24 \%)$$

$$\left(\frac{\text{B}_4\text{G}}{\text{MB}_1\text{G}}\right)_{\text{calc.}} = \left(\frac{\text{B}_4\text{G}}{\text{FB}_2\text{G}}\right) \left(\frac{\text{FB}_2\text{G}}{\text{MB}_1\text{G}}\right) = (2.61 \pm 0.29) \cdot (2.19 \pm 0.20) = 5.72 \pm 0.82 (14 \%)$$

$$\begin{aligned} \left(\frac{\text{MB}_4\text{G}}{\text{B}_1\text{G}}\right)_{\text{calc.}} &= \left(\frac{\text{MB}_4\text{G}}{\text{B}_4\text{G}}\right) \left(\frac{\text{B}_4\text{G}}{\text{MB}_2\text{G}}\right) \left(\frac{\text{MB}_2\text{G}}{\text{B}_1\text{G}}\right) = (0.97 \pm 0.08) \cdot (2.86 \pm 0.64) \cdot (3.14 \pm 0.41) \\ &= 8.71 \pm 2.37 (27 \%) \end{aligned}$$

**Table A23.** Comparison of calculated and experimental overall initiation efficiency for validation purposes. Adapted with permission from ref. 146. Copyright 2019 American Chemical Society. Modified presentation.

cocktail experiment	radical fragments	calculated overall initiation efficiency $m$	experimental overall initiation efficiency $m$	deviation / % $\left 1 - \left(\frac{m_{\text{exp}}}{m_{\text{pred}}}\right)\right  \cdot 100$
FB <sub>1</sub> G:B <sub>1</sub> G	FB:B	1.31 ± 0.44	1.00 ± 0.05	23.66
MB <sub>1</sub> G:B <sub>1</sub> G	MB:B	1.35 ± 0.54	1.40 ± 0.10	3.70
FB <sub>2</sub> G:MB <sub>1</sub> G	FB:MB	2.23 ± 0.62	2.19 ± 0.20	1.79
MB <sub>2</sub> G:FB <sub>1</sub> G	MB:FB	2.29 ± 0.57	2.40 ± 0.42	4.80
MB <sub>2</sub> G:B <sub>1</sub> G	MB:B	2.4 ± 0.44	3.14 ± 0.41	30.83
B <sub>4</sub> G:MB <sub>2</sub> G	B:MB	2.73 ± 1.07	2.86 ± 0.64	4.76
B <sub>4</sub> G:FB <sub>2</sub> G	B:FB	2.60 ± 0.63	2.61 ± 0.29	0.38
B <sub>4</sub> G:FB <sub>1</sub> G	B:FB	6.86 ± 1.62	6.55 ± 1.62	4.52
B <sub>4</sub> G:MB <sub>1</sub> G	B:MB	5.72 ± 0.82	5.81 ± 0.35	1.57
MB <sub>4</sub> G:B <sub>1</sub> G	MB:B	8.71 ± 2.37	5.26 ± 0.79	39.61

## Non-stoichiometric increase of overall initiation efficiency

**Equations A11-A18.** Adapted with permission from ref. 146. Copyright 2019 American Chemical Society. Modified presentation.

$$\left(\frac{B_2G}{B_1G}\right)_{\text{calc.}} = \left(\frac{MB_2G}{B_1G}\right) \left(\frac{MB_2G}{B_2G}\right)^{-1} = \frac{3.14 \pm 0.41}{1.14 \pm 0.25} = 2.75 \pm 0.98 (36 \%)$$

$$\begin{aligned} \left(\frac{FB_2G}{FB_1G}\right)_{\text{calc.}} &= \left(\frac{FB_2G}{MB_1G}\right) \left(\frac{B_4G}{FB_1G}\right) \left(\frac{B_4G}{MB_1G}\right)^{-1} = \frac{(2.19 \pm 0.20) \cdot (6.55 \pm 1.62)}{(5.81 \pm 0.35)} \\ &= 2.47 \pm 0.67 (27 \%) \end{aligned}$$

$$\left(\frac{MB_2G}{MB_1G}\right)_{\text{calc.}} = \left(\frac{B_4G}{MB_1G}\right) \left(\frac{B_4G}{MB_2G}\right)^{-1} = \frac{5.81 \pm 0.35}{2.86 \pm 0.64} = 2.03 \pm 0.76 (37 \%)$$

$$\left(\frac{B_4G}{B_2G}\right)_{\text{calc.}} = \left(\frac{B_4G}{FB_2G}\right) \left(\frac{FB_2G}{B_2G}\right) = (2.61 \pm 0.29) \cdot (1.07 \pm 0.18) = 2.79 \pm 0.56 (20 \%)$$

$$\begin{aligned} \left(\frac{MB_4G}{MB_2G}\right)_{\text{calc.}} &= \left(\frac{MB_4G}{B_4G}\right) \left(\frac{B_4G}{MB_2G}\right) = (0.97 \pm 0.08) \cdot (2.86 \pm 0.64) \\ &= 2.77 \pm 0.66 (24 \%) \end{aligned}$$

$$\left(\frac{B_4G}{B_1G}\right)_{\text{calc.}} = \left(\frac{B_4G}{MB_1G}\right) \left(\frac{MB_1G}{B_1G}\right) = (5.81 \pm 0.35) \cdot (1.40 \pm 0.10) = 8.31 \pm 0.76 (9 \%)$$

$$\begin{aligned} \left(\frac{MB_4G}{MB_1G}\right)_{\text{calc.}} &= \left(\frac{B_4G}{MB_1G}\right) \left(\frac{MB_4G}{B_4G}\right) = (5.81 \pm 0.35) \cdot (0.97 \pm 0.08) \\ &= 5.64 \pm 0.58 (10 \%) \end{aligned}$$

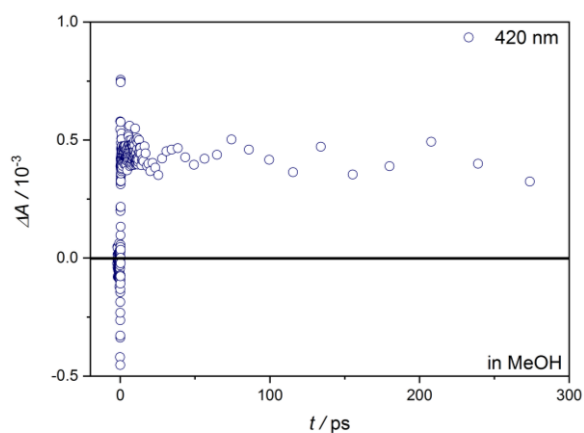
**Table A24.** Comparison of calculated overall initiation efficiencies  $m$  and ratios of  $\varepsilon_{\max}(X_jG) / \varepsilon_{\max}(X_{k<j}G)$ . Adapted with permission from ref. 146. Copyright 2019 American Chemical Society. Modified presentation.

cocktail experiment	calculated $m(X_jG : X_{k<j}G)$	$\varepsilon_{\max}(X_jG) / \varepsilon_{\max}(X_{k<j}G)$	deviation / % $\left  1 - \left( \frac{m_{\text{calc}}}{\varepsilon_{\max}(X_jG) / \varepsilon_{\max}(X_{k<j}G)} \right) \right  \cdot 100$
B <sub>2</sub> G : B <sub>1</sub> G	2.75 ± 0.98	2.89	4.84
FB <sub>2</sub> G : FB <sub>1</sub> G	2.51 ± 0.95	3.66	31.42
MB <sub>2</sub> G : MB <sub>1</sub> G	2.03 ± 0.76	2.56	20.70
B <sub>4</sub> G : B <sub>2</sub> G	2.79 ± 0.56	2.81	0.71
MB <sub>4</sub> G : MB <sub>2</sub> G	2.77 ± 0.66	2.34	18.37
B <sub>4</sub> G : B <sub>1</sub> G	8.13 ± 0.76	8.14	0.12
MB <sub>4</sub> G : MB <sub>1</sub> G	5.64 ± 0.58	11.54	51.13

## fs-TA of Monoacylgermanes

### B<sub>1</sub>G

a)



b)

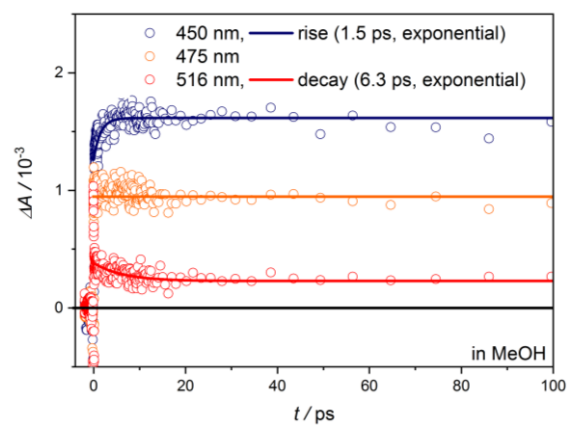
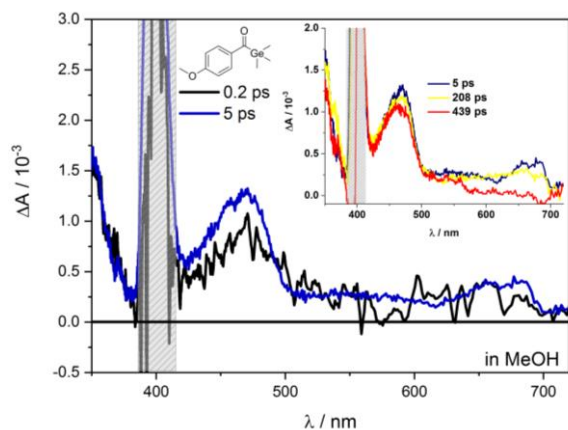


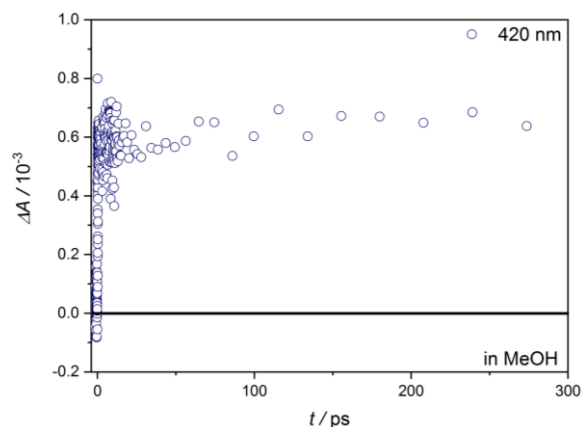
**Figure A32.** **a)** Transient response at 420 nm after excitation at 400 nm of B<sub>1</sub>G in MeOH in the region of expected GSB. In fact, no ground state recovery is observed, which implies ISC as the dominant pathway. **b)** Transient responses at 450 (blue), 475 (orange) and 516 nm (red) after excitation at 400 nm of B<sub>1</sub>G in MeOH for illustration of the superposition of ISC and VR. Blue and red lines are exponential fits. Orange line for guiding the eye. Adapted with permission from ref. 144. Copyright 2017 American Chemical Society. Modified presentation.

## MB<sub>1</sub>G

a)



b)



c)

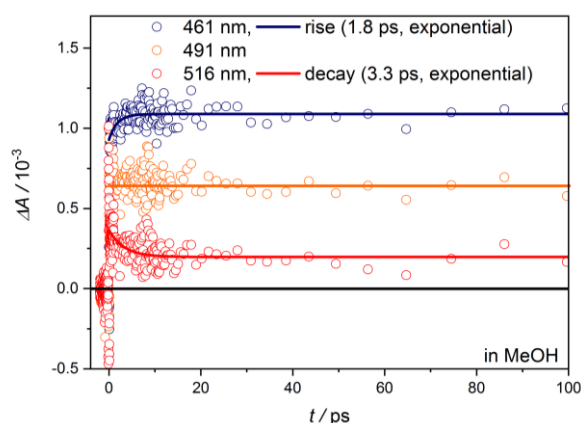
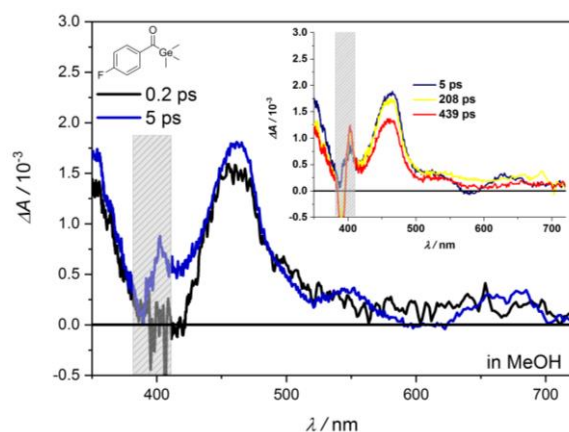


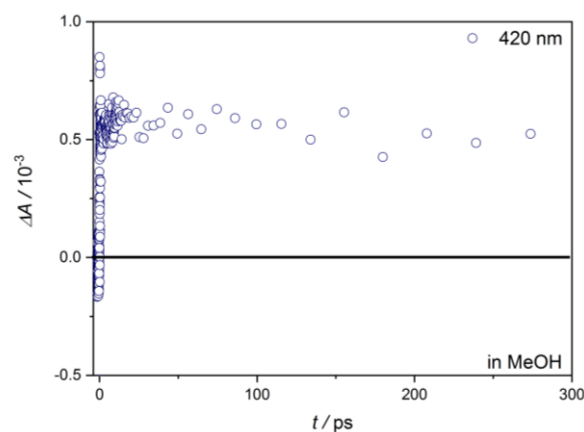
**Figure A33.** **a)** Transient broadband absorption spectrum of MB<sub>1</sub>G in MeOH of the first ps and longer delay times (inset) after excitation at 400 nm and probing with a CaF<sub>2</sub>-white light continuum from 350-720 nm. Time delays as indicated. Transient response at 400 nm omitted due to scattering from pump pulse. **b)** Transient responses at 420 nm after excitation at 400 nm of MB<sub>1</sub>G in MeOH in the region of expected GSB. In fact, no ground state recovery is observed, which implies ISC as the dominant pathway. **c)** Transient response at 461 (blue), 491 (orange) and 516 nm (red) after excitation at 400 nm of MB<sub>1</sub>G in MeOH for illustration of the superposition of ISC and VR. Blue and red lines are exponential fits. Orange line for guiding the eye. For a detailed discussion refer to main text **section 4.4.1**. Adapted with permission from ref. 144. Copyright 2017 American Chemical Society. Modified presentation.

## FB<sub>1</sub>G

a)



b)



c)

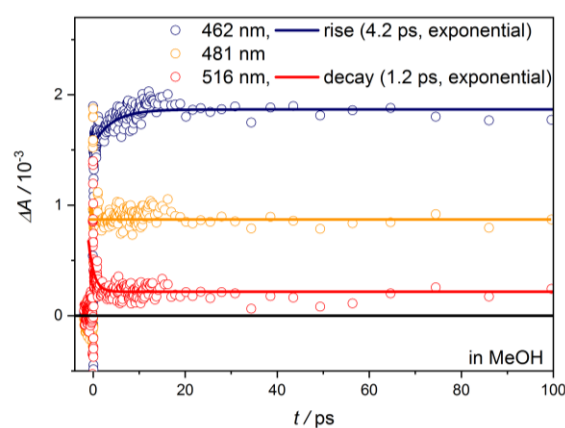
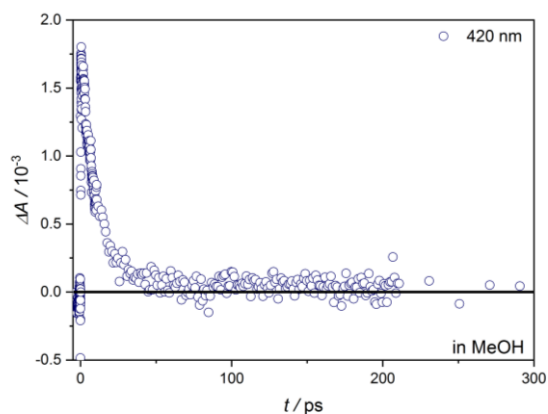


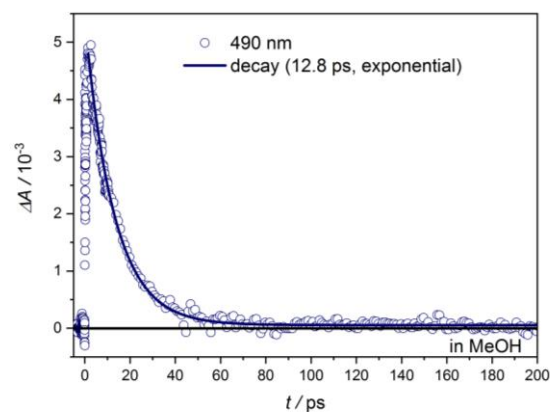
**Figure A34.** **a)** Transient broadband absorption spectrum of FB<sub>1</sub>G in MeOH of the first ps and longer delay times (inset) after excitation at 400 nm and probing with a CaF<sub>2</sub>-white light continuum from 350-720 nm. Time delays as indicated. Transient response at 400 nm omitted due to scattering from pump pulse. **b)** Transient responses at 420 nm after excitation at 400 nm of MB<sub>1</sub>G in MeOH in the region of expected GSB. In fact, no ground state recovery is observed, which implies ISC as the dominant pathway. **c)** Transient response at 462 (blue), 481 (orange) and 516 nm (red) after excitation at 400 nm of FB<sub>1</sub>G in MeOH for illustration of the superposition of ISC and VR. Blue and red lines are exponential fits. Orange line for guiding the eye. For a detailed discussion refer to main text **section 4.4.1**. Adapted with permission from ref. 144. Copyright 2017 American Chemical Society. Modified presentation.

## CB<sub>1</sub>G

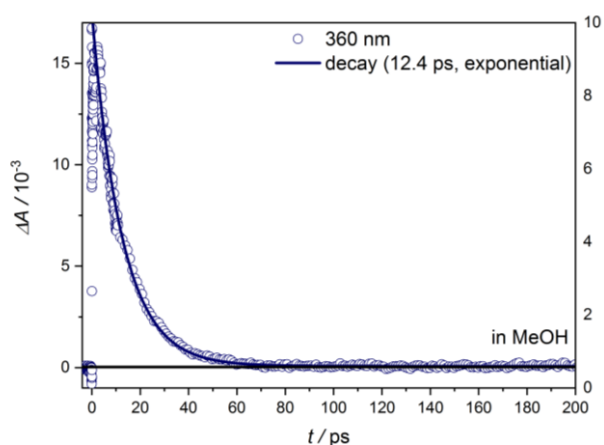
a)



b)



c)



d)

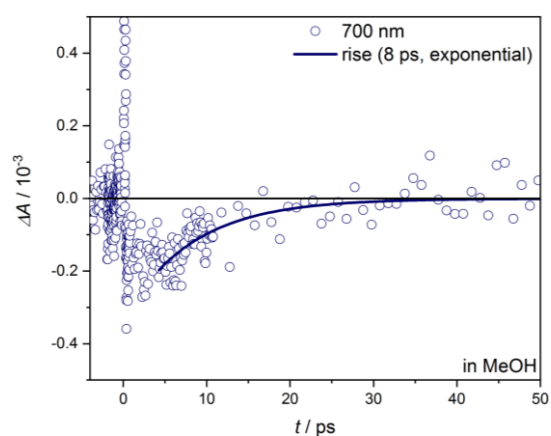
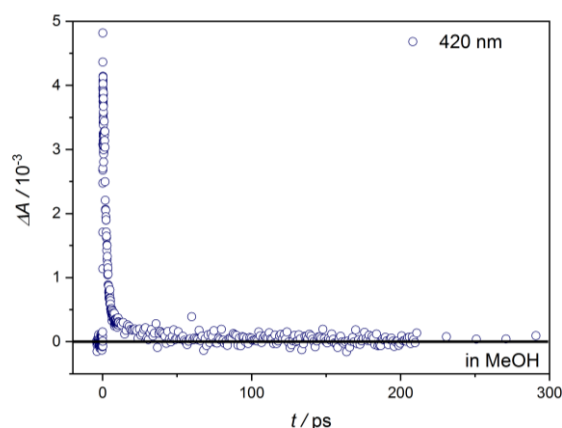


**Figure A35.** Transient response of CB<sub>1</sub>G dissolved in MeOH recorded after excitation at 400 nm and probing with a CaF<sub>2</sub>-white light continuum from 350-720 nm. **a)** Transient response at 420 nm in the region of GSB indicates approximately complete ground state recovery. **b), c)** Transient response at 490 and 360 nm, respectively, as used for exponential fitting. Singlet state relaxation via IC within 12-13 ps. **d)** Exponential fitting of SE-recovery within 8 ps at 700 nm indicates a weak fluorescence pathway. Adapted with permission from ref. 144. Copyright 2017 American Chemical Society. Modified presentation.

## NB<sub>1</sub>G

a)



b)

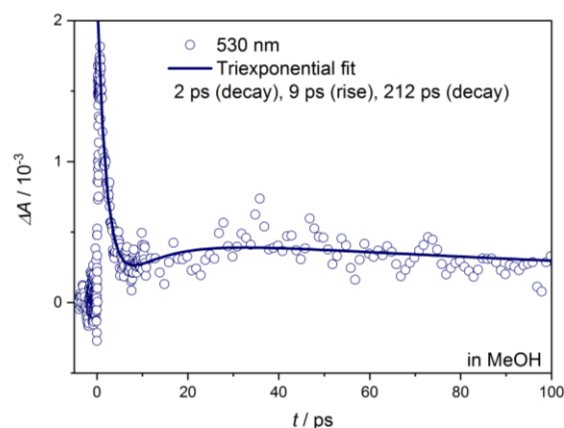


**Figure A36.** Transient response of NB<sub>1</sub>G dissolved in MeOH recorded after excitation at 400 nm and probing with a CaF<sub>2</sub>-white light continuum from 350-720 nm. **a)** Transient response at 420 nm in the region of GSB indicates approximately complete ground state recovery. **b)** Transient response at 530 nm as used for exponential fitting. Singlet state relaxation via IC within 2 ps. An additional rise within 9 ps indicates channel branching due weak competing ISC. Adapted with permission from ref. 144. Copyright 2017 American Chemical Society. Modified presentation.

## fs-TA of Tetraacylgermanes

### B<sub>4</sub>G

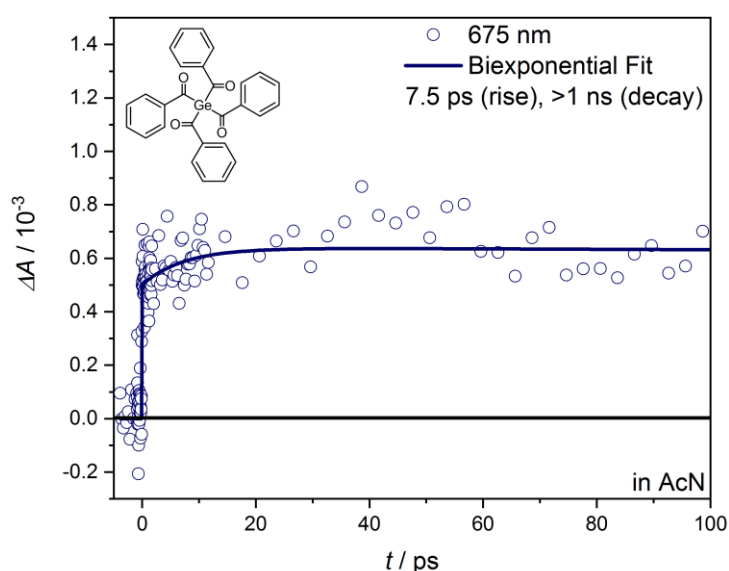
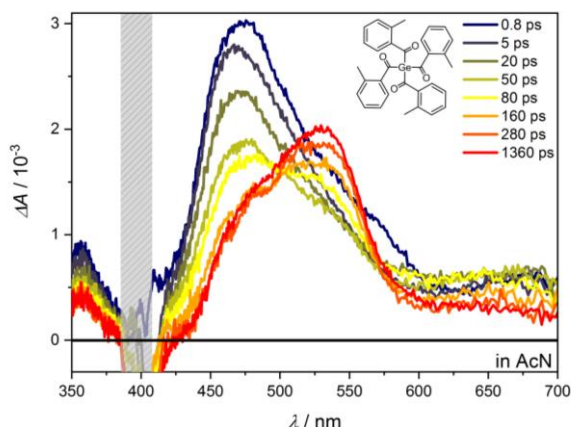


**Figure A37.** Transient response at 675 of B<sub>4</sub>G dissolved in AcN after excitation at 400 nm for comparison with DAS in **Figure 4.35**. Fast Increasing TA-band at 620-720 nm is correlated to fast decay of ESA between 350 and 600 nm caused by ISC from excited singlet to triplet states. The risen ESA remains within the recorded time window, which is reflected by C<sub>3</sub> from global analysis.

## oMeB<sub>4</sub>G

a)



b)

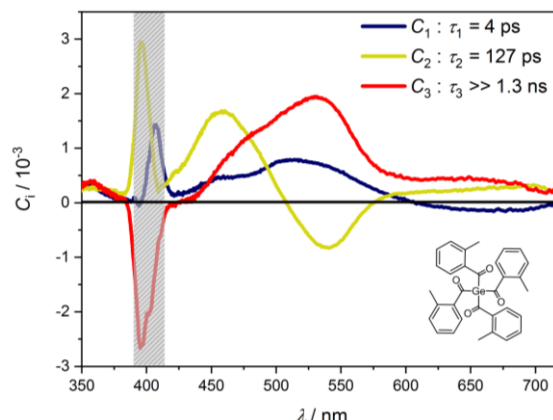
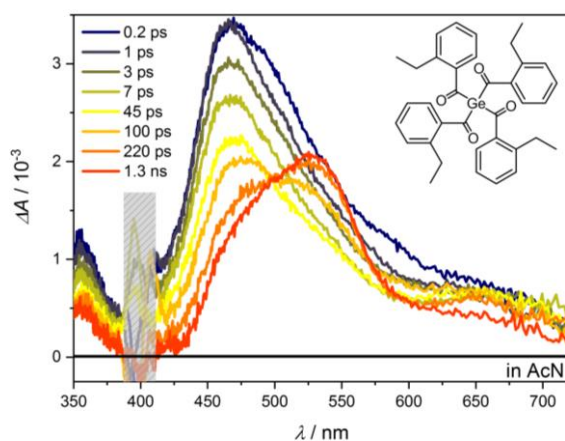


**Figure A38. a)** Transient broadband absorption spectrum of oMeB<sub>4</sub>G dissolved in AcN excited at 400 nm and probed by a CaF<sub>2</sub>-white light continuum between 350-720 nm. The wavelength region at ~400 nm is omitted due to scattering from pump pulse. Time delays as indicated. **b)** Decay associated spectrum (DAS) derived from triexponential global analysis of the TA-spectrum of oMeB<sub>4</sub>G dissolved in AcN. Time constants according to three exponential functions as indicated. For a detailed discussion refer to main text **section 4.4.2**.

## oEtB<sub>4</sub>G

a)



b)

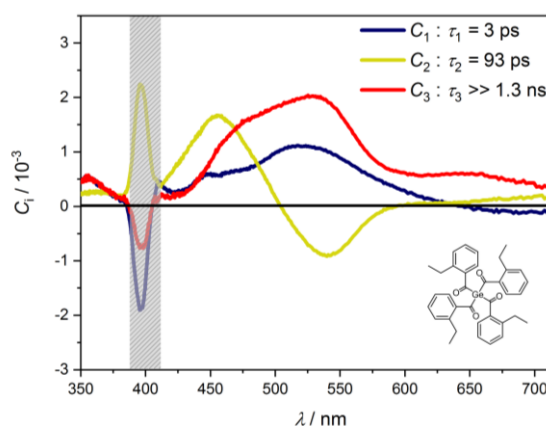
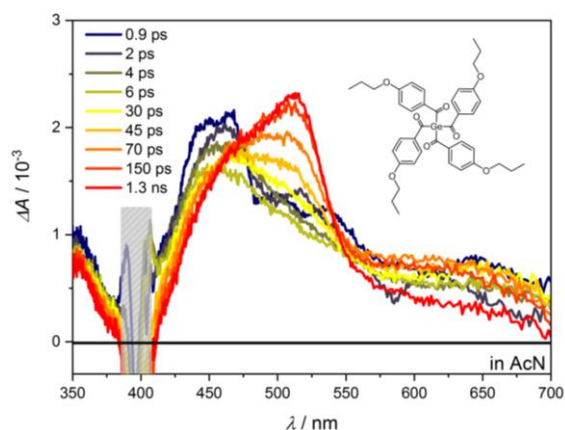


**Figure A39. a)** Transient broadband absorption spectrum of oEtB<sub>4</sub>G dissolved in AcN excited at 400 nm and probed by a CaF<sub>2</sub>-white light continuum between 350-720 nm. The wavelength region at ~400 nm is omitted due to scattering from pump pulse. Time delays as indicated. **b)** Decay associated spectrum (DAS) derived from triexponential global analysis of the TA-spectrum of oEtB<sub>4</sub>G dissolved in AcN. Time constants according to three exponential functions as indicated. For a detailed discussion refer to main text **section 4.4.2**.

## PrOB<sub>4</sub>G

a)



b)

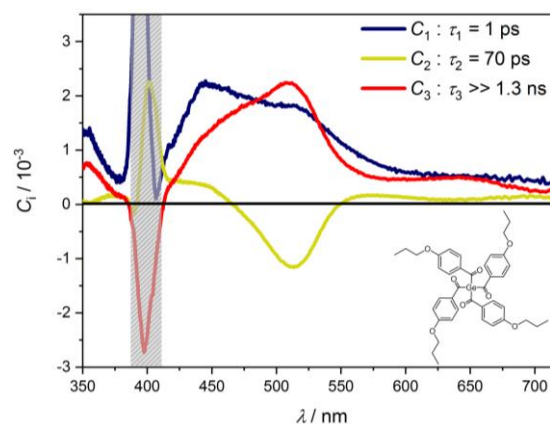
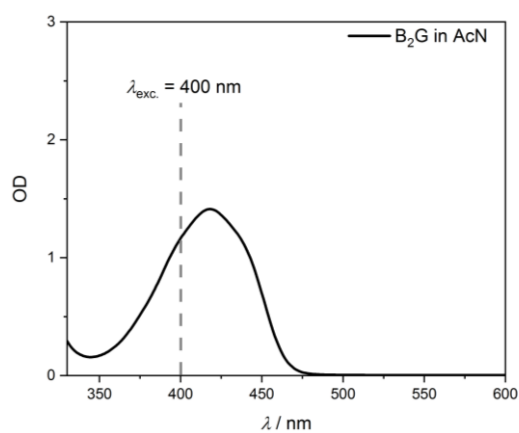


**Figure A40.** a) Transient broadband absorption spectrum of PrOB<sub>4</sub>G dissolved in AcN excited at 400 nm and probed by a CaF<sub>2</sub>-white light continuum between 350-720 nm. The wavelength region at ~400 nm is omitted due to scattering from pump pulse. Time delays as indicated. b) Decay associated spectrum (DAS) derived from triexponential global analysis of the TA-spectrum of PrOB<sub>4</sub>G dissolved in AcN. Time constants according to three exponential functions as indicated. For a detailed discussion refer to main text **section 4.4.2**.

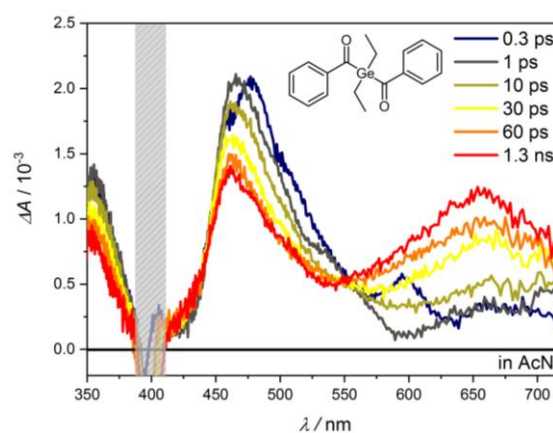
## fs-TA of Bisacylgermane B<sub>2</sub>G

### B<sub>2</sub>G

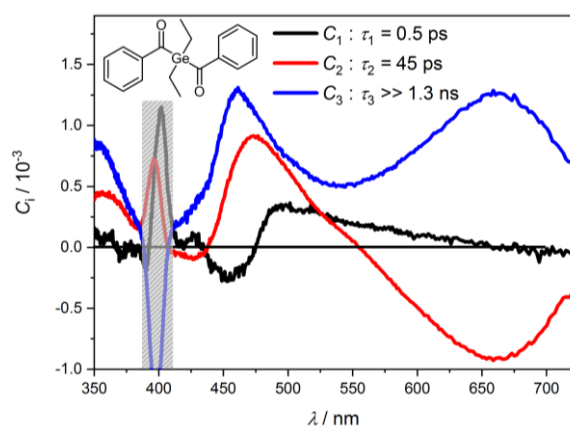
a)



b)



c)



d)

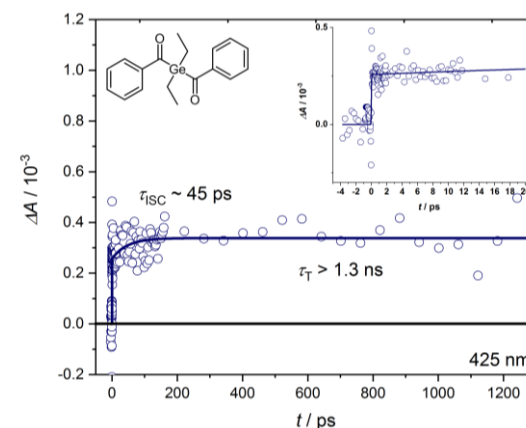


**Figure A41.** a) UV/Vis spectrum of B<sub>2</sub>G dissolved in AcN recorded in a 1 mm cuvette as used for fs-TA b) Transient broadband absorption spectrum of B<sub>2</sub>G dissolved in AcN excited at 400 nm and probed by a CaF<sub>2</sub>-white light continuum between 350-720 nm. The wavelength region at ~400 nm is omitted due to scattering from pump pulse. Time delays as indicated. c) Decay associated spectrum (DAS) derived from triexponential global analysis of the TA-spectrum of B<sub>2</sub>G dissolved in AcN. Time constants according to three exponential functions as indicated. d) Transient of B<sub>2</sub>G in AcN at 425 nm. After ISC within 45 ps, triplet ESA remains within the recorded time window. In addition, no ground state recovery is observed. Thus, no triplet relaxation is observed, e.g. via radical formation. The findings are in line with literature,<sup>43</sup> which reports the primary radical formation of B<sub>2</sub>G to proceed within tens of ns after ISC. For a detailed discussion with respect to tetraacylgermanes refer to main text **section 4.4.2**.

## Outlook: wavelength dependent PLP

$$E_{\text{pulse}}^i = \frac{E_{\text{pulse}}^0 N_{\text{pulse}}^0 T(\lambda^0) \lambda^0}{N_{\text{pulse}}^i T(\lambda^i) \lambda^i} \quad \text{Eq. A19}$$

$E_{\text{pulse}}^i, N_{\text{pulse}}^i$ : energy and count of pulse  $i$ .

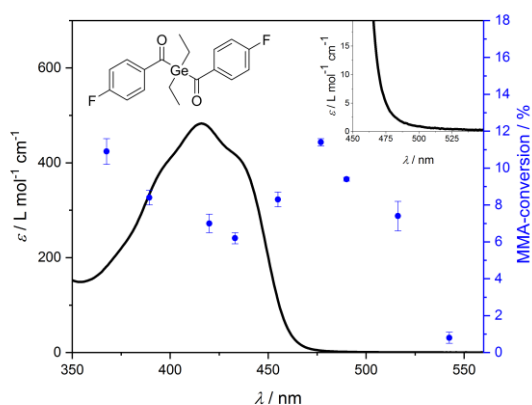
$E_{\text{pulse}}^0, N_{\text{pulse}}^0$ : energy and count of initial pulse  $i = 0$ .

$\lambda^i, \lambda^0$ : wavelength for pulse  $i$  and the initial pulse  $0$ .

$T$ : wavelength-dependent transmittance.

**Eq A19**<sup>75, 156</sup> enables the calculation of the wavelength dependent energy of a pulse  $i$  based on the energy and pulse count of an initial pulse  $0$ . The results can be used to align the tunable ns-laser system for wavelength-dependent PLP-conversion experiments at constant photon count.

a)



b)

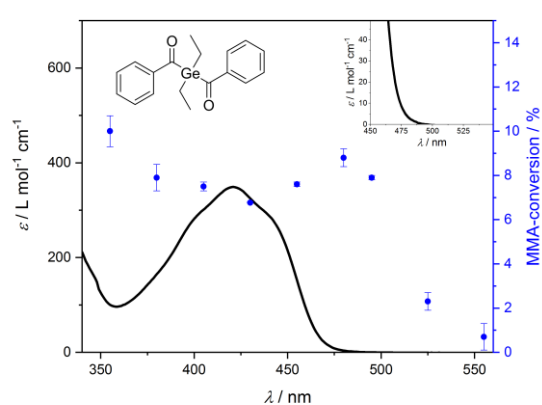
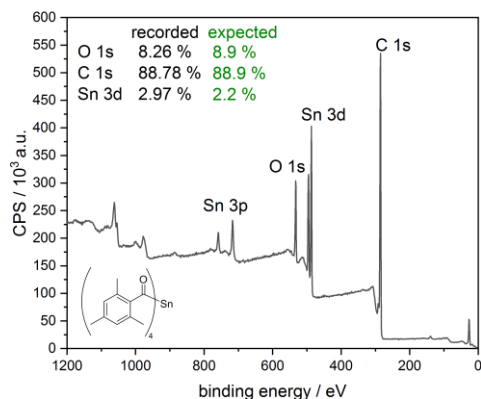


**Figure A42.** MMA-conversion plot of a wavelength-dependent PLP-experiment of **a)** FB<sub>2</sub>G and **b)** B<sub>2</sub>G in MMA reproduced from master thesis by P.W. Kamm.<sup>156</sup> Both experiments show a significant MMA-conversion within wavelength regions with low extinction coefficients of the initiators.

## B. Appendix of Chapter 5

### Tin-Based Photoinitiators

a)



b)

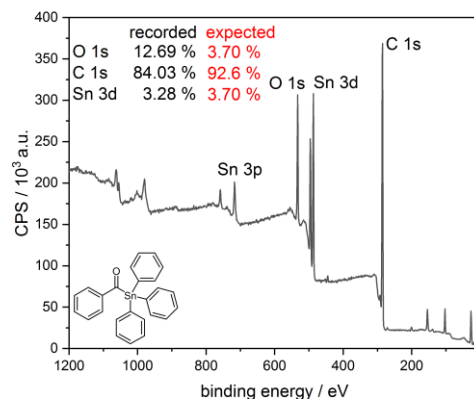


**Figure B1.** Solid state X-ray photoelectron (XPS) spectra of **a)** Mes<sub>4</sub>T and **b)** TPBT. **a)** XPS-spectrum of Mes<sub>4</sub>T reflects the atomic ratio of C:O:Sn (40:4:1) as seen from comparison of recorded and expected ratios. **b)** Deviations between the recorded and expected atomic ratio of C:O:Sn (25:1:1) indicate the decomposition of TPBT within solid state. The spectra are recorded by Lukas Michalek at the Queensland University of Technology (QUT, Brisbane, Australia).

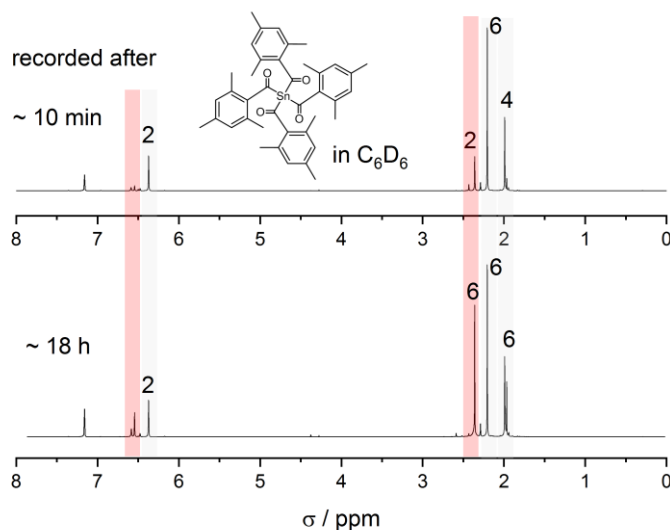


**Figure B2.** <sup>1</sup>H-NMR spectra of Mes<sub>4</sub>T in deuterated benzene (C<sub>6</sub>D<sub>6</sub>) are conducted by Markus Zieger (Karlsruhe Institute of Technology (KIT), Karlsruhe) after times as indicated. The sample was not exposed to light. From H-atoms with a different chemical environment in Mes<sub>4</sub>T a ratio of 2:6:3 is expected in line with a NMR-spectrum from literature (marked in blue).<sup>41</sup> However, already after 10 min not expected additional peaks (marked in red) can be observed, which result in a different ratio as indicated. After further 18 h, the additional peaks are clearly increased, which is an evidence for the decomposition of Mes<sub>4</sub>T in solution without light-irradiation.

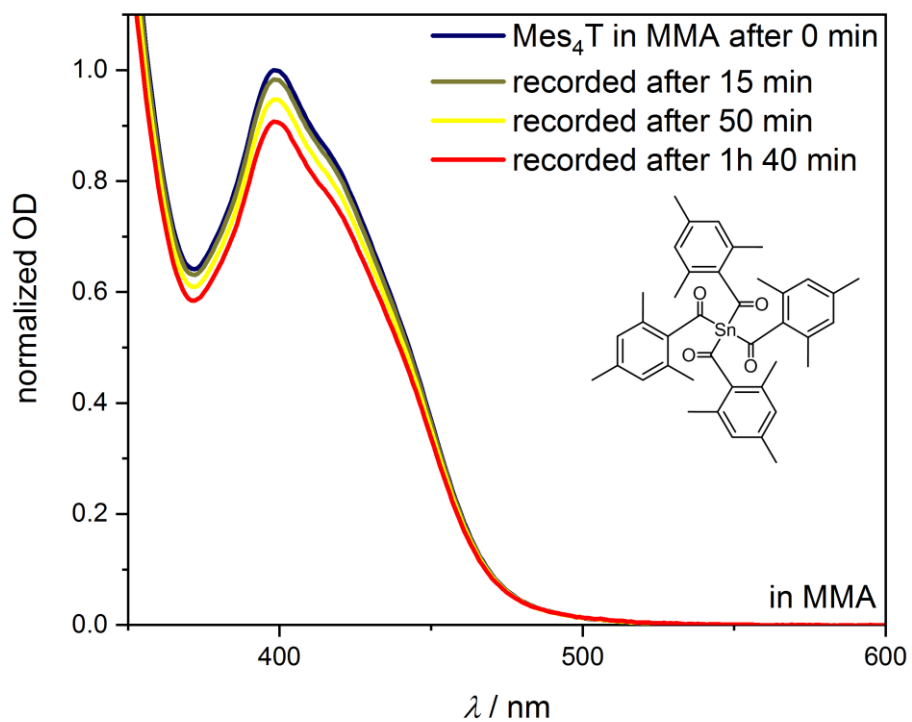


**Figure B3.** Steady-state UV/Vis spectra of Mes<sub>4</sub>T in MMA for inspecting the decomposition under light-exclusion after various waiting times as indicated. After 15 min a decay of ~2 % is observed.

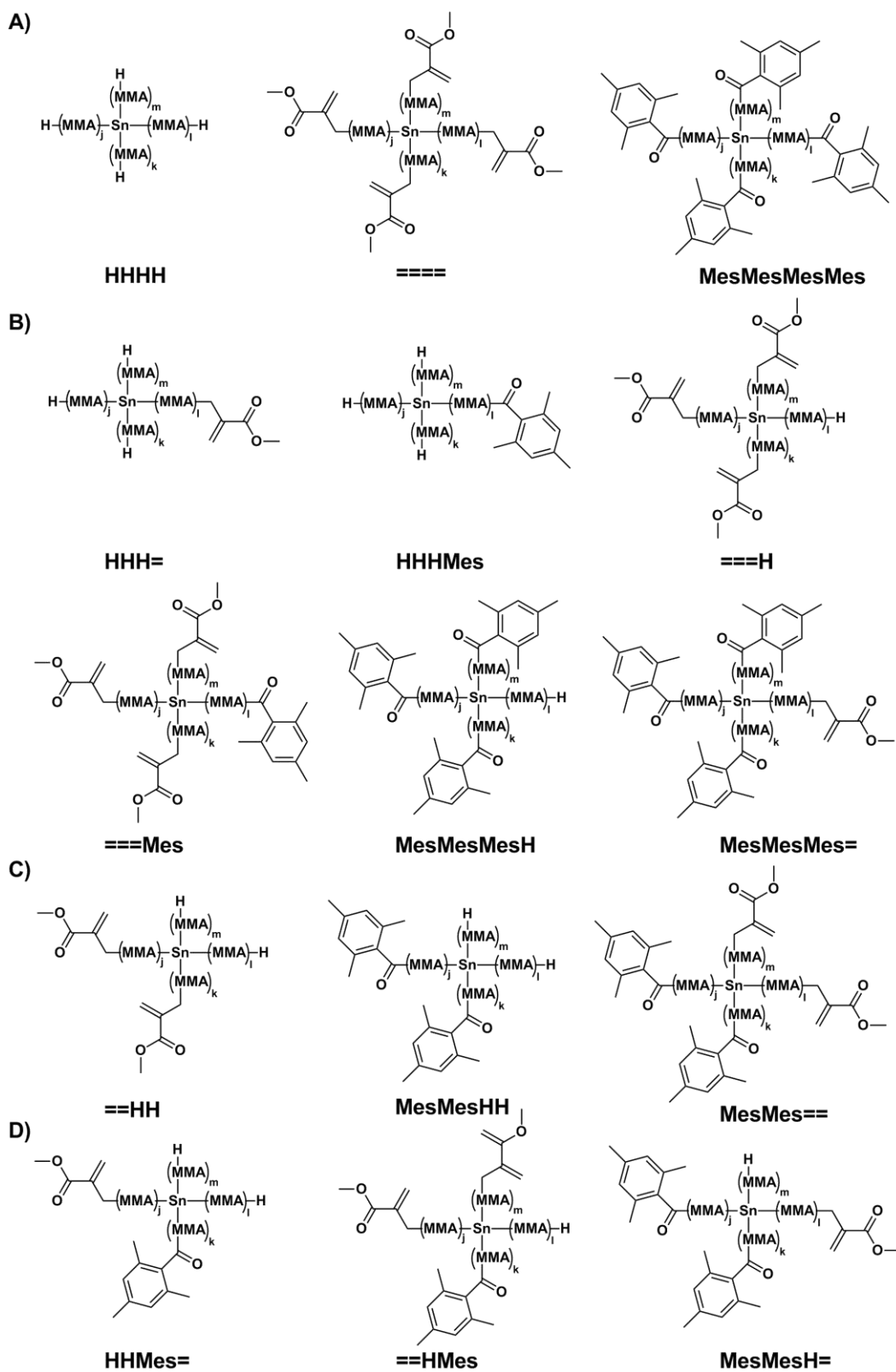
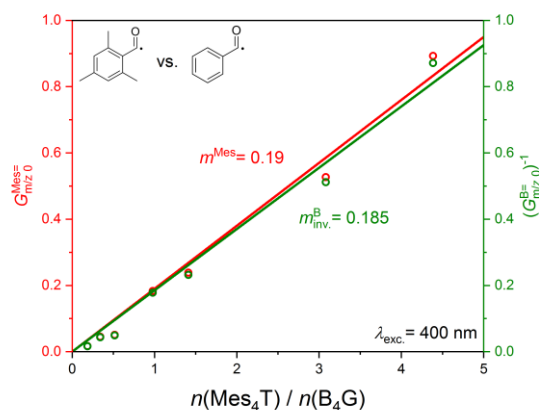


**Figure B4.** Tin-centered 4-armed star polymers as predicted for polymerization with tetramethylsilyloxytinane by assuming a complete multiple cleavage mechanism.

a)



b)

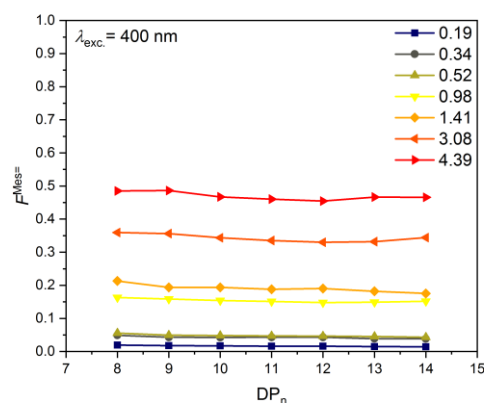
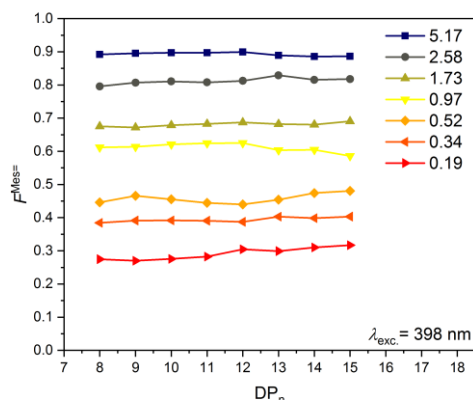


**Figure B5. a)**  $G_{m/z0}^{X=}$  vs initial molar ratios-plot of the cocktail experiment Mes<sub>4</sub>T: B<sub>4</sub>G in MMA without further purification to determine the overall initiation efficiencies of the radicals Mes and B at excitation wavelength 400 nm. Red: Linear regression of all mass-bias-free ratios  $G_{m/z0}^{B=}$  of the disproportionation product Mes= initiated by the radical Mes originated from the initiator Mes<sub>4</sub>T versus the initial molar ratios  $n(\text{Mes}_4\text{T})/n(\text{B}_4\text{G})$  resulting in an overall initiation efficiency of  $m^{\text{Mes}} = 0.19$ . Green: Linear regression of all inverse mass-bias-free ratios  $(G_{m/z0}^{MB=})^{-1}$  of the disproportionation product B= initiated by the radical B originated from the initiator B<sub>4</sub>G versus the initial molar ratios  $n(\text{Mes}_4\text{T})/n(\text{B}_4\text{G})$  resulting in an overall initiation efficiency of  $m_{\text{inv.}}^{\text{B}} = 0.185$ . Deviations between  $m^{\text{Mes}}$  and  $m_{\text{inv.}}^{\text{B}}$  reflect the scattering of the experiment. The averaged overall initiation efficiency is obtained to  $m(\text{Mes}_4\text{T}:\text{B}_4\text{G}) = 0.19 \pm 0.003$ . **b)** Corresponding  $F$  vs DP-plot indicating a weak chain length-dependent ionization bias during the ESI-process.

a)



b)

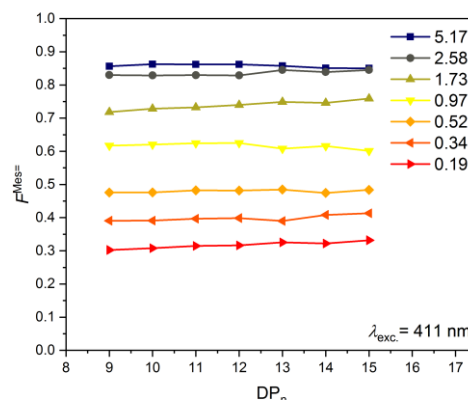


**Figure B6.**  $F$  vs DP-plots corresponding to the cocktail experiment Mes<sub>4</sub>T:MB<sub>2</sub>G at 398 and 411 nm indicating a weak chain length-dependent ionization bias.

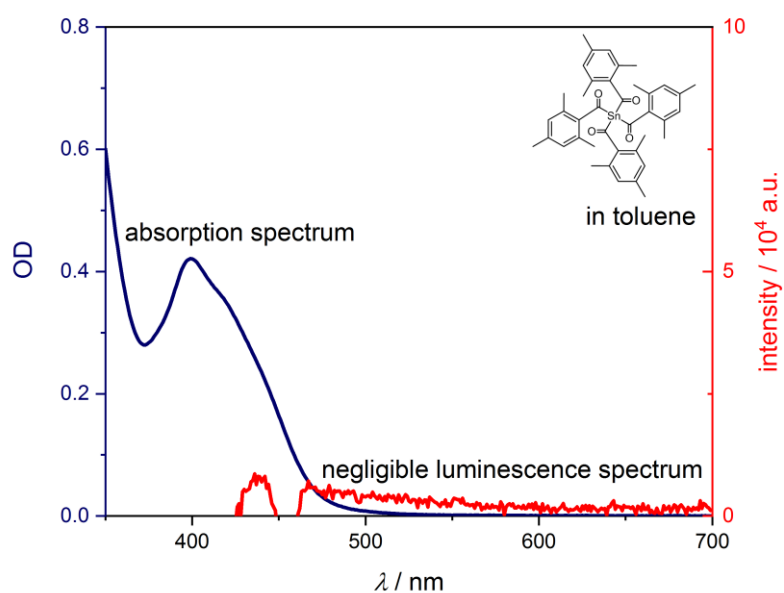


**Figure B7.** Mes<sub>4</sub>T in toluene shows no significant fluorescence band after excitation at 400 nm.

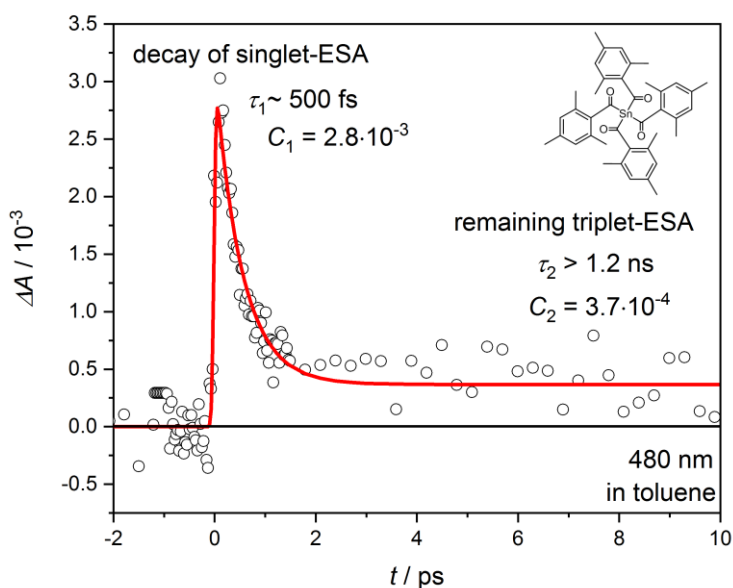


**Figure B8.** Singlet transient response at 480 nm of Mes<sub>4</sub>T dissolved in MMA after excitation at 400 nm. Red line is received from biexponential fitting routine resulting in two time constants.  $\tau_1$  reflects the decay of singlet ESA within 500 fs.  $\tau_2$  corresponds to a long-living triplet ESA, which lasts longer than the recorded time window of 1.2 ns. From the ratio of amplitudes  $\frac{C_1}{C_1+C_2}$  the channel branching is estimated by 88 % singlet decay and 12 % remaining triplet ESA.

## C. Appendix of Chapter 6

### Steady-State Fluorescence Spectroscopy of Tetrazoles

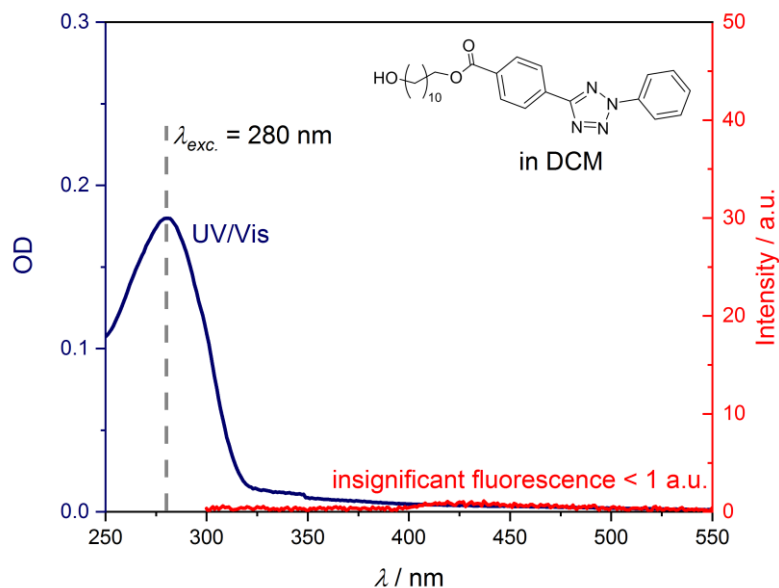


**Figure C1.** Steady-state UV/Vis and fluorescence spectrum of Tet dissolved in DCM. Excitation within the absorption maximum at 280 nm leads to an insignificant fluorescence of < 1 a.u. which supersedes the quantification of a fluorescence quantum yield <  $10^{-4}$ .

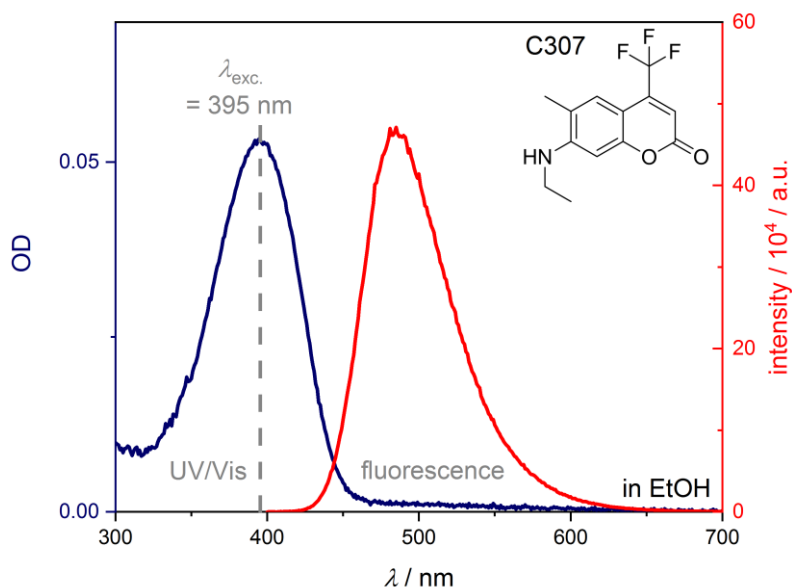


**Figure C2.** Reference steady-state UV/Vis and fluorescence spectra of Coumarin 307 in ethanol recorded at excitation of 395 nm for quantification of fluorescence quantum yields of PyTet and BiphTet in DCM and DCM:IEt mixtures according to **Figure 6.2**. Reference quantum yield of 56 % obtained at 395 nm is drawn from literature <sup>135</sup>.

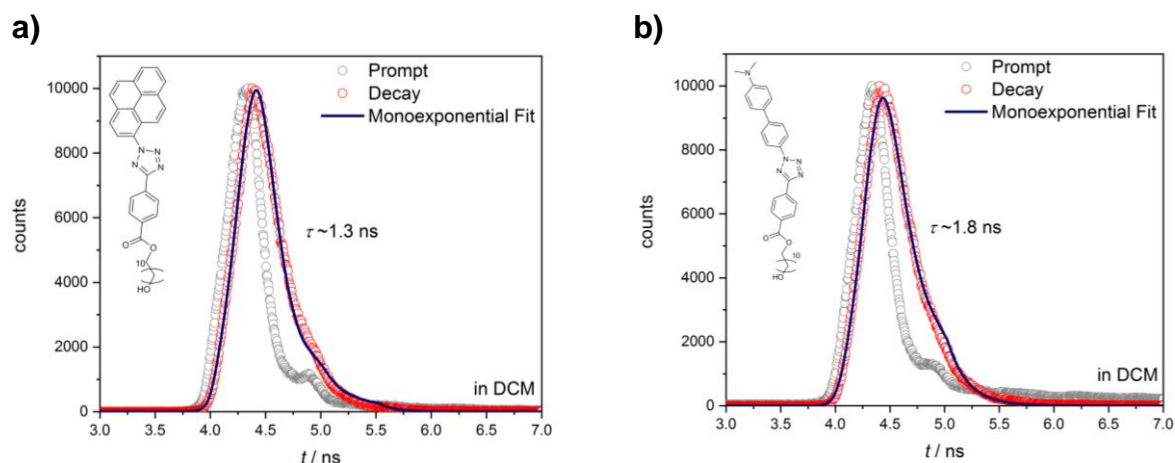


**Figure C3.** Decay of fluorescence of **a)** PyTet within  $\sim 1.3$  ns and **b)** BiphTet in DCM within 1.8 ns observed via TCSPC. Prompt is recorded for a 30 % ludox reference solution. The decay of PyTet is recorded at very low dilutions. Time constants are obtained by monoexponential fitting routine, which is implemented in the deconvolution software Decay Analysis Data Set 6 (Horiba).

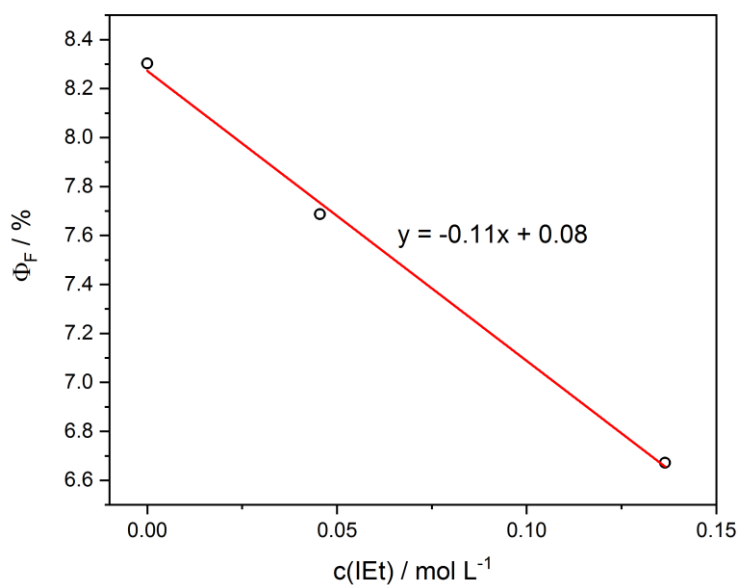


**Figure C4.** Fluorescence quantum yield of PyTet in DCM:IEt mixtures versus quencher concentration.

## fs-TA of 2,5-Diaryl-Tetrazole

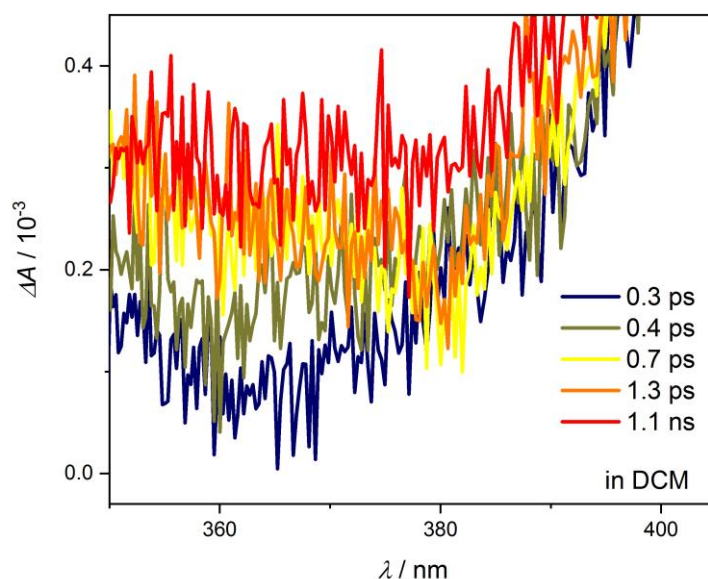


**Figure C5.** Zoom into UV-A range of TA-spectrum of Tet in DCM: Increase of ESA at ~370 nm correlates with ultrafast decay of ESA peaking at ~475 nm (refer to **Figure 6.4**). For further information refer to main text (**section 6.2.1**).

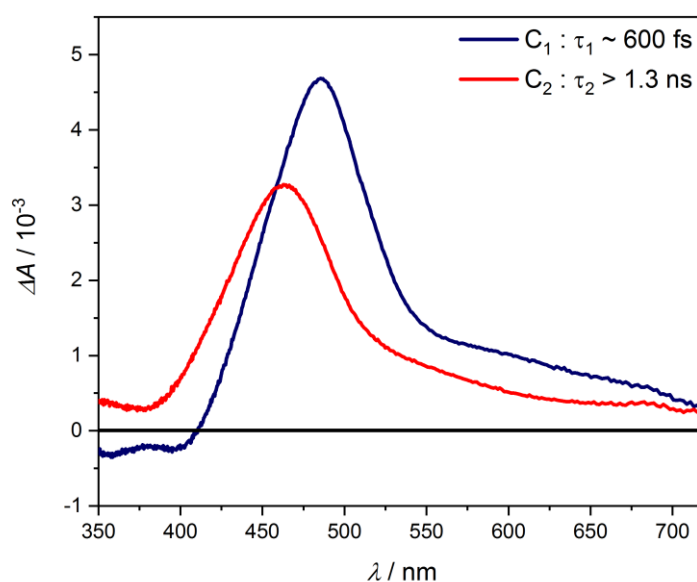


**Figure C6.** DAS of Tet in DCM obtained from biexponential global analysis, resulting in two time constants as indicated. Negative amplitudes  $C_1$  correspond to increasing and positive to decreasing transient responses. Zero-crossing is interpreted as an isosbestic point. In line with the discussion of **Figure 6.4**, the superposition of a fast and slow decaying process within ~600 fs and >1.3 ns, respectively, is observed. The fast decay is correlated to a rising TA between 350 and 400 nm, which is indicated by the zero-crossing at ~410 nm. For further information refer to main text (**section 6.2.1**).

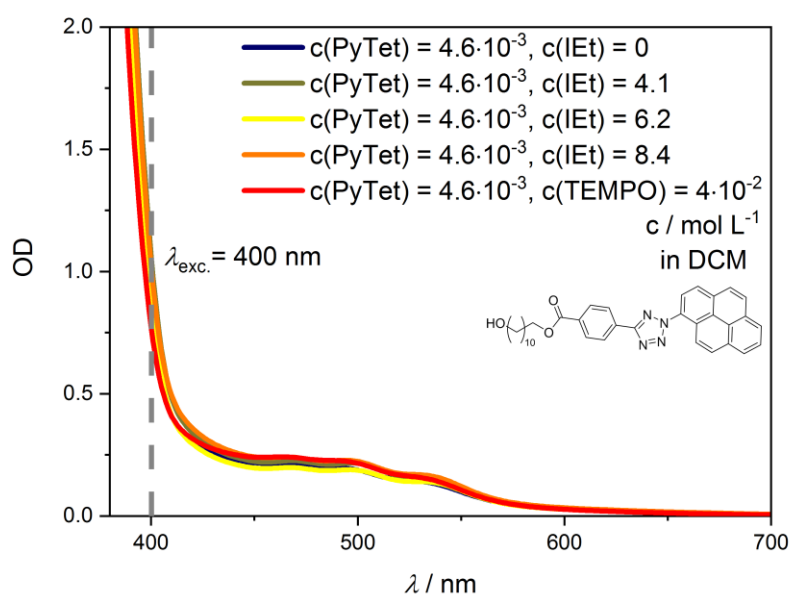


**Figure C7.** UV/Vis spectra of PyTet dissolved in DCM, DCM:IEt mixtures and DCM with TEMPO as used for fs-TA. Grey dashed line indicates similar sample-OD  $\sim 0.7$  for excitation at 400 nm.

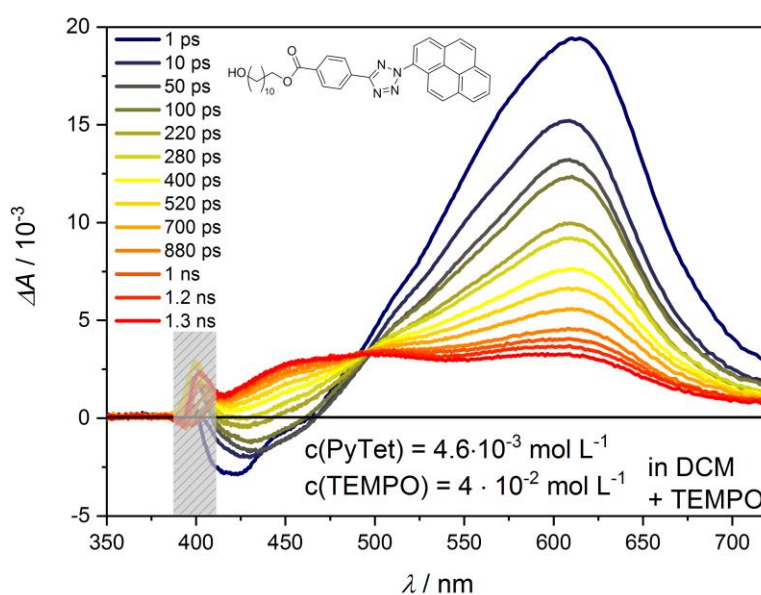


**Figure C8.** TA spectrum of PyTet dissolved in DCM with TEMPO used as a quencher, which was excited at 400 nm and probed with a  $\text{CaF}_2$ -white light continuum between 350 and 720 nm. Significant increase of ESA at  $\sim 450 \text{ nm}$  is an evidence for a triplet state. Time delays and concentrations of PyTet and TEMPO as indicated. Transient responses at  $\sim 400 \text{ nm}$  are omitted due to scattering from pump pulse. Corresponding UV/Vis spectrum in **Figure C7**.

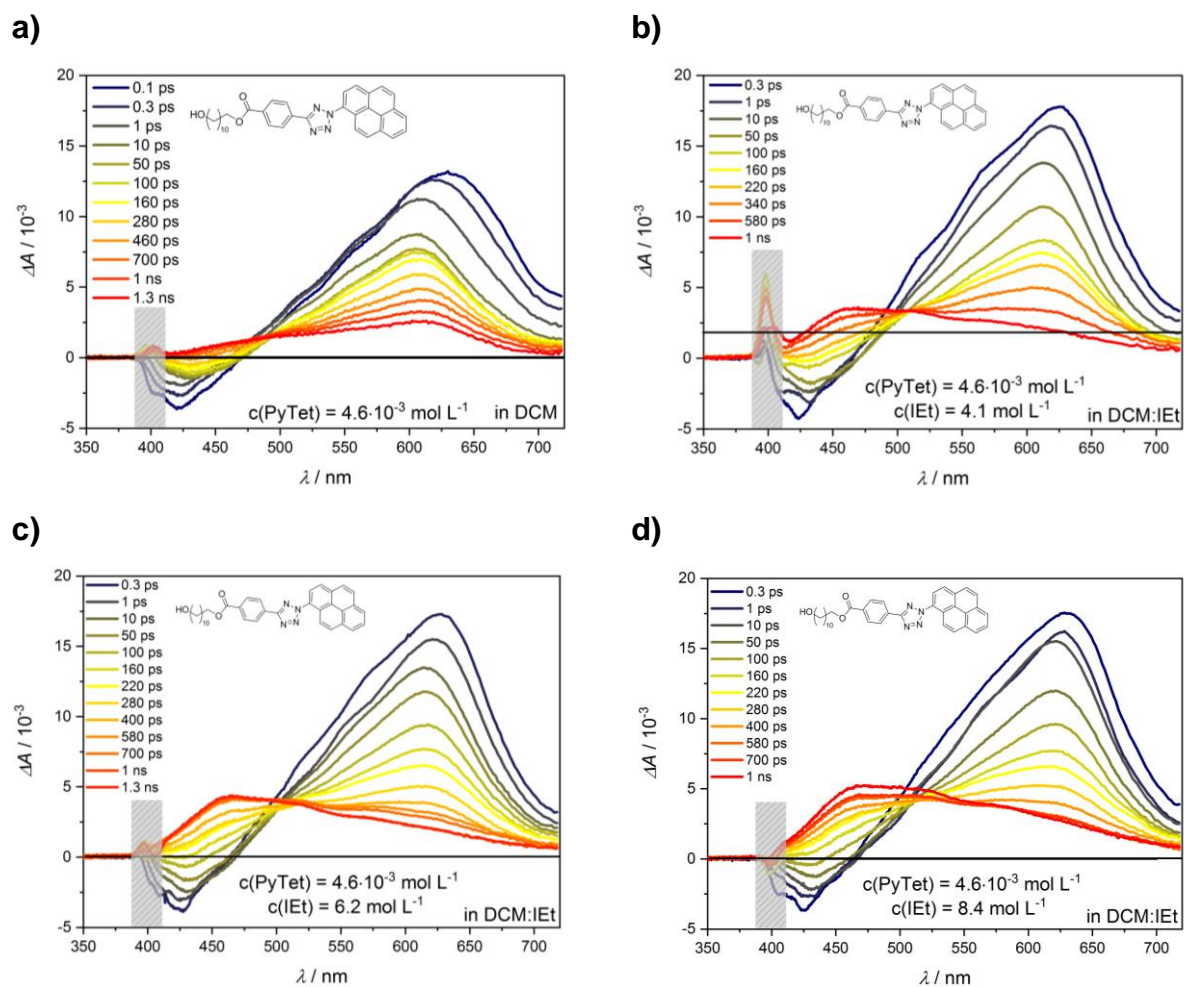


**Figure C9.** TA spectra of PyTet dissolved in **a)** DCM and **b), c), d)** various DCM:IEt mixtures, which were excited at 400 nm and probed with a  $\text{CaF}_2$ -white light continuum between 350 and 720 nm. Significant increase of ESA at  $\sim 450$  nm is an evidence for a triplet state. Time delays and concentrations of PyTet and IEt as indicated. Transient responses at  $\sim 400$  nm are omitted due to scattering from pump pulse. Corresponding UV/Vis spectra in **Figure C7**.

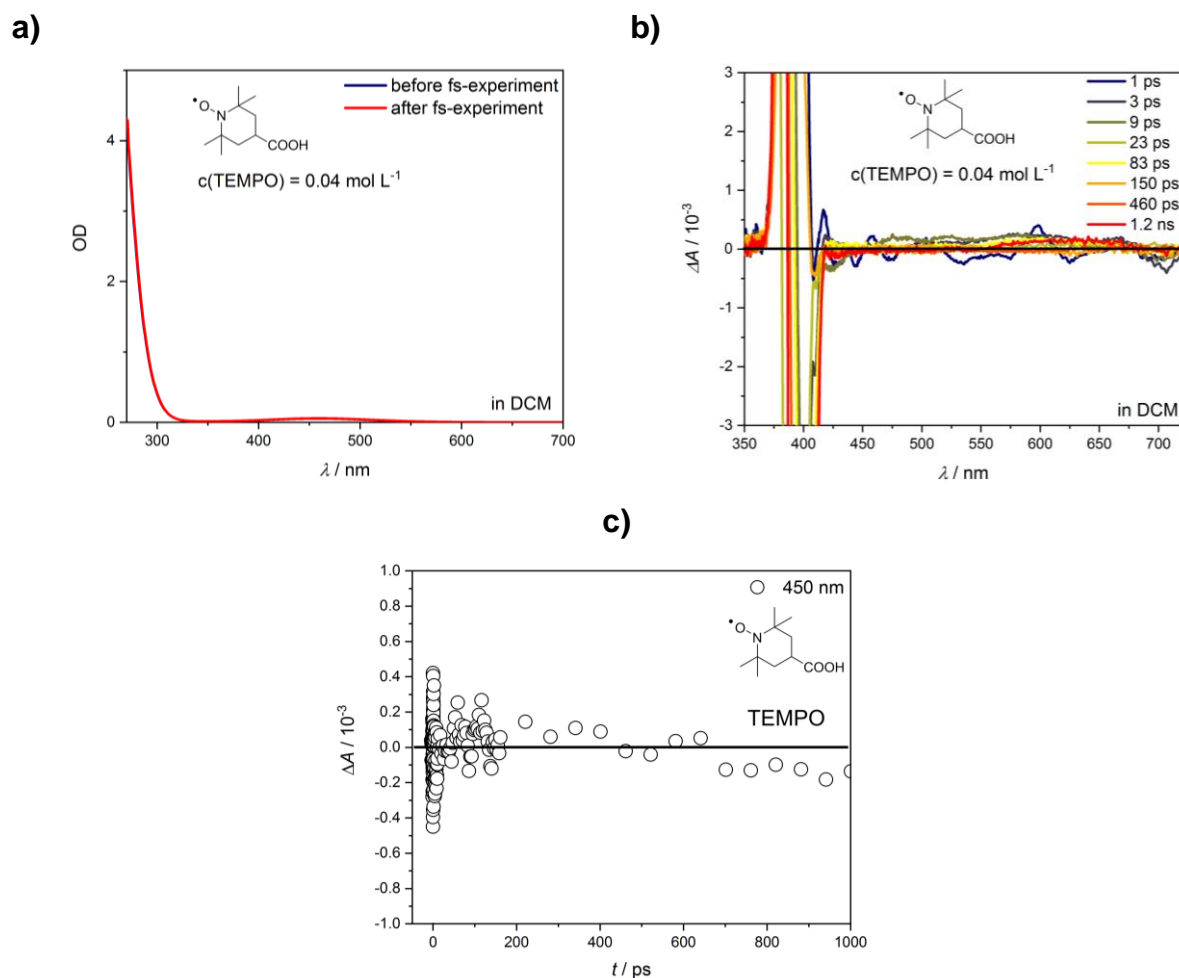


**Figure C10.** **a)** UV-Vis spectrum of TEMPO in DCM before and after fs-experiment. Absence of changes in OD before and after the fs-experiment indicates an insignificant decomposition of TEMPO. **b)** TA-spectrum of IET in bulk after excitation at 400 nm and probing with a white light continuum between 350 and 720 nm. After excitation at 400 nm, no significant transient response of TEMPO in DCM as shown in **b)** and **c)**.

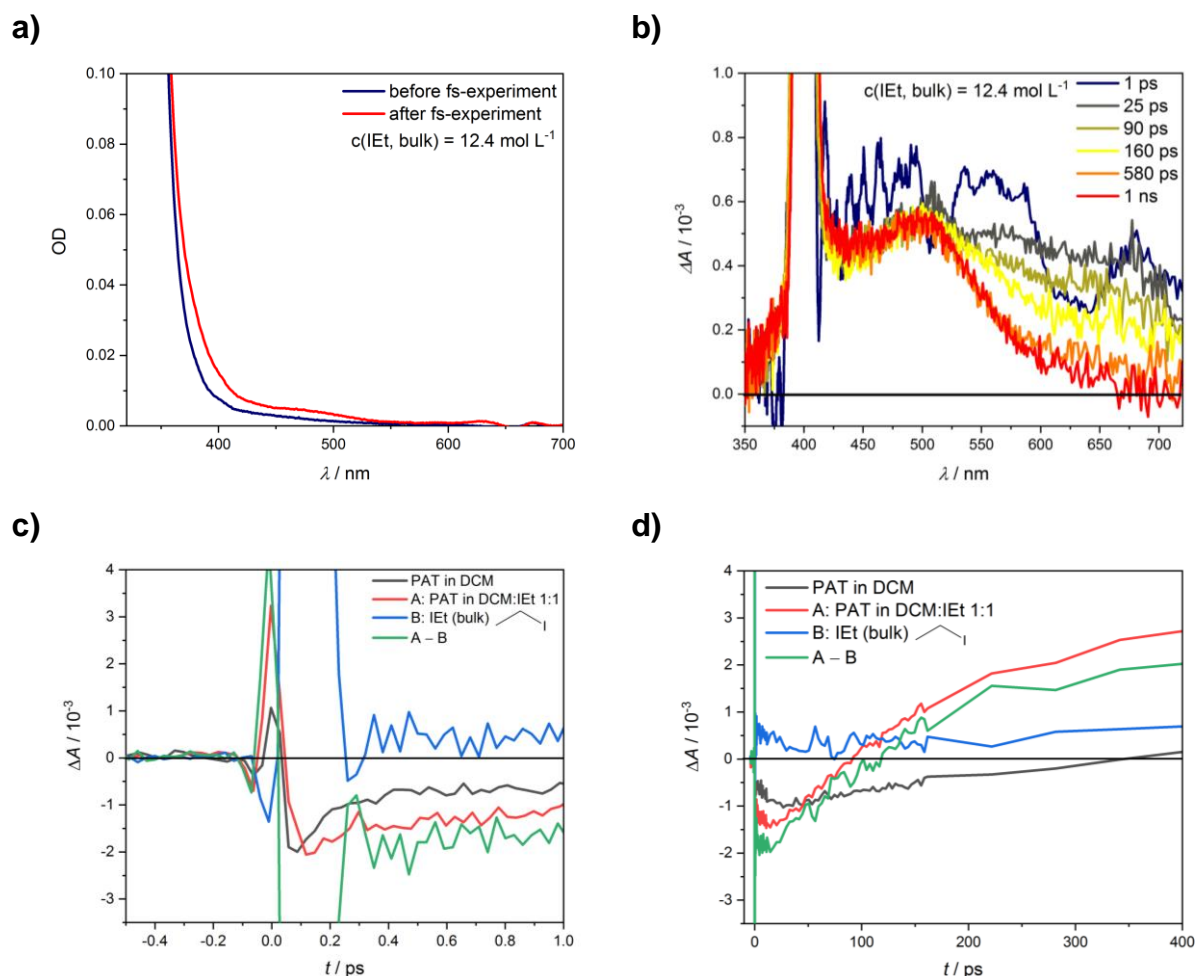


**Figure C11.** **a)** UV-Vis spectrum of IET in bulk before and after fs-experiment. An increase in OD  $\sim$ 500 nm indicates the decomposition of IET under formation of an additional species. **b)** TA-spectrum of IET in bulk after excitation at 400 nm and probing with a white light continuum between 350 and 720 nm. Despite of the very low OD  $<$  0.01 at 400 nm, IET reveals a weak transient band peaking at 500 nm, which lasts longer than the accessible time window of 1.3 ns. The decomposition of IET is literature-known to proceed from the repulsive potential  $S_1$ -surface after excitation between 245 and 283 nm.<sup>181-184</sup> In addition, the transient response according to IET cleavage is associated to an ultrafast process within a few hundreds of fs.<sup>181</sup> Cleavage via multi-photon excitation is possible<sup>185</sup> but negligible at a pulse diameter of  $\sim$ 200  $\mu$ m.<sup>186</sup> Thus, decomposition of IET after excitation at 400 nm under formation of a long-living transient response is improbable. Despite of that, CaF<sub>2</sub>-white light reaches down to 350 nm and can trigger the cleavage reaction of IET. Possible follow-up products are ions and covalent compounds of I, I<sub>2</sub>, I<sub>3</sub> and I<sub>4</sub>.<sup>181-183, 187</sup> The additional band of the steady-state UV/Vis spectrum **a)** after the fs-experiment is possibly according to I<sub>2</sub>,<sup>188</sup> which could be accumulated during probing at 350 nm. However, this species is not necessarily related to the TA-spectrum. In fact, an exact overlapping TA-spectrum of the aforementioned products is not found in literature.<sup>188</sup> Consequently, further investigations would be necessary for an in-depth understanding of TA-spectrum of IET after excitation in a quasi-off-resonant region. Importantly, the fluorescence-quenching effect of iodine accompanied by the additional ESA in PyTet in DCM:IET mixtures is not significantly affected by the dynamics of IET, which is discussed below. In addition, the quencher-influence is as well evidenced by TEMPO, which does not reveal intrinsic excited state dynamics after excitation at 400 nm as presented in **Figure C10**.

**c), d)** Transients at 450 nm after excitation at 400 nm of PyTet in DCM (black) PyTet in a DCM:IET mixture (A, red), IET in bulk (B, blue), and transient response of PyTet in DCM:IET mixture after subtraction of response of IET in bulk (A - B). **(c)**, IET reveals an ultrafast increase of ESA superimposed by the cross-correlation artifact of the experiment due to the

small optical density of IET at the pump wavelength of 400 nm. The increase in less than 500 fs is in the same range compared to the rise of ESA in PyTet in DCM. Thus, the first time constant of multiexponential analysis of PyTet in DCM:IET mixtures can be affected by the rise of IET. However, the ultrafast ISC within 500 fs of PyTet in DCM can be as well evidenced in the absence of IET (refer to **chapter 6.2**). In addition, the transient response of PyTet in DCM:IET mixture (A) is unaffected by long-lasting transient response of the quencher IET (B) as one can observe in minor differences in the rise of A compared to (A - B) in **(d)**. In conclusion, the rise on a long time scale in PyTet in a DCM:IET mixture in comparison to PyTet in DCM occurs clearly from the response of a triplet state uncovered by the fluorescence quenching HAE of IET (further details in **chapter 6.2**).

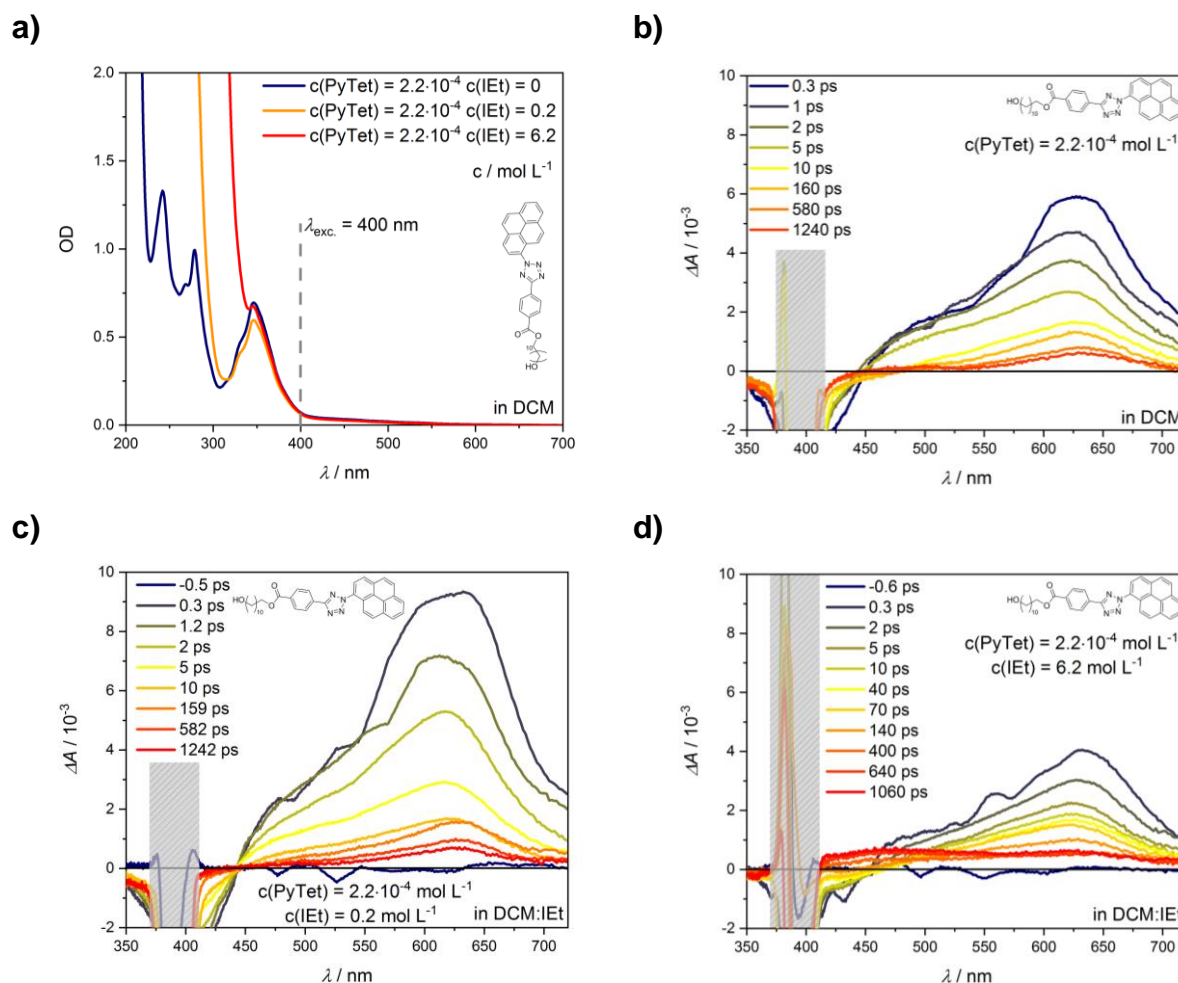


**Figure C12.** Fs-TA of PyTet at low-concentration conditions. **a)** Steady-state UV/Vis spectra of PyTet in DCM and DCM:IET mixtures. TA spectra of PyTet dissolved in **b)** DCM, **c)** in DCM:IET mixture with low  $c(\text{IET})$  and **d)** in DCM:IET mixture with high  $c(\text{IET})$ . Samples are pumped at 400 nm and probed with a CaF<sub>2</sub>-white light continuum between 350 and 720 nm. Time delays and concentrations of PyTet and IET as indicated. Transient response at ~400 nm are omitted due to scattering from pump pulse.

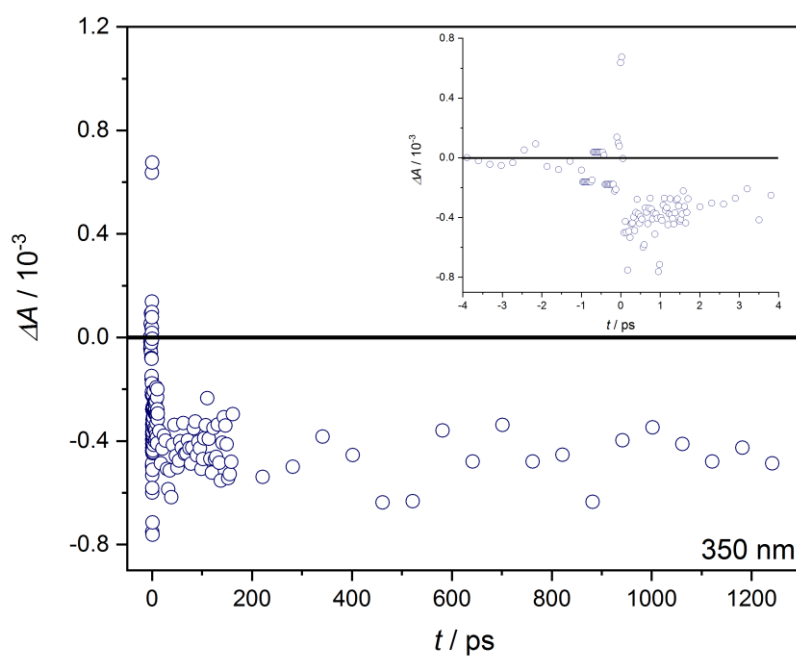


**Figure C13.** Transient response at 350 nm of PyTet in DCM at low concentration  $2.2 \cdot 10^{-4} \text{ mol L}^{-1}$  for inspecting GSB. After excitation, no GSB-recovery is observed within the recorded time window, which is in line with singlet-depopulation via ISC into a long-living triplet state. Inset shows short time scale: Immediately after excitation GSB is observed.

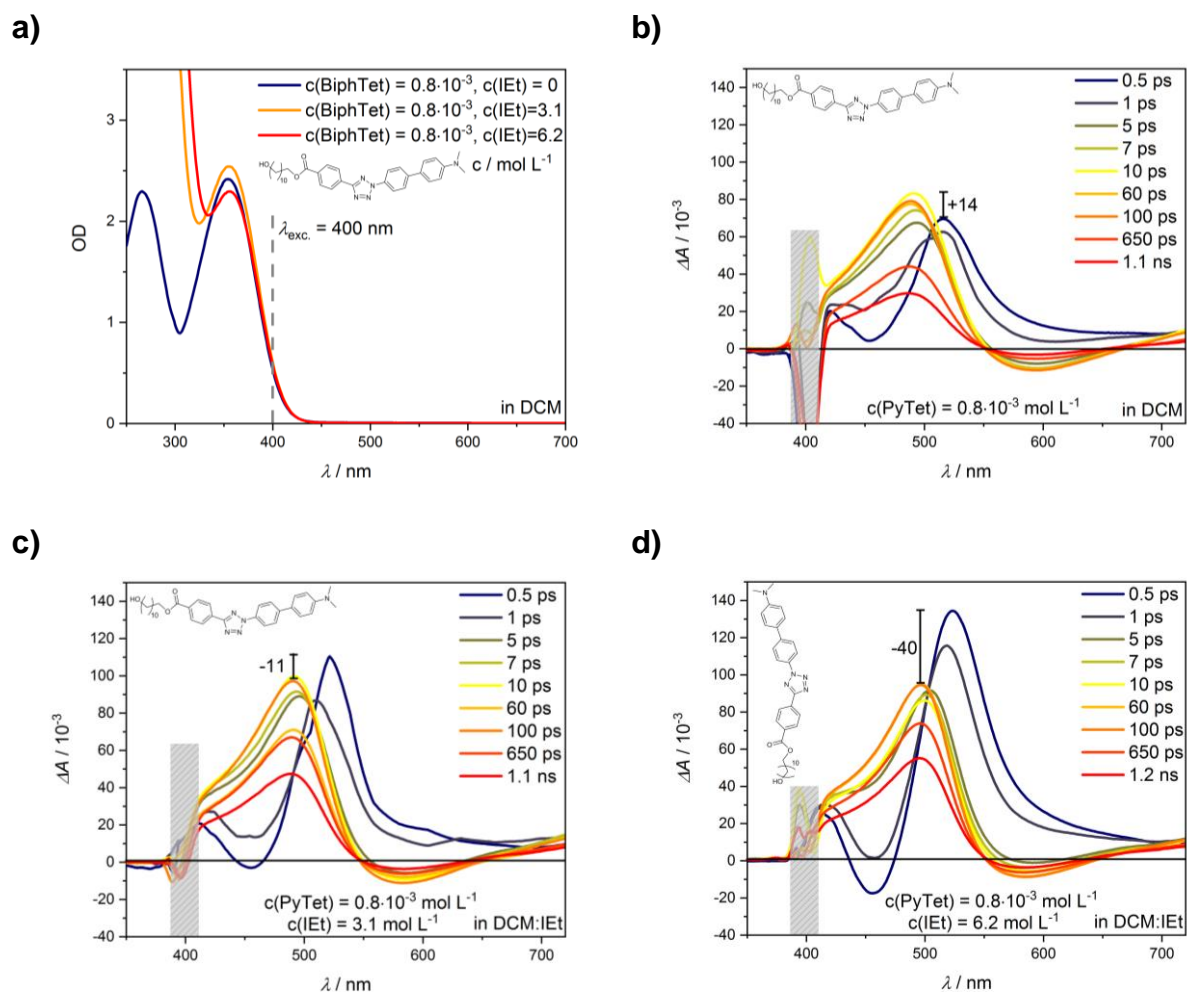


**Figure C14.** **a)** Steady-state UV/Vis spectra of BiphTet in DCM and DCM:IEt mixtures. TA spectra of BiphTet dissolved in **b)** DCM, **c)** in DCM:IEt mixture with low  $c(\text{IEt})$  and **d)** in DCM:IEt mixture with high  $c(\text{IEt})$ . Samples are pumped at 400 nm and probed with a  $\text{CaF}_2$ -white light continuum between 350 and 720 nm. Time delays and concentrations of BiphTet and IEt as indicated. Transient responses at  $\sim 400 \text{ nm}$  are omitted due to scattering from pump pulse. Black lines indicate the change in  $\Delta A$  after blue shift of ESA.

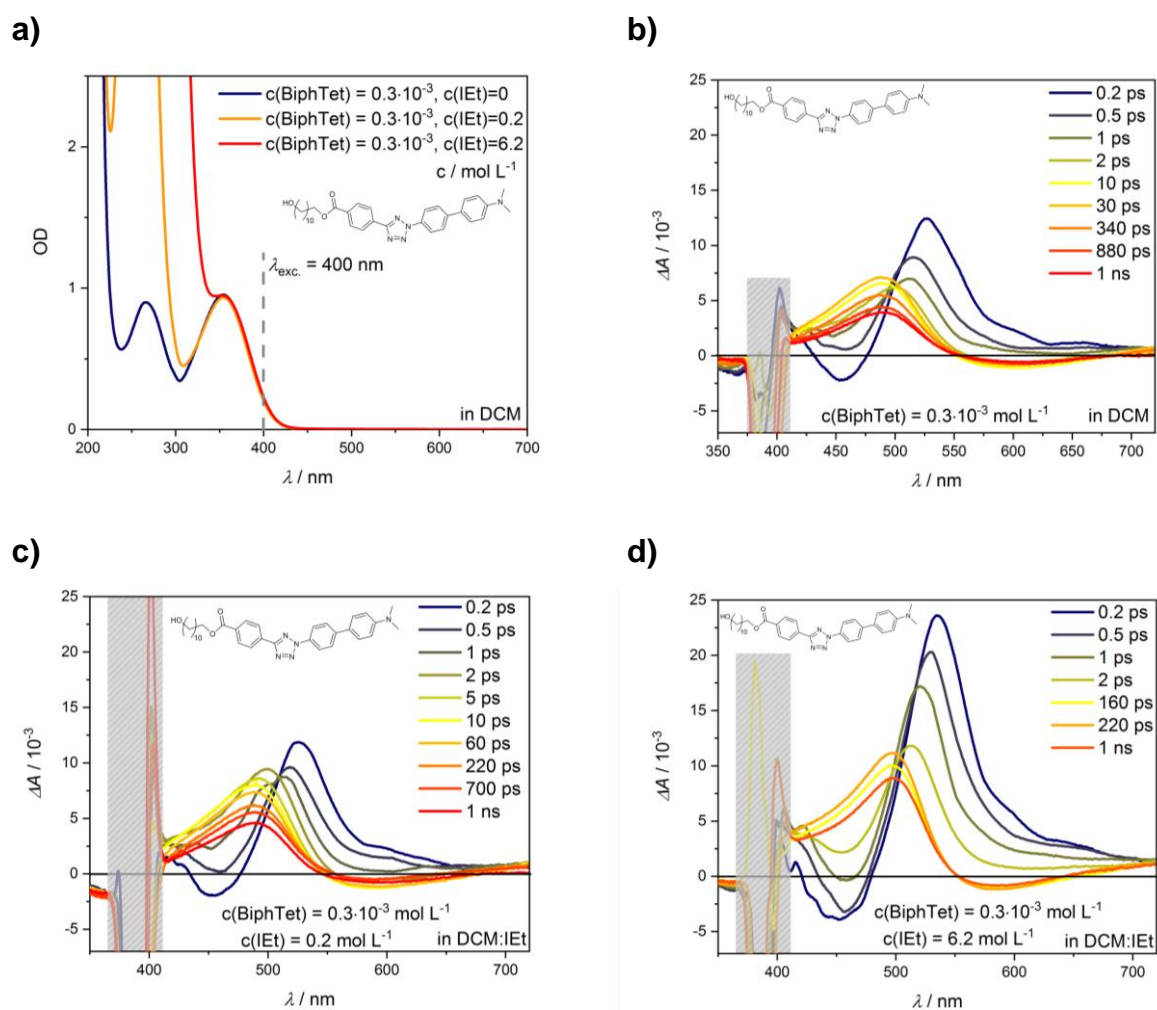


**Figure C15.** fs-TA of BiphTet at low-concentration conditions. **a)** Steady-state UV/Vis spectrum of BiphTet in DCM and DCM:IEt mixtures. TA spectra of BiphTet dissolved in **b)** DCM, **c)** in DCM:IEt mixture with low  $c(\text{IEt})$  and **d)** in DCM:IEt mixture with high  $c(\text{IEt})$ . Samples are pumped at 400 nm and probed with a  $\text{CaF}_2$ -white light continuum between 350 and 720 nm. Time delays and concentrations of BiphTet and IEt as indicated. Transient response at  $\sim 400 \text{ nm}$  are omitted due to scattering from pump pulse.

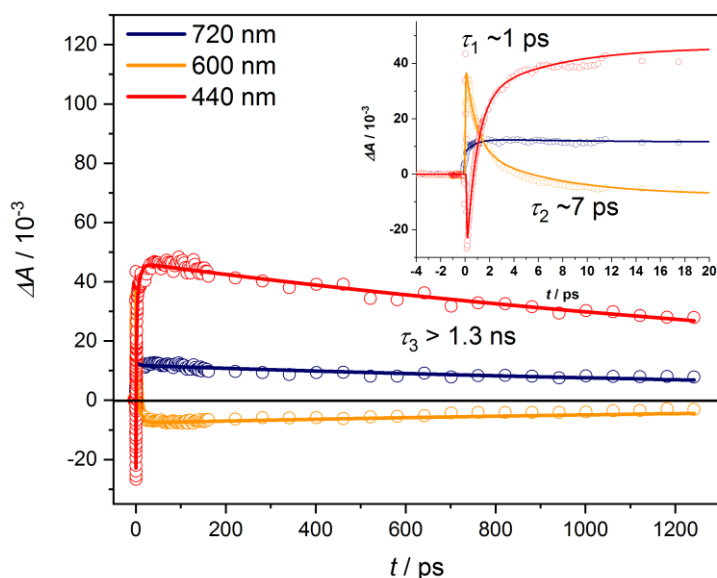


**Figure C16.** Transient response of BiphTet dissolved in DCM:IEt mixture recorded at 720, 600 and 440 nm after excitation at 400 nm (3.1 eV). Transient response at 720 and 440 nm correspond to the same ESA-band, which is superimposed by SE at 600 nm. Decay of ESA-band is correlated to SE-recovery within  $>1.1$  ns. Inset figure: VR within singlet states is changed in the presence of IEt indicated by an additional time constant.

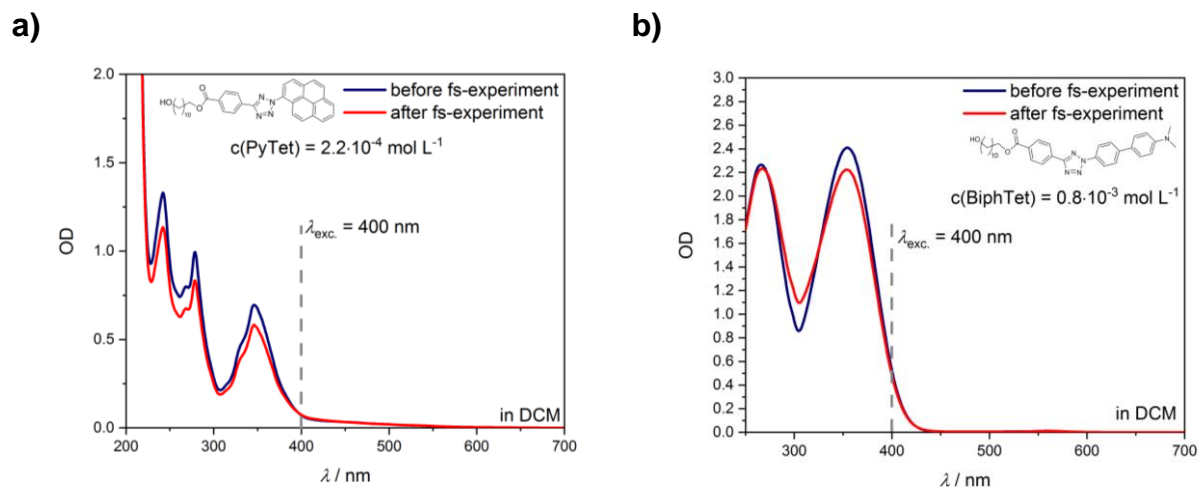


**Figure C17.** Steady-state UV/Vis spectra of **a)** PyTet and **b)** BiphTet in DCM before and after fs-experiment. The lowered OD indicates decomposition of both tetrazoles during the recording of the TA-spectra.

## References

- [1] D. Polli, P. Altoe, O. Weingart, K. M. Spillane, C. Manzoni, D. Brida, G. Tomasello, G. Orlandi, P. Kukura, R. A. Mathies, M. Garavelli, G. Cerullo, *Nature* **2010**, *467*, 440-443.
- [2] A. H. Zewail, *Science* **1988**, *242*, 1645-1653.
- [3] A. H. Zewail, *Pure Appl. Chem.* **2000**, *72*, 2219-2231.
- [4] C. Schweigert, O. Babii, S. Afonin, T. Schober, J. Leier, N. C. Michenfelder, I. V. Komarov, A. S. Ulrich, A. N. Unterreiner, *ChemPhotoChem* **2019**, *3*, 1-9.
- [5] Y. Hontani, M. Broser, A. Silapetere, B. S. Krause, P. Hegemann, J. T. M. Kennis, *Phys. Chem. Chem. Phys.* **2017**, *19*, 30402-30409.
- [6] V. I. Minkin, *Russ. Chem. Rev.* **2013**, *82*, 1-26.
- [7] M. A. Tasdelen, Y. Yagci, *Angew. Chem., Int. Ed.* **2013**, *52*, 5930-5938.
- [8] J.-P. Fouassier, J. Lalevée, *Photoinitiators for Polymer Synthesis: Scope, Reactivity, and Efficiency*, Wiley & Sons, **2012**.
- [9] M. Kasha, *Discuss. Faraday Soc.* **1950**, *9*, 14-19.
- [10] I. V. Khudiyakov, Y. A. Serebrennikov, N. J. Turro, *Chem. Rev.* **1993**, *93*, 537-570.
- [11] M. Kasha, *J. Chem. Phys.* **1952**, *20*, 71-74.
- [12] A. P. Demchenko, J. Heldt, J. Waluk, P.-T. Chou, P. K. Sengupta, L. Brizhik, J. C. del Valle, *Angew. Chem.* **2014**, *126*, 14542-14551.
- [13] A. B. Beeler, *Chem. Rev.* **2016**, *116*, 9629-9630.
- [14] J. T. Offenloch, M. Gernhardt, J. P. Blinco, H. Frisch, H. Mutlu, C. Barner-Kowollik, *Chemistry* **2019**, *25*, 3700-3709.
- [15] K. Dietliker, R. Hüsler, J. L. Birbaum, S. Ilg, S. Villeneuve, K. Studer, T. Jung, J. Benkhoff, H. Kura, A. Matsumoto, H. Oka, *Prog. Org. Coat.* **2007**, *58*, 146-157.
- [16] F. Karasu, C. Croutxé-Barghorn, X. Allonas, L. G. J. Van Der Ven, *J. of Polym. Sci, Part A: Polym. Chem.* **2014**, *52*, 3597-3607.
- [17] N. Moszner, U. K. Fischer, B. Ganster, R. Liska, V. Rheinberger, *Dent. Mater.* **2008**, *24*, 901-907.
- [18] K. Ikemura, T. Endo, *Dent. Mater. J.* **2010**, *29*, 481-501.
- [19] T. Billiet, M. Vandenhoute, J. Schelfhout, S. Van Vlierberghe, P. Dubruel, *Biomaterials* **2012**, *33*, 6020-6041.
- [20] J. Fischer, G. von Freymann, M. Wegener, *Adv. Mater.* **2010**, *22*, 3578-3582.
- [21] P. Lederhose, K. N. Wust, C. Barner-Kowollik, J. P. Blinco, *Chem. Commun.* **2016**, *52*, 5928-5931.
- [22] C. Heiler, J. T. Offenloch, E. Blasco, C. Barner-Kowollik, *ACS Macro Lett.* **2016**, *6*, 56-61.
- [23] C. Heiler, S. Bastian, P. Lederhose, J. P. Blinco, E. Blasco, C. Barner-Kowollik, *Chem. Commun.* **2018**, *54*, 3476-3479.

- [24] J. O. Mueller, D. Voll, F. G. Schmidt, G. Delaittre, C. Barner-Kowollik, *Chem. Commun.* **2014**, 50, 15681-15684.
- [25] K. Hildebrandt, T. Pauloehrl, J. P. Blinco, K. Linkert, H. G. Borner, C. Barner-Kowollik, *Angew. Chem., Int. Ed.* **2015**, 54, 2838-2843.
- [26] Y. Wang, W. J. Hu, W. Song, R. K. V. Lim, Q. Lin, *Org. Lett.* **2008**, 10, 3725-3728.
- [27] W. Song, Y. Wong, J. Qu, Q. Lin, *J. Am. Chem. Soc.* **2008**, 130, 9654-9655.
- [28] P. Lederhose, D. Abt, A. Welle, R. Muller, C. Barner-Kowollik, J. P. Blinco, *Chemistry* **2018**, 24, 576-580.
- [29] E. Blasco, M. Piñol, L. Oriol, B. V. K. J. Schmidt, A. Welle, V. Trouillet, M. Bruns, C. Barner-Kowollik, *Adv. Func. Mater.* **2013**, 23, 4011-4019.
- [30] E. Blasco, Y. Sugawara, P. Lederhose, J. P. Blinco, A.-M. Kelterer, C. Barner-Kowollik, *ChemPhotoChem* **2017**, 2, 1-6.
- [31] W. Feuerstein, S. Höfener, W. Klopfer, I. Lamparth, N. Moszner, C. Barner-Kowollik, A.-N. Unterreiner, *ChemPhysChem* **2016**, 17, 3460-3469.
- [32] D. Voll, T. Junkers, C. Barner-Kowollik, *Macromolecules* **2011**, 44, 2542-2551.
- [33] T. J. A. Wolf, D. Voll, C. Barner-Kowollik, A. N. Unterreiner, *Macromolecules* **2012**, 45, 2257-2266.
- [34] E. Frick, H. A. Ernst, D. Voll, T. J. A. Wolf, A.-N. Unterreiner, C. Barner-Kowollik, *Polym. Chem.* **2014**, 5, 5053-5068.
- [35] E. Frick, C. Schweigert, B. B. Noble, H. A. Ernst, A. Lauer, Y. Liang, D. Voll, M. L. Coote, A. N. Unterreiner, C. Barner-Kowollik, *Macromolecules* **2016**, 49, 80-89.
- [36] H. Hayashi, K. Mochida, *Chem. Phys. Lett.* **1983**, 101, 307-311.
- [37] M. Wakasa, K. Mochida, Y. Sakaguchi, J. Nakamura, H. Hayashi, *J. Phys. Chem.* **1991**, 95, 2241-2246.
- [38] A. Eibel, J. Radebner, M. Haas, D. E. Fast, H. Freißmuth, E. Stadler, P. Faschauner, A. Torvisco, I. Lamparth, N. Moszner, H. Stueger, G. Gescheidt, *Polym. Chem.* **2018**, 9, 38-47.
- [39] B. Ganster, U. K. Fischer, N. Moszner, R. Liska, *Macromolecules* **2008**, 41, 2394-2400.
- [40] J. Radebner, A. Eibel, M. Leybold, C. Gorsche, L. Schuh, R. Fischer, A. Torvisco, D. Neshchadin, R. Geier, N. Moszner, R. Liska, G. Gescheidt, M. Haas, H. Stueger, *Angew. Chem., Int. Ed.* **2017**, 56, 3103-3107.
- [41] M. Mitterbauer, P. Knaack, S. Naumov, M. Markovic, A. Ovsianikov, N. Moszner, R. Liska, *Angew. Chem.* **2018**, 130, 12323-12327.
- [42] Z. Rappoport, *The chemistry of organic germanium, tin and lead compounds*, 2 ed., Wiley & Sons, **2002**.
- [43] D. Neshchadin, A. Rosspeintner, M. Griesser, B. Lang, S. Mosquera-Vazquez, E. Vauthey, V. Gorelik, R. Liska, C. Hametner, B. Ganster, R. Saf, N. Moszner, G. Gescheidt, *J. Am. Chem. Soc.* **2013**, 135, 17314-17321.
- [44] E. W.-G. Diau, C. Kötting, A. H. Zewail, *ChemPhysChem* **2001**, 2, 273-293.
- [45] J. S. Clovis, A. Eckell, R. Huisgen, R. Sustmann, *Chem. Ber.* **1967**, 100, 60-70.

- [46] J. P. Menzel, B. B. Noble, A. Lauer, M. L. Coote, J. P. Blinco, C. Barner-Kowollik, *J. Am. Chem. Soc.* **2017**, *139*, 15812-15820.
- [47] B. Yuan, E. R. Bernstein, *J. Chem. Phys.* **2016**, *144*, 234302.
- [48] N. J. Turro, *Modern Molecular Photochemistry*, University Science Books, **1991**.
- [49] E. Fermi, *Nuclear Physics*, University of Chicago Press - Midway Print, **1950**.
- [50] A. Jablonski, *Z. Phys.* **1935**, *94*, 38-46.
- [51] P. W. Atkins, J. d. Paula, *Physikalische Chemie*, 5 ed., Wiley-VCH, Weinheim, **2013**.
- [52] O. Schalk, A.-N. Unterreiner, *J. Phys. Chem. A* **2007**, *111*, 3231–3240.
- [53] N. C. Michenfelder, H. A. Ernst, C. Schweigert, M. Olzmann, A. N. Unterreiner, *Phys. Chem. Chem. Phys.* **2018**, *20*, 10713-10720.
- [54] G. A. Worth, L. S. Cederbaum, *Annu. Rev. Phys. Chem.* **2004**, *55*, 127-158.
- [55] S. A. Trushin, S. Diemer, W. Fuß, K. L. Kompa, W. E. Schmid, *Phys. Chem. Chem. Phys.* **1999**, *1*, 1431-1440.
- [56] L. S. Cederbaum, W. Domcke, H. Koppel, W. Vonniessen, *Chem. Phys.* **1977**, *26*, 169-177.
- [57] H. Koppel, W. Domcke, L. S. Cederbaum, *Adv. Chem. Phys.* **1984**, *57*, 59-246.
- [58] T. J. Martinez, *Nature* **2010**, *467*, 412-413.
- [59] W. Demtröder, *Molekülphysik - Theoretische Grundlagen und experimentelle Methoden*, Oldenbourg Wissenschaftsverlag, **2003**.
- [60] M. Spichy, N. J. Turro, G. Rist, J. L. Birbaum, K. Dietliker, J. P. Wolf, G. Gescheidt, *J. Photochem. Photobiol. A* **2001**, *142*, 209-213.
- [61] P. Atkins, R. Friedman, *Molecular Quantum Mechanics*, 4 ed., Oxford University Press, **2005**.
- [62] G. J. Hoijtink, *Mol. Phys.* **1960**, *3*, 67-70.
- [63] H. Haken, H. C. Wolf, *Atom- und Quantenphysik*, 6 ed., Springer, Berlin, **1996**.
- [64] M. Monsigny, F. Delmotte, C. Hélène, *Proc. Natl. Acad. Sci. USA* **1978**, *75*, 1324-1328.
- [65] D. O. Cowan, J. C. Koziar, *J. Am. Chem. Soc.* **1975**, *97*, 249-253.
- [66] M. K., T. P. Davis, *Handbook of radical polymerization*, Wiley & Sons, **2003**.
- [67] G. Odian, *Principles of polymerization*, Wiley & Sons, **2004**.
- [68] C. J. Hawker, *J. Am. Chem. Soc.* **1994**, *116*, 11185-11186.
- [69] P. E. M. Allen, C. R. Patrick, *Macromol. Chem. Phys.* **1961**, *47*, 154-167.
- [70] J. Krstina, G. Moad, E. Rizzardo, C. L. Winzor, *Macromolecules* **1995**, *28*, 5381-5385.
- [71] D. R. Hensley, S. D. Goodrich, A. Y. Huckstep, H. J. Harwood, P. L. Rinaldi, *Macromolecules* **1995**, *28*, 1586-1591.
- [72] R. G. W. Norrish, C. H. Bamford, *Nature* **1936**, *138*, 1016.

- [73] D. S. Esen, N. Arsu, J. P. Da Silva, S. Jockusch, N. J. Turro, *J. Polym. Sci. Part A: Polym. Chem.* **2013**, *51*, 1865-1871.
- [74] S. Jockusch, M. S. Landis, B. Freiermuth, N. J. Turro, *Macromolecules* **2001**, *34*, 1619-1626.
- [75] D. E. Fast, A. Lauer, J. P. Menzel, A.-M. Kelterer, G. Gescheidt, C. Barner-Kowollik, *Macromolecules* **2017**, *50*, 1815-1823.
- [76] L. Gonsalvi, M. Peruzzini, *Angew. Chem.* **2012**, *124*, 8017-8019.
- [77] S. Straub, J. Lindner, P. Vöhringer, *J. Phys. Chem. A* **2017**.
- [78] G. Temel, B. Enginol, M. Aydin, D. K. Balta, N. Arsu, *J. Photochem. Photobio. A* **2011**, *219*, 26-31.
- [79] R. Liska, *J. Polym. Sci. Part A Polym. Chem.* **2004**, *42*, 2285-2301.
- [80] J. Jakubiak, X. Allonas, J. P. Fouassier, A. Sionkowska, E. Andrzejewska, L. Å. Linden, J. F. Rabek, *Polymer* **2003**, *44*, 5219-5226.
- [81] Y. N. T. Yamaoka, K. Koseki, T. Shirosaki, *Polym. Adv. Technol.* **1990**, *1*, 287-295.
- [82] V. Lohse, P. Leihkauf, C. Csongar, G. Tomaschewski, *J. prakt. Chem.* **1988**, *330*, 406-414.
- [83] Y. Wang, C. I. R. Vera, Q. Lin, *Org. Lett.* **2007**, *9*, 4155-4158.
- [84] Y. Wang, W. Song, W. J. Hu, Q. Lin, *Angew. Chem., Int. Ed.* **2009**, *48*, 5330-5333.
- [85] S. L. Zheng, Y. Wang, Z. Yu, Q. Lin, P. Coppens, *J. Am. Chem. Soc.* **2009**, *131*, 18036-18037.
- [86] C. J. Dürr, P. Lederhose, L. Hlalele, D. Abt, A. Kaiser, S. Brandau, C. Barner-Kowollik, *Macromolecules* **2013**, *46*, 5915-5923.
- [87] W. Demtröder, *Laserspektroskopie 2*, Springer, **2013**.
- [88] P. An, Z. Yu, Q. Lin, *Chem. Commun.* **2013**, *49*, 9920-9922.
- [89] E. Hecht, *Optik*, 6 ed., De Gruyter, **2014**.
- [90] H. Zeng, X.-W. Du, S. C. Singh, S. A. Kulinich, S. Yang, J. He, W. Cai, *Adv. Func. Mater.* **2012**, *22*, 1333-1353.
- [91] U. K. Tirlapur, K. König, *Nature* **2002**, *418*, 290-291.
- [92] A. P. Aleksandrov, V. N. Genkin, M. S. Kitai, I. M. Smimova, V. V. Sokolov, *Sov. J. Quant. Electron.* **1977**, *7*, 547-550.
- [93] O. F. Olaj, I. Bitai, F. Hinkelmann, *Makromol. Chem.* **1987**, *188*, 1689-1702.
- [94] T. Junkers, M. Schneider-Baumann, S. S. P. Koo, P. Castignolles, C. Barner-Kowollik, *Macromolecules* **2010**, *43*, 10427-10434.
- [95] K. B. Kockler, A. P. Haehnel, T. Junkers, C. Barner-Kowollik, *Macromol. Rapid Commun.* **2016**, *37*, 123-134.
- [96] T. Gruending, S. Weidner, J. Falkenhagen, C. Barner-Kowollik, *Polym. Chem.* **2010**, *1*, 599-617.
- [97] W. Lauterborn, T. Kurz, M. Wiesenfeldt, *Coherent Optics. Fundamentals and Applications*, Springer, **1993**.

- [98] J. Lu, M. Prabhu, J. Song, C. Li, J. Xu, K. Ueda, A. A. Kaminskii, H. Yagi, T. Yanagitani, *Appl. Phys. B* **2000**, *71*, 469-473.
- [99] D. S. Sumida, T. Y. Fan, *Opt. Lett.* **1994**, *19*, 1343-1345.
- [100] J. O. White, *IEEE J Quantum Elect* **2009**, *45*, 1213-1220.
- [101] C. Rullière, *Femtosecond Laser Pulses - Principles and Experiments*, Springer, **1998**.
- [102] J.-C. Diels, W. Rudolph, *Ultrashort Laser Pulse Phenomena* 2ed., Elsevier, **2006**.
- [103] R. W. Boyd, *Nonlinear Optics*, 3 ed., Academic Press, **2008**.
- [104] W. Koechner, *Solid-State Laser Engineering*, 6 ed., Springer, **2006**.
- [105] E. Riedle, M. Beutter, S. Lochbrunner, J. Piel, S. Schenkl, S. Spörlein, W. Zinth, *Appl. Phys. B* **2000**, *71*, 457-465.
- [106] A. Couairon, A. Mysyrowicz, *Phys. Rep.* **2007**, *441*, 47-189.
- [107] R. Huber, H. Satzger, W. Zinth, J. Wachtveitl, *Opt. Commun.* **2001**, *194*, 443-448.
- [108] D. Strickland, G. Mourou, *Opt. Commun.* **1985**, *56*, 219-221.
- [109] R. I. Fork, O. E. Martinez, J. P. Gordon, *Opt. Lett.* **1984**, *9*, 150-152.
- [110] J. H. Gross, *Massenspektrometrie*, Springer Spektrum, **2011**.
- [111] C. Enjalbal, D. Maux, R. Combarieu, J. Martinez, J.-L. Aubagnac, *J. Comb. Chem.* **2003**, *5*, 102-109.
- [112] D. Maux, C. Enjalbal, J. Martinez, J.-L. Aubagnac, *J. Am. Soc. Mass Spectrom.* **2001**, *12*, 1099-1105.
- [113] D. Kretschy, G. Koellensperger, S. Hann, *Anal. Chim. Acta* **2012**, *750*, 98-110.
- [114] M. Yuan, S. B. Breitkopf, X. Yang, J. M. Asara, *Nat. Protoc.* **2012**, *7*, 872-881.
- [115] G. Danger, F. R. Orthous-Daunay, P. de Marcellus, P. Modica, V. Vuitton, F. Duvernay, L. Flandinet, L. Le Sergeant d'Hendecourt, R. Thissen, T. Chiavassa, *Geochim. Cosmochim. Acta* **2013**, *118*, 184-201.
- [116] J. F. Greisch, K. Y. Amsharov, J. Weippert, P. Weis, A. Bottcher, M. M. Kappes, *J. Am. Chem. Soc.* **2016**, *138*, 11254-11263.
- [117] S. Castellino, M. R. Groseclose, D. Wagner, *Bioanalysis* **2011**, *3*, 2427-2441.
- [118] A. K. Malik, C. Blasco, Y. Pico, *J. Chromatogr. A* **2010**, *1217*, 4018-4040.
- [119] C. B. Kowollik, T. Gruending, J. Falkenhagen, S. Weidner, *Mass Spectrometry in Polymer Chemistry*, Wiley VCH, **2012**.
- [120] J. J. Thomson, *Lond. Edinb. Dubl. Phil. Mag.* **1897**, *44*, 293-316.
- [121] A. Makarov, *Anal. Chem.* **2000**, *72*, 1156-1162.
- [122] G. I. Taylor, *Proc. Roy. Soc. A* **1964**, *280*, 383-397.
- [123] M. Hardman, A. Makarov, *Anal. Chem.* **2003**, *75*, 1699-1705.

- [124] F. Jensen, *Introduction to Computational Chemistry*, 3. ed., Wiley & Sons, **2017**.
- [125] T. Helgaker, W. Klopper, D. P. Tew, *Mol. Phys.* **2008**, *106*, 2107-2143.
- [126] F. Furche, *J. Chem. Phys.* **2001**, *114*, 5982-5992.
- [127] A. D. Laurent, D. Jacquemin, *Int. J. Quant. Chem.* **2013**, *113*, 2019-2039.
- [128] P. Hohenberg, W. Kohn, *Phys. Rev.* **1964**, *136*, B864-B871.
- [129] W. Kohn, L. J. Sham, *Phys. Rev.* **1965**, *140*, A1133-A1138.
- [130] A. D. Becke, *J. Chem. Phys.* **1993**, *98*, 5648-5652.
- [131] P. J. Stephens, F. J. Devlin, C. F. Chabalowski, M. J. Frisch, *J. Phys. Chem.* **1994**, *98*, 11623-11627.
- [132] A. D. Becke, *J. Chem. Phys.* **2014**, *140*, 18A301.
- [133] E. Runge, E. K. U. Gross, *Phys. Rev. Lett.* **1984**, *52*, 997-1000.
- [134] K. Rurack, M. Spieles, *Anal. Chem.* **2011**, *83*, 1232-1242.
- [135] G. A. Reynolds, K. H. Drexhage, *Opt. Commun.* **1975**, *13*, 222-225.
- [136] C. Schweigert, *Untersuchung lokaler Umgebungsvariation auf das Relaxationsverhalten photoangeregter Zustände von Moleküle in Lösung mittels Femtosekunden-Breitband-Absorptionsspektroskopie*, Logos Verlag (Dissertation, Karlsruhe Institute of Technology), Berlin, Karlsruhe, ISBN 978-3-8325-4823-0, **2018**.
- [137] S. Pedersen, A. H. Zewail, *Mol. Phys.* **1996**, *89*, 1455-1502.
- [138] I. H. van Stokkum, D. S. Larsen, R. van Grondelle, *Biochim. Biophys. Acta* **2004**, *1657*, 82-104.
- [139] TURBOMOLE V7.0 2015, a development of University of Karlsruhe and Forschungszentrum Karlsruhe GmbH: 1989-2007, TURBOMOLE GmbH, since 2007; available from <http://www.turbomole.com>.
- [140] F. Weigend, M. Häser, H. Patzelt, R. Ahlrichs, *Chem. Phys. Lett.* **1998**, *294*, 143-152.
- [141] P. Deglmann, F. Furche, R. Ahlrichs, *Chem. Phys. Lett.* **2002**, *362*, 511-518.
- [142] G. H. Wu, S. H. Hsu, *J. Med. Biol. Eng.* **2015**, *35*, 285-292.
- [143] F. Günzler, E. H. H. Wong, S. P. S. Koo, T. Junkers, C. Barner-Kowollik, *Macromolecules* **2009**, *42*, 1488-1493.
- [144] P. Jöckle, C. Schweigert, I. Lamparth, N. Moszner, A.-N. Unterreiner, C. Barner-Kowollik, *Macromolecules* **2017**, *50*, 8894-8906.
- [145] P. Jöckle, J. Radebner, M. Haas, I. Lamparth, H. Stueger, N. Moszner, A.-N. Unterreiner, C. Barner-Kowollik, *ACS Macro Lett.* **2018**, *7*, 132-136.
- [146] P. Jöckle, P. W. Kamm, I. Lamparth, N. Moszner, A.-N. Unterreiner, C. Barner-Kowollik, *Macromolecules* **2019**, *52*, 281-291.
- [147] J. Radebner, M. Leybold, A. Eibel, J. Maier, L. Schuh, A. Torvisco, R. Fischer, N. Moszner, G. Gescheidt, H. Stueger, M. Haas, *Organometallics* **2017**.
- [148] K. De Bruycker, T. Krappitz, C. Barner-Kowollik, *ACS Macro Lett.* **2018**, *7*, 1443-1447.

- [149] S. Jockusch, N. J. Turro, *J. Am. Chem. Soc.* **1989**, *120*, 11773-11777.
- [150] K. Dietliker, J. L. Birnbaum, R. Hüsler, G. Baudin, J. P. Wolf, *CHIMIA* **2002**, *56*, 197-202.
- [151] D. E. Fast, M. Zalibera, A. Lauer, A. Eibel, C. Schweigert, A.-M. Kelterer, M. Spichy, D. Neshchadin, D. Voll, H. Ernst, Y. Liang, K. Dietliker, A.-N. Unterreiner, C. Barner-Kowollik, H. Grützmaker, G. Gescheidt, *Chem. Commun.* **2016**, *52*, 9917-9920.
- [152] P. Mladenovic, *Combinatorics. A Problem-Based Approach*, Springer, **2019**.
- [153] S. Jockusch, I. V. Koptug, P. F. McGarry, G. W. Sluggett, N. J. Turro, D. M. Watkins, *J. Am. Chem. Soc.* **1997**, *119*, 11495-11501.
- [154] H. A. Ernst, T. J. A. Wolf, O. Schalk, N. González-García, A. E. Boguslavskiy, A. Stolow, M. Olzmann, A.-N. Unterreiner, *J. Phys. Chem. A* **2015**, *119*, 9225-9235.
- [155] M. Wojdyla, S. A. Gallagher, M. P. Moloney, Y. K. Gun'ko, J. M. Kelly, L. M. Magno, S. J. Quinn, I. P. Clark, G. M. Greetham, M. Towrie, *J. Phys. Chem. C* **2012**, *116*, 16226-16232.
- [156] P. W. Kamm, *Physical and Chemical Properties of Photoinitiators Based on Mono-, Bis- and Tetraacylgermanes after Visible Light Excitation*, Karlsruhe Institute of Technology, **2018**.
- [157] D. E. Marschner, H. Frisch, J. T. Offenloch, B. T. Tuten, C. R. Becer, A. Walther, A. S. Goldmann, P. Tzvetkova, C. Barner-Kowollik, *Macromolecules* **2018**, *51*, 3802-3807.
- [158] J. Radebner, A. Eibel, M. Leybold, N. Jungwirth, T. Pickl, A. Torvisco, R. Fischer, U. K. Fischer, N. Moszner, G. Gescheidt, H. Stueger, M. Haas, *Chemistry* **2018**, *24*, 8281-8285.
- [159] G. J. D. Peddle, *J. Organometal. Chem.* **1968**, *14*, 139-147.
- [160] J. Duhamel, *Langmuir* **2012**, *28*, 6527-6538.
- [161] T. Medinger, F. Wilkinson, *Trans. Faraday Soc.* **1966**, *62*, 1785-1792.
- [162] J. W. Bridges, P. J. Creaven, R. T. Williams, *Biochem. J.* **1965**, *96*, 872-878.
- [163] P. Foggi, L. Pettini, I. Santa, R. Righini, S. Califano, *J. Phys. Chem.* **1995**, *99*, 7439-7445.
- [164] J. Bendig, M. Siegmund, S. Helm, *Advances in Molecular Relaxation and Interaction Processes* **1979**, *14*, 121-132.
- [165] D. O. Cowan, J. C. Koziar, *J. Am. Chem. Soc.* **1975**, *97*, 249-254.
- [166] T. Medinger, F. Wilkinson, *Trans. Faraday Soc.* **1965**, *61*, 620-630.
- [167] M. Baba, M. Saitoh, Y. Kowaka, K. Taguma, K. Yoshida, Y. Semba, S. Kasahara, T. Yamanaka, Y. Ohshima, Y. C. Hsu, S. H. Lin, *J. Chem. Phys.* **2009**, *131*, 224318.
- [168] H. Gustmann, D. Lefrancois, A. J. Reuss, D. B. Gophane, M. Braun, A. Dreuw, S. T. Sigurdsson, J. Wachtveitl, *Phys. Chem. Chem. Phys.* **2017**, *19*, 26255-26264.
- [169] F. Kanal, D. Schleier, P. Nuernberger, *ChemPhysChem* **2015**, *16*, 3143-3146.
- [170] P. Sen, D. Roy, S. K. Mondal, K. Sahu, S. Ghosh, K. Bhattacharyya, *J. Phys. Chem. A* **2005**, *109*, 9716-9722.
- [171] T. Takaya, H. O. Hamaguchi, K. Iwata, *J. Chem. Phys.* **2009**, *130*, 014501.
- [172] A. Rupenyan, I. H. M. v. Stokkum, J. C. Arents, R. v. Grondelle, K. J. Hellingwerf, M. L. Groot, *J. Phys. Chem. B* **2009**, *113*, 16251-16256.

- [173] T. W. Kee, *J. Phys. Chem. Lett.* **2014**, *5*, 3231-3240.
- [174] B. Lang, S. Mosquera-Vazquez, D. Lovy, P. Sherin, V. Markovic, E. Vauthey, *Rev. Sci. Instrum.* **2013**, *84*, 073107.
- [175] U. Megerle, M. Wenninger, R. J. Kutta, R. Lechner, B. Konig, B. Dick, E. Riedle, *Phys. Chem. Chem. Phys.* **2011**, *13*, 8869-8880.
- [176] J. L. Pérez-Lustres, F. Rodriguez-Prieto, M. Mosquera, T. A. Senyushkina, N. P. Ernsting, S. A. Kovalenko, *J. Am. Chem. Soc.* **2007**, *129*, 5408-5418.
- [177] M. Gerecke, G. Bierhance, M. Gutmann, N. P. Ernsting, A. Rosspeintner, *Rev. Sci. Instrum.* **2016**, *87*, 053115.
- [178] R. Schanz, S. A. Kovalenko, V. Kharlanov, N. P. Ernsting, *Appl. Phys. Lett.* **2001**, *79*, 566-568.
- [179] E. C. Carroll, M. P. Hill, D. Madsen, K. R. Malley, D. S. Larsen, *Rev. Sci. Instrum.* **2009**, *80*, 026102.
- [180] P. T. Snee, C. K. Payne, K. T. Kotz, H. Yang, C. B. Harris, *J. Am. Chem. Soc.* **2001**, *123*, 2255-2264.
- [181] G. Knopp, P. Beaud, P. P. Radi, M. Tulej, A. P. Kouzov, B. Bourgie, T. Gerber, *PSI Sci. Rep.* **2001**, *5*, 55-56.
- [182] S. Marggi Poullain, P. Recio, D. V. Chicharro, L. Rubio-Lago, J. Gonzalez-Vazquez, L. Banares, *Phys. Chem. Chem. Phys.* **2018**.
- [183] Y. Tang, W. B. Lee, Z. Hu, B. Zhang, K. C. Lin, *J. Chem. Phys.* **2007**, *126*, 064302.
- [184] D. L. Phillips, B. A. Lawrence, J. J. Valentini, *J. Phys. Chem.* **1991**, *95*, 9085-9091.
- [185] N. Knoblauch, A. Strobel, I. Fischer, V. E. Bondybey, *J. Chem. Phys.* **1995**, *103*, 5417-5427.
- [186] M. Oheim, D. J. Michael, M. Geisbauer, D. Madsen, R. H. Chow, *Adv. Drug. Deliv. Rev.* **2006**, *58*, 788-808.
- [187] R. Xian, G. Corthey, D. M. Rogers, C. A. Morrison, V. I. Prokhorenko, S. A. Hayes, R. J. D. Miller, *Nature Chem.* **2017**, *9*, 516-522.
- [188] H. J. Liu, S. H. Pullen, L. A. W. II, R. J. Sension, *J. Chem. Phys.* **1998**, *108*, 4992-5001.

## List of Publications

P. Jöckle, C. Schweigert, I. Lamparth, N. Moszner, A.-N. Unterreiner, C. Barner-Kowollik, *Macromolecules* **2017**, *50*, 8894-8906.

P. Jöckle, J. Radebner, M. Haas, I. Lamparth, H. Stueger, N. Moszner, A.-N. Unterreiner, C. Barner-Kowollik, *ACS Macro Lett.* **2018**, *7*, 132-136.

A. Lauer, J. Steinkönig, P. Jöckle, A.-M. Kelterer, A.-N. Unterreiner, C. Barner-Kowollik, *Polym. Chem.* **2018**, *9*, 3336-3341.

P. Jöckle, P. W. Kamm, I. Lamparth, N. Moszner, A.-N. Unterreiner, C. Barner-Kowollik, *Macromolecules* **2019**, *52*, 281-291.

## Conference Contributions

P. Jöckle, C. Schweigert, I. Lamparth, N. Moszner, A.-N. Unterreiner, C. Barner-Kowollik, „An In-Depth Mechanistic Investigation of the Radical Initiation Behavior of Monoacylgermanes”, *Photopolymerization Fundamentals*, Boulder (Colorado, USA), **2017**, poster.

P. Jöckle, C. Barner-Kowollik, A.-N. Unterreiner, „Understanding Visible Light Tetrazole Chemistry via Transient Absorption Spectroscopy“, *Symposium on Molecular Architectures for Fluorescent Imaging of Cells – GRK 2039*, Karlsruhe, **2017**, poster.

P. Jöckle, C. Heiler, C. Barner-Kowollik, A.-N. Unterreiner, „Investigations on visible light-driven tetrazole chemistry via femtosecond absorption spectroscopy“, *Bunsen-tagung 2018 – 117<sup>th</sup> General Assembly of the German Bunsen Society for Physical Chemistry*, Hannover, **2018**, poster.

P. Jöckle, P. W. Kamm, I. Lamparth, N. Moszner, A.-N. Unterreiner, C. Barner-Kowollik, „Comparing Overall Initiation Efficiencies of (*para*-substituted) Mono-, Bis- and Tetraacylgermane Radical Initiators”, *Makromolekulares Kolloquium*, Freiburg, **2019**, poster.